Università degli Studi di Torino
Doctoral School of the University of Torino
PhD Programme in Chemical and Materials Sciences XXXIV Cycle

Hydrogen Storage and Compression based on Metal Hydrides

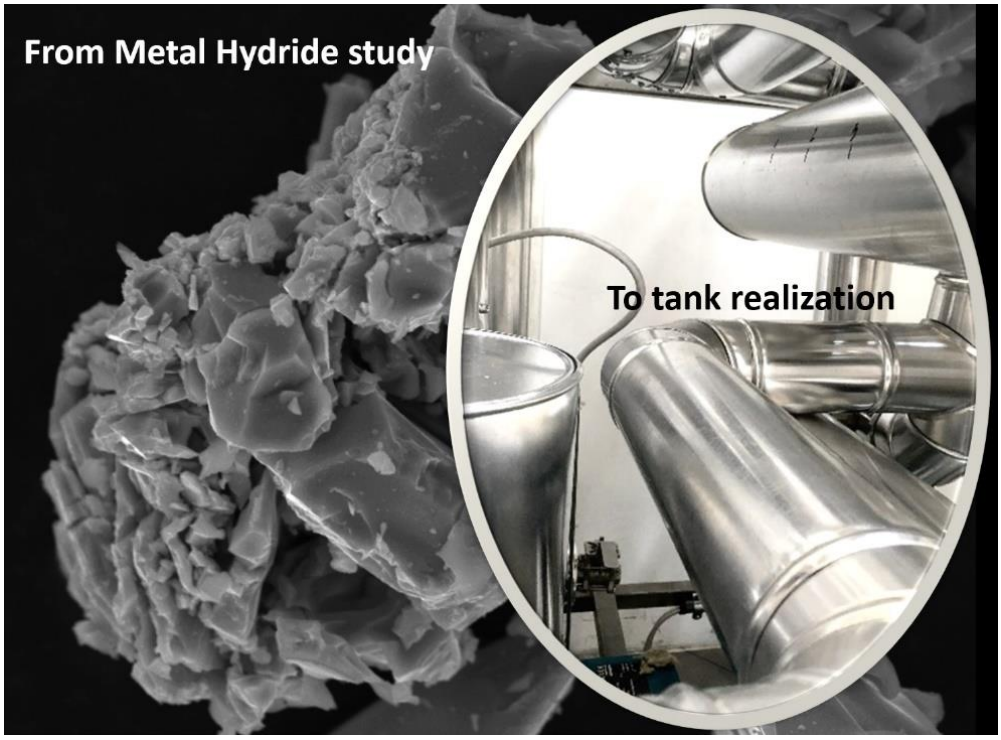

Jussara Barale

Supervisor:
Prof. Marcello Baricco

Università degli Studi di Torino

Doctoral School of the University of Torino

PhD Programme in Chemical and Materials Sciences XXXIV cycle

Hydrogen Storage and Compression based on Metal Hydrides

Candidate: **Jussara Barale**

Supervisor: Prof. **Marcello Baricco**

Jury Members: Prof. **Paola Rizzi**
Università di Torino, Torino, Italy
Dipartimento di Chimica

Prof. **Jose Ramón Ares Fernández**
Universidad Autónoma de Madrid, Madrid, Spain
Grupo de Física de Materiales de Interés en Energías Renovables

Dott. **Giovanni Capurso**
Università degli Studi di Udine, Udine, Italy
Dipartimento Politecnico di Ingegneria e Architettura

Head of the Doctoral School: Prof. Alberto Rizzuti
PhD Programme Coordinator: Prof. Bartolomeo Civalleri

Torino, 1st June 2022

Summary

List of Acronyms

CR	Compression ration
EDX	Energy Dispersive X-Ray
EL	Electrolyser
ENG	Expanded Natural Graphite
EPS	External power source
FC	Fuel Cell
H2CG	Hydrogen as compress gas
H2RS	Hydrogen refuelling station
H2SS	Hydrogen storage system
IMC	Intermetallic compound
MH	Metal hydride
MHC	Metal hydride compressor
PCM	Phase Change Material
PEM	Proton Exchange Membrane
PXD	Powder X-Ray Diffraction
SEM	Scanning Electron Microscopy
Ø	Diameter
TVF	Thermal vector fluid

PhD Activities

List of publications

i. J. Bellosta von Colbe, J.-R. Ares, J. Barale, M. Baricco, C. Buckley, G. Capurso, N. Gallandat, D. M. Grant, M. N. Guzik, I. Jacob, E. H. Jensen, T. Jensen, J. Jepsen, T. Klassen, M. V. Lototskyy, K. Manickam, A. Montone, J. Puszkiel, S. Sartori, D. A. Sheppard, A. Stuart, G. Walker, C. J. Webb, H. Yang, V. Yartys, A. Zuttel, M. Dornheim, "Application of hydrides in hydrogen storage and compression: achievement, outlook and perspective", *Int. J. of Hydrogen Energy, 2019, 15, vol 44, 7780-7808*

ii. J. Barale, S. Deledda, E. M. Dematteis, M. H. Sørby, M. Baricco, B. C. Hauback, "Synthesis and characterization of Magnesium-Iron-Cobalt complex hydrides", *Scientific Report, 2020, 10, 9000*

iii. E. M. Dematteis, J. Barale, M. Corno, A. Sciullo, M. Baricco, P. Rizzi, Solid-state hydrogen storage system and the relevance of a gender perspective, *Energies 2021, 14, 6158*

iv. M. Costamagna, J. Barale, C. Carbone, C. Luetto, A. Agostini, M. Baricco, P. Rizzi, Environmental and economic assessment of hydrogen compression with the metal hydride technology, *Int. J. of Hydrogen. Energy,2022, 47, 10122-10136*

v. E. M. Dematteis, M. B. Amdisen, T. Autrey, J. Barale, M. E. Bowden, C. E. Buckley, Y. Whan Cho, S. Deledda, M. Dornheim, P. de Jongh, J. B. Grinderslev, G. Gizer, V. Gulino, B. C. Hauback, M. Heere, T. Wook Heo, T. D. Humphries, T. R. Jensen, S. Young Kang, Y.-Su Lee, H.-W. Li, S. Li, K. T. Møller, P. Ngene, S. Orimo, M. Paskevicius, M. Polanski, S. Takagi, L. Wan, B. C. Wood, M. Hirscher, M. Baricco, Hydrogen storage in complex hydrides: past activities and new trends, *accepted by Progress in Energy*

vi. J. Barale, E. M. Dematteis, G. Capurso, B. Neuman, S. Deledda, F. Cuevas, M. Latroche, and M. Baricco, "Industrial production and characterisation of $TiFe_{0.85}Mn_{0.05}$ alloy for a hydrogen storage plant", *accepted with revision by Int. J. of Hydrogen. Energy*

vii. M. Dornheim, L. Baetcke, E. Akiba, J.-R. Ares, T. Autrey, J. Barale, M. Baricco, K. Brooks, N. Chalkiadakis, V. Charbonnier, S. Christensen, J. Bellosta von Colbe, M. Costamagna, E. Dematteis, J.-F. Fernández, T. Gennett, D. Grant, T. Wook Heo, K. Hurst, M. Lototskyy, O. Metz, P. Rizzi, K. Sakaki, S. Sartori, E. Stamatakis, A. Stuart, A. Stubos, G. Walker, C. J. Webb, B. Wood, V. Yartys, E. Zoulias, Research and development on hydrogen carrier based solutions for hydrogen compression and storage, *accepted with revision by Progress in Energy*

viii. E. M. Dematteis, J. Barale, G. Capurso, S. Deledda, M. H. Sørby, F. Cuevas, M. Baricco, In-situ neutron diffraction during reversible deuterium loading in Ti-rich and Mn-substituted $Ti(Fe,Mn)_{0.90}$ alloys, *in writing*

ix. J. Barale, F. Nastro, P. Rizzi, C. Luetto, M. Baricco, A metal hydride compressor based on commercial alloys for a small scale H_2 refuelling station, *in writing*

x. J. Barale, G. Capurso, T. Stühff, F. Nastro, B. Neumann, J. Bellosta von Colbe, P. Rizzi, C. Luetto, H. Stühff, M. Baricco, Hydrogen - heat storage system based on metal hydride and phase change material, *in writing*

xi. J. Barale, P. Rizzi, M. Baricco, Evaluation of system parameters of a H_2 storage systems based on metal hydride and compress gas, *in writing*

xii. J. Barale, J.-R. Ares, P. Rizzi, M. Baricco, J.-F. Fernández, $Ti_{1.1}(CrMnV)_2$ and $Ti_{1.1}(CrMnVFe)_2$ alloys for high pressure hydrogen compression, *in writing*

Conference Talk

- J. Barale, F. Nastro, P.Rizzi, C. Luetto, M. Baricco, Project Clean-DronHy: a two stage metal hydride compressor based on commercial alloys, *Conf. WOCST* (19/03/2021)
- J. Barale, F. Nastro, P.Rizzi, C. Luetto, M. Baricco, A two stage metal hydride compressor based on commercial alloys, *Conf. ihtec* (26/05/2021).
- J. Barale, F. Nastro, P.Rizzi, C. Luetto, M. Baricco, Project Clean-DronHy: a two stage metal hydride compressor based on commercial alloys, *Conf. New Times* (16/06/2021).
- J. Barale, E. M. Dematteis, G. Capurso, B. Neuman, S. Deledda, F. Cuevas, P. Rizzi, M. Latroche, and M. Baricco, Industrial production and characterization of $TiFe_{0.85}Mn_{0.05}$ alloy for a large-scale hydrogen storage plant, *Conf. Euromat* (17/09/2021)
- J. Barale, E. M. Dematteis, G. Capurso, B. Neuman, S. Deledda, F. Cuevas, P. Rizzi, M. Latroche, and M. Baricco, Industrial production and characterization of $TiFe_{0.85}Mn_{0.05}$ alloy for a large-scale hydrogen storage plant, *Conf. EFC21* (16/12/2021).

Poster

- J. Barale, P. Rizzi, C. Luetto, M. Baricco, Modelling of the gravimetric and volumetric capacity of hydrogen storage system based on metal hydrides, *INSTM: Workshop* (03/06/2019).
- J. Barale, S. Deledda, E. M. Dematteis, M. H. Sørby, M. Baricco, B. C. Hauback, Synthesis and characterization of magnesium-iron-cobalt complex hydrides, *GRS* (29/06/2019).
- J. Barale, P. Rizzi, E. Casella, M. V. Abbas, C. Luetto, S. Staulo, M. Baricco, Metal-Hydride compressor for a small scale H2-refuelling station, *EMRS* (17/09/2019)
- J. Barale, P. Rizzi, E. Casella, M. V. Abbas, C. Luetto, S. Staulo, M. Baricco, Small scale H2-refuelling station based on MH-compressor, *EIT Raw Material* (08/10/2019)
- J. Barale, P. Rizzi, C. Luetto, S. Staulo and M. Baricco, Project Clean DronHy: A Hydrogen Power Drone at High Performances, *EFC19* (08-09/12/2019)
- J. Barale, M. Costamagna, P. Rizzi, C. Luetto, F. Nastro, S. Staulo, and M. Baricco, A Hydrogen Powered Drone with Hydrogen Refuelling Station, *Hypothesis XV* (03/06/2020)

Conference and Workshop

- INSTM: Workshop: Materials for Today's energy Challenges, Italy (Padova), 3-4/06/2019.
- Gordon Research Seminar (GRS): Hydrogen-Metals Systems, Spain (Castelldefels), 29-30/06/2019.
- EMRS: Beyond Hydrogen Symposium, Poland (Warsaw), 16-19/09/2019.
- Eit Raw Material, Italy (Torino), 7-9/10/2019.
- European Fuel Cell conference & exhibition, Italy (Napoli), 9-11/12/2019.
- Hypothesis XV 2020 – international web conference, 3-5/06/2020.
- Il futuro dell'idrogeno in Italia, online workshop organized by H2IT and ENEA for the Ecomondo Key Energy the circular economy and renewable energy expo, 04/11/2020.
- 38° Convegno Nazionale AIM, online conference, 19, 20, 26/01/2021.
- World Online Conference on Sustainable Technologies, online conference, 17-19/03/2021.
- 5th International Hydrogen Technologies Congress, online conference, 26-28/05/2021.
- New Times: New trend in material science and engineering, online conference, 14-18/06/2021.
- Euromat 2021, online conference, 13-17/09/2021.
- European Fuel Cell conference & exhibition, online conference, 15-17/12/2021.

Period Abroad

- 13 September 2020 – 6 December 2020, Helmholtz-Zentrum- Geesthacht (now Hereon), Dept. of nanotechnology materials technology, Germany, Supervisor: Dr. Giovanni Capurso.
- 2 May 2021 – 2 July 2021, Universidad Autónoma de Madrid, Dept. of physic, Spain, Supervisor: Prof. José Ramon Ares Fernandez.

Laboratory Assistance

- Laboratory of Chemical Plants, Bachelor course in Chemistry and Chemical Technologies, Dr. A. Castellero, 38 h (16-19/11/2018).
- Laboratory of Chemical Plants, Bachelor course in Chemistry and Chemical Technologies, Dr. A. Castellero, 40 h (11-22/11/2019).
- Laboratory of Selection and Use of material, Master course in Material Science, Prof. P. Rizzi, 8 h (3 and 5/12/2019).
- Laboratory of Metallic materials with laboratory, Bachelor course in Material Science, Prof. P. Rizzi, 24 h (19 -27/04/2021).
- Laboratory of Chemical Plants, Bachelor course in Chemistry and Chemical Technologies, Dr. A. Castellero, 24 h (3-30/11/2021).

Seminar

- Elettrico, idrogeno, gas ibrido, Italy (Torino), 2/10/2018.
- Chimica Passione Periodica: Energia: rinnovabile, pulita, efficiente, Italy (Torino), 4/10/2018.
- NIS Colloquium – STAMP Dissemination: Materials and microstructures in Additive Manufacturing, Italy (Torino), 14/02/2019
- Giornate del CrisDi: X-ray Powder Diffraction: a useful tool for Chemistry and Material Science, Italy (Torino), organized by CrisDi, 28/02/2019.
- Selected metallic materials and technologies for aerospace industry, Italy (Torino), Seminar by prof. M. Motyka, 05/04/2019.
- Metal powder for additive manufacturing, Italy (Torino), Seminar by Dr. V. Uhlenwinkel, 15/11/2019.
- Energia dall'idrogeno: trasporto, stoccaggio e handling dell'idrogeno, online seminar organized by Confindustria, 28/05/2020.
- Simulare idrogeno: elettrolizzatori e celle a combustibile, online seminar organized by COMSOL team, 23/06/2021.
- Various seminars organized by the laboratory of Metallurgy and PhD defences.

Course and School

- Introduction Scientific programming of Python, Univ. of Turin, Dep. Of Chemistry, 20 h (2018).
- Aerospace metallic materials and technologies, Univ. of Turin, Dep. Of Chemistry, 8 h (2019).
- Introduction to Crystallography, Univ. of Turin CRISDI School, 6 h (2019).
- Instrumentation for X-Ray Diffraction, Univ. of Turin CRISDI School, 4 h (2019).
- Electron Diffraction, Univ. of Turin CRISDI School, 4 h (2019).
- X-Ray Diffraction, Univ. of Turin CRISDI School, 4 h (2019).
- X-Ray Diffraction Methods: Polycrystalline, Univ. of Turin CRISDI School, 10 h (2019).
- In situ/operando X-Ray Powder Diffraction, Univ. of Turin CRISDI School, 4 h (2019).
- The Rietveld Method, Univ. of Turin CRISDI School, 8h (2019).
- Introduction to Crystal Growth, Univ. of Turin CRISDI School, 6h (2019).
- X-Ray Diffraction applications on Materials Study, Polytechnic of Turin CRISDI School, 8h (2019).
- Optimization and Computation of Thermodynamic Properties and Phase Diagrams, Univ. of Turin, Dep. Of Chemistry, 12 h (2020).
- The vitreous state, University Turin, Dep. Of Chemistry, 12 h (2020).

Objectives and Motivation

This PhD project is linked to the energy topic and in particular to the storage of hydrogen as energy vector, by exploiting metal hydrides based on intermetallic compounds. The goal of the thesis is to bridge the gaps between laboratory research and implementation of devices, by investigating metal hydrides properties to develop hydrogen compression and storage systems, using also modelling for their design. The red thread of the work is the study of metal hydrides from an industrial point of view, looking for suitable compositions (commercial or not), that can fit final plant requests. Indeed, for an effective industrial exploitation of the H_2 economy, it is now the time to move from laboratory to real scale industrial H_2 systems.

A series of consideration on the size of hydrogen storage systems were performed thanks to lumped elemental model, focusing the attention on system weight and volume, and on the main parameters that can affect these features.

Concerning the storage of H_2, a commercial alloy was characterized and then integrated in a prototype to be tested.

A commercial market survey and study of a series of market available alloys allowed to find the proper compositions for the realization of a prototype of metal hydride compressor. Then, a series of new compounds were synthetized and characterized to individuate a proper composition that can be added at the realized compressor. The goal is to improve plant performances but considering processing the compounds in view of an industrial possible production.

Thesis Outline

This work entitles “Hydrogen Storage and Compression based on Metal Hydrides” is the results of the work performed as PhD candidate of the XXXIV cycle (2018 – 2021) in Chemical and Material Science of the University of Torino.

The thesis is organized as follow:

- Chapter 1 provides an overview on the use of metal hydrides as H_2-carriers, highlighting pro and cons and their application in H_2 storage and compression.
- Chapter 2 summaries the experimental instruments and theoretical methods used.
- Chapter 3 reports the results of lumped elemental model performed to evaluate the influence of metal hydride properties and of the design on the weight and volume of hydrogen storage system. The chapter consists of three parts: the first one considers several hydrides and design; the second one shows a case study comparing a storage system based on MH and compress gas; the third one reports results of a case study for a large storage system for a ship.
- Chapter 4 presents the work performed linked to a hydrogen storage system based on metal hydride, developed in the framework of the HyCARE project. The first part of the chapter reports the results of the characterization of the selected H_2-carrier, *i.e.* a $TiFe_{0.85}Mn_{0.05}$ alloy. Then, in the second part, it is reported the work performed on the prototype of the final storage system. The latter work was performed during the period abroad in the laboratory of the Helmholtz-Zentrum Hereon in Geesthacht (Germany).
- Chapter 5 reports the work related to the compression of H_2 based on metal hydride. The first part is linked to the realization of a two-stage metal hydride compressor performed in the framework of the regional project Clean-DronHy, presenting the selection and study of the alloys and the design and testing of the final item. The second part of the work is dedicated to the synthesis and characterization of $Ti_{1.1}(Cr,Mn,V,Fe)_2$ compounds as high-pressure alloys for hydrogen compression. This work was performed during the period abroad spent in the laboratory of the Universidad Autonoma de Madrid (Spain).

From chapter 3 a more detailed introduction is reported per each theme, together with the experimental conditions applied, the discussion of the results and conclusions. The bibliography is associated at each chapter.

Chapter 1
General Introduction

1.1 Hydrogen as energy vector

To face the energy crises and climate change, the use and the storage of renewable energy is fundamental. At this regard, H_2 as energy vector is a promising widespread solution and could play a key role in the decarbonization of the energy and transport sectors, enlarging the use of renewables. Indeed, over the last years, significant investments have been promoting the development of H_2 infrastructures.

H_2 needs to be produced from a primary energy source, renewable or not, and depending on the sources and CO_2 emission it is named, *grey*, *blue*, *turquoise* and *green* hydrogen, with only the latter exploiting renewables [1]. The grey H_2 is produced by steam reforming of natural gas implying a high emission of CO_2, on the contrary of the blue one, in which the amount of CO_2 delivered in the atmosphere is decreased thanks to its capture. Completely CO_2 free, even if a fossil fuel is used, is the turquoise hydrogen, that is produced through methane pyrolysis of the natural gas. Finally, the green hydrogen is produced exploiting renewables to supply electrolyser (EL), in which hydrogen is generated by the splitting of water, forming also O_2 [1]. Green H_2 is now particularly encouraged since from the production to the final usage, there are not harmful products and pollutants emitted in the atmosphere, as can be seen from the hydrogen cycle reported in Figure 1.

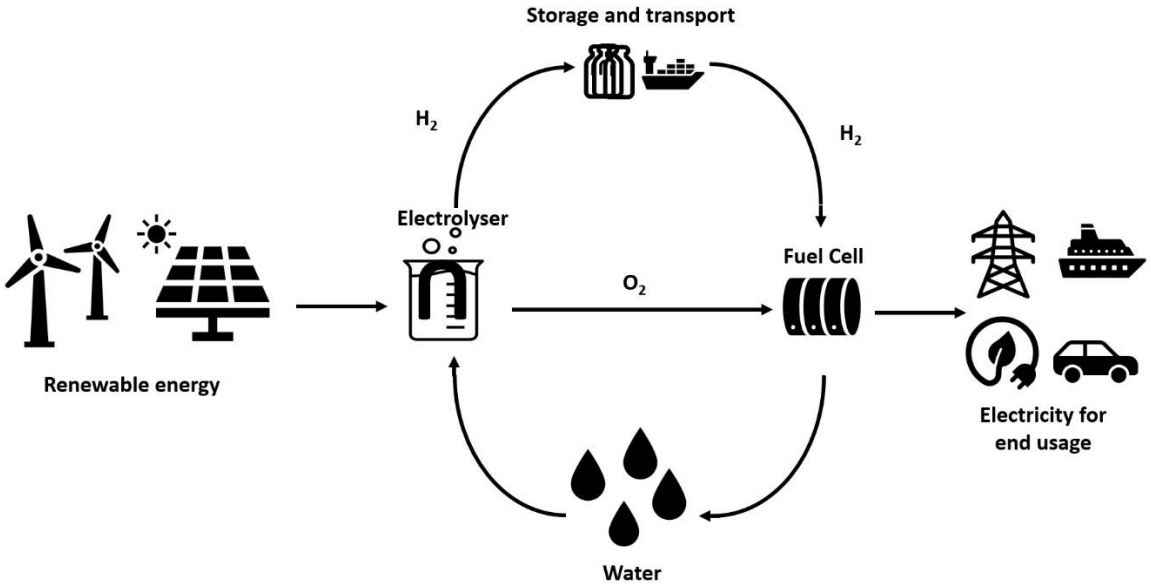

Figure 1: Hydrogen cycle based on renewable energy.

The advantage of hydrogen is that it can be stored for long time, being even transport to the final application site. When energy is required, Fuel Cell (FC) are used, generating electricity

and heat by electrochemical recombination of H_2 and O_2, forming water [2]. Final uses of hydrogen can be for stationary or mobile applications. In the first case, for smart/off grid application, implying the use of hydrogen to generate electricity, respectively, to be directly supply in the grid or in remote zone where there is not access to the grid. Regarding mobile sector, the H_2 storage system and the FC are directly placed in the final items, running from light weight application, like cars or drones, to heavy ones, like trains and ships [3,4]. The storage of hydrogen plays a crucial role in its usage, since a drawback is its energy-to-volume power ratio, with 8.5 MJ/l of liquified H_2 compared to 27.5 MJ/l of gasoline [5], implying significant efforts to achieve high hydrogen storage densities. The storage of hydrogen can occur as liquid and compress H_2 or through carriers, at the solid state, like in hydrides or porous materials (e.g. zeolites), or as a liquid phase, like Liquid Organic Hydrogen Carrier (LOHC) or ammonia [3,6–8]. Each technology presents advantages and disadvantages.
Hydrides are interesting for the storage of hydrogen at the solid state and for the compression of the gas. Indeed metal hydrides based on intermetallic compounds can allow to store H_2 in mild conditions and can compress hydrogen in the as called "thermally driven compressor", resulting more economically favourable than conventional mechanical ones, thanks to lower cost of maintenance [9].

1.2 Metal Hydrides

Hydrogen can react and form stable bonds with many metals or alloys and a huge number of hydride formers have been investigated [10]. H_2 can create ionic bonds with element of s-block, covalent bonds with elements of the p-block, and metallic bonds, but also ionic and covalent ones, with d and f – block elements, as can be visualized in Figure 2. Metal and ionic hydrides are generally described with the formula MH_x. In ionic hydrides there is the formation of an ionic bond between M^{n+} and H^-, with alkali metals, like LiH or NaH. While in Metal hydrides (MH), H_2 is located in interstitial sites of metal lattice and has a partial negative charge, depending on the metal electronegativity, forming metallic bond [11]. In complex hydrides, with general formula $M_nX_mH_y$, there is the formation of a complex anion, $[XH_y]^{\delta-}$ bonded with M^{n+}. The bond between X and H is covalent, whereas the bond between the complex anion and M has a prevalently ionic character. M can typically be light metal (*e.g.* Mg, Li) or have high affinity with H_2 like Zr. X can be or a metal with low affinity with H_2, like some transition metals (*e.g.* Fe, V, Mn, Ni) or forms quite stable complex anion (*e.g.* B, Al) [6]. Hydrides are interesting in hydrogen technologies thanks to their high volumetric

hydrogen capacity, as an example up to 150 gH_2/m^3 of Mg_2FeH_6. While the gravimetric capacity can vary from 1-2 H_2 wt.% of MHs, up to 18.4 H_2 wt.% of complex hydrides, like for $LiBH_4$ [12].

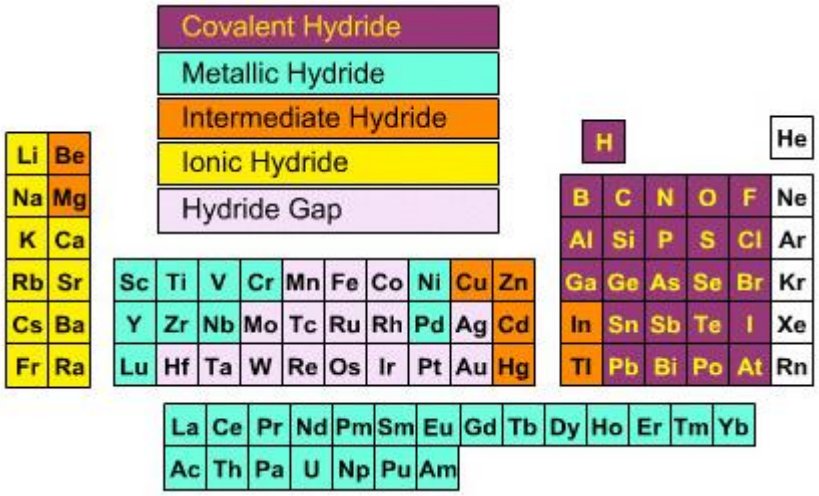

Figure 2: Period tables of elemental hydride types.

Table 1 reports some examples of hydride divided per class of hydride, reporting the storage properties in terms of gravimetric and volumetric capacity and storage working temperatures.

Table 1: Examples of hydride composition with some hydrogen storage properties divided per class of hydride.

Class of hydride	**Example of composition**	**General Properties**
Metal hydride	$LaNi_5$, TiFe, $TiMn_2$	Grav. Cap. 1- 2 H_2 wt.% Vol. Cap. 115 kgH_2/l T < 100 °C [12]
Ionic hydride	LiH	Grav. Cap. 12.7 H_2 wt.% T ≈ 900 °C [13]
Intermediate hydride	MgH_2	Grav. Cap. 7.6 H_2 wt.% Vol. Cap. 110 kgH_2/l T > 300 °C [14]
Complex hydride	$LiBH_4$	Grav. Cap. 18.5 H_2 wt.% Vol. Cap. 121 kgH_2/l T> 380 °C [15]
Complex metal hydride	$Mg_2(Fe,Co)H_{5-6}$	Grav. Cap. 4.5- 5.6 H_2 wt.% Vol. Cap. 110 – 150 kgH_2/l T 287 - 312 °C [14]

1.2.1 Intermetallic compounds

Metal hydride based on the intermetallic compound (IMC) AB, AB_2 and AB_5 are particularly promising in hydrogen storage and compression [9,16,17]. A is an element that forms stable hydrides, AH_k, *e.g.* transition metals of the left side of the periodic table or rare earth metals (Figure 2). On the contrary, B elements form unstable hydrides, BH_g, *e.g.* transition metals at the right side of the period table (Figure 2). The affinity between the metal and hydrogen is linked to the difference in electronegativity between the metal and hydrogen itself. A element has a difference in electronegativity in a range from 0.5 to 1.0, while B element in a range from 0.2 to 0.5, presenting high valences, large cohesive energies, and small lattices not forming hydride as Fe, or forming hydride in a complex way like Ni, adding electrons both to the nearly filled metal d-states and also to the new state drawn below the Fermi level [11]. The appropriate combination in the A and B elements results in $A_yB_xH_l$ with intermediate stability of the corresponding binary hydride. The main advantage of the intermetallic compounds for hydrogen storage is that they can absorb and desorb hydrogen in mild conditions, even close to room temperature, being easily integrated with EL (supply pressure lower than 30 bar) and able to directly supply a FC at about 1-2 bar. As stated previously, a drawback is their low gravimetric capacity, generally below 2.0 H_2 wt.%. Table 2 summarizes main properties of AB, AB_5 and AB_2 compounds, referring to the most representative composition, TiFe, $LaNi_5$ and $Ti(Mn,Cr)_2$ [18].

Table 2: Properties of AB, AB_5 and AB_2 IMC [18].

AB (TiFe)	**AB_5 ($LaNi_5$)**	**AB_2 ($Ti(Mn,Cr)_2$)**
Difficult activation	Disproportion while cycling	Easy activation
Sensitivity to gas impurities	Resistance to gas impurities	Low resistance to gas impurities

In the following, a brief description of TiFe, $LaNi_5$ and $Ti(Mn,Cr)_2$ compounds is reported.

1.2.1.1 AB: TiFe

The AB compound ZrNi was the first hydride discovered displaying reversible H_2 properties [19], and, afterwards, a huge variety of Ti- and Zr- based AB alloys have been studied. The most known is the TiFe, that is interesting as H_2-carrier in stationary applications, since it stores H_2 at mild pressures and temperatures (*e.g.* 10-20 bar and 30-70 °C). Moreover, it is not expensive, non-toxic and the raw materials are abundant [20,21]. TiFe has a cubic

CsCl-type structure, space group $Pm\bar{3}m$, with a cell parameter from 2.974 to 2.978 Å, depending on Ti at.%, *i.e.* from 49.5 % to 52.5 % [21–23]. After dissolving hydrogen in solid solution (α-$TiFeH_{0.06}$), it forms two subsequent hydrides, visible in pcT curves through two consequent plateaux: a monohydride (β-TiFeH) and a dihydride (γ-$TiFeH_2$), presenting a maximum gravimetric capacity close to 2.0 H_2 wt.% [19]. A large hysteresis gap between absorption and desorption pressure is usually observed, which depends on the sample history (*e.g.* synthesis, activation) [19]. A drawback is its hard activation conditions, which usually require high temperatures (*e.g.* 400 °C) [19,20,24] and/or high hydrogen pressures (up to 100 bar) [18]. A strategy to overcome this problem and to tailor H_2 sorption properties involves the substitution of Ti and/or Fe with other elements [25–31], and/or the enrichment of Ti in the composition [32], to promote the formation of secondary phases, that have been found to help in the activation process. Two common substitutions element are Mn and Ni, that have found to help in the activation, to decrease the plateau pressure, thanks to the enlargement of the cell dimension, and to increase the sorption rate [33,34]. Finally, mechanical treatments are also used to improve the activation and sorption rate, especially at laboratory scale [35,36]. Recently, an industrial scale-up of a ball milling production of a Ti(Fe,Mn) alloy was proposed [37]. The alloy after the synthesis did not require activation and displayed good cycle stability, compared to a commercial one prepared with melting techniques.

1.2.1.2 AB_5: $LaNi_5$

AB_5 compounds involves rare earth metals and transition metals, resulting costly, since based on material critical to be supplied. The most representative of this class is $LaNi_5$, that has the hexagonal $CaCu_5$-type structure, space group *P6/mmm*, with a cell parameter *a* of 5.0615 Å and *c* of 3.9794 Å [38,39]. Most of the storage system realized so far are based on $LaNi_5$ and $LaNi_5$-based alloys, thanks to a fast activation, reversibility at low temperatures, fast sorption rate and resistance to gas impurities [12,18,40–42]. Moreover, it shows flat plateaux and limited hysteresis [39,42]. It forms the $LaNi_5H_6$ hydride, with a structure described by the space group *P31m* [43], but also $LaNi_5H_x$ (with x between $5<x<7$) are reported [18]. $LaNi_5$ has a hydrogen volumetric capacity of 115 kgH_2/m^3 and a maximum gravimetric capacity of 1.5 H_2 wt% [12,41,42]. A drawback is its poor stability over cycling, because of the occurrence of disproportion, in which the $LaNiH_6$ tends to decompose into

Ni precipitate and into the more thermodynamically stable LaH_2, as reported in Reaction (1) [44,45]:

$$LaNiH_6 \rightarrow Ni + LaH_2 + 2H_2 \quad (1)$$

Disproportion promotes the progressive loss in capacity of the material. To tailor with the sorption properties and to reduce/prevent disproportion, substitutions of both La and Ni are possible. Ni promotes the dissociation of H_2 molecules, and its partial substitution is beneficial improving the thermal resistance, limiting disproportion and changing in the equilibrium pressure [42]. Common substituted elements of Ni are Al, Co, Mn, Sn and Fe offering a wide range of hydrogen sorption properties. Al sensitively reduces the plateau pressure, but a slight decrease is obtained with Mn substitutions; Co increases the stability towards disproportion; Sn decreases the plateau pressure and increases the stability, while Fe improves the storage capacity [40,42,46–49]. The substitution of La can be partial or total with other rare earth metals [40]. An interesting substitution is with Ce, that improves the cycling stability, limiting the disproportion and increasing the plateau pressure thanks to cell dimension reduction compared to parent $LaNi_5$, being promising for high-pressure applications [42,50].

1.2.1.3 AB_2: Laves phase $TiMn_2$ and $TiCr_2$

In the AB_2 compounds, A is Ti and/or Zr, while B is usually a transition metal, resulting economically advantageous. It is worth noting that also rare earth metals can form AB_2 Laves phases, but they are not typically considered due to their cost. AB_2 compounds present the crystal structure of Laves phases: the hexagonal $MgZn_2$-type (C14), the cubic $MgCu_2$-type (C15) and the hexagonal $MgNi_2$-type (C36) [51]. The AB_2 based hydrides present high storage capacity, even up to 2.0 - 2.5 H_2 wt.%, easy activation, fast hydrogen sorption rate, but they are sensitive to impurities in the gas supply and present marked sloping plateaus [18,41,42]. Interesting AB_2 Laves phase compounds are the hexagonal (C14) $TiMn_2$ and $TiCr_2$. Both need to be substituted to tailor sorption properties, since both present rather high plateau pressures, hard activations. The $TiMn_2$ has even marked sloping plateau, observing a considerably decrease in storage capacity while cycling [52,53]. Mn and Cr represent suitable substituting element for each other, forming a series of Ti(Mn,Cr)-based alloys. Some common substitution elements for Cr and/or Mn are V, Fe, Co, Ni, Cu, Mo. While Ti is commonly substituted by Zr. In general V, Zr and Ti-rich compositions help in decreasing

the hysteresis gap and Cu flatten the plateau pressure. Then, V decreases the H_2 gravimetric capacity, while Zr increases it [41,42,54]. Thanks to substitutions, a wide number of alloys have been investigated, presenting different properties. Compared to the parent $TiMn_2$ and $TiCr_2$, substitutions help in the activation and in tailoring the plateau pressure, giving rise to a wide range of application, from mild pressure and temperature H_2 storage to high pressure H_2 compression [55,56].

1.2.2 Properties

1.2.2.1 Thermodynamics

Absorption and desorption of H_2 occurs through several steps, as stated in Figure 3.

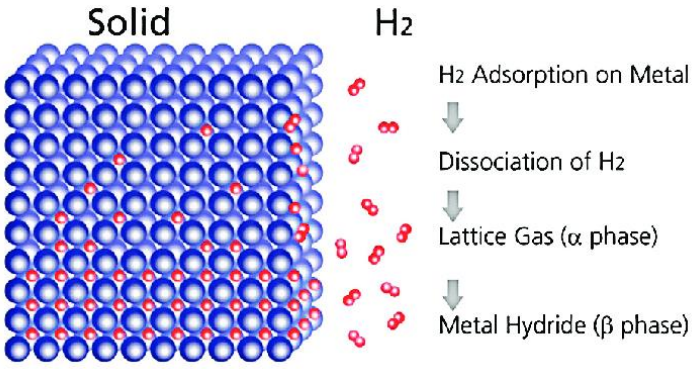

Figure 3: Scheme of absorption steps into a metal to form a hydride.

In absorption, H_2 physisorption is followed by molecule dissociation into atoms, diffusion of the atoms into the metal subsurface and bulk lattice, formation of a solid solution (α-phase), and nucleation and growth of the hydride (β-phase). The reverse steps occur in desorption. In case of complex hydrides, the reaction mechanism can be rather complicated, displaying slower kinetics than for MHs [12].

At the base of hydrides usage there is the reversible reaction between a metal/alloy (M) with H_2 forming a hydride (MH) and heat (Q), according to Reaction (2):

$$M + {}^{x}/_{2}\, H_2 \leftrightarrows MH_x + Q \qquad (2)$$

The thermodynamics of the reaction is related to H_2 pressure (p), H_2 concentration (cH) in the solid phase and temperature (T), which is described in pcT-diagrams (Figure 4-a).

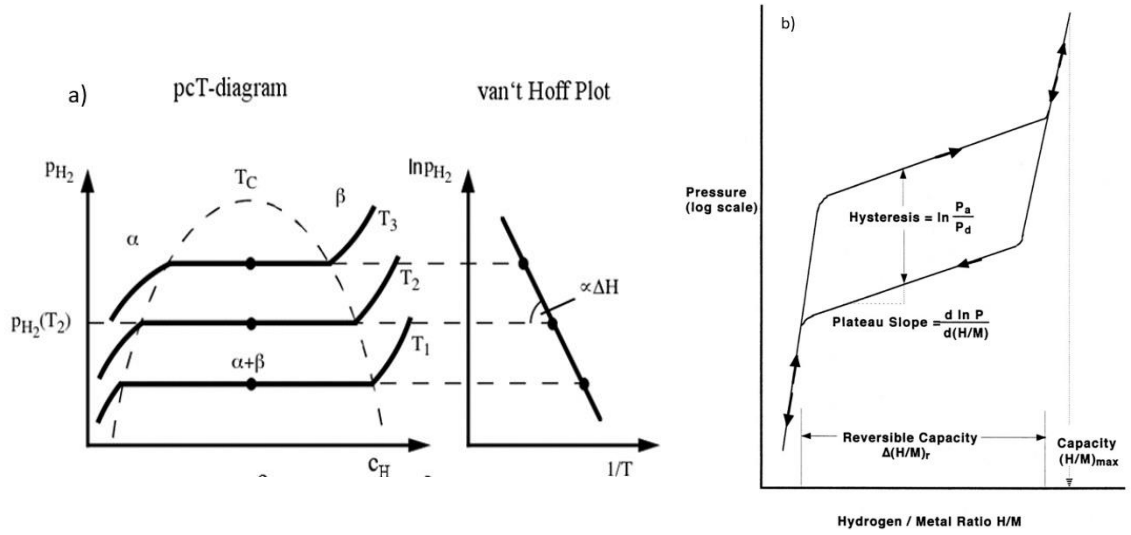

Figure 4: (a) pcT-diagram and Van't Hoff plot; (b) pcT-diagram displaying hysteresis and slope [41].

In the plateau region, the equilibrium pressure (p_{eq}) is related to the temperature according to the Van't Hoff equation (Equation 1), from which is possible to obtain the variation in enthalpy (ΔH) and entropy (ΔS) of absorption and desorption through a logarithmic plot (Figure 4-a).

$$ln\, p_{eq} = \frac{\Delta H}{RT} - \frac{\Delta S}{R} \quad \text{(Eq. 1)}$$

Depending on the application, ΔH and ΔS are fundamental parameters to select the proper H_2-carrier and evaluate the operative pressure and temperature. As can be seen from (1), hydride formation is exothermic, while its decomposition is endothermic. Ideally, absorption and desorption isotherms should follow the same curve in opposite direction, but in reality, absorption and desorption plateau pressure occur at different values, with absorption higher than desorption. This complex phenomenon is called hysteresis and can be visualized in the pcT-diagram reported in Figure 4-b. Hysteresis is linked to sample history, like preparation conditions, microstructure, and it's not unique for the same material. This implies that it can be controlled with treatments after the synthesis or by alloying with specific additives [18]. Hysteresis should be as little as possible for applications, in which reversibility and no loss of efficiency are required, like for H_2 storage. Hysteresis is described by the free energy difference (Equation 2):

$$\Delta G_{H2}(hyst) = RTln\frac{pA}{pD} \quad \text{Eq. (2)}$$

The plateau pressure should be flat (Figure 4), but in reality slope can occur, like presented in Figure 4-b, because of compositional fluctuations due to impurities and/or fluctuations of stoichiometry or to para-equilibrium phenomena [18,47]. The slope can be reduced by thermal treatments after the synthesis. The plateau width can provide the reversibility capacity, Δ(H/M) Figure 4-b, that can be expressed as atomic ratio, H/M, as weight percentage on weight [18] and can be less than the maximum, $(H/M)_{max}$, since the material can lose its properties during cycling because of material degradation or impurities introduced. It is worth to note that cell volume contraction/expansion takes place upon de/hydrogenation, leading to ΔV/V of the order of 20 %. Finally, in metal hydride a strong relation exists between the cell dimension, and in turns in the dimension of interstitial site exists with the equilibrium pressure. The lower is the lattice dimension, the higher is the equilibrium pressure, since high energy is required from H_2 to occupy the interstitial sites and vice versa. This implies that to tailor with the equilibrium pressure for a given compounds, proper substitutions need to be also evaluated to act on lattice dimension.

1.2.2.2 Kinetics

For the selection of a suitable H_2-carrier, also kinetics is important [57], since MH formation and decomposition must be as fast as possible in the considered conditions of pressure and temperature. One of the most important kinetic parameters is the activation energy (*Ea*), which expresses the energy barrier necessary to activate the process. The reaction rate changes with temperature according to Arrhenius relation (Equation 3):

$$k = Ae^{-Ea/RT} \qquad \text{Eq. (3)}$$

in which *k* is the rate constant, *A* is the pre-exponential factor and *R* is the gas constant. Different methods have been developed to determine the *Ea*, *e.g.* the Kissinger method, usually based on results from thermal analysis [58]. During a kinetic study, it should be taken into account that experimental conditions and artefacts can affect the results of measurements [59].

The reaction mechanism can be determined through different models, which describe experimental kinetic data. The rate determining step of the reaction can be determine through Johnson-Mehl-Avrami (JMA) (Equation 4) [60]:

$$\alpha = 1 - e^{-kt^n} \qquad \text{Eq. (4)}$$

in which α is the reacted fraction, t is time, n is an exponent linked to phase growth mechanism and k is the rate constant. Depending on the value of n, it is possible to evaluate the rate determining mechanism by the linear logarithmic form. Kinetic study is performed by registering several curves in isobaric conditions at different temperatures, like reporting as an example in Figure 5, from which is possible to evaluate the k and in turn the Ea. This approach implies different ΔG of reaction, *i.e* a different driving force. However, a more accurate kinetic study should involve a constant ΔG, implying a properly variation in pressure depending on the temperature used [61].

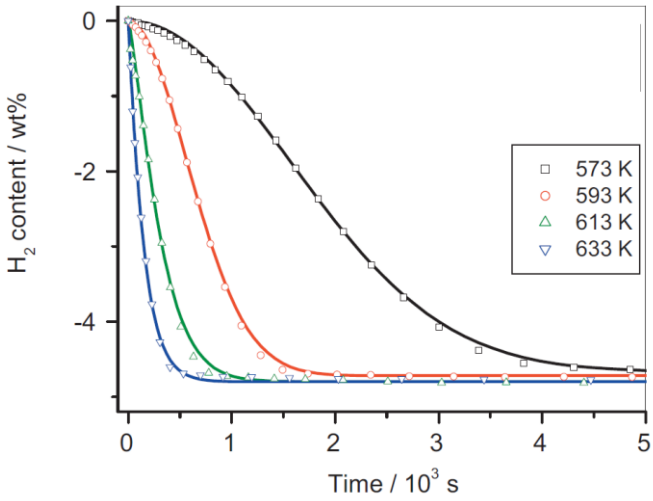

Figure 5: Example of kinetic curves recorded in isobaric conditions at 1 bar, reporting the amount of H_2 processed as a function of time at different temperatures for MgH_2, and $MgH_2/BaRuO_3$ Experiments are performed by maintaining the same ΔG for a given pressure appropriately changing the temperature. Points refers to experimental data while the line to the fitting obtained by applying Equation 4 [62].

Hydrides are often handled in the form of powder to enhance the hydrogen sorption compared to bulk. The hydrogen sorption rate is also linked to the powder microstructure. Materials with small grains or crystallites (dimension of nanometres) show faster sorption rates, due to the faster diffusion along grain boundaries. Grain boundaries have a favourable energy for nucleation and for decomposition of hydride phase [63]. The powder particle dimension and the specific surface area, can also affect the kinetics, which is enhanced when the contact surface with the gas increases [59]. Finally, also additives can play a role in enhancing the kinetics, by reducing, as an example, the hydride nucleation barrier. Additives (Y) can act as a catalyst, MH-Y, so not being part of the hydrides, or be an integrated element of the hydride, MYH [18,59].

1.2.2.3 Others

The ability of MHs to process H_2 depends also on material purity, surface composition and particles morphology [64]. Other properties to be taken into account when realizing an H_2 storage system (H2SS) are: alloy's activation, compactness, thermal conductivity, and cyclability.

Activation: metal surfaces could be generally covered by an oxide layer that might hinder the first hydrogenation. So, it is usually necessary to process the material in temperatures and pressures to facilitate the first H_2 absorption. This process is called activation and it changes for different hydrides and also for the same compound, depending on its processing [63]. The goal of activation is to crack the powder particles and promote the creation of new fresh surfaces to allow hydrogen absorption [59]. Indeed, an example of activation treatment involves cycles alternating loading and unloading of H_2, which are able to promote the cracking of the surface thanks to the metal lattice expansion and shrunk in absorption and desorption, respectively. Thanks to the process of the alloy in H_2, the particle size is usually refined, contributing to the enhancement of the H_2 sorption rate, as explained previously. At this regard, especially at laboratory level, milling techniques are often used [65]. Nevertheless, when realizing a hydride-based system for a real application, it must be taken into account that the activation should be performed directly inside the reactor, implying that the conditions used need to fit the plant constraints of maximum affordable temperature and pressure. This is particularly important since often to allow an easy activation, an overpressure or overheating is applied compared to the defined plant working conditions.

Compaction: alloys for H_2 sorption can be used as loose powder or compact in pellets. Pelletized powder has the advantage to reduce the empty spaces, increasing the volumetric capacity [66]. The pressure applied to pelletize affects the compactness, as well as the final volumetric capacity. Pellets usually need to be mechanically stabilized using additives, like Expanded Natural Graphite (ENG), to be stable upon cycling, avoiding being transformed back in powder form [66]. Due to the change in volume between the hydrogenated and not hydrogenated phases, when design a reactor some free volume needs to be left to allow alloy's expansion, preventing tank mechanical instabilities. At this regard, in the case of pellets, tank needs to be carefully designed considering the growth of the pellets in all the directions. If the material is used as a loose powder, the reactor design is easier.

Thermal conductivity: Thermal conductivity is fundamental for the heat transfer in MH-reactor. The latter is considered the rate determining step during H_2 absorption/desorption

reactions [67]. Indeed, thermal conductivity affects the homogeneous uptake and release of H_2 through the material, being crucial for the reaction rate at macroscopic scale. MH has bad thermal properties as loose powder, with a thermal conductivity of the order of 0.1-1.0 W/mK [59]. To increase the thermal conductivity, powders can be mixed with suitable additives, *e.g.* ENG, heat-conductive metal foam [67,68], and/or pelletized with additives, *e.g* with ENG [66]. The advantage of pellets compared to loose powders is the enhanced of the thermal conductivity, due to the reduction of voids that act as insulants [67]. As an example, the Hydralloy-C5 ($TiMn_2$-based compound) as loose powder has a thermal conductivity of 1.0 W/mK that rises to 3.7 W/mK with a 2.5 wt.% of ENG and 75 MPa of pelletize pressure [66]. The value becomes of the order of the 60 W/mK, by increasing the pressure and/or the ENG content up 600 MPa and/or 12 wt.%, respectively. Finally, when realizing a system, to face the poor thermal conductivity of the alloy, the heat management can play a crucial role and a proper heat exchanger need to be considered also involving particular design of the reactor [67,69].

Impurities and cyclability: Impurities present in the gas supply may cause some loss in hydrogen sorption properties of the material, like reducing kinetic properties and/or the storage capacity. The presence and accumulation of impurities decreases the partial pressure of the H_2, inducing a slowdown of the reactions in comparison to high purity H_2 [70]. Moreover, impurities can poison the surface and the bulk of the material, preventing the processing of H_2 and decreasing the capacity [59]. Oxygen and/or water are possible impurities of a H_2 flow produced by an EL, and the ability to resist to poison depends on the material. If the material is poisoned, it could be re-activated through a series of absorption and desorption cycles or by using a chemical activation with a proper chemical solution. A step of re-activation or an irrecoverable poisoning is not convenient in real applications, implying a frequent substitution of the compound with fresh material or a long and hard reactivation process, being not economically advantageous. Thus, to limit the quantity of impurities in the inlet gas, a suitable purification should be considered to preserve H_2-carrier life. Finally, another important property is the stability of the material over hydrogen sorption cycling, avoiding the degradation of hydrogen sorption properties, as occur for the $LaNi_5$ (section 1.2.1.2).

1.2.3 Design of metal hydride tank

As previously discussed, concerning the thermal conductivity, the H_2 response at macroscopic level is strongly affected by the heat management [67,69]. After having chosen the proper H_2-carrier based on thermodynamic and kinetic properties, activation procedure, stability over cycling and resistance to impurities, the rate of H_2 uptake/release is influenced by tank geometry, size and layout [17], which are features linked to the heat exchange. The realization of a hydrogen tank requires a proper design to achieve the right compromise among the H_2 uptake and release conditions, the H_2 storage density, the integrity of the container at the operative condition, [67] and the entire gravimetric density of the system, which is fundamental especially for mobile applications. The easier design involves a double tubes geometry, in which the alloy is placed internally, and an outer jacket is dedicated to the heat exchanger fluid (steam, water, oils). It is important to minimize the heat pathway, to maximize the removal/supply of heat. This implies that tubes need to have a low ratio tube diameter and length, involving tube longer than wider. All variations in geometry are brought to optimize the heat management, like the use of traverse or longitudinal fins in close contact with the MH-bed [71], or of planar or disc-shaped tank geometries [67]. The choice of the fluid for thermal exchange (gaseous or liquid) is linked to the working temperature of the system. For temperatures lower than 100 °C, it is possible to use water, while for higher temperatures, catalytic combustor or electric heater, or fluid like steam and oil are often used [72]. Promising results comes from the use of Phase Change Material (PCM) as heat storage system for the heat management of MH-tank [67]. When realizing a tank, the economical aspect of the manufacture needs also to be considered, and it is linked to the material used for the container. Usually, working pressure and temperature allow the use of steel or aluminium alloys, with the latter helpful when low system weight are required [9]. The thickness of reactor wall is also to be considered, since it also plays a role in the heat management. It should be as thinner as possible, to maximize the heat flow, assuring at the same time safety at the applied conditions of pressure and temperature. Finally, also tank displacement in the plant is fundamental. Indeed, reactors are usually placed horizontally, since it reduces the tension on reactor walls induced by the material expansion in absorption, preventing tank fractures. Moreover, it is shown that upon cycling, vertical displacement is underproductive in terms of thermodynamic properties, and it reduces the hydrogen sorption kinetics and storage capacity, respectively, due to distortion of the crystal structure because

of internal stress and material self-densification, in which the decrease in porosity hinders the diffusion of H_2, *i.e.* the capacity [44]. Indeed, the diffusion of hydrogen in MH is lower than in the compound [73] and in vertical displacement of reactor a first layer of MH is formed, hindering the hydrogenation of the rest of the alloy.

1.3 H_2 storage

Lototskyy et al. summarized integrated system MH-FC realized in the past years The total amount of H_2 stored is between 0.006 and 12 kg. In a recent paper, Bellosta von Colbe et al. [9] reports hydrides storage systems from stationary to mobile applications, also presenting technology's future perspectives. The systems realized so far are mostly based on MH (*i.e.* on IMC) [9,17], since, as previously discussed, H_2 is processed in mild conditions, being integrated with EL and FC, resulting safer than compressed and liquefied H_2. Indeed, storage plant realization are favourable when H_2 is processed at temperature below 100 °C and even close to room temperature, not implying in this case any cooling or heating source. Afterwards, it is advantaging when H_2 can be supplied directly by an EL, that up to now have a maximum release pressure of 30 bar, without requiring any compression or decompression stage. Then, at the storage defined temperatures, it is a key point if the H_2 can be desorbed supplying directly the FC to avoid, also in this case, any compression/decompression of the gas.

When design a H2SS, it is important to take into account the volumetric and gravimetric capacities of the system, that represent the hydrogen amount over the weight and volume of the storage system itself [9]. At this regard, MH results promising only for stationary uses for smart-grid and off-grid energy management, because of their low gravimetric capacity, implying tons of carrier to store tens of kilos of H_2. Nevertheless, they result promising also for vehicles with high weight, like submarine, in which the weight is advantageous of the balance of the system [74]. Even if the weight is not a problem in stationary application, important is the volume of the system, and MH fits the request, thanks to high volumetric densities, of the above 100 kgH_2/m^3. Large energy storage implies the use of large amount of H_2-carrier, as far as big devices, that need to be properly designed for the correct management of the heat transfer [17]. As summarize in refs. [9,17], a large part of MH-H2SS is just demonstrative, prototype or simulated plants. Nevertheless, in the past years some systems have been realized, being available in the market, storing even hundreds of kg of H_2. Concerning AB TiFe-based compound, the industry GKN, firstly realized in the South

Tyrolean Alps (Italy) an H2SS, as called Hy2green, integrated with an EL and a FC to provide energy for a house, which has no access to the grid [75]. Then, GKN recently launched on the market three sizes of MH-H2SS: the HY2MINI, storing from 10 to 25 kg of H_2, passed through the HY2MEDI from 60 to 125 kg of H_2, up to HY2MEGA, for above 250 kg of H_2 [75]. A H2SS based on AB_5, $LaNi_5$-compound, is the H2ONE, realized in Japan, commercialized by Toshiba [76]. It presents a storage capacity of about 150 Nm^3 per module, being easily assembled to increase the capacity. The system can be easily integrated with EL and FC. It is used for smart/off grid applications like in backup system in case of grid problems, as week storage system for weekend uses, like for the supply of stadium, and as charge station for fuel cell and electric vehicles. While in Europe, the industry LabTech commercialized MH-tank, as called HBond, that can work in a range of temperature from -20 ° to 100 °C, releasing high purity H_2, at low pressure (not -specified). The storage capability is from 0.005 to 10 Nm^3 and H_2 charging and discharging time is about 10-15 min [77]. Finally concerning AB_2, $TiMn_2$-compounds are particularly used in the maritime sector and in mobile applications, like in forklift storing hundreds of kg of H_2 [74,78,79].

1.4 H_2 compression

Compressed gas is a common and well-known H2SS [6,80]. H_2 is usually stored at about 200 bar, but even higher pressures (up to 700 bar) are required to store high amount of gas in a small volume. As an example, 1 kg of H_2 at 200 and 700 bar occupies a volume of 0.056 l and 0.016 l, respectively, to be compared to 11.200 l at 1 bar. Four types of storage cylinders exist: type I is in stainless steel or aluminium and can afford only up to 200 bar. Type II, III and IV are made in composite materials, allowing high pressure of charge (up to 700 bar), but implying a considerable cylinder cost [81]. In spreading the use of H_2 as an energy vector, its compression plays a key role, since the gas phase is still one of the most widely used storage methods [80]. However, high pressure implies high cost and large facility of compression [80]. Nowadays, conventional mechanical compressors imply loss in heat and low efficiency, requiring high energy consumption and high maintenance cost, resulting one of the main investments in a hydrogen refuelling station [80,82,83]. To overcome these problems, several non-mechanical technologies are considered as alternatives, *i.e.* electrochemical, cryogenic, adsorption and thermal compressor based on MH [80]. The latter one presents several advantages, *e.g.* no moving parts, low maintenance cost, and easy design [9,16]. This technology exploits the heat to release high purity compress gas, being

promising from an environmental point of view, when waste heat can be used instead of electricity for the heat management of the MH-reactors [84]. The thermodynamic of the equilibrium of MH absorption/desorption (Reaction (2)) is at the base of the use of MH compressor (MHC). Indeed, a low temperature implies a low pressure, and a high temperature implies a high pressure. Thus, compression occurs since M can absorbs H_2 at low supply pressure (pin) and temperature, the as called T_{low}, forming the MH. Afterwards, heating the MH at higher temperatures, as called the T_{high}, H_2 is desorbed at pressures higher than absorption (pout), according to the equilibrium, as can be schematically visualized by reporting the pcT-curves coupled with the Van't Hoff plot seen in Figure 6.

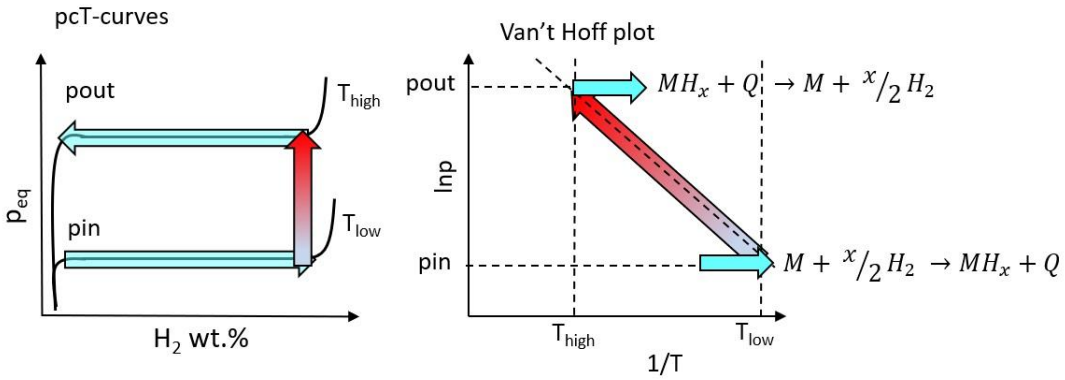

Figure 6: Schematic pcT-diagrams and Van't Hoff plot to explain a compression stage based on MH. The green star refers to the absorption stage with the formation of the MH at the pin and T_{low}, followed by the red arrow to indicate the heating of the MH from the T_{low} to the T_{high}. The blue arrow refers to the desorption stage at the T_{high} that implies the release of H_2 at the p_{out}.

During last years, the feasibility of MH to compress H_2 has been widely proven through a series of laboratory scale compressors, reaching even high delivery pressure, *e.g.* > 350 bar [85–94]. The goal of research is to achieve pressures as high as possible above 200 bar, in a temperature range nearby or even lower than 100 °C, to allow the use of water for the heat management of MH-tank and also for safety issues. Hydrides used for compression are MH based on AB (TiFe-based), AB_2 (Ti-based) and AB_5 ($LaNi_5$-based) compounds [16,80]. In particular, Yartys et al. listened a series of developed compounds used in MHC at laboratory scale [68]. From this work and the wide literature available on the compounds used in MHC, it can be deduced that particularly favourable are $LaNi_5$-based alloys substituting in La, like with Ce or Mm (Mischmetal, a mix of rare-earth metals with variable compositions based on Ce, La, Pr and Nd), the AB_2 $TiMn_2$, $TiCr_2$ and $Ti(Cr,Mn)_2$- based compounds C14 Laves phase. Nowadays, this technology is not widely available on the market, and the maximum

achievable release pressure is of the order of 200 bar at about 150 °C [9]. Devices are presented in the "*Introduction*" paragraph of Chapter 5 section 5.1.

References

[1] M. Hermesmann, T.E. Müller, Green, Turquoise, Blue, or Grey? Environmentally friendly Hydrogen Production in Transforming Energy Systems, Prog. Energy Combust. Sci. 90 (2022) 100996. https://doi.org/10.1016/j.pecs.2022.100996.

[2] S. Mekhilef, R. Saidur, A. Safari, Comparative study of different fuel cell technologies, Renew. Sustain. Energy Rev. 16 (2012) 981–989. https://doi.org/10.1016/j.rser.2011.09.020.

[3] J. Topler, J. Lehmann, Hydrogen and Fuel Cell, Springer Berlin Heidelberg, 2016. https://doi.org/10.1007/978-3-662-44972-1.

[4] A. Psoma, G. Sattler, Fuel cell systems for submarines: From the first idea to serial production, J. Power Sources. 106 (2002) 381–383. https://doi.org/10.1016/S0378-7753(01)01044-8.

[5] C. press edited by Michael Ball and Martin Wietschel, The Hydrogen Economy, Opportunities and Challenges, 2009.

[6] A. Züttel, Materials for hydrogen storage, Mater. Today. 6 (2003) 24–33. https://doi.org/10.1016/S1369-7021(03)00922-2.

[7] A.W.C. Van Den Berg, C.O. Area, Materials for hydrogen storage : current research trends and perspectives, Chem. Commun. (2008) 668–681. https://doi.org/10.1039/b712576n.

[8] T. He, Q. Pei, P. Chen, Liquid organic hydrogen carriers ☆, J. Energy Chem. 24 (2015) 587–594. https://doi.org/10.1016/j.jechem.2015.08.007.

[9] J. Bellosta von Colbe, J.-R. Ares, J. Barale, M. Baricco, C. Buckley, G. Capurso, N. Gallandat, D.M. Grant, M.N. Guzik, I. Jacob, E.H. Jensen, T. Jensen, J. Jepsen, T. Klassen, M.V. Lototskyy, K. Manickam, A. Montone, J. Puszkiel, S. Sartori, D.A. Sheppard, A. Stuart, G. Walker, C.J. Webb, H. Yang, V. Yartys, A. Züttel, M. Dornheim, Application of hydrides in hydrogen storage and compression: Achievements, outlook and perspectives, Int. J. Hydrogen Energy. 44 (2019). https://doi.org/10.1016/j.ijhydene.2019.01.104.

[10] M. Hirscher, V.A. Yartys, M. Baricco, J. Bellosta von Colbe, D. Blanchard, R.C. Bowman, D.P. Broom, C.E. Buckley, F. Chang, P. Chen, Y.W. Cho, J.C. Crivello, F. Cuevas, W.I.F. David, P.E. de Jongh, R. V. Denys, M. Dornheim, M. Felderhoff, Y. Filinchuk, G.E. Froudakis, D.M. Grant, E.M.A. Gray, B.C. Hauback, T. He, T.D. Humphries, T.R. Jensen, S. Kim, Y. Kojima, M. Latroche, H.W. Li, M. V. Lototskyy, J.W. Makepeace, K.T. Møller, L. Naheed, P. Ngene, D. Noréus, M.M. Nygård, S. ichi Orimo, M. Paskevicius, L. Pasquini, D.B. Ravnsbæk, M. Veronica Sofianos, T.J. Udovic, T. Vegge, G.S. Walker, C.J. Webb, C. Weidenthaler, C. Zlotea, Materials for hydrogen-based energy storage – past, recent progress and future outlook, J. Alloys Compd. 827 (2020). https://doi.org/https://doi.org/10.1016/j.jallcom.2019.153548.

[11] D.O. Northwood, Review Storing energy in metal hydrides : a review of the physical metallurgy, J. Mater. Sci. 18 (1983) 321–347.

[12] E.. Dematteis, J. Barale, M. Corno, A. Sciullo, M. Baricco, P. Rizzi, Solid-State Hydrogen Storage Systems and the Relevance of a Gender Perspective, Energies Rev. 14 (2021) 6158. https://doi.org//doi.org/10.3390/ en14196158 Academic.

[13] J.J. Vajo, F. Mertens, C.C. Ahn, R.C. Bowman, B. Fultz, Altering hydrogen storage properties by hydride destabilization through alloy formation: LiH and MgH 2 destabilized with Si, J. Phys. Chem. B. 108 (2004) 13977–13983. https://doi.org/10.1021/jp040060h.

[14] J. Barale, S. Deledda, E.M. Dematteis, M.H. Sørby, M. Baricco, B.C. Hauback, Synthesis and characterization of Magnesium-Iron-Cobalt complex hydrides, Sci. Rep. 10 (2020) 1–11. https://doi.org/10.1038/s41598-020-65774-8.

[15] C. Li, P. Peng, D.W. Zhou, L. Wan, Research progress in LiBH4 for hydrogen storage: A review, Int. J. Hydrogen Energy. 36 (2011) 14512–14526.

https://doi.org/10.1016/j.ijhydene.2011.08.030.
[16] M. V. Lototskyy, V.A. Yartys, B.G. Pollet, R.C. Bowman, Metal hydride hydrogen compressors: A review, Int. J. Hydrogen Energy. 39 (2014) 5818–5851. https://doi.org/10.1016/j.ijhydene.2014.01.158.
[17] M. V. Lototskyy, I. Tolj, L. Pickering, C. Sita, F. Barbir, V. Yartys, The use of metal hydrides in fuel cell applications, Prog. Nat. Sci. Mater. Int. 27 (2017) 3–20. https://doi.org/10.1016/j.pnsc.2017.01.008.
[18] A. Léon, Green Energy and Technology Hydrogen Storage, Springer, 2008.
[19] Fermin Cuevas et al., Hydrogen storage, in: Landolt-Börnstein Application (Ed.), Appl. - Hydrog. Technol., 2018: pp. 1–36. https://doi.org/0.1007/978-3-662-54261-3.
[20] J.J. Reilly, R.H. Wiswall, Formation and properties of iron titanium hydride, Inorg. Chem. 13 (1974) 218–222. 10.1021/ic50131a042.
[21] G.K. Sujan, Z. Pan, H. Li, D. Liang, N. Alam, An overview on TiFe intermetallic for solid-state hydrogen storage: microstructure, hydrogenation and fabrication processes, Crit. Rev. Solid State Mater. Sci. (2019) 1–18. 10.1080/10408436.2019.1652143.
[22] P. Thompson, F. Reidinger, J.J. Reilly, L.M. Corliss, J.M. Hastings, Neutron diffraction study of β-iron titanium deuteride, J. Phys. F Met. Phys. 8 (1978) L75–L80. 10.1088/0305-4608/10/2/001.
[23] P. Fischer, W. Hälg, L. Schlapbach, F. Stucki, A.F. Andresen, Deuterium storage in FeTi. Measurement of desorption isotherms and structural studies by means of neutron diffraction, Mater. Res. Bull. 13 (1978) 931–946. 10.1016/0025-5408(78)90105-8.
[24] T. Schober, D.G. Westlake, The activation of FeTi for hydrogen storage: A different view, Scr. Metall. 15 (1981) 913–918. 10.1016/0036-9748(81)90277-5.
[25] M.H. Mintz, S. Vaknin, S. Biderman, Z. Hadari, Hydrides of ternary TiFexM1-x(M=Cr, Mn, Co, Ni) intermetallics, J. Appl. Phys. 52 (1981) 463–467. 10.1063/1.329808.
[26] D. Dew-Hughes, The addition of Mn and Al to the hydriding compound FeTi: Range of homogeneity and lattice parameters, Metall. Trans. A. 11 (1980) 1219–1225. 10.1007/BF02668146.
[27] N. Nishimiya, T. Wada, A. Matsumoto, K. Tsutsumi, Hydriding characteristics of zirconium-substituted FeTi, J. Alloys Compd. 313 (2000) 53–58. 10.1016/S0925-8388(00)01181-6.
[28] P. Jain, C. Gosselin, J. Huot, Effect of Zr, Ni and Zr7Ni10 alloy on hydrogen storage characteristics of TiFe alloy, Int. J. Hydrogen Energy. 40 (2015) 16921–16927. 10.1016/j.ijhydene.2015.06.007.
[29] A. Guéguen, M. Latroche, Influence of the addition of vanadium on the hydrogenation properties of the compounds TiFe0.9Vx and TiFe0.8Mn 0.1Vx (x = 0, 0.05 and 0.1), J. Alloys Compd. 509 (2011) 5562–5566. 10.1016/j.jallcom.2011.02.036.
[30] H. Nagai, M. Nakatsu, K. Shoji, H. Tamura, Effect of simultaneous addition of oxygen with copper or niobium on the hydriding characteristics of FeTi for hydrogen storage, J. Less Common Met. 119 (1986) 131–142. 10.1016/0022-5088(86)90203-1.
[31] E.M. Dematteis, F. Cuevas, M. Latroche, Hydrogen storage properties of Mn and Cu for Fe substitution in TiFe0.9 intermetallic compound, J. Alloys Compd. 851 (2021) 156075. 10.1016/j.jallcom.2020.156075.
[32] S.M. Lee, T.P. Perng, Microstructural correlations with the hydrogenation kinetics of FeTi1+ξ alloys, J. Alloys Compd. 177 (1991) 107–118. 10.1016/0925-8388(91)90061-Y.
[33] J.R. Johnson, J.J. Reilly, The Use of Manganese Substituted Ferrotitanium Alloys for Energy Storage, Altern. Energy Sources. 8 (1978) 3739–3769.
[34] K.D. Ćirić, A. Kocjan, A. Gradišek, V.J. Koteski, A.M. Kalijadis, V.N. Ivanovski, Z. V. Laušević, D.L. Stojić, A study on crystal structure, bonding and hydriding properties of Ti-Fe-Ni intermetallics - Behind substitution of iron by nickel, Int. J. Hydrogen Energy. 37 (2012) 8408–8417. 10.1016/j.ijhydene.2012.02.047.
[35] K. Edalati, J. Matsuda, H. Iwaoka, S. Toh, E. Akiba, Z. Horita, High-pressure torsion of TiFe intermetallics for activation of hydrogen storage at room temperature with heterogeneous nanostructure, Int. J. Hydrogen Energy. 38 (2013) 4622–4627. 10.1016/j.ijhydene.2013.01.185.
[36] H. Emami, K. Edalati, J. Matsuda, E. Akiba, Z. Horita, Hydrogen storage performance of TiFe after processing by ball milling, Acta Mater. 88 (2015) 190–195. 10.1016/j.actamat.2014.12.052.

[37] J.M. Bellosta von Colbe, J. Puszkiel, G. Capurso, A. Franz, H.U. Benz, H. Zoz, T. Klassen, M. Dornheim, Scale-up of milling in a 100 L device for processing of TiFeMn alloy for hydrogen storage applications: Procedure and characterization, Int. J. Hydrogen Energy. 44 (2019) 29282–29290. 10.1016/j.ijhydene.2019.01.174.
[38] G. Liang, J. Huot, R. Schulz, Hydrogen storage properties of the mechanically alloyed LaNi5-based materials, J. Alloys Compd. 320 (2001) 133–139. 10.1016/S0925-8388(01)00929-X.
[39] X.H. An, Q.F. Gu, J.Y. Zhang, S.L. Chen, X.B. Yu, Q. Li, Experimental investigation and thermodynamic reassessment of La-Ni and LaNi5-H systems, Calphad Comput. Coupling Phase Diagrams Thermochem. 40 (2013) 48–55. 10.1016/j.calphad.2012.12.002.
[40] J.M. Joubert, V. Paul-Boncour, F. Cuevas, J. Zhang, M. Latroche, LaNi5 related AB5 compounds: Structure, properties and applications, J. Alloys Compd. 862 (2021). 10.1016/j.jallcom.2020.158163.
[41] M. Bououdina, D. Grant, G. Walker, Review on hydrogen absorbing materials - Structure, microstructure, and thermodynamic properties, Int. J. Hydrogen Energy. 31 (2006) 177–182. 10.1016/j.ijhydene.2005.04.049.
[42] N.A.A. Rusman, M. Dahari, A review on the current progress of metal hydrides material for solid-state hydrogen storage applications, Int. J. Hydrogen Energy. 41 (2016) 12108–12126. 10.1016/j.ijhydene.2016.05.244.
[43] D. Noreus, L.G. Olsson, P. -E.werner, The structure and dynamics of hydrogen in LaNi5H6 studied by elastic and inelastic neutron scattering, J. Phys. F Met. Phys. 13 (1983) 715–727. 10.1088/0305-4608/13/4/007.
[44] E.H. Jensen, M. Dornheim, S. Sartori, Scaling up metal hydrides for real-scale applications: Achievements, challenges and outlook, Inorganics. 9 (2021) 1–20. 10.3390/inorganics9050037.
[45] M. Palumbo, J. Urgnani, D. Baldissin, L. Battezzati, M. Baricco, CALPHAD : Computer Coupling of Phase Diagrams and Thermochemistry Thermodynamic assessment of the H – La – Ni system, CALPHAD Comput. Coupling Phase Diagrams Thermochem. 33 (2009) 162–169. 10.1016/j.calphad.2008.09.003.
[46] R. Sharma, E.A. Kumar, A Comparative Thermodynamic Analysis of Gas-Solid Sorption System Based on H2-La0.9Ce0.1Ni5/LaNi4.7Al0.3 and NH3-NaBr/MnCl2, Energy Procedia. 109 (2017) 48–55. 10.1016/j.egypro.2017.03.047.
[47] E.R. Pinatel, M. Palumbo, F. Massimino, P. Rizzi, M. Baricco, Hydrogen sorption in the LaNi5-xAlx-H system ($0 \leq x \leq 1$), Intermetallics. 62 (2015) 7–16. 10.1016/j.intermet.2015.03.002.
[48] S.K. Pandey, A. Srivastava, O.N. Srivastava, Improvement in hydrogen storage capacity in LaNi5 through substitution of Ni by Fe, Int. J. Hydrogen Energy. 32 (2007) 2461–2465. 10.1016/j.ijhydene.2006.12.003.
[49] J.S. Cantrell, T.A. Beiter, R.C. Bowman, Crystal structure and hydriding behavior of LaNis _ ySny, J. Alloys Compd. 208 (1994) 372–376.
[50] M. Odysseos, P. De Rango, C.N. Christodoulou, E.K. Hlil, T. Steriotis, G. Karagiorgis, G. Charalambopoulou, T. Papapanagiotou, A. Ampoumogli, V. Psycharis, E. Koultoukis, D. Fruchart, A. Stubos, The effect of compositional changes on the structural and hydrogen storage properties of (La-Ce)Ni5type intermetallics towards compounds suitable for metal hydride hydrogen compression, J. Alloys Compd. 580 (2013) S268–S270. 10.1016/j.jallcom.2013.01.057.
[51] F. Stein, M. Palm, G. Sauthoff, Structure and stability of Laves phases . Part I . Critical assessment of factors controlling Laves phase stability, Intermetallics. 12 (2004) 713–720. 10.1016/j.intermet.2004.02.010.
[52] J.. Johnson, J.J. Reilly, Reaction of Hydrogen with the Low-Temperature Form (C15) of TiCr2, Inorg. Chem. 17 (1978) 3103. 10.1021/ic50189a027.
[53] M. Au, F. Pourarian, S.G. Sankar, W.E. Wallace, L. Zhang, TiMn2-based alloys as high hydrogen storage materials, Mater. Sci. Eng. B. 33 (1995) 53–57.
[54] B. Liu, D. Kim, K. Lee, J. Lee, Hydrogen storage properties of TiMn2-based alloys, J. Alloys Compd. 240 (1996) 214–218.
[55] X. Wang, H. Liu, H. Li, A 70 MPa hydrogen-compression system using metal hydrides, Int. J. Hydrogen Energy. 36 (2011) 9079–9085. 10.1016/j.ijhydene.2011.04.193.
[56] S. Nayebossadri, D. Book, Development of a high-pressure Ti-Mn based hydrogen storage

alloy for hydrogen compression, Renew. Energy. 143 (2019) 1010–1021. 10.1016/j.renene.2019.05.052.
[57] J. Graetz, 2, Chem. Soc. Rev. (2009) 73–82.
[58] H.E. Kissinger, Reaction Kinetics in Differential Thermal Analysis, Anal. Chem. 303 (1957) 1702–1706. 10.1021/ac60131a045.
[59] D.P. Broon, Hydrogen Storage Materials The Characterisation of their storage properties, Springer-Verlag London, 2011.
[60] J. Málek, The applicability of Johnson-Mehl-Avrami model in the thermal analysis of the crystallization kinetics of glasses, Thermochim. Acta. 267 (1995) 61–73. 10.1016/0040-6031(95)02466-2.
[61] L. Pasquini, E. Callini, E. Piscopiello, A. Montone, M.V. Antisari, L. Pasquini, E. Callini, E. Piscopiello, A. Montone, M.V. Antisari, Metal-hydride transformation kinetics in Mg nanoparticles Metal-hydride transformation kinetics in Mg nanoparticles, Appl. Phys. Lett. 041918 (2009) 10–13. 10.1063/1.3077186.
[62] M. Baricco, M.W. Rahman, S. Livraghi, A. Castellero, S. Enzo, E. Giamello, Effects of BaRuO 3 addition on hydrogen desorption in MgH 2, J. Alloys Compd. 536 (2012) S216–S221. 10.1016/j.jallcom.2011.12.008.
[63] M. Dornheim, S. Doppiu, G. Barkhordarian, U. Boesenberg, T. Klassen, O. Gutfleisch, R. Bormann, Hydrogen storage in magnesium-based hydrides and hydride composites, Scr. Mater. 56 (2007) 841–846. 10.1016/j.scriptamat.2007.01.003.
[64] E. David, An overview of advanced materials for hydrogen storage, J. Mater. Process. Technol. 162–163 (2005) 169–177. 10.1016/j.jmatprotec.2005.02.027.
[65] C. Suryanarayana, Mechanical Alloying and Milling Mechanical Engineering, Prog. Mater. Sci. 46 (2004) 488.
[66] C. Pohlmann, L. Röntzsch, F. Heubner, T. Weißgärber, B. Kieback, Solid-state hydrogen storage in Hydralloy-graphite composites, J. Power Sources. 231 (2013) 97–105. 10.1016/j.jpowsour.2012.12.044.
[67] M. V Lototskyy, I. Tolj, L. Pickering, C. Sita, F. Barbir, Progress in Natural Science : Materials International The use of metal hydrides in fuel cell applications, Prog. Nat. Sci. Mater. Int. 27 (2017) 3–20. 10.1016/j.pnsc.2017.01.008.
[68] V.A. Yartys, M. Lototskyy, V. Linkov, D. Grant, A. Stuart, J. Eriksen, R. Denys, R.C. Bowman, D. Grant, A. Stuart, Metal hydride hydrogen compression : recent advances and future prospects, Appl. Phys. A. 122 (2016) 1–18. 10.1007/s00339-016-9863-7.
[69] S.S. Mohammadshahi, T. Gould, E.M.A. Gray, C.J. Webb, An improved model for metal-hydrogen storage tanks - Part 1: Model development, Int. J. Hydrogen Energy. 41 (2016) 3537–3550. 10.1016/j.ijhydene.2015.12.050.
[70] D. Dunikov, V. Borzenko, S. Malyshenko, Influence of impurities on hydrogen absorption in a metal hydride reactor, Int. J. Hydrogen Energy. 37 (2012) 13843–13848. 10.1016/j.ijhydene.2012.04.078.
[71] E.I. Gkanas, D.M. Grant, M. Khzouz, A.D. Stuart, K. Manickam, G.S. Walker, Efficient hydrogen storage in up-scale metal hydride tanks as possible metal hydride compression agents equipped with aluminium extended surfaces, Int. J. Hydrogen Energy. 41 (2016) 10795–10810. 10.1016/j.ijhydene.2016.04.035.
[72] P. Muthukumar, M. Groll, Erratum to " Metal hydride based heating and cooling systems : A review ," Int. J. Hydrogen Energy. 35 (2010) 8816–8829. 10.1016/j.ijhydene.2010.04.087.
[73] A.N. Kazakov, D. V. Blinov, V.Y. Bodikov, S. V. Mitrokhin, A.A. Volodin, Hydrogen storage and electrochemical properties of annealed low-Co AB5 type intermetallic compounds, Int. J. Hydrogen Energy. 46 (2021) 13622–13631. 10.1016/j.ijhydene.2020.12.071.
[74] C. Fiori, A. Dell'Era, F. Zuccari, A. Santiangeli, A. D'Orazio, F. Orecchini, Hydrides for submarine applications: Overview and identification of optimal alloys for air independent propulsion maximization, Int. J. Hydrogen Energy. 40 (2015) 11879–11889. 10.1016/j.ijhydene.2015.02.105.
[75] GKN web site: https://www.gknhydrogen.com.
[76] Toshiba web site: https://www.toshiba-energy.com.
[77] LabTech web site: https://www.labtechsrl.com/en/.
[78] A.I. Bevan, A. Züttel, D. Book, I.R. Harris, Performance of a metal hydride store on the "ross

Barlow" hydrogen powered canal boat, Faraday Discuss. 151 (2011) 353–367. 10.1039/c0fd00025f.
[79] M. V. Lototskyy, I. Tolj, M.W. Davids, Y. V. Klochko, A. Parsons, D. Swanepoel, R. Ehlers, G. Louw, B. van der Westhuizen, F. Smith, B.G. Pollet, C. Sita, V. Linkov, Metal hydride hydrogen storage and supply systems for electric forklift with low-temperature proton exchange membrane fuel cell power module, Int. J. Hydrogen Energy. 41 (2016) 13831–13842. 10.1016/j.ijhydene.2016.01.148.
[80] G. Sdanghi, G. Maranzana, A. Celzard, V. Fierro, Review of the current technologies and performances of hydrogen compression for stationary and automotive applications, Renew. Sustain. Energy Rev. 102 (2019) 150–170. 10.1016/j.rser.2018.11.028.
[81] H. Barthélémy, Hydrogen storage - Industrial prospectives, Int. J. Hydrogen Energy. 37 (2012) 17364–17372. 10.1016/j.ijhydene.2012.04.121.
[82] M. Lototskyy, M.W. Davids, D. Swanepoel, G. Louw, Y. Klochko, F. Smith, F. Haji, I. Tolj, S. Chidziva, S. Pasupathi, V. Linkov, Hydrogen refuelling station with integrated metal hydride compressor: Layout features and experience of three-year operation, Int. J. Hydrogen Energy. 45 (2020) 5415–5429. 10.1016/j.ijhydene.2019.05.133.
[83] J.O. Jensen, A.P. Vestbø, Q. Li, N.J. Bjerrum, The energy efficiency of onboard hydrogen storage, J. Alloys Compd. 446–447 (2007) 723–728. 10.1016/j.jallcom.2007.04.051.
[84] M. Costamagna, J. Barale, C. Carbone, C. Luetto, A. Agostini, M. Baricco, P. Rizzi, Environmental and economic assessment of hydrogen compression with the metal hydride technology, Int. J. Hydrogen Energy. 47 (2022) 10122–10136. 10.1016/j.ijhydene.2022.01.098.
[85] F. Laurencelle, Z. Dehouche, J. Goyette, T.K. Bose, Integrated electrolyser-metal hydride compression system, Int. J. Hydrogen Energy. 31 (2006) 762–768. 10.1016/j.ijhydene.2005.06.019.
[86] M. Visaria, I. Mudawar, Experimental investigation and theoretical modeling of dehydriding process in high-pressure metal hydride hydrogen storage systems, Int. J. Hydrogen Energy. 37 (2012) 5735–5749. 10.1016/j.ijhydene.2011.12.140.
[87] G. Karagiorgis, C.N. Christodoulou, H. von Storch, G. Tzamalis, K. Deligiannis, D. Hadjipetrou, M. Odysseos, M. Roeb, C. Sattler, Design, development, construction and operation of a novel metal hydride compressor, Int. J. Hydrogen Energy. 42 (2017) 12364–12374. 10.1016/j.ijhydene.2017.03.195.
[88] B.S. Sekhar, P. Muthukumar, Performance investigation of a single-stage metal hydride heat transformer, Int. J. Green Energy. 13 (2016) 102–109. 10.1080/15435075.2014.892879.
[89] Y. Madaria, E. Anil Kumar, Effect of heat transfer enhancement on the performance of metal hydride based hydrogen compressor, Int. J. Hydrogen Energy. 41 (2016) 3961–3973. 10.1016/j.ijhydene.2016.01.011.
[90] A.R.E. Galvis, F. Leardini, J.R. Ares, F. Cuevas, J.F. Fernandez, Experimental behaviour of a three-stage metal hydride hydrogen compressor, JPhys Energy. 2 (2020). 10.1088/2515-7655/ab869e.
[91] X.C. Hu, Z.G. Qi, M. Yang, J.P. Chen, A 38MPa compressor based on metal hydrides, J. Shanghai Jiaotong Univ. 17 (2012) 53–57. 10.1007/s12204-012-1229-5.
[92] X.H. Wang, Y.Y. Bei, X.C. Song, G.H. Fang, S.Q. Li, C.P. Chen, Q.D. Wang, Investigation on high-pressure metal hydride hydrogen compressors, Int. J. Hydrogen Energy. 32 (2007) 4011–4015. 10.1016/j.ijhydene.2007.03.002.
[93] H. Li, X. Wang, Z. Dong, L. Xu, C. Chen, A study on 70 MPa metal hydride hydrogen compressor, J. Alloys Compd. 502 (2010) 503–507. 10.1016/j.jallcom.2010.04.206.
[94] V. V. Solovey, A.I. Ivanovsky, V.I. Kolosov, Y.F. Shmal'ko, Series of metal hydride high pressure hydrogen compressors, J. Alloys Compd. 231 (1995) 903–906. 10.1016/0925-8388(95)01780-1.

Chapter 2
Experimental and methods

This chapter lists the experimental techniques used during the work and the relative instruments, presenting also the methods applied in the simulation and data elaboration. Afterwards, in the following chapters, in the *"Experimental"* section, the experimental conditions applied will be reported per each case study and work. Samples are handled in air or in glovebox in argon atmosphere with low concentration of oxygen and water (≤ 1 ppm).

2.1 Lumped elemental simulations

Simulations were performed to evaluate the parameters that influence the system weight and volume. Simple simulations, as called lumped, were performed, considering the geometry of systems, but neglecting the variation of parameters as a function of time. Simulations were carried out with MATLAB software and Excel. When the thickness of reactor walls needs to be considered and/or calculated, it takes into account the theoretical minimum value, depending on the selected internal diameter (Øint) and working condition (Equation. 1):

$$e = \frac{øintP}{4fz-P} + c + ce + \delta \qquad \text{(Eq. 1)}$$

where *e* is the theoretical minimum thickness (mm); *f* is the nominal admissible strength at the working temperature (MPa); *P* represent the pressure that the system can stand (MPa); *z* is the welding efficiency (constant value equal to 1); *c* is the corrosion overpressure (mm); *ce* is the tolerance at external corrosion (mm) and δ is the tolerance (mm). In all simulations performed, thanks to the defined working conditions, the contribution to *e*, provided by *c*, *ce* and δ is neglected. The formula belongs to the legislation EN 13445.

2.2 Synthesis by arc melting

When the synthesis of alloys was to be performed, samples were prepared by arc melting, with the instrument by Edmund Bühler GmbH, starting from elemental metals in Argon atmosphere (gas purity 5.5). Residual traces of oxygen were removed by melting Ti and Zr getters.

2.3 Chemical, morphological, and structural characterization

2.3.1 Powder X-Ray Diffraction (PXD)

Structural and phase investigations were performed through Powder X-Ray Diffraction (PXD). The instruments are the X'Pert Bragg-Brentano diffractometer and the X'Pert Pro

diffractometer in Debye-Scherrer geometry, which are equipped with a X'celerator detector. Finally, some measures occurred also in the diffractometer Bruker D8 in Bragg-Brentano geometry (Universidad Autònoma de Madrid). All the diffractometers are equipped with a Cu-Kα radiation. Samples studied in Debye-Scherrer geometry were prepared in glovebox by filling glass capillaries, while in Bragg-Brentano geometry analysis occurred in air. Qualitative analyses of the patterns were performed with the software X-Pert High Score, while the Rietveld refinements of the crystal structures were carried out with the Maud software [1].

2.3.2 Scanning Electron Microscopy (SEM)

The study of samples microstructure and of powder morphology was performed by Scanning Electron Microscopy (SEM). The instruments used are the Tescan Vega and the Hitachi S300, equipped with the Energy Dispersive X-ray (EDX) Quantax model (Universidad Autònoma de Madrid). Also, a Field Emission Gun - Scanning Electron Microscopy (FEG-SEM) instrument Tescan 9000 was used. Samples were observed embedded in a conductive resin and polished or just located on a stub, in particular as loose powders. EDX elemental measurements were performed. Some Monte Carlo simulations were carried out with the software CASINO [2] to simulate the penetration depth of the electronic beam inside the material.

2.4 Hydrogen sorption properties

A volumetric Sievert's type apparatus was used to perform the thermodynamic study of the MH by acquiring pcT-curves in absorption and desorption and to evaluate the H_2 reaction rates. High purity (6.0) H_2 gas was used. The used instruments are the pcT-Pro by Setaram and the volumetric apparatus by the AMC of Pittsburgh, studying about 2 g and 300 mg of sample as loose powder, respectively. In both instruments, temperature is controlled through an electric furnace.

At the Universidad Autònoma de Madrid, the homemade volumetric apparatus shown in Figure 1 was used. The H_2 line is connected to an H_2 cylinder that can supply up to 60 bar and involves also a 3 stage MHC based on $Ti_{0.85}Zr_{0.15}Mn_{1.33}V_{0.3}$, $Ti_{0.8}Zr_{0.2}Mn_{1.2}Cr_{0.6}V_{0.2}$ and $Ti_{0.9}Zr_{0.1}Mn_{1.47}Cr_{0.4}V_{0.2}$ alloys that allows to reach a maximum pressure of about 140 bar at 140 °C [3]. During measurements, H_2 required by the sample came from the H_2 line and when high pressure is required, it is compressed by only the 3rd stage of the MHC.

Temperature and pressure are monitored as a function of time thanks to sensors, allowing the calculation of the amount of H_2 processed thanks to calibrated volumes. About 0.80 g of sample was located in a stainless-steel reactor (Figure 1). Temperature is controlled by electric resistance and the sample can be cooled at temperatures lower than the room one, thanks to a water bath thermostated by a chiller.

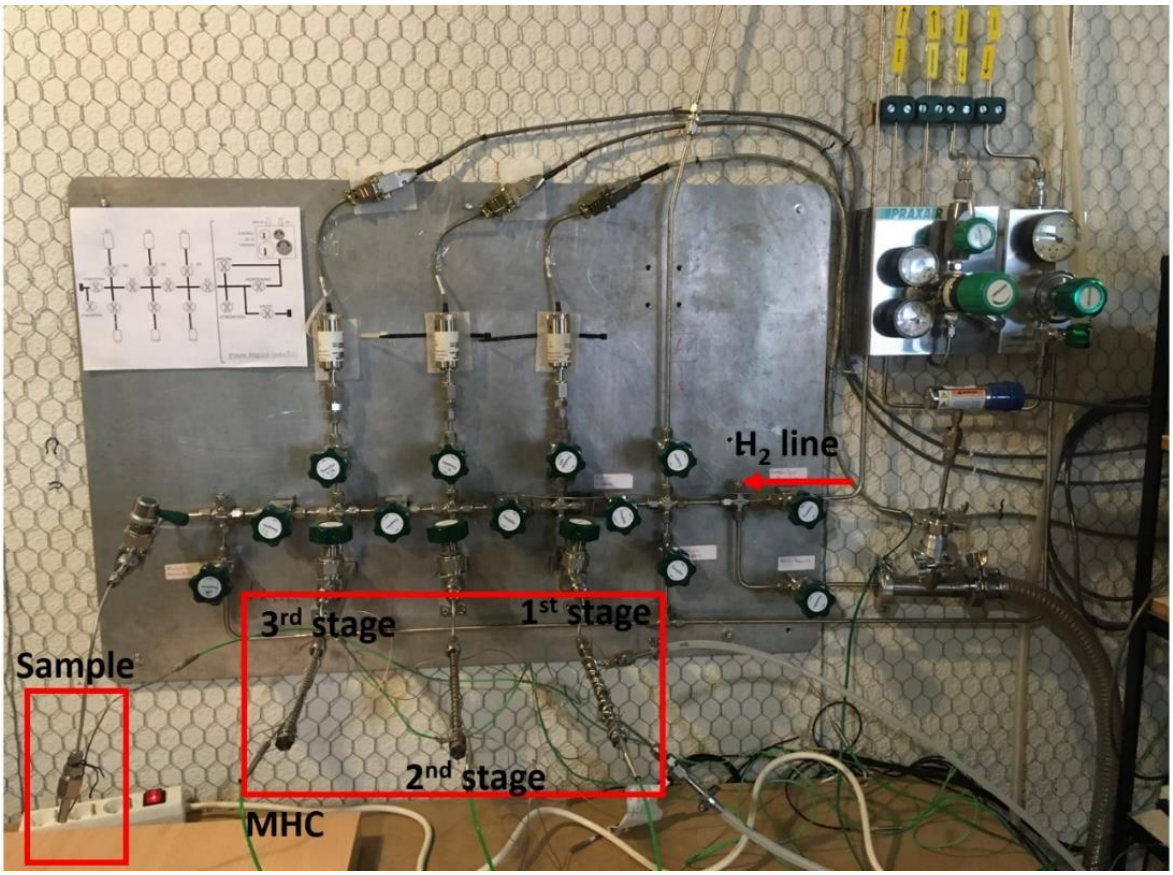

Figure 1: Setup of the volumetric apparatus used at the Universidad Autonòma de Madrid.

References

[1] L. Lutterotti, S. Matthies, H.R. Wenk, A.S. Schultz, J.W. Richardson, Combined texture and structure analysis of deformed limestone from time-of-flight neutron diffraction spectra, J. Appl. Phys. 81 (1997) 594–600. doi.org/10.1063/1.364220.

[2] P. Hovington, D. Drouin, R. Gauvin, CASINO: A New Monte Carlo Code in C Language for Electron Beam Interaction - Part I: Description of the Program, Scanning. 19 (1997) 1–14.

[3] A.R.E. Galvis, F. Leardini, J.R. Ares, F. Cuevas, J.F. Fernandez, Experimental behaviour of a three-stage metal hydride hydrogen compressor, JPhys Energy. 2 (2020). 10.1088/2515-7655/ab869e.

Chapter 3
Lumped element model of hydrogen storage systems

3.1 Modelling of the gravimetric and volumetric capacity of hydrogen storage system based on MH [1]

3.1.1 Introduction

The definition of a hydrogen storage system (H2SS), aiming to meet the needs required by specific applications, is mainly related to the selection of the proper MH properties and to the design of the container [2]. Design of a tank strongly influences gravimetric and volumetric capacities of a H2SS. These two parameters are the amount of H_2 stored, respectively, over the weight and volume of the whole system. First of all, it is necessary to define the boundaries of the system, which can be described as the tank, the H_2-carrier and the thermal fluid necessary for the heat transfer, neglecting piping and valves used as auxiliaries. The main parameters that influence gravimetric and volumetric density of the H2SS are MH properties (*i.e.* the gravimetric and volumetric density of the H_2-carrier) and the tank geometry. For the latter, the most common geometry is tubular, but it can be also planar or disc-shaped [2]. All variations in geometry are brought to optimize the heat management necessary for the H_2 sorption reactions [2]. The challenge is to develop a container in which the right compromise is achieved, especially for mobile applications, among H_2 storage gravimetric and volumetric density, integrity of the containment at operative condition and dynamic performances of the gas and safety [2]. In this paragraph we proposed a simple approach, based on a series of simulations, to evaluate the influence of MH property of gravimetric and volumetric and tank geometry (*i.e.* tube diameter and length) on the gravimetric and volumetric capacity of a H2SS. Simulations do not take into account the operating conditions, *i.e.* the kinetics of the reaction and thermo-fluid dynamics of hydrogen and heat flow.

3.1.2 Boundary conditions

The tank has a simple double tube geometry, with the solid-state H_2-carrier in the inner tube and thermal fluid exchanger in the outer one. The diameter of the external jacket is 10 % higher than the internal one and tubes are 3 mm thick. In the model, a liquid with a density of 1 g/cm^3 is considered (*e.g.* water) as thermal fluid and it contributes to the gravimetric capacity of the system in relation to the amount of fluid flowing in the jacket, without considering its flow rate. The latter value is related to the thermal exchange necessary for

the H_2 sorption reactions, but it does influence neither the gravimetric nor the volumetric density of the system. As a reference, the amount of H_2 stored by the system is fixed to 1 kg. The H_2-carrier powder presents a percentage of compactness of 90 % and, inside the tube a free volume of 20 % is left to allow MH expansion during the absorption of H_2. To evaluate the effect of the material of the container, simulations include the use of both aluminium and steel. In each simulation, the length of tube is calculated in relation to its diameter, from the volume necessary for the H_2-carrier. The volume of the system is then constant after having defined the volumetric capacity of MH. Simulations considered arbitrary and real MH, neglecting their real working condition of pressure and temperature.

3.1.3 Results and discussion

Figure 1 shows how the gravimetric capacity of the system changes as a function of the gravimetric (a) and volumetric (b) capacity of arbitrary H_2-carrier (MH). The internal diameter of tube was fixed at 10 cm and both aluminium and steel materials have been considered. The gravimetric and volumetric capacity of the arbitrary MH are selected to cover a wide range of values.

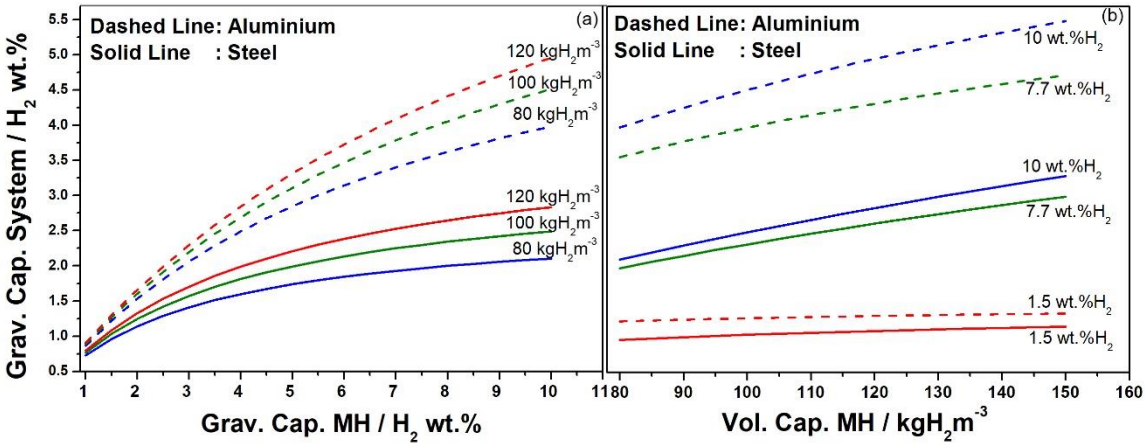

Figure 1: (a) Gravimetric capacity of the system as a function of the gravimetric capacity of MH, using a volumetric capacity of MH equal to 80-100-120 kgH_2m^{-3} (b) Gravimetric capacity of the system as a function of the volumetric capacity of the MH, using a gravimetric capacity of MH of 1.5-7.7-10 wt.%H_2. In both cases, it was considered a diameter of tube of 10 cm in aluminium (dashed lines) and steel (continuous lines).

In Figure 1-a, for the MH, three volumetric capacities of MH were compared. The gravimetric capacity of system grows fast for low gravimetric capacity values, but it seems to bring to a plateau for high values of MH H_2 wt.%. Thus, on the gravimetric capacity of the system, an increase of the carrier gravimetric capacity has a higher influence for low values of H_2 wt.%, with respect to the high ones. In addition, the higher is the given MH

volumetric capacity (80, 100 and 120 kgH_2/m^3), the higher is the gravimetric capacity of the system. Finally, the gravimetric capacity of the system reaches about half of that of the MH when using aluminium for tubes, and it reaches about one fourth in case of using steel. In Figure 1-b, the gravimetric capacity of the system is reported as a function of the MH volumetric capacity, considering three values for the MH gravimetric capacity. The influence on system gravimetric capacity is roughly linear as a function of the MH volumetric capacity. Changes in gravimetric capacity of the system as a function of MH volumetric capacity are more remarkable for carriers with values of 7.7 and 10 H_2 wt.%, rather than for carriers with 1.5 H_2 wt.%. Moreover, the use of aluminium instead of steel has a minimal difference for carriers with 1.5 H_2 wt.%, while a strong effect is registered for higher values of capacity.

Figure 2-a shows the results of the estimation of the gravimetric capacity of the system as a function of the diameter of tube, considering a MH with a gravimetric and volumetric capacity of 1.5 H_2 wt.% and 100 kgH_2/m^3, respectively.

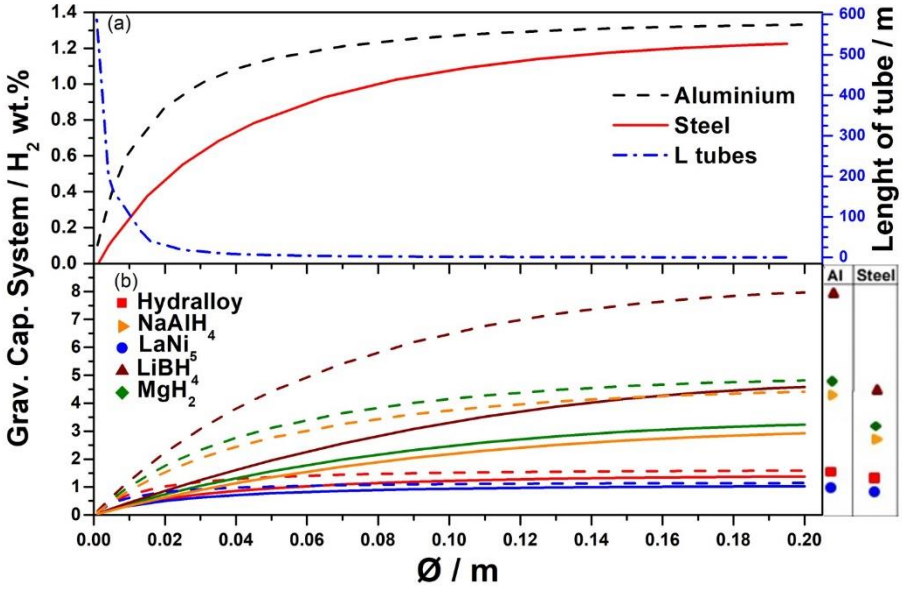

Figure 2: The gravimetric capacity of the system as a function of the diameter of tube. (a) Curves have been obtained considering a MH with a gravimetric and volumetric capacity of 1.5 wt.%H_2 and 100 kgH_2m^{-3}, respectively. The gravimetric capacity of the system is calculated for aluminium (dashed lines) and steel (continuous lines) tube. It is also reported in dashed dot line the variation of the length of tube as a function of the diameter. (b) The gravimetric capacity of the system is reported considering different hydrides.

To maximize the heat management, the container should have a diameter as smallest as possible, since the heat transfer distance is short and there is a better heat dissipation compared to large diameters. Thus, the simulation considers tubes longer than wide, until the difference between the length and diameter becomes minimal (Figure 2-a). As expected,

the length of tube decreases asymptotically increasing the diameter. The gravimetric capacity of the system grows progressively increasing the tube diameter, moving towards a plateau for high values. This result suggests that very small diameters are not practical, but from a certain value, an increase of the tube diameter does not have a relevant impact on the system gravimetric capacity. In practice, tubes need to be longer than wide, but without exceeding with dimension. Moreover, the use of steel or aluminium as material for tubes does not influence the gravimetric capacity considerably. The gravimetric capacity of the system was also evaluated as a function of the diameter of the internal tube considering specific H_2-carriers, *i.e.* Hydralloy-C5 ($TiMn_2$-based alloy), $NaAlH_4$, $LaNi_5$, $LiBH_4$ and MgH_2 (Figure 2-b). Corresponding values of gravimetric and volumetric capacity of the carriers are reported in Table 1.

Table 1: Gravimetric and volumetric capacity of Hydralloy-C5, $NaAlH_4$, $LaNi_5$, $LiBH_4$ and MgH_2.

MH	**Hydralloy**[3]	**$NaAlH_4$**[4]	**$LaNi_5$**[5]	**$LiBH_4$**[4]	**MgH_2**[5]
Grav. Cap. wt.%	1.6	7.3	1.5	18.4	7.7
Vol. Cap. kgH_2m^{-3}	115	93.4	115	122	110

Low values of MH gravimetric capacity (*i.e.* $LaNi_5$ and Hydralloy-C5) do not have a particular influence on the system and the difference in using of aluminium or steel for tubes is negligible. On the contrary, for high value of MH gravimetric capacity (*i.e.* MgH_2, $NaAlH_4$ and $LiBH_4$) there is a much more increase in the gravimetric capacity of the system by increasing the diameter of tube. In addition, the use of aluminium or steel for tubes has a bigger influence for $LiBH_4$, which has an elevated gravimetric capacity, with respect to the other two hydrides. The reduction of the gravimetric capacity of the system is higher for materials with higher values of MH gravimetric capacity. Finally, considering the volumetric capacity of the system (Figure 3), there is a linear trend as a function of the volumetric one of MHs, reaching a value close to the half of that of MHs.

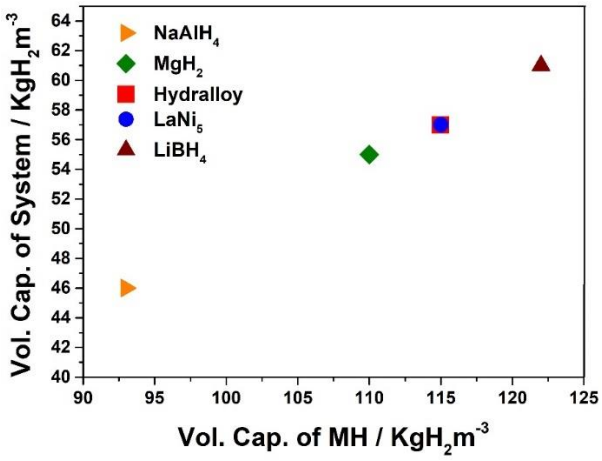

Figure 3: Volumetric capacity of the system considering the Hydralloy-C5, $NaAlH_4$, $LaNi_5$, $LiBH_4$ and MgH_2.

3.1.4 Conclusion

From these simulations, it was highlighted the importance of tank geometry on a H2SS. A right compromise needs to be reached between length and diameter of tubes, without exceeding in both dimensions. Moreover, the material used for tubes has a high influence on gravimetric capacity of H2SS, mainly in case of light hydrogen carriers. Finally, MH volumetric capacity has a high influence on system for high values of MH gravimetric capacity. On the contrary, the gravimetric capacity of the system is less affected for high values of MH gravimetric capacity.

3.2 Evaluation of system parameters of a H2SS based on MH and compressed gas

3.2.1 Introduction

Depending on the final application, the volumetric and gravimetric density of a H2SS is important in the selection of the storage technology. For stationary applications, the volume density plays a key role, while in mobile applications, especially in light ones, low volume and weight are required. Considering the storage of hydrogen as MH and as compressed gas, in the first case, the system represents the H_2-carrier, the thermal fluid and the tank, as discussed in section 3.1 [1]. While as compressed gas (H2CG), the system is easier and consists only in the cylinders. When considering IMC, a problem is the weight of the system, due to their low gravimetric capacities, implying a high amount of alloy. On the contrary, for compress gas, less weight of system is guarantee, and when a high pressure is reached, it might be also advantageous from volumetric point of view. Nevertheless, conventional mechanical compression is energy consuming and costly [6].

In this work, a comparison between the H2CG and MH is performed in terms of volumetric and gravimetric density of a H2SS. Through simple simulations, it is considered to design two H2SSs with a capacity of 50 kg of H_2, in which the gas is stored directly from an EL at 30 bar. In this way, the two systems result to be comparable, since not an additional compression stage is considered for the H2CG case study and implies the use of IMC as H_2-carrier. 50 kg of H_2 has been selected, since it can represent a promising quantity of hydrogen storage, with an available power of about 1665 kWh. As an example, for a stationary application, five independent houses with a consumption of 8 kWh/day, could be roughly continuously supplied for 21 days, supposing the use of a PEM-FC of 15 kW with a hydrogen flow of 10 Nm^3/h. Then, 50 kg of H_2 could be also interesting in heavy mobile applications, like small-medium scale ships, since the weight of the system could be advantageous in terms of balance. As an example, the industry Fincantieri is developing a prototype of ship as called Zeus, based on 50 kg of H_2 stored as MH [7] and it is reported in literature as a quantity of compress gas to allow 7 h operation at 100 kWe load [8].

3.2.2 Boundary conditions

The material of container is stainless steel AISI316, that is a common material of MH tank and can be associated to a type I cylinder for the H2CG. Tubes generally refer to commercial dimensions, and their thickness takes into account the theoretical minimum one (Chapter 2).

It is assumed to store 50 kg of H_2 at 30 bar and, to make considerations on system volume, it is also assumed to allocate the H2SS in a standard ISO container (length 6100 mm, height 2590 mm, width 2440 mm).

50 kg of H_2 as MH is considered based on IMCs, since their use allow low working temperatures (*e.g.* $\leq$ 50 °C), enabling the use water as thermal fluid for the heat management. The alloy is considered with a powder density of 3.5 g/cm^3. A 30 % of free volume is left inside the reactor to allow powder expansion in absorption. A 30 % is used, since referring to IMC, a variation in volume between the not hydrogenated form and the hydride one is reported up to 20-25 %, evaluating suitable a 30 % independently by the IMC considered, to avoid any tension on reactor structure [9]. At this regards, reactor are also placed horizontally [10]. A double tube geometry is considered as tank design, with an inner tube for the MH powder and an outer jacket for the thermal fluid. The latter has a Øint higher of the 10 % of the Øext of the inner tube. The wall thickness of the jacket is estimated from the minimum one (Chapter 2), considering a maximum water pressure of 5 bar and evaluating commercial dimension. In the simulations the design is evaluated in term of reactor length and diameter and IMCs property of MH gravimetric capacity.

The storage as compressed gas occurs in tube of 4 and 6 inch, *i.e.* with Øext of 114.3 and 168.3 mm, and a thickness of 3.2 and 4.8 mm, respectively.

3.2.3 Results and discussion

3.2.3.1 Case study: H2SS based on MH

On the base of the MH storage capacity, *i.e.* between 1.0 and 2.0 H_2 wt.%, the amount of carrier is evaluated (Figure 4). To store 50 kg of H_2, tons of carrier are required, passing from 5 ton for 1.0 H_2 wt.% to 2.5 ton for 2.0 H_2 wt.%. As expected, the amount progressively decreases increasing the gravimetric capacity, but not linearly.

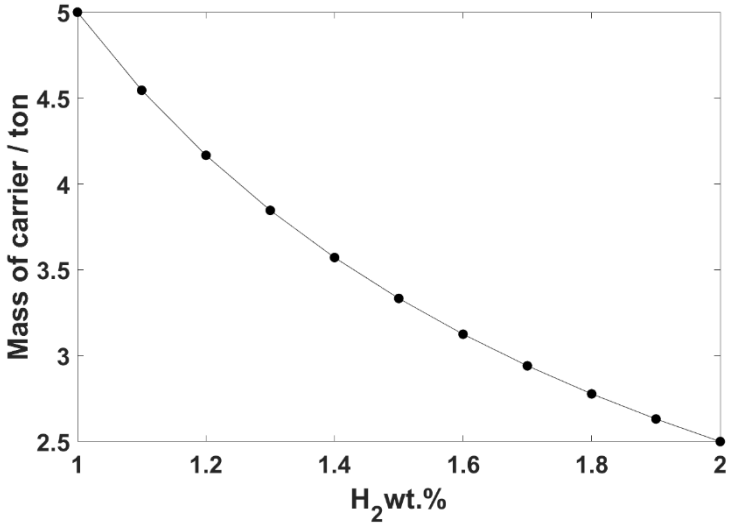

Figure 4: Mass of carrier in form of powder as a function of the MH gravimetric capacity.

The number of tubes depends on their geometry. Reactor's length (Lr) can reasonably vary from 3.0 m up to 5.0 m (with a step of 0.5 m), to leave a minimum of 1 m of free space inside the container to allows the allocation of auxiliaries (pipes, valves). When choosing the proper tube diameter, it needs to be considered that MH presents poor thermal conductivity [2]. Thus, to reduce the heat path, tubes are always longer than wide, with a diameter as small as possible. In this case, the evaluation of the inner tube dimension, *i.e.* the one in which the MH powder is located, was made considering various diameter from 2 to 8 inch, and details on tubes dimension are reported in Table 2. The thickness refers to the smallest commercially available per each corresponding diameter, that was checked to be suitable up to 80 bar and 100 °C (Chapter 2). Latter conditions refer to the maximum affordable temperature and pressure, taking into account a possible over pressure and heating for powder activation.

Table 2: Values of Øext and thickness considered for MH-inner tube.

Øext	2”	3”	4”	5”	6”	8”
	60.3 mm	88.9 mm	114.3 mm	141.3 mm	168.3 mm	219.1 mm
Thickness	3.7 mm	3.2 mm	3.2 mm	4.0 mm	4.8 mm	4.8 mm

Per each tube dimension, Figure 5 shows the number of tubes as a function of the MH gravimetric capacity obtained for the different Lr per a given Øext. Then, as an example, Table 3 reports the number of tubes obtained considering the extreme condition in Lr, *i.e.* 3.0 and 5.0 m, and MH gravimetric capacity, *i.e.* 1.0 and 2.0 H_2 wt.%, for Øext.

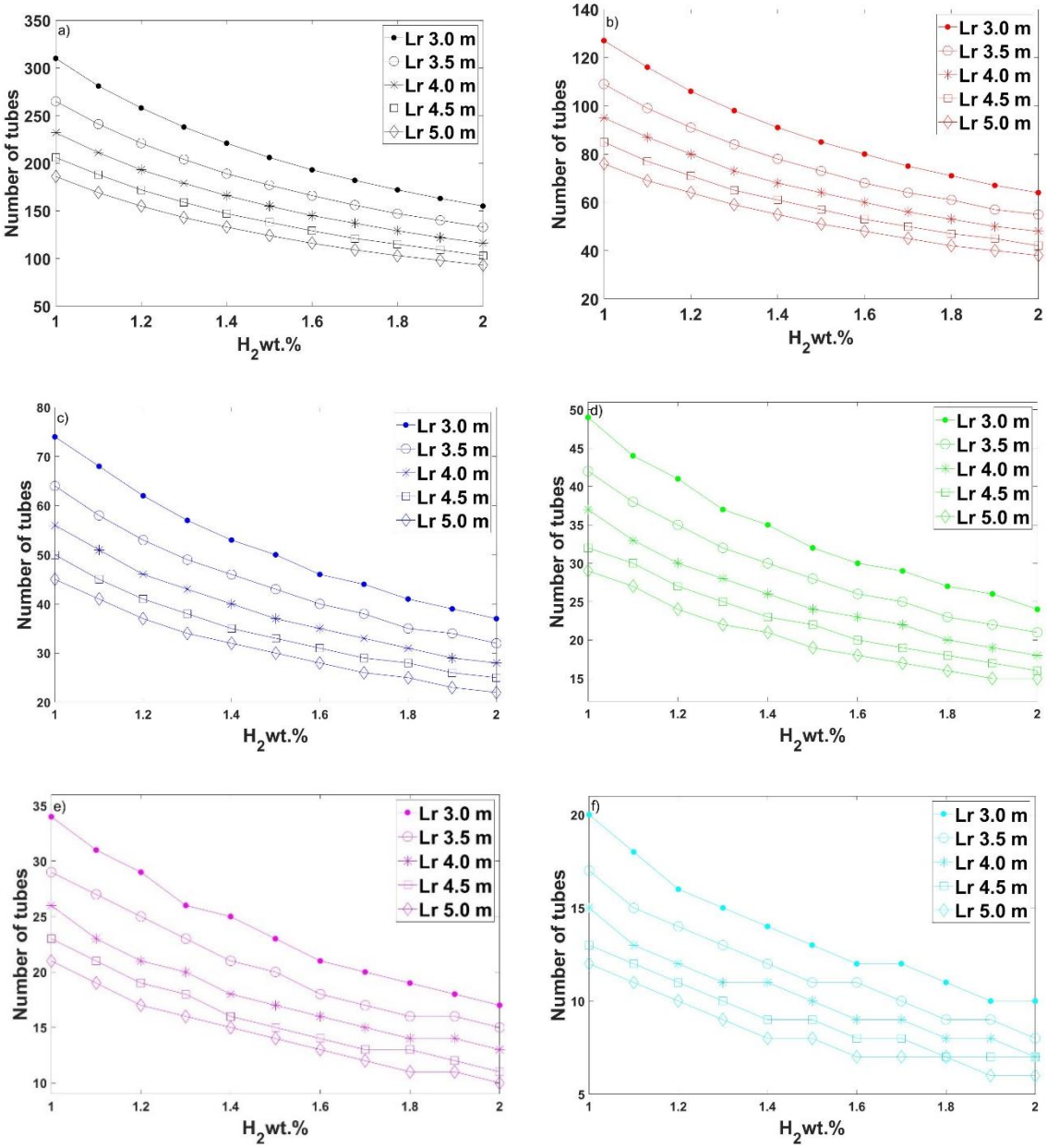

Figure 5: The number of tubes as a function of the MH gravimetric capacity for tube Øext (a) 2 inch; (b) 3 inch; (c) 4 inch; (d) 5 inch; (e) 6 inch; (f) 8 inch. Values are calculated considering different Lr.

Table 3: Number of tubes per each geometry considering the extreme conditions, i.e. 1.0 and 2.0 H_2 wt.% and Lr of 3.0 and 5.0 m.

Øext	2”	3”	4”	5”	6”	8”
1.0 H_2 wt.%						
Lr 3.0 m	310	127	74	49	34	20
Lr 5.0 m	186	76	45	29	21	12
2.0 H_2 wt.%						
Lr 3.0 m	155	64	37	24	17	10
Lr 5.0 m	93	38	22	15	10	6

The number of tubes as a function of the MH does not follow a linear trend, as can be seen from Figure 5. For small Øext, the number of tubes at a given Lr decreases moving towards a plateau increasing the gravimetric capacity (Figure 5). While increasing the diameter from 5", this effect is less evident, observing similar number of tubes for MH gravimetric capacity equal or above 1.6 H_2 wt. %, as can be observed from Figure 5. This effect depends on the fact that integer values of tube are considered, and, as long as the dimension increases, the effect of the length and of the gravimetric capacity is less remarkable on the final number of tubes required. The need of integer numbers of tubes at a given design implies that at the end, the final amount of powder required for a given capacity is not exactly the same one supposed by Figure 4, and therefore the final amount of H_2 can slightly differ from 50 kg. Per a given diameter, the longer is the tube the fewer are the number of tubes required for a given storage capacity (Figure 5 and Table 3). The difference became smaller and smaller while increasing the diameter. The same trend is observed for a given tank dimension in Lr and Øext comparing the number of tubes by increasing the MH gravimetric capacity. By increasing tubes dimension and/or MH gravimetric capacity the number of tubes to be handled is sensitively decreased. As an example, the number of tubes with Lr of 3.0 m at Øext 2" and 8" for a MH of 1.0 H_2 wt.% passes from 310 to 20, respectively, that became respectively 155 and 10 with a MH of 2.0 H_2 wt.% (Table 3). Per a given Lr and MH gravimetric capacity, the number of tubes decreased remarkably of about 94 % by increasing the Øext from 2" to 8" (Table 3). The number of tubes decreases of about 40 % by increasing the Lr from 3.0 m to 5.0 Lr, per a given Øext and MH gravimetric capacity (Table 3).

Based on the consideration made so far, to proceed with system evaluation it is important to fix some constraints regarding the MH capacity and tank design. Small diameters and lengths cause a considerably high number of tubes, that should result in a hard displacing inside the container. Thus, suitable dimension can be considered Lr of 4.0, 4.5 and 5.0 m with Øext of 5", 6" and 8". It is hard to have commercially available IMC with 2.0 H_2 wt.%, while 1.0, 1.4 and 1.6 H_2 wt.% are realistic values. As an example, commercial alloys have been considered: TiFe-based, $LaNi_5$-based and $TiMn_2$-based [1,11]. Figure 6 shows the number of tubes for the considered MH capacity as a function of the Øext and the considered Lr. Evaluating the effect of tank design in terms of Lr and Øext for a given IMC, tubes longer and wider allow to almost halve the final number of tubes required, *e.g.* for 1.0 H_2 wt.% (Figure 6-a) with 37 tubes of Øext 5" and 4.0 m and 12 tubes of Øext 8" and 5.0 m. Furthermore, considering MH gravimetric capacity, for a fixed design, the number of tubes

can be sensitively decreased from 1.4 H_2 wt.% (Figure 6-b) to 1.0 H_2 wt.% (Figure 6-a), *e.g.* with Øext 5" and 4.0 m, 26 tubes are required despite 37, respectively. While the difference between 1.4 H_2 wt.% and 1.6 H_2 wt.% is smaller, with 26 and 23 tubes, respectively.

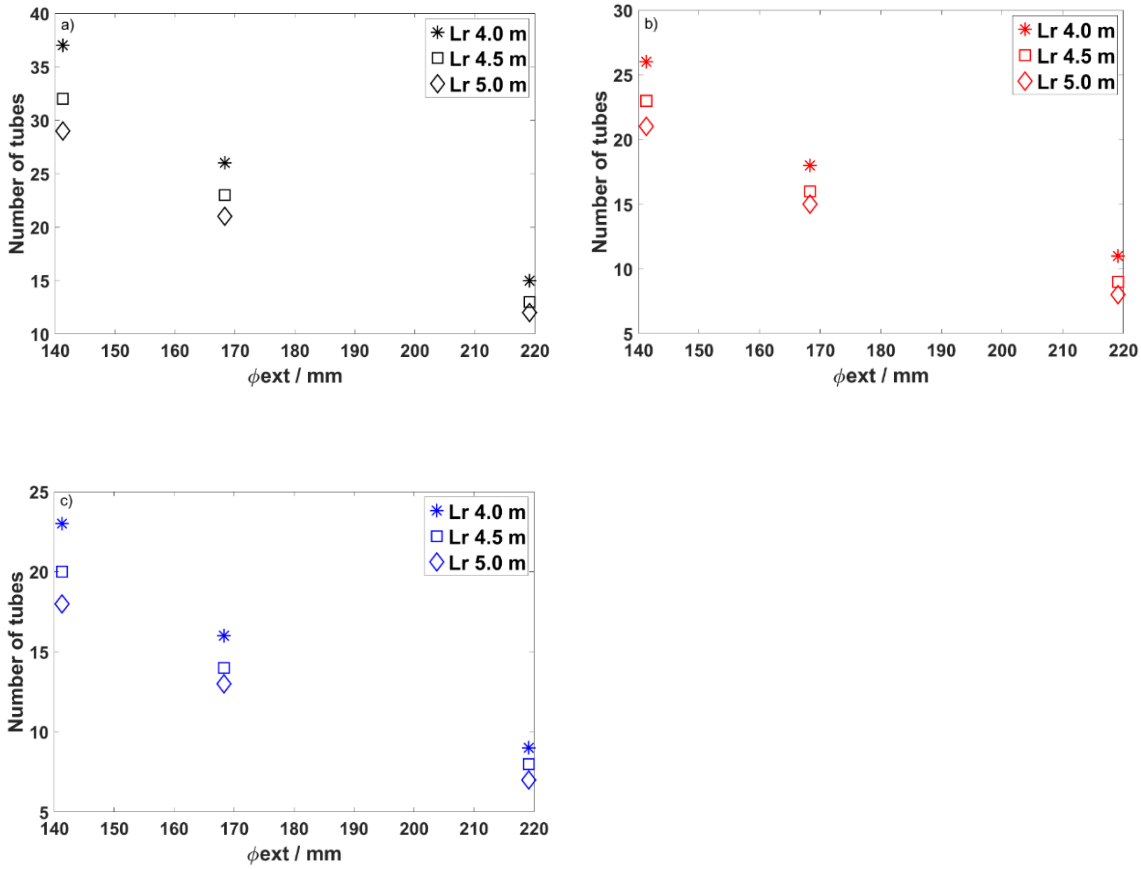

Figure 6: Number of tubes as a function of the Øext per each Lr for a given IMC: (a) with 1.0 H_2 wt.%; (b) with 1.4 H_2 wt.%; (c) with 1.6 H_2 wt.%.

The dimension of the jacket was evaluated as defied in the boundary condition (section 3.2.2). It results in a jacket dimension with an Øext of 167.4, 215.1 and 271.0 mm and a thickness of 6, 15 and 15 mm related to the inner tube with Øext 5", 6" and 8", respectively. The system weight, *i.e.* the total amount of steel, powder, water and H_2 stored, is reported together with the gravimetric capacity of the system (the amount of H_2 stored over the weight of steel, water and powder) as a function of the Øext per a given Lr, in Figure 7 for the MH gravimetric capacity of 1.0 (a, b), 1.4 (c, d) and 1.6 H_2 wt.% (e, f).

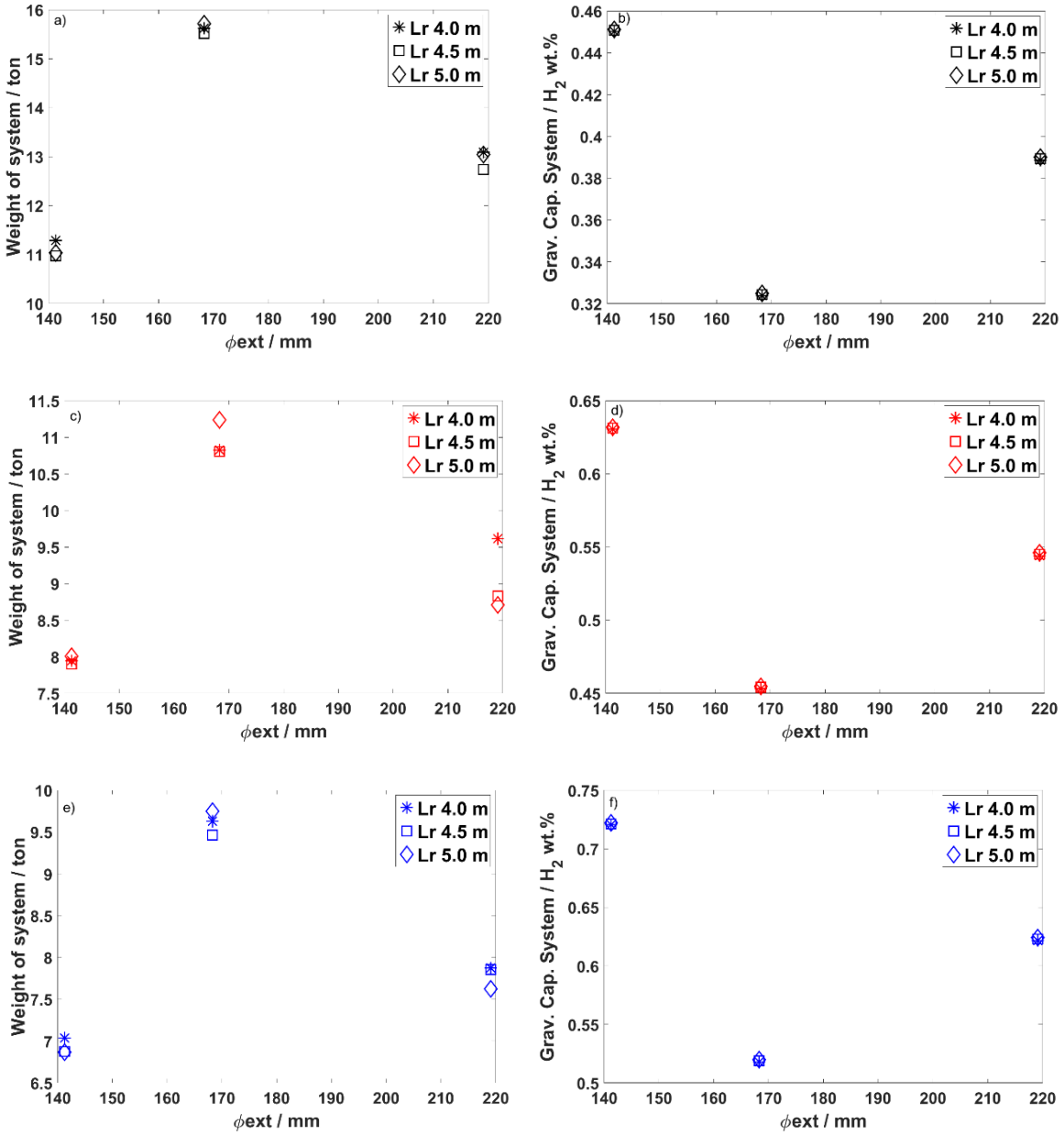

Figure 7: Weight of system and gravimetric capacity of system per each configuration considered for a given IMC: (a) and (b) with 1.0 H_2 wt.%; (c) and (d) with 1.4 H_2 wt.%; (e) and (f) with 1.6 H_2 wt.%.

The effective amount of powder and H_2 stored was recalculated on the base of the number of tubes. In general, after having fixed the MH and the design in terms of Øext of tubes, the length has not a big influence on system weight. At a given Øext, the effect of Lr is negligible at 1.0 H_2 wt.% (Figure 7-a), while a slightly difference is noticed both at 1.4 H_2 wt.% and 1.6 H_2 wt.% (Figure 7-c,e) due to similar number of tubes required between 4.5 and 5.0 m in these capacity (Figure 6-b,c). On the contrary, the Øext of tube has a remarkable effect on the system weight and in turns in the gravimetric capacity. Indeed, at 6" the highest weight of system and as a consequence the lowest value of system gravimetric capacity is always

registered independently by the MH. This effect is due to the similar amount of steel between one tube of Øext 6" and 8", caused by the equal thickness of both inner tube and jacket. Thus, because of the similar weight of one single tube, the higher number of tubes required with 6" results in a heavier system than Øext 8". The Øext 6" seems to not have an optimal ratio weight of one single tube and the overall number required, on the contrary of Øext 8" implying a less weight of the system compared to Øext 6". The ratio weight of one single tube and the number of tubes is the best one when using tubes with 5" of Øext. Therefore, the weight of the system is always the lowest, allowing to reach the highest gravimetric capacity of the system. As already observed concerning the number of tubes, by changing the IMC gravimetric capacity, system weight and gravimetric capacity are not considerably different between an IMC with 1.4 H_2 wt.% and 1.6 H_2 wt.%. On the contrary a remarkable difference occurred comparing their results with an IMC of 1.0 H_2 wt.%. When using IMC, the system weight is so huge that the gravimetric capacity of the system results to be poor and below 1.0 H_2 wt.% in all cases (Figure 7- b,d,f), in good agreement with system consideration discussed in section 3.1. It can be concluded that, after having chosen the proper IMC, tube dimensions, and in particular the diameter, significantly affect the system weight.

For the proper geometry, it is important to consider system volume, its occupancy inside the container and the arrangement of tubes. Figure 8 shows the percentage of volume occupied by the system inside the container and the volumetric capacity of the system (the amount of H_2 stored over the total volume of the tubes) as a function of the Øext per a given Lr, for a given IMC. Calculations were made considering the volume occupied by the total numbers of tubes, and as can be seen from Figure 8-a, c, d, less than 10 % of the volume of the container is occupied by the tubes. As already observed, concerning the weight of the H2SS, for 6" tubes, a proper combination of the amount of tube and their dimension, results always in the highest fraction of volume occupied inside the container. On the contrary, this combination results in a poor difference between Øext 5" and Øext 8". Then, as already stated for the weight of the system, the length of tube doesn't have a high impact on the final volume. As expected, by increasing the gravimetric capacity of the MH, the volume decreases, with a little difference between 1.4 and 1.6 H_2 wt.% compared to 1.0 H_2 wt.% (Figure 8-a, c, e). The amount of volume occupied inside the container is an index of the system volume, and in turns of the volumetric capacity of the system (Figure 8-b, d, f). This value is in between 13 and 25 kgH_2/m^3, with a slight difference between tube dimension Lr

and Øext for a given MH. While, for a giving tube dimension, it is sensitively affected by the MH.

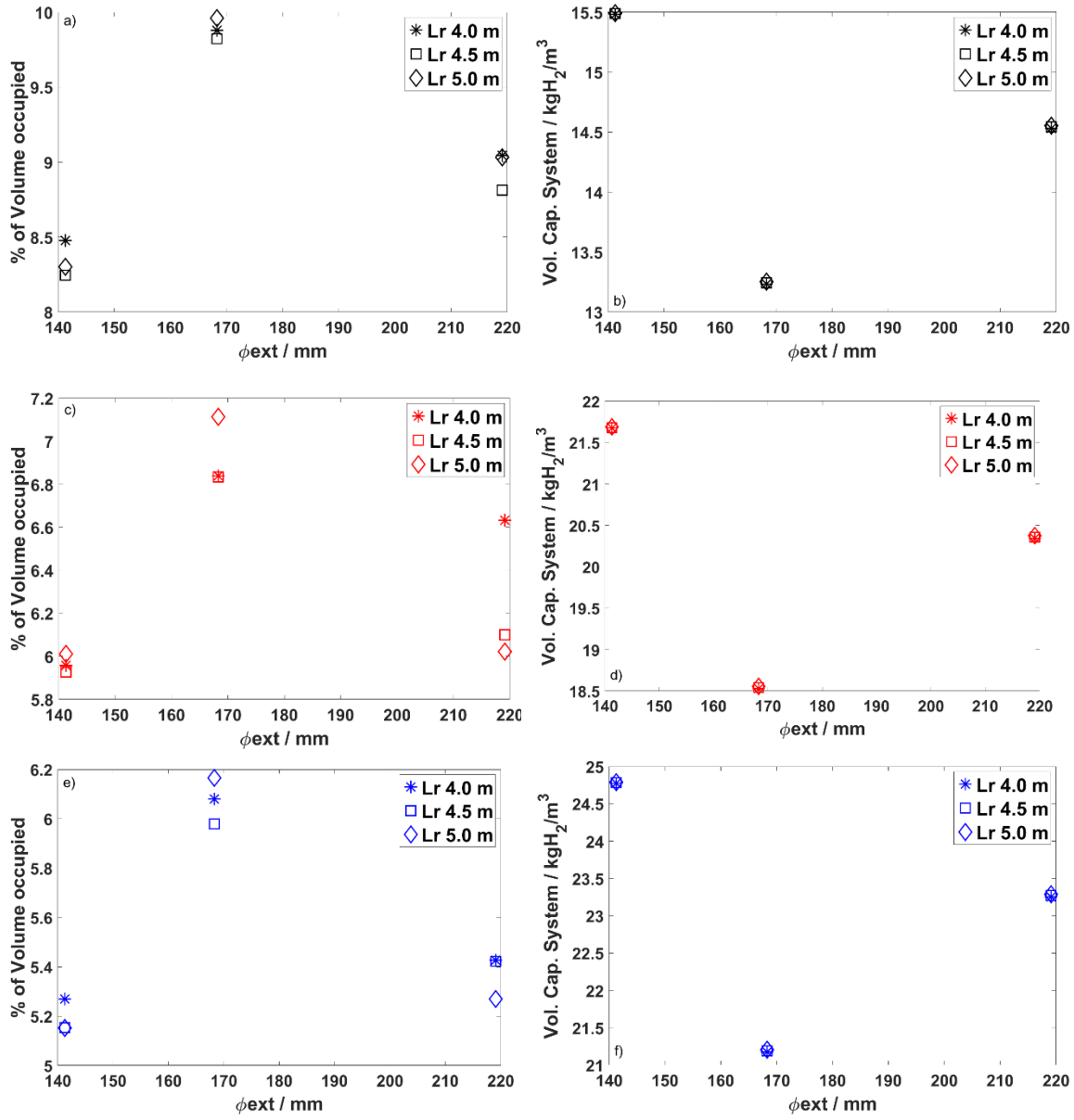

Figure 8: The percent occupied by the H2SS inside the container of the only tubes and the volumetric capacity of the system, depending on the IMC: (a) with 1.0 H_2 wt.%; (b) with 1.4 H_2 wt.%; (c) with 1.6 H_2 wt.%.

Simulations confirm the effect of the MH gravimetric capacity on system weight and volume observed in section 3.1. Indeed, by changing the gravimetric capacity of the IMC from 1.0 to 1.4 H_2 wt.%, the effect on the system properties (weight, volume and gravimetric and volumetric capacity) is consistent, for a given tube dimension. As an example, using a tube of Øext 5", there is an improvement of about 40 % in system volumetric and gravimetric capacity choosing an IMC from 1.0 to 1.4 H_2 wt.%. While, for a given IMC, the choice

between Øext 5" and Øext 8" implies an effect of about 13 % on the system gravimetric capacity and of about 5 % on the volumetric one, with a negligible effect of tube length for a given Øext and IMC. Results stated also that Øext 6" has not good combination of tubes dimension and number, observing the worst values on gravimetric and volumetric capacity, while Øext 5" is the one that allows to reach the highest values. Nevertheless, this dimension implies the highest number of tubes that need to be arranged inside the container. Thus, it is now evaluated the displacement of the tubes inside the container, considering leaving about 5 mm of space around the tubes for a structural gate and 1 m of free space inside the container in width (wc) and height (hc). Figure 9 shows a schematic representation of tube arrangement inside the container. The check of the displacements of the tubes was made as follow: firstly, by calculating the maximum number of tubes that can be located in a row (red arrow limited by wc). Secondly, by evaluating the number of rows required to locate all tubes (yellow arrow limited by hc).

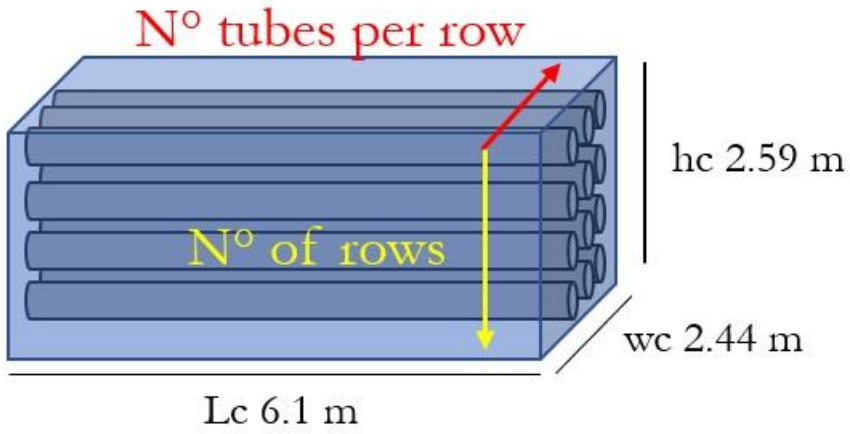

Figure 9: Schematic arrangement of the MH-tubes inside the standard ISO container, reporting its dimension (Lc, wc and hc, respectively container length, width and height) indicating with the red arrow the number of tubes that can be placed in a row along container width and with the yellow arrow the number of rows that can be placed along container height.

By checking tubes displacement inside the container, in all cases, it is possible to arrange the entire number of tubes observed without exceeding container dimension. From these results, it turns out that a tube of Øext 5" is advantageous, obtaining the maximum results in volumetric and gravimetric capacity of the system, resulting also promising for the heat management, since it is the lowest diameter considered. The length of the tubes has not a big impact on the system gravimetric and volumetric capacity, but it is influencing the overall

number of tubes required. The number of tubes could be the discriminating factor in the choice of tube dimension. Indeed, it must be taken into account that simulations do not consider the use of auxiliaries, like valves and pipes, and the highest is the number of tubes, the highest is the number of auxiliaries required. Thus, for a tube of Øext 5" it could be advantaging a length of 5.0 m but could be even useful the use of a tube of Øext 8", that allows to almost halve the number of tubes despite a decrease in gravimetric and volumetric capacity of about 15 % and 6 %, respectively. In section 3.1, it was shown how the material of the container might have a high impact on the gravimetric capacity of the system, especially for MHs with a high gravimetric capacity. Considering Øext 5" and 8" with a Lr of 5.0 m as the optimal tube dimension, we assumed the use of aluminium as material for the tubes and we performed the simulation, maintaining the same dimensions considered for steel, as shown in section 3.1. Figure 10 reports the obtained gravimetric capacity of the system as a function of MH storage capacity for Øext of 5" and 8". The capacity of the system increases linearly with that of MH, with a slight difference between Øext 5" and 8", as discussed previously. The system weight decreases if compared to the use of steel, allowing a considerable increase in the gravimetric capacity of the system, reaching about 1.0 H_2 wt.% for high MH gravimetric capacities. Considering Øext 5", the rise in system capacity is of about 34 % passing from steel to aluminium. The use of steel instead of aluminium is not linked only to the effect of system, but other parameters influence the choice, like economic and environmental aspects and system working conditions.

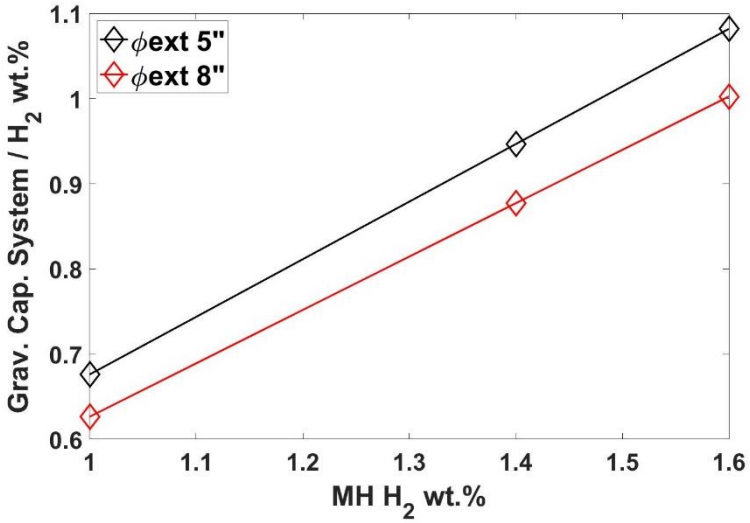

Figure 10: Gravimetric capacity of the system as a function of MH gravimetric capacity considering tubes in Al with Lr of 5.0 m with tubes diameter of 5 inch and 8 inch.

As observed in Figure 8, the container is not totally filled by the MH tubes, allowing the allocation of auxiliaries, but it cannot be excluded also a possible displacement of devices like a FC and/or an EL, depending on tubes arrangement. Supposing to totally fill the container with just MH tubes, the maximum amount of H_2 that could be stored was calculated considering tube of 5" and 8" with 5.0 m of length. This evaluation could be of interest, supposing to transfer H_2 using MH, from a site of production to that of utilization, as it is under developed in Japan [12]. The constrain in container dimension and tube arrangement, *i.e.* 1 m of free space in container width and height and 5 mm for a structural gate around the tubes, are maintained. 72 and 30 tubes of Øext 5" and 8", respectively, can be allocated inside the container. Figure 11 shows the amount of H_2 that could be stored as a function of the MH gravimetric capacity.

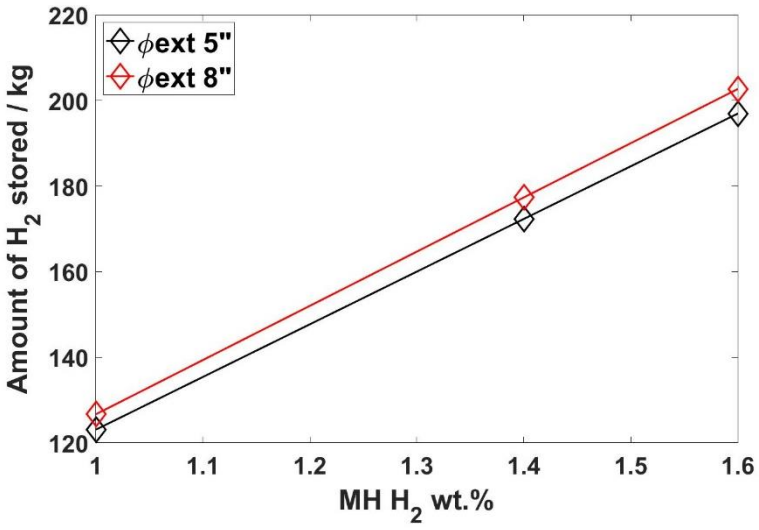

Figure 11: Amount of H_2 stored as a function of MH gravimetric capacity with tubes of 5.0 m of length with Øext of 5 inch and 8 inch.

A linear dependence is observed in the amount of hydrogen stored as a function of the MH capacity. After having fixed the MH, the amount of H_2 stored by increasing tube dimension in diameter is almost constant, *e.g* for 1.6 H_2 wt.%, 197 kg H_2 with Øext 5" compared to 203 kg H_2 with Øext 8" (Figure 11). On the contrary, fixing the tube dimension, the amount of H_2 stored can be increased of about 40 % moving from 1.0 to 1.6 H_2 wt.%. Considering the amount of H_2 stored inside the container compared to the 50 kg of H_2 considered so far, the amount of H_2 is roughly doubled with a MH capacity of 1.0 H_2 wt.% and quadrupled with 1.6 H_2 wt.%. In developing H_2 technologies, it could be considered the transport of hundreds

of kg of H_2 in a standard ISO container filled with MH tubes, from a site of production to the final user.

Summarizing, results confirm the strong impact of the material of the container on the system weight, passing form steel to aluminium. In the selection of tubes design, the effect of the length is less remarkable than the diameter, resulting also in not advantaging dimension when considering Øext 6" due to the not optimal number of tubes compared to Øext 5" and 8". A high impact on the system is also due to the MH gravimetric capacity, with a substantial difference in system weight and volume when passing from 1.0 H_2 wt.% to 1.4 H_2 wt.%. Due to the low gravimetric capacity of the IMC, the final weight of the system results in a poor gravimetric capacity of the system far from the 1.0 H_2 wt.%. On the contrary the volumetric capacity of the system is always higher than 14 kgH_2/m^3. Simulations highlighted that when design a H2SS based on MH a right compromise between tube dimension and material and MH is fundamental.

3.2.3.2 Case study: H2SS based on GC

An extreme case study is the storage of the 50 kg of H_2 at 30 bar in one single tube located inside a standard ISO container (Figure 12-a). Figure 13 shows the length of the tube (Lt) and its thickness as a function of its Øext.

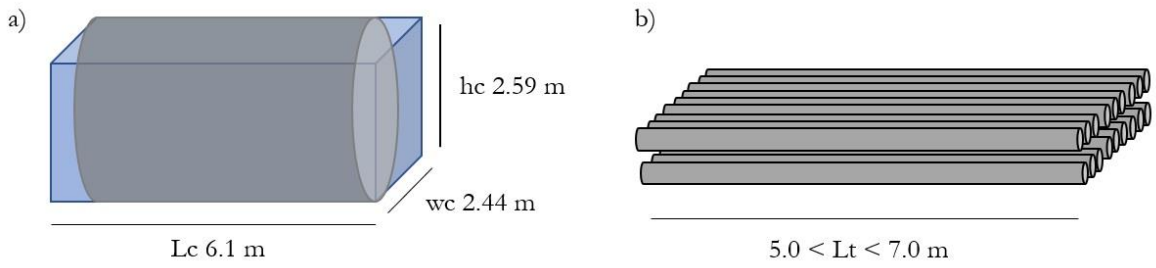

Figure 12: Schematic representation (a) one single tube inside a standard ISO container; (b) tubes of Øext 4 inch and 6 inch with a variable Lt between 5.0 and 7.0 m.

The length of the tube is considered between 4.0 and 6.0 m, the diameter is calculated from the volume of gas and the minimum thickness has been considered (Chapter 2). The use of a single tube implies a diameter between 2.0 and 2.4 m, with a length from 6.0 to 4.2 m. Indeed, 4.0 m cannot be reached since it would imply a diameter over the maximum width of the container of 2.44 m. As can be observed in Figure 13, the tube is embedded in the container occupying the 49 % of its volume and resulting in a volumetric capacity of the system of 2.6 kgH_2/m^3.

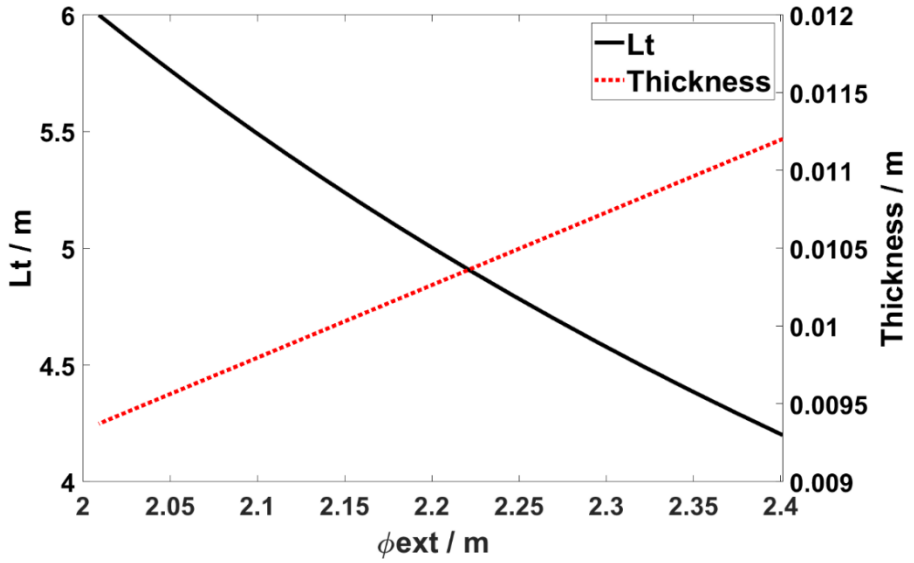

Figure 13:Length and thickness of the tube as a function of the Øext.

Figure 14 shows the gravimetric capacity of the system as a function of the Øext of the tube.

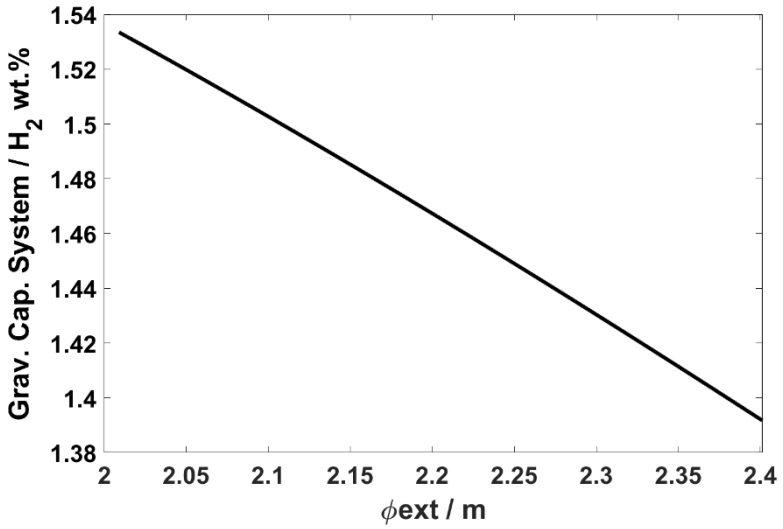

Figure 14:Gravimetric capacity of the system as a function of the Øext.

The capacity of the system results always higher than 1.0 H_2 wt.% and decreases increasing the diameter of the tube, almost linearly. This case study is extreme and not reliable, due to the tube dimension. To move towards a more reliable storage solution, tubes with Øext 4" and 6" have been considered (Figure 12-b; section 3.2.2). As primary thing it is evaluated the same tube dimension in length, Lt, of the MH, *i.e.* 5.0 m. The number of tubes required is 408 for Øext 4" tube and 189 for Øext 6". Considering the same tube arrangement inside the standard ISO container of the MH-H2SS evaluated in section 3.2.3.1. (5 mm of space around the tubes for a structural gate and 1 m of free space in container width and height),

the number of tubes cannot be arranged inside the container. Thus, since it is not possible to store the tubes inside the standard ISO container, it is decided to consider a variable Lt between 5.0 and 7.0 m to decrease the number of tubes required. Figure 15 reports the number of tubes as a function of Lt for Øext of 4" and 6".

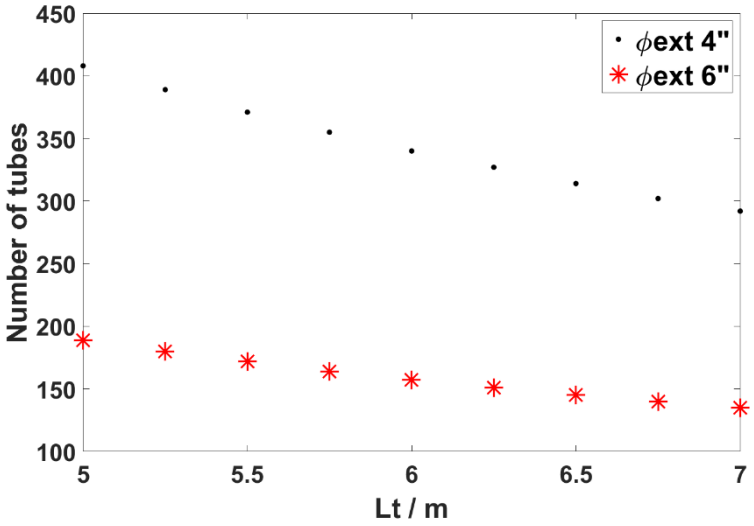

Figure 15: The number of tubes of 4 inch and 6 inch as a function of tubes length.

As can be stated from Figure 15, the number of tubes is sensitively high and of the order of hundreds of tubes. Passing from Øext 4" to 6" is possible to almost halve the amount required, *e.g.* at 6.0 m from 340 to 157. For a given diameter, the number of tubes decreases of about 28 % by increasing the length from 5.0 to 7.0 m, with a not linear dependence.

Figure 16 shows the gravimetric (a) and volumetric (b) capacity of the system as a function of Lt using tubes Øext 4" and 6", neglecting a possible tubes displacement. Due to the high number of tubes, the amount of steel is high (of the order of 18 ton), implying low values of gravimetric capacity of the system, *i.e.* about 0.275 H_2wt% for Øext 4" and 0.268 H_2 wt.% for Øext 6", with a negligible variation as a function of the length (Figure 16-a). Low values are also observed in the volumetric capacity of the system (Figure 16-b), that is between 2.375 and 2.39 kgH_2/m^3. The elevated number of tubes required results in an overall volume that is comparable with the volume of one single tube. Indeed, moving from one large single tube to hundreds of small tubes (Figure 12), the volumetric capacity of the system doesn't change significantly. On the contrary, the gravimetric capacity does, observing a remarkable decrease passing from one single tube to hundreds of tubes and resulting even less competitive than MH (Figure 7-b, d, f) because of the elevated number of tubes required.

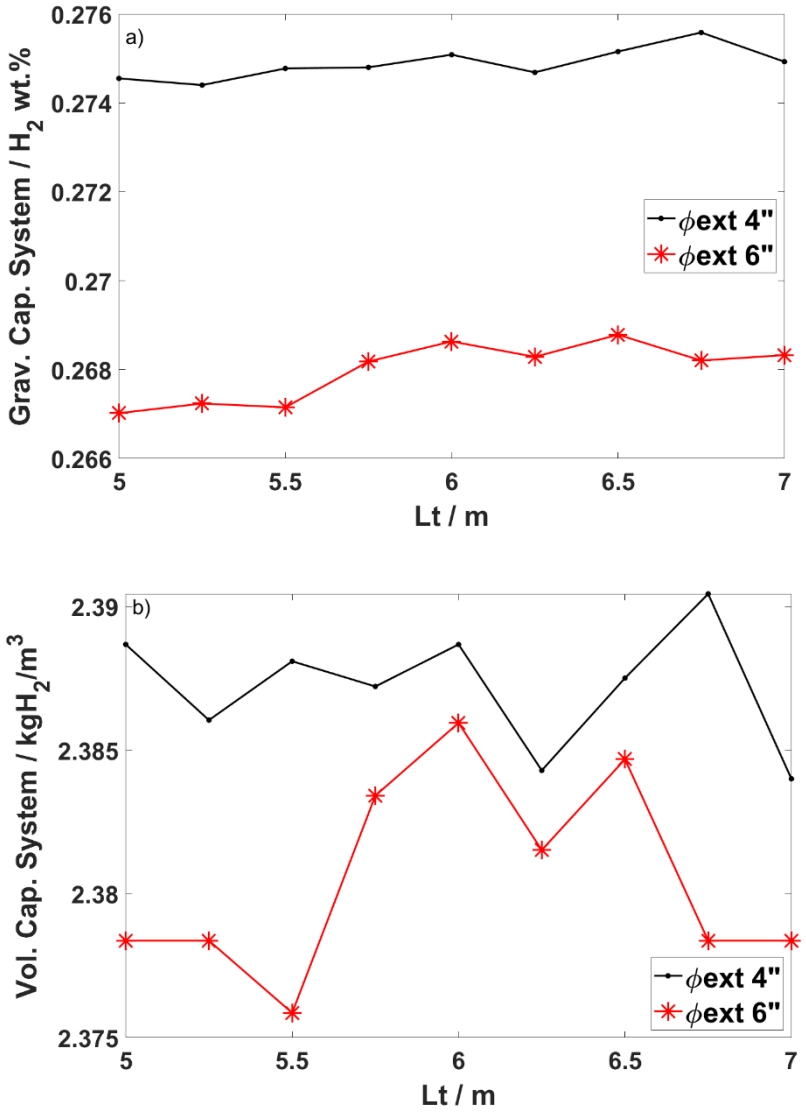

Figure 16: (a) gravimetric capacity of the system and (b) volumetric capacity of the system as a function of the length of the tubes at 4 inch and 6 inch.

Since the system cannot be arranged inside a standard ISO container, it has been evaluated the dimension for a dedicated container, considering arranging tubes in 2 and 3 rows. The arrangement inside a container could be useful, thinking to a possible displacement underground of the system. The dimension of the container is evaluated, as already done for the MH, leaving 1 m of free space in length, width, and height to allow the location of auxiliaries and with 5 mm around the tubes for a structural gate. The container in height for tubes of Øext 4" is about 1.2 and 1.4 m for two and three rows with a variable width between 26.4 and 19.1 m and between 17.9 and 13.1 m, respectively. While for tubes of Øext 6" in height is about 1.4 and 1.5 m for two and three rows with a width between 19.9 and 13.0 m

and between 12.2 and 9.0 m, respectively. The volume of the container as a function of Lt for the arrangement of the tubes of Øext 4" and 6" in two and three rows is reported in Figure 17-a, b, respectively.

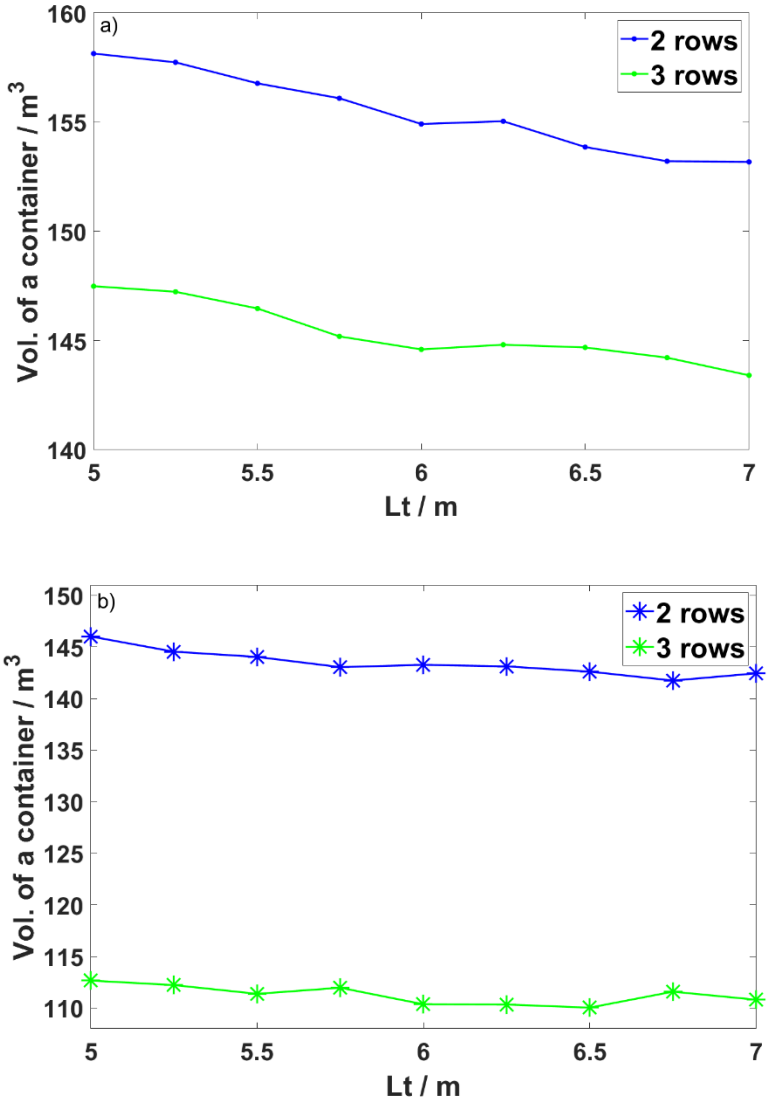

Figure 17: Volume of the container as a function of the length of tubes with a displacement in two and three rows: (a) with tube of 4 inch and (b) with tube of 6 inch.

The volume of the container decreases with Lt thanks to the decrease in width due to the number of tubes. For a given arrangement, an increase of the diameter from 4" to 6" allows to sensitively decrease the dimension of the system and, in both cases, a minimum size is observed with a tubes length of 6.0 m. The displacement in two rows is not advantageous, but similar values are observed between tubes of Øext 4" tubes arranged in three rows and tubes of Øext 6" tubes arranged in two rows.

Summarising, the storage of 50 kg of H_2 at 30 bar shows low values in volumetric and gravimetric capacity, both considering one single tube quite large, or a more reliable system made of tubes of Øext 4" and 5". In the latter case, the 30 bar of storage pressure implies hundreds of tubes to be managed, resulting disadvantaging in terms of gravimetric capacity compared to one single tube. While similar values are observed for the volumetric capacity, that results rather low in both cases. For a storage system at 30 bar, the most promising tube dimension involves tube wide and long, *i.e.* Øext of 6" with a Lt of 7 m, to limit the number of tubes, without observing a substantial decrease in gravimetric and volumetric capacities of the system. Results highlight how is important to compress the hydrogen at least to 200 bar to allows a significant increase in volumetric and gravimetric capacity. As an example, taking into account tubes with Øext 6" and 7 m of length, moving from 30 to 200 bar of storage, the number of tubes passes from 135 to 20, the volumetric capacity of the system from 2.4 to 16.1 kgH_2/m^3 and the gravimetric capacity from 0.27 to 1.81 H_2 wt.%.

3.2.4 Conclusion

In storing H_2 directly from an EL at 30 bar, MH is advantaging in terms of system dimension and in turns in system capacity compared to the directly storage of the gas in tubes.

Main results in MH shows how by increasing MH storage capacity, system volumetric and gravimetric capacity is more affected than change in tubes dimension, in which the effect of the length is almost negligible compared to the Ø of tubes. Indeed, the combination of tube dimension and the resulting number of tubes shows that the optimal configuration implies a Øext of 5", with 6" being the worst. However, the high number of tubes required by smallest tubes dimensions could be not advantaging in system handling, resulting in a promising dimension of Øext of 8" with 5.0 m of length. Indeed, compared to tubes of Øext 5", the number of tubes is almost halved, observing a slight decrease in gravimetric and volumetric capacity of the system. Nevertheless, it was confirmed the remarkable effect of tubes material on the gravimetric capacity of the system, passing from steel to aluminium, as already noticed in ref. [1]. Main results in the H2GC storage system show that mild conditions of storage are not advancing because of poor values in gravimetric and volumetric capacity. Simulations of an extreme case of one single tube compared to a more reliable arrangement in tubes with Øext 4 and 6" shows that one single tube is more advantaging in terms of gravimetric capacity of the system. Indeed, the high number of tubes required using

tubes with Øext 4'' and 6" has a high impact on the system weight, resulting in a poor gravimetric capacity. While the volume is not affected by tube dimension (one single tube or hundreds of tubes with Øext 4" and 6").

Comparing the two H2SS, MH are advantaging in both gravimetric and volumetric capacity, implying a system volume that can be easily arranged in a standard ISO container. On the contrary of the H2CG, in which the high number of tubes required for the storage do not allow the allocation inside a standard ISO container. Comparing results with the optimal MH tube dimension, *i.e.* Øext 8" and Lr of 5.0 m, with the optimal one in H2CG, *i.e.* Øext 6" and Lt of 7.0 m, it can be seen that higher values in gravimetric and volumetric capacity are always obtained considering even a MH with 1.0 H_2 wt.%. Indeed, for this type of MH capacity, the gravimetric capacity of the system is 0.4 H_2 wt.% compared to 0.27 H_2 wt.% of the H2GC, with a volumetric capacity of 14.6 kgH_2/m^3 compared to 2.4 kgH_2/m^3, respectively. Thus, it is not suitable the storage of H_2 as gas in mild conditions (*i.e.* 30 bar), but only at high pressure. Comparing same tube dimension of MH at 200 bar of storage (Øext 8" and Lr of 5.0 m), it can be noticed a high increase in system gravimetric capacity with the compressed gas, moving from 0.4 H_2 wt.% of the MH (1.0 H_2 wt.%) to 2.4 H_2 wt.% at 200 bar. However, the volumetric capacity is less affected, with 14.6 kgH_2/m^3 for the MH (1.0 H_2 wt.%) compared to 16.8 kgH_2/m^3. A higher value can be reached by increasing the storage capacity of the MH at 1.4 H_2 wt.%, obtaining a volumetric capacity of the system of 20.4 kgH_2/m^3. This implies that MH are most promising in the volumetric capacity of the system resulting competitive with compress gas already with poor MH storage capacity. However, the system weight of a H2SS based on MH is strongly affected, resulting always sensitively low compared to compress gas. Nevertheless, when realizing a system, it cannot be neglected how the hydrogen is produced and so MH can be considered extremely advantageous in stationary applications or for the transport of hundreds of kg of H_2, thanks to the mild conditions of storage avoiding compression, that implies high running costs (frequent maintenance) and lower safety (high pressure) [6].

3.3 Simulation of a large-scale hydrogen storage system for maritime application

3.3.1 Introduction

In the last decades, among devices developed based on MH, there are submarine, *i.e.* the as called U212 and U214 [1]. Indeed, the maritime sector is interested in reducing pollutants emissions to face climate change and the use of FC supplied by H_2 have found high potential in the last years. Van Biert et al. [13] and McConnel [14] recently reviewed FC systems for maritime applications, including H_2 as a promising energy carrier to be exploited. A special focus on hydrogen storage at the solid state for submarine applications has been review by Fiori et al.[15], and many other reviews describe the development of fuel cell vessels and the potential of hydrogen for maritime and submarine applications [16–20]. The use of H_2 in the maritime sector involve already 3 PEM-FC powered devices [13]. Together with the already mentioned class U212 submarines based on a MH H2SS, the other two applications are passenger vessels based on compressed H_2, the ZEMSHIP [21] and Nemo H2 [14]. Recently, the yacht Aqua has been realized which runs thanks to liquid H_2. Kickulies [8] reports the potential of the use of FC for a module of 4 FCs of 40 kW for maritime application. The operation time depends on the H_2 storage system considered and the storage capacity was based on design evaluation. As compressed gas, 50 kg of H_2 allows 7 h uninterrupted operation at 100 kWe load. As liquid H_2, 1000 kg can be stored allowing 144 h, while 200 kg of H_2 as MH allows 28 h of operation.

Table 4 summarized the type of IMCs used for maritime applications reporting the properties of the system developed. Concerning the use of MH as H2SS, Fiori et al. [15] presented various $TiMn_2$-based compounds for submarine applications. This class of IMC is the most used in the maritime sector. Test for submarine based on MH and FC started already in 1980s and at the early 2000s the class U212A were sold for the German and Italian Navy [22]. Six units of Class 212A were built at the HDW, now Thyssen Kroupp Marine System, and TNSW yards in Germany and in La Spezia, Italy, at the Fincantieri yard [22]. The submarine has about 300 kW FC and the MH-H2SS is based on an a $TiMn_2$-based alloy commercialized by Gfe and works between 20 and 50 °C [1]. Another application of a $TiMn_2$ alloy, with composition $(Ti_{0.93}Zr_{0.05})(Mn_{0.73}V_{0.22}Fe_{0.04})_2$ is in the canal boat Ross Barlow, in UK [23]. Eight cylinders contain about 30 kg of MH powder each, and 4 kg of H_2 are stored to supply

a 1 kW FC. H_2 discharge is at 9 °C and 1 atm with a total flow of 40 L/min, allowing 10 h of operation. Activation occurred at room temperature in 5-6 cycle, alternating 30 bar of H_2 and vacuum. In the last couple of years, Fincantieri is developing a boat as called Zeus based on MH to store 50 kg of H_2 to supply a 120 kW FC in order to guarantee 6 h operation [7,24]. Finally, an Italian start-up based in Genova, as called H2Boat [25], has the goal to develop green energy solutions for boat. They have already realized some prototypes of H2SS based on $LaNi_5$-based alloy, commercialized by LabTech. The goal is to develop integrated solutions MH-tank, EL and FC located directly on board, for a completely energy independent system.

Table 4: Summary of the type of IMC used for the specific maritime applications and properties of system.

IMC	Application	Properties of system	Reference
$TiMn_2$-based alloy	Submarine	FC of 300 kW ; MH-H2SS working temperature of 20 ° - 50 °C	[1]
$(Ti_{0.93}Zr_{0.05})(Mn_{0.73}V_{0.22}Fe_{0.04})_2$	Canal boat Ross Barlow	FC of 1 kW ; 240 kg of IMC for 4 kg of H_2 ; H_2 flow rate of 40 l/min ; MH-H2SS working temperature of 9 °C	[23]
Ti(Fe,Mn)-based alloy	Ship Zeus	FC of 120 kW; 50 kg of H_2 stored	[7,24]
$LaNi_5$-based alloy	Boat	-	[25]

In this work, a particular case study has been defined to individuate, thanks to a series of simulations, the proper MH and system design that can allow to satisfy some system constrains in maritime applications. The case study involves the setup of H2SS for a large-scale maritime sector based on IMC, considering the work reported in ref. [8]. Indeed, since about 200 kg of H_2 as MH were evaluated for about 28 h of operations, moving the system towards about 9 - 12 days of operation, about 1500 – 2000 kg of H_2 are considered to be stored. Nevertheless, the H2SS requires to achieve a volumetric capacity as highest as possible, without constrain in system weight.

3.3.2 Boundary condition

IMCs compounds are considered as H_2-carrier, in agreement with the literature reported concerning the maritime sectors [1,15,22,23,25], implying a MH gravimetric capacity lower than 2.0 H_2 wt.% and allowing the use of water as thermal fluid, fixing a working temperature of 45 °C. The system is defined as reported in ref. [1] and a 30 % of free volume is left inside the reactor to allow the material expansion (section 3.2). Then, concerning the tube dimension, the selection of the proper commercial tube needs to be considered in stainless steel, without exceeding a length of 5300 mm and an Øint of 250 mm (since lower dimension will results in a too elevated number of tubes (section 3.2)). The thickness is defined according to the minimal one (Chapter 2). The apparent density of the powder [26] is considered between 3 and 4 t/m^3.

3.3.3 Results and discussion

3.3.3.1 Evaluation of the IMC and tubes dimension

The amount of IMC and tubes have been calculated as a function of the MH gravimetric capacity, considering tube dimension reported in section 3.3.2. Parameters are evaluated storing 1500, 1800, 2000 kg of H_2, with MH gravimetric capacity between 1.0 and 2.0 H_2 wt.%, and with a powder apparent density of the carrier of 3.0, 3.5, 4.0 t/m^3. Figure 18-a shows the mass of carrier as a function of the MH gravimetric capacity, obtained for the three selected amounts of H_2 stored. While Figure 18-b shows the number of tubes as a function of the MH gravimetric capacity, for the three amounts of H_2 stored and for the three selected values for carrier apparent density, *i.e.* 3.0 t/m^3, 3.5 t/m^3 and 4.0 t/m^3. As expected, the amount of carrier increases increasing the amount of H_2 stored, but it decreases considerably increasing the MH gravimetric capacity (Figure 18-a). It implies the decrease of the number of tubes necessary, that also decreases increasing carrier hydrogen gravimetric density (Figure 18-b). As an example, considering 1.0 H_2 wt.% and 1500 kg of H_2 stored, with 3.0 t/m^3 275 tubes are necessary, while with 4.0 t/m^3 they become 206. Based on this evaluation, it was decided to go on in simulating the system storing 1800 kg of H_2 with a carrier density of 3.5 t/m^3, that consists in a number of tubes between 282 and 141 (Figure 18-b).

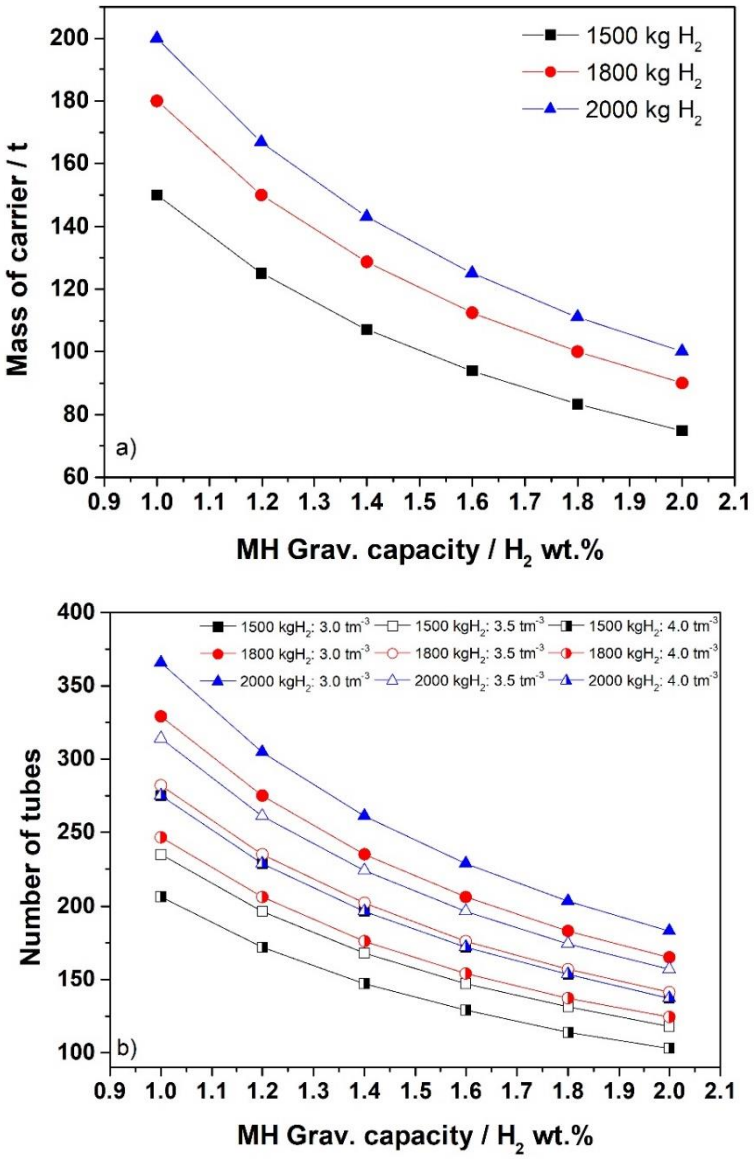

Figure 18: (a) Mass of carrier as a function of MH gravimetric capacity for 1500, 1800 and 2000 kg H_2; (b) number of tubes as a function of the MH gravimetric capacity obtained for 1500, 1800 and 2000 kg H_2 stored using 3.0, 3.5 and 4.0 t/m^3 as carrier density.

3.3.3.2 Evaluation of system density

An Øint of 250 mm is close to the size of a commercial tube of 10" and Table 5 reports its dimension.

Table 5: MH-tube dimension considering a 10" tube in stainless steel.

Tube	Øint	Øext	Thickness	L
	mm	mm	mm	mm
10"	250.8	273	11.1	5300

The thickness was checked to be suitable to resist up to 50 °C and 60 bar of H_2. The value in pressure considers an absorption pressure of 30 bar from an EL and an overpressure for

the activation of the IMC up to 60 bar. Based on the final tube dimension, the quantity of carrier was recalculated, and therefore, the number of tubes (Figure 19).

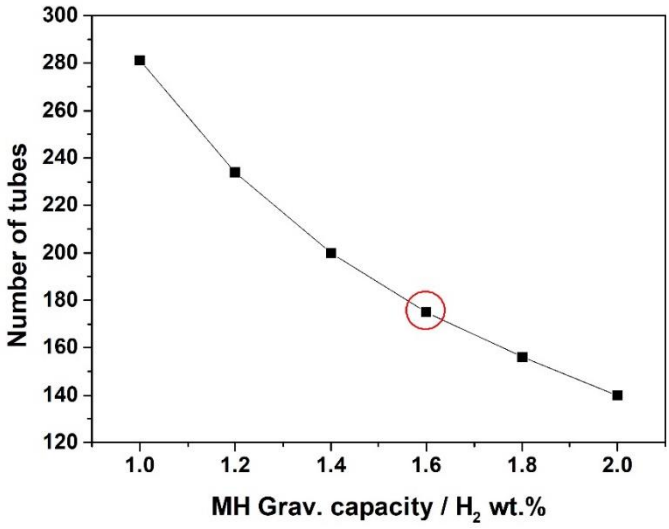

Figure 19: Amount of tube of 10 inch as a function of the gravimetric capacity for a density of carrier of 3.5 t/m³ to store 1800 kg of H_2.

The number of tubes decreases increasing the gravimetric capacity, as reported also previously in Figure 18-b. 281 tubes are necessary in case of use of a MH with a gravimetric capacity of 1.0 H_2 wt.%, while 140 are sufficient for compound with a gravimetric density of 2.0 H_2 wt.%. According to the literature, most of the MH-based H2SS for maritime application are based on $TiMn_2$ IMC, that generally presents a capacity of about 1.6 H_2 wt.% [11]. Thus, for the considered system, an IMC $TiMn_2$-based is selected as MH, that, as can be seen from Figure 19 (red circle), required 175 tubes. Due to the high number of tubes, it is considered to design the system as shown in Figure 20, in which MH-tubes are displaced in a vessel in which water flows, exchanging heat with them.

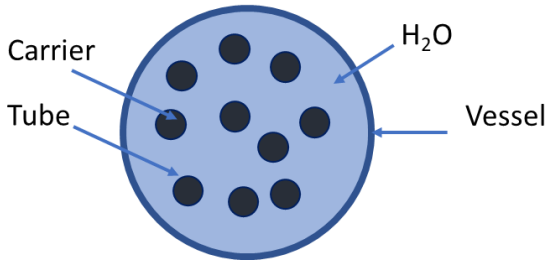

Figure 20: Schematic representation of the design considered for the system, i.e. n-tubes of carrier located inside a vessel in which water flows for the heat management.

Supposing to allocate all the 175 MH-tubes in one vessel, Table 6 reports its dimensions. The inner diameter of the vessel is obtained taking into account, per each tube, an addition

in thickness of 5 mm, available for the heat exchange with water and also for a structural gate. The Øext of the vessel was estimated according to the minimal thickness required to afford a water pressure of 5 bar at 50 °C, adding 40 mm to consider commercial tubes.

Table 6: Vessel dimension.

Øint	**Øext**	**Thickness**	**L**
m	**m**	**mm**	**mm**
4.27	4.357	43.5	5300

Table 7 reports obtained results for the system, *i.e.* its weight, volume and volumetric and gravimetric capacity.

Table 7: Results related to the system in terms of volume, weight and volumetric and gravimetric capacity of the system.

Volume of system	**Weight of system**	**Vol. cap. of system**	**Grav. cap. of system**
m^3	**t**	**kgH_2/m^3**	**H_2 wt.%**
79	237.8	22.8	0.76

The weight of the system considers the amount of carrier and steel necessary for both tubes and vessel and the amount of water to be inserted inside the vessel (*i.e.* vessel free volume). The weight is high resulting in a gravimetric capacity of the system of less than 1.0 H_2 wt.%, *i.e.* 0.76 H_2 wt.%. Then, considering the amount of H_2 stored inside the volume of the system, the volumetric capacity is equal to 22.8 kgH_2/m^3.

A higher number of vessels has been then evaluated. Figure 21-a shows the number of tubes per vessel and the vessel Øint, while Figure 21-b the system weight and volume are reported as a function of the number of vessels. As expected, by decreasing the number of vessels, its dimension is considerably decreasing, *i.e.* from 1vessel with Øint of 4.27 m to 8 vessels with Øint 1.58 m (Figure 21-a). However, this implies an increase in system weight and volume, with a rise of about 55 t in weight, and of about 14 m^3 in volume (Figure 21-b).

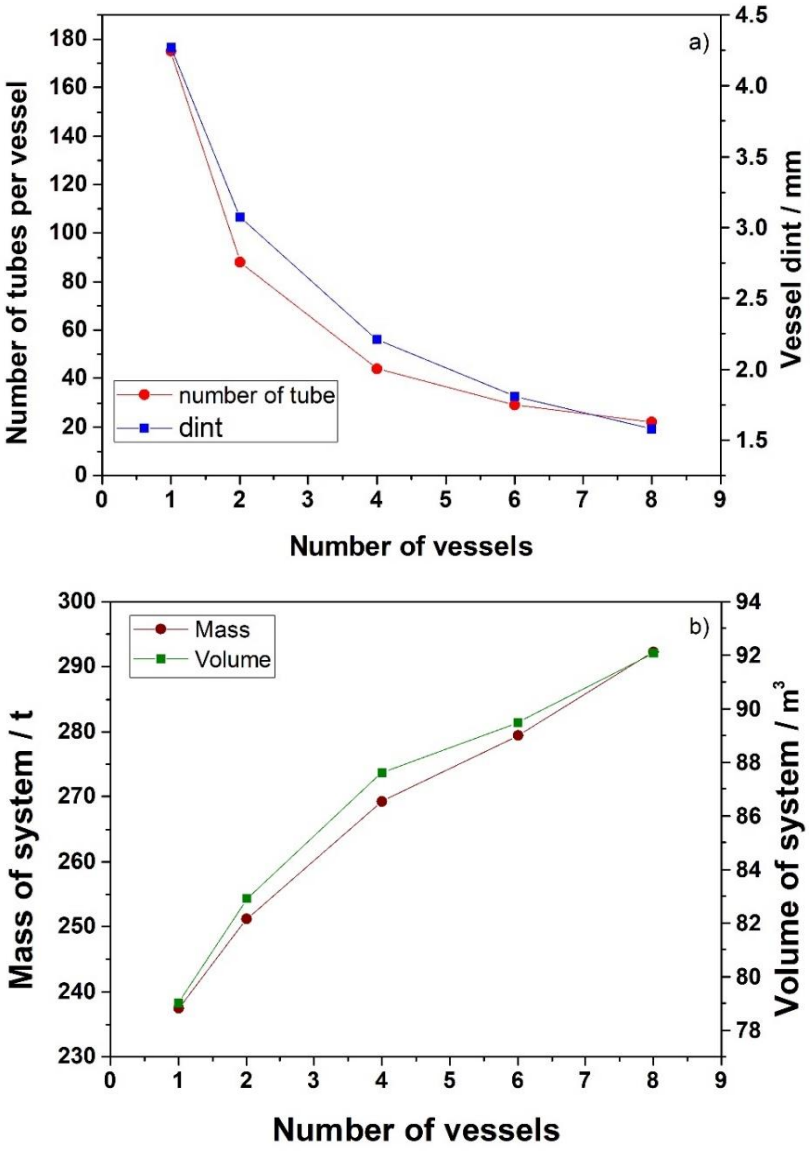

Figure 21: (a) number of tubes and vessel internal diameter as a function of the number of vessels; (b) mass and volume of the system as a function of the number of vessels.

The increase in the system volume causes a decrease in system volumetric capacity, as shown Figure 22, not allowing to achieve the goal in system volume to maximize the volumetric capacity of the system.

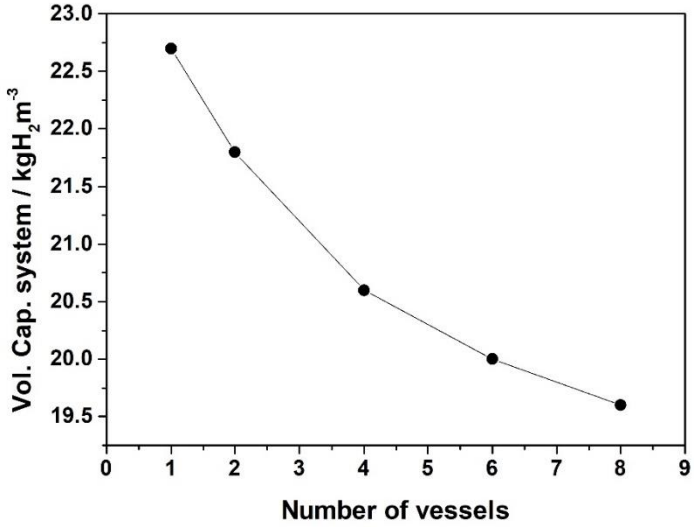

Figure 22: Volumetric capacity of the system as a function of the number of vessels.

In the light of the system design, the solution with one vessel seems to be the optimal one. So, it has been considered to store different amount of H_2, *i.e.* 2000 and 1500 kg of H_2, implying the use of 146 and 195 tubes, respectively (Figure 23).

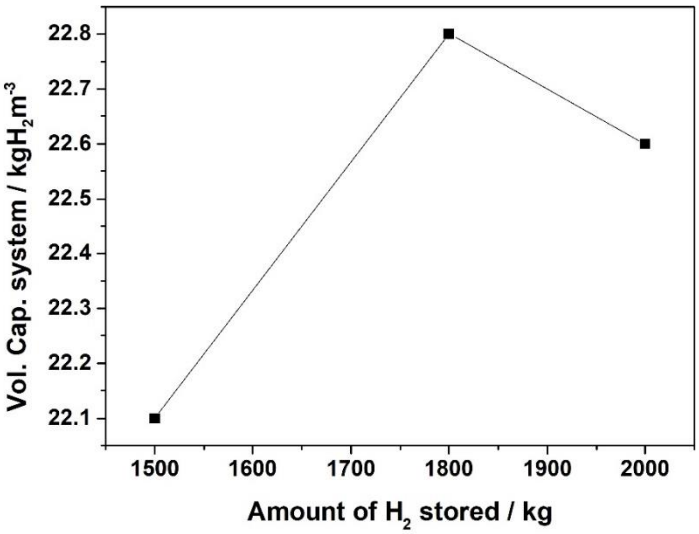

Figure 23: Volumetric capacity of the system as a function of the amount of H_2 stored.

As can be seen from Figure 23, the volumetric capacity of the system is rather constant, being unaffected by the amount of H_2 stored when the design and the MH are fixed. Thus, it has been evaluated the influence of the MH on system volumetric capacity, considering storing 1800 kg of H_2 with a carrier density of 3.5 t/m^3 and one vessel. As a function of the gravimetric capacity of the MH, Figure 24-a shows the number of tube and vessel dimension, while Figure 24-b reports the mass and volume of the system.

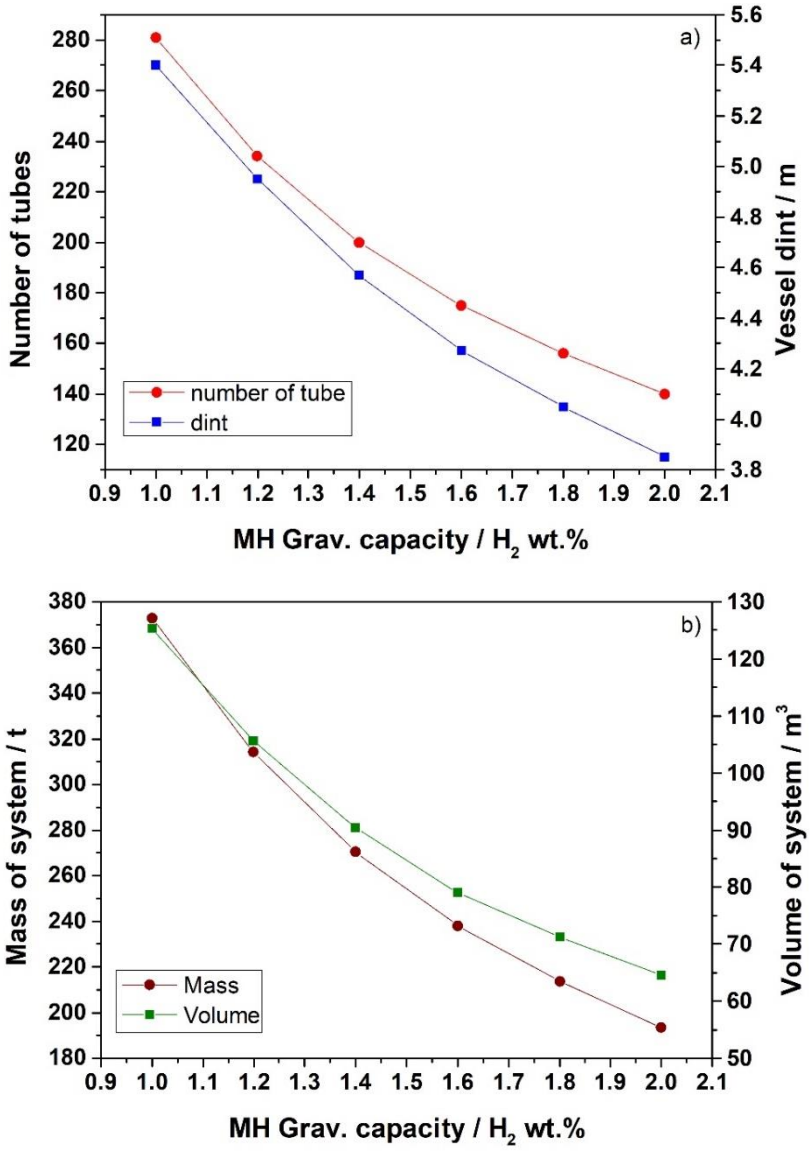

Figure 24: (a) number of MH-tubes and vessel internal diameter as a function of MH gravimetric capacity; (b) mass and volume of the system as a function of the MH gravimetric capacity considering one vessel.

As already reported in Figure 19, the number of tubes decreased from 281 to 140, increasing the MH gravimetric capacity from 1.0 to 2.0 H_2 wt.%. It implies a considerable decrease in vessel diameter (Figure 24-a), decreasing system weight and volume, as can be seen from Figure 24-b. It results in an increase in system volumetric capacity that is almost linear as a function of the MH gravimetric capacity, as it can be seen from Figure 25.

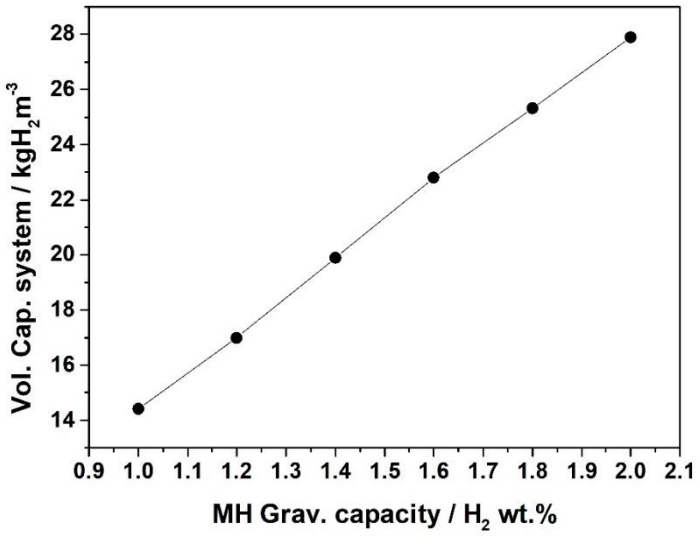

Figure 25: Volumetric capacity of the system as a function of the MH gravimetric capacity per one vessel.

Using a MH gravimetric capacity of 2.0 H_2 wt.%, it is possible to reach the highest volumetric capacity for the considered design with 27.9 kgH_2/m^3, compared to the value of 14.4 kgH_2/m^3 obtained using a carrier with 1.0 H_2 wt.%.

A final simulation has been performed for the volumetric capacity of the system, changing the apparent density of the powder (3.0, 3.5 and 4.0 t/m^3) and considering storing 1800 kg of H_2 in one vessel. Results have been compared considering a MH gravimetric capacity of 1.6 H_2 wt. % and 2.0 H_2 wt. % (Figure 26).

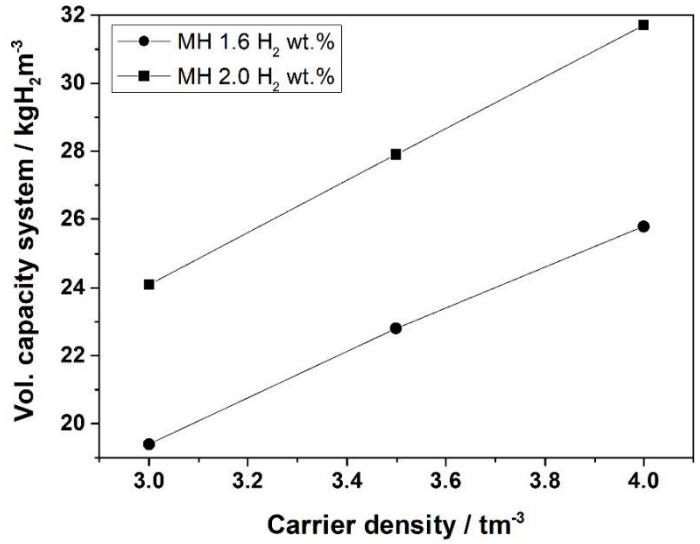

Figure 26: Volumetric capacity of the system as a function of the density of the carrier with a MH gravimetric capacity of 1.6 H_2 wt.% and 2.0 H_2 wt.%.

Increasing carrier apparent density, the system volumetric capacity increases linearly, thanks to a decrease in the system volume. Higher values can be obtained with a MH gravimetric

density of 2.0 H_2 wt.%, as shown in Figure 26, with a value of 31.7 kgH_2/m^3. To take into account is the few availabilities at commercial level of IMC with about 2.0 H_2 wt.%. According to literature, the use of $TiMn_2$-based compounds allows to reach in the optimal condition of design and MH density a volumetric capacity of 25.8 kgH_2/m^3.

3.3.3.3 Integration of the H2SS with an EL and a FC

Considering the case study with a MH of 1.6 H_2 wt.% storing 1800 kg of H_2, it was supposed to integrate the system with an EL in a refuelling station on the mainland and a FC on board. Concerning the refuelling, it is considered to load the entire amount of H_2 at 30 bar in a day, *i.e.* 24 h. This implies an EL with H_2 flow of 28 Nm^3/h. Taking into account that for the production of 1 kg of H_2 an electrolyser consumes 39.4 kWh for a 100 % of efficiency [27], considering a 70 % efficiency, an EL of about 2 MW should be required. Assuming 240 h of discharge, *i.e.* 10 days, a FC of 124 kW should be necessary, considering an efficiency of 50 % [28]. Evaluating a FC working at 1 bar of supply, an H_2 flow of supply of 7.5 kg/h was calculating, implying a FC consumption of 0.68 Nm^3/kWh.

Regarding the MH H2SS with the design of the MH-tubes in one vessel, the power required during the loading and unloading of H_2 at 30 and 45 °C, respectively, was calculated, taking into account an enthalpy in both absorption and desorption of about 30 $kJ/molH_2$. Then, it is assumed a difference in temperature between the inlet and outlet of the thermal fluid of about 3 °C. This requires a water flow of 26 kg/s and 4 kg/s for absorption and desorption reactions, respectively. The calculated power includes the heat of reaction in absorption/desorption, and the heat necessary to heat/cool the powder and the steel, for both tubes and vessel. The amount of power required in absorption to cool down the system is of about 331 kW, while in desorption to heat is of 33 kW. These results would highlight the power consumption required when considering large amount of H_2 stored as MH, if a fast refuelling is necessary, implying large amount of power for both the production of H_2 through electrolysis and for the cool down of the MH H2SS.

3.3.4 Conclusion

When design a H2SS based on MH for the storage of tons of H_2, the selection of the design of the system and of the MH plays a key role in the volumetric capacity of the system itself. Using commercial stainless-steel tubes of 10”, the design involves the allocation of the MH tubes inside one vessel, in which the thermal fluid flows for the heat exchange, optimising

the system weight and volume. It was found that increasing the number of vessels, passing from 1 to 8, the volumetric capacity of the system decreases of about 14 % moving towards of a plateau. With the use of IMC, the volumetric capacity of the system increases increasing the MH gravimetric capacity and carrier density, while it is not affected by the amount of hydrogen stored, after having fixed the design and the MH. Regarding the MH, the rise of one unit in powder density implies an increase of about 25 % in volumetric capacity of the system. While, for a given powder density, a rise of 0.4 H_2 wt.% in gravimetric capacity promotes an increase of about 20 % in system volumetric density. Finally, the amount of power involved for the management of tons of hydrogen in both production and storage has been evaluated, giving an idea of the size of the infrastructure required.

Final remarks

A key point for the realization of a H2SS is played by modelling and simulations, that provide parameters to predict the system response at macroscopic scale, to be verified experimentally. For a proper design of a H_2 tank, a suitable model is fundamental. Through a series of lumped element model, the main parameters that affect the design of a H_2 storage systems based on MH were evaluated. It is proven how it could be challenging the fit of some constrain in gravimetric and volumetric capacity of the system.

The influence of MH properties and tube design on the volumetric and gravimetric capacity of the system was shown through a series of simulation without taking into account real design or operative conditions. The material of the tube plays a key role on system gravimetric capacity, especially for high gravimetric capacity of MH. The volumetric capacity has a linear correlation with that of the MH, while the gravimetric capacity moves towards a plateau by increasing the storage capacity of the MH, observing sensitive changes for low values.

Observation made previously were confirmed investigating the storage of 50 kg of H_2 as MH through commercial IMC and considering commercial dimensions of tubes. On the gravimetric capacity a key role is played by the material of the reactor and by the MH storage capacity, with a sensitive increase of the system passing from 1.0 H_2 wt.% to 1.4 H_2 wt.%. Changes with the MH storage system are observed also in the volumetric capacity of the system. The latter is influenced by the dimension of tubes, affecting the number of tubes required for the storage and a right compromise need to be found. Comparing the system

with a storage of 50 kg of H_2 at 30 bar in commercial tubes, it can be seen that MH is advantaging in the volumetric capacity of the system, but even in the gravimetric one, since the storage as low pressure gas implies hundreds of tubes resulting in a system weigh higher than the one observed exploiting MH. MH and compressed gas are competitive in volumetric capacity just when hydrogen is compressed as an example at 200 bar, observing comparable or even higher volumetric capacity using MH, depending on the H_2-carrier. However, compressing H_2 at high pressures, the system weight decreases sensitivity resulting always advantaging than MH, even if in the latter case, less tubes need to be handled. Thus, MH are competitive as storage system in stationary applications or in transporting H_2, thanks to their safety and low footprint.

Evaluating high amount of H_2 storage and considering a different design of the H2SS, *i.e.* one vessel filled with the thermal fluid and the MH tubes, it was shown how the volumetric capacity of the system is sensitive to MH powder density and gravimetric capacity. Considering tons of H_2 stored as MH for heavy mobile vehicle, the application could imply relatively fast production and refuelling resulting in high amount of power required to produce the H_2 with electrolysis and in managing the heat of reaction developed in hydride formation. This gives an idea of the design of a H_2 chain depending on the final application.

Finally, focus the attention on the data obtained in gravimetric and volumetric capacity of the system in all the three case studies faced in this chapter, it could be seen that changing tubes dimension and the amount of hydrogen stored, but considering similar geometry and the same class of compounds (IMC), the order of magnitude of both gravimetric and volumetric capacity is similar, with the first lower than 1.0 H_2 wt.% and the second one of the order of 20 kgH_2/m^3. Double values of volumetric capacity are observed only in the first section due to tubes dimension completely not commercial. This means that to promote a variation on system volumetric and gravimetric capacity, it is necessary to change the MH properties (like gravimetric capacity or powder density) and/or the design, tube dimension and its material.

References

[1] J. Bellosta von Colbe, J.-R. Ares, J. Barale, M. Baricco, C. Buckley, G. Capurso, N. Gallandat, D.M. Grant, M.N. Guzik, I. Jacob, E.H. Jensen, T. Jensen, J. Jepsen, T. Klassen, M.V. Lototskyy, K. Manickam, A. Montone, J. Puszkiel, S. Sartori, D.A. Sheppard, A. Stuart, G. Walker, C.J. Webb, H. Yang, V. Yartys, A. Züttel, M. Dornheim, Application of hydrides in hydrogen storage and compression: Achievements, outlook and perspectives, Int. J. Hydrogen Energy. 44 (2019). 10.1016/j.ijhydene.2019.01.104.

[2] M. V. Lototskyy, I. Tolj, L. Pickering, C. Sita, F. Barbir, V. Yartys, The use of metal hydrides in fuel cell applications, Prog. Nat. Sci. Mater. Int. 27 (2017) 3–20. 10.1016/j.pnsc.2017.01.008.
[3] K. Herbrig, L. Röntzsch, C. Pohlmann, T. Weißgärber, B. Kieback, Hydrogen storage systems based on hydride-graphite composites: Computer simulation and experimental validation, Int. J. Hydrogen Energy. 38 (2013) 7026–7036. 10.1016/j.ijhydene.2013.03.104.
[4] S. Orimo, Y. Nakamori, J.R. Eliseo, A. Zu, C.M. Jensen, Complex Hydrides for Hydrogen Storage, Chem. Rev. 107 (2007) 4111–4132. 10.1021/cr0501846.
[5] G.P. Ordaz, C. Read, S. Satyapal, DOE Hydrogen Program 2005 Annual Merit Review and Peer Evaluation Report. p. 730., 2005.
[6] G. Sdanghi, G. Maranzana, A. Celzard, V. Fierro, Review of the current technologies and performances of hydrogen compression for stationary and automotive applications, Renew. Sustain. Energy Rev. 102 (2019) 150–170. 10.1016/j.rser.2018.11.028.
[7] M. Cavo, E. Gadducci, M. Rivarolo, L. Magistri, A. Dellacasa, M. Romanello, G. Borgogna, C. Davico, Thermal integration of PEM Fuel Cells and metal hydrides storage system for Zero Emission Ultimate Ship (ZEUS), in: E3S Web Conf., 2022: p. 04004.
[8] M. Kickulies, Fuel cell power for maritime applications, Fuel Cells Bull. 2005 (2005) 12–15. 10.1016/S1464-2859(05)70758-6.
[9] V.I. Borzenko, I.A. Romanov, D.O. Dunikov, A.N. Kazakov, Hydrogen sorption properties of metal hydride beds: Effect of internal stresses caused by reactor geometry, Int. J. Hydrogen Energy. 44 (2019) 6086–6092. 10.1016/j.ijhydene.2019.01.052.
[10] E.H. Jensen, M. Dornheim, S. Sartori, Scaling up metal hydrides for real-scale applications: Achievements, challenges and outlook, Inorganics. 9 (2021) 1–20. 10.3390/inorganics9050037.
[11] E.M. Dematteis, J. Barale, M. Corno, A. Sciullo, M. Baricco, P. Rizzi, Solid-State Hydrogen Storage Systems and the Relevance of a Gender Perspective, Energies Rev. 14 (2021) 6158. 10.3390/ en14196158 Academic.
[12] Hydrogen Supply Chain Platform, Ministry of the Environment, Japan. https://www.env.go.jp/seisaku/list/ondanka_saisei/lowcarbon-h2-sc/en/demonstration-business/index.html.
[13] L. van Biert, M. Godjevac, K. Visser, P. V. Aravind, A review of fuel cell systems for maritime applications, J. Power Sources. 327 (2016) 345–364. 10.1016/j.jpowsour.2016.07.007.
[14] V.P. McConnell, Now, voyager? The increasing marine use of fuel cells, Fuel Cells Bull. 2010 (2010) 12–17. 10.1016/S1464-2859(10)70166-8.
[15] C. Fiori, A. Dell'Era, F. Zuccari, A. Santiangeli, A. D'Orazio, F. Orecchini, Hydrides for submarine applications: Overview and identification of optimal alloys for air independent propulsion maximization, Int. J. Hydrogen Energy. 40 (2015) 11879–11889. 10.1016/j.ijhydene.2015.02.105.
[16] P.C. Ghosh, U. Vasudeva, Analysis of 3000T class submarines equipped with polymer electrolyte fuel cells, Energy. 36 (2011) 3138–3147. 10.1016/j.energy.2011.03.003.
[17] Y. Bicer, I. Dincer, Clean fuel options with hydrogen for sea transportation: A life cycle approach, Int. J. Hydrogen Energy. 43 (2018) 1179–1193. 10.1016/j.ijhydene.2017.10.157.
[18] H. Weydahl, M. Gilljam, T. Lian, T.C. Johannessen, S.I. Holm, J.Ø. Hasvold, Fuel cell systems for long-endurance autonomous underwater vehicles – challenges and benefits, Int. J. Hydrogen Energy. 45 (2020) 5543–5553. 10.1016/j.ijhydene.2019.05.035.
[19] G. Sattler, Fuel cells going on-board, J. Power Sources. 86 (2000) 61–67. 10.1016/S0378-7753(99)00414-0.
[20] K. Swider-Lyons, D. Deitz, Hydrogen Fuel Cells for Unmanned Undersea Vehicle Propulsion, ECS Meet. Abstr. MA2016-02 (2016) 2464–2464. 10.1149/ma2016-02/38/2464.
[21] J. Schneider, S. Dirk, P. Motor, ZEMShip, in: 18th World Hydrog. Energy Conf., 2010.
[22] A. Psoma, G. Sattler, Fuel cell systems for submarines: From the first idea to serial production, J. Power Sources. 106 (2002) 381–383. 10.1016/S0378-7753(01)01044-8.
[23] A.I. Bevan, A. Züttel, D. Book, I.R. Harris, Performance of a metal hydride store on the "ross Barlow" hydrogen powered canal boat, Faraday Discuss. 151 (2011) 353–367. 10.1039/c0fd00025f.
[24] Fincantieri, Bilancio di sostenibilità, 2016. https://www.coni.it/it/.

[25] h2boat web site: https://www.h2boat.it/#gref.
[26] D.F. Heaney, Powders for metal injection molding (MIM), in: W.P. Limited (Ed.), Handb. Met. Inject. Molding, Woodhead Publishing Limited, 2012: pp. 50–63. 10.1533/9780857096234.1.50.
[27] N. Gallandat, K. Romanowicz, A. Züttel, An Analytical Model for the Electrolyser Performance Derived from Materials Parameters, J. Power Energy Eng. 05 (2017) 34–49. 10.4236/jpee.2017.510003.
[28] C. Lamy, From hydrogen production by water electrolysis to its utilization in a PEM fuel cell or in a SO fuel cell: Some considerations on the energy efficiencies, Int. J. Hydrogen Energy. 41 (2016) 15415–15425. 10.1016/j.ijhydene.2016.04.173.

Chapter 4
Hydrogen storage

This chapter is linked to the work performed in the framework of the EU-project HyCARE, supported by FCH-JU [1]. The goal of the project is to store renewables using H_2 as energy vector, developing an integrated system composed by an electrolyzer (EL), a hydrogen - heat storage system, and a Fuel Cell system (FC), for the storage of energy for smart grid applications. The innovation of the project is the coupling of a hydrogen storage with a heat storage system, using a phase change material (PCM) for the heat management of the MH-tank. The plant will be installed at ENGIE Crigen lab near Paris in 2022 and involves European industries, research institutes and universities.

4.1 $TiFe_{0.85}Mn_{0.05}$ alloy produced at industrial level for a hydrogen storage plant

4.1.1 Introduction

A drawback of TiFe IMC as hydrogen carrier for mild conditions application is its hard activation (Chapter 1), and elemental substitution and Ti-rich compositions have found to be promising to overcome this problem and to tailor sorption properties, as comprehensive overviewed in two recent reviews [2,3].

Mn is a common substitution for Fe in TiFe, forming $TiFe_xMn_{(1-x)}$ alloys [4]. As reported by Jhonson et al. [4], Mn containing compounds showed a decrease in the equilibrium pressures for hydrogen sorption and an increase in cell dimension, with respect to the original TiFe phase. On the contrary, no changes in gravimetric capacity were evidenced by x = 0.70. Mn additions results in the occurrence of sloping plateaux in the pcT-curves, which can be limited by suitable annealing, as well as to a reduction of the hysteresis gap [4]. Challet et al. [5], prepared and studied $Ti(Fe_{0.70+x}Mn_{0.20-x})$ alloys, with x = 0.00, 0.05, 0.10 and 0.15. Samples were synthesised by induction melting, annealed at 1000 °C for 1 week and then quenched. For the first hydrogenation, activation was not necessary for any sample and pcT-curves presented two distinct plateaux with limited slope. Increasing the fraction of Fe, the unit cell dimension progressively decreased, coupled with an increase of the plateaux pressure from 4 to 20 bar at 65 °C. All alloys displayed fast kinetics and no relevant changes on gravimetric capacity were reported, compared to the parent TiFe. In a recent study, Dematteis et al. [6] investigated the storage properties of a series of TiFe-based compounds and evaluated the effect of Mn and Ti substituting Fe in the alloy, by mapping Ti:Fe ratio from 1.0:1.0 to 1.0:0.9 and by varying the Mn content between 0 and 5 at.%. Samples were prepared at laboratory scale, similarly to Challet et al. [5]. Secondary phases of $Ti_4Fe_2O_x$,

β-Ti-type or $TiFe_2$ were detected, always with an abundance below 10 wt.%. The occurrence of the latter two compounds agrees with the TiFe phase diagram [7]. Ti-rich compositions, as compared to stoichiometric TiFe, form β-Ti-rich solid solution precipitates whereas, for Ti-poor compositions, the formation of $TiFe_2$ precipitates is expected. It is worth noting that the oxide was detected only in Ti-rich compositions, *i.e.* with Ti > 50 at.%, due to the high reactivity of Ti with oxygen, the latter being incorporated during sample preparation and/or already present in the starting materials [8]. Nevertheless, it was observed that a suitable quantity of secondary phases helped the activation process, but an excess causes a decrease in the gravimetric capacity. The addition of Mn in TiFe-based alloys increases the unit cell dimension, and a linear dependence was observed between the cell dimension and the equilibrium pressure for hydrogen sorption, as well as the pressure step between two plateaux in the pcT-curves and the hysteresis gap [4,5]. Authors concluded that the $TiFe_{0.85}Mn_{0.05}$ composition is the most promising for practical applications, thanks to an easy activation with 7 h of incubation time under H_2 at 25 bar and 25 °C, which results in fast absorption kinetics and a reversible capacity of 1.63 H_2 wt.%.

Thanks to the suitable H_2 sorption properties reported for $TiFe_{0.85}Mn_{0.05}$ [5,6], this composition was selected as H_2-carrier for the HyCARE plant designed to store up to 50 kg of H_2. To operate the plant, the designated temperature is 55 °C. Thanks to the observed equilibrium pressure at about 5.9 bar and 10.6 bar for the first and second absorption plateau, respectively [6], this alloy is suitable to absorb H_2 directly from a PEM-EL, with a supply pressure close to 30 bar. Then, the H_2 could be released supplying a PEM-FC at 1-2 bar, thanks to an equilibrium pressure of about 3.1 bar and 6.8 bar for the first and second desorption plateau, respectively [6]. The production and integration of a large-scale storage plant requires preliminary stages of prototyping, including a careful evaluation of the properties of the hydrogen storage material, which can differ moving from laboratory to industrial scale production. Indeed, the design can impose both technical and economic requirements that can drastically change the sorption properties of the selected materials. In particular, the purity of the starting raw materials will be dictated by the price and availability of parent elements. Processing techniques will differ, passing from a laboratory arc or induction melting to an industrial plant. The degree of control of the oxygen level at each step changes, due to a lower grade of vacuum during the synthesis and the occurrence of steps in air at high temperatures at an industrial level, compared to the controlled atmosphere maintained during the whole process at the laboratory scale.

Finally, the economic design requirements limit the possibility after the synthesis to perform heat treatments at high temperatures and for long times, such as those described for laboratory scale processing in the literature [5,6]. This will lead to an industrial powdered material that, compared to that prepared at laboratory scale, is expected to be characterised by a higher oxygen content and a lower homogeneity, with the formation of gradients in composition or in secondary phases distribution, as well as by changes in microstructure and in surface properties.

Therefore, the first stage of prototyping the hydrogen storage plant was the characterization of a preliminarily batch of 5 kg of powder of a $TiFe_{0.85}Mn_{0.05}$ alloy produced under industrial conditions, to understand how the final hydrogen properties can be affected by the upscaling and to verify if the materials would be suitable for the final application. This section reports a detailed study of the phase composition, the microstructure and hydrogen sorption properties of an industrially produced $TiFe_{0.85}Mn_{0.05}$ alloy, comparing results with those obtained on a sample with the same overall composition prepared a laboratory scale, as reported in ref. [5,6]. The goal is to understand if the industrially prepared alloy is suitable to be used in the final plant, investigating its activation and operation at 55 °C, appropriate for the integration with a PEM-EL and PEM-FC.

4.1.2 Experimental

4.1.2.1 Synthesis

An amount of 5 kg of $TiFe_{0.85}Mn_{0.05}$ was prepared at industrial level at the GKN industry, starting from the parent elements by melting. Raw materials are electrolytic grade Fe and Mn and commercially pure (CP) Ti Grade 1 (minimal purity about 99.1 %). The chemical composition was obtained by taking a Ti-Fe-Mn master alloy with a nominal composition of 5.8 wt.% Mn and diluting the manganese to the target composition by additions of Fe and Ti. Dilution and melting were performed in a skull melter [9] under vacuum (10^{-2} mbar). Then, the liquid alloy was poured in a water-cooled Cu-crucible. The resulting ingots were grinded in air in two steps. Firstly, the bulk was crushed in a jaw crusher to chunks, and then it was micronized in a hammer mill. The obtained powder was then poured in a sieve to select only the particle size with a dimension lower than 420 μm. Finally, the powder was delivered in air and then stored in glovebox.

4.1.2.2 Characterization

4.1.2.2.1 Powder X-Ray Diffraction (PXD)

The PXD patterns of the synthetized powder were acquired in Bragg-Brentano geometry, with an acquisition time of 1100 s per scan, steps of 0.016°, from 35° to 120° in 2θ. After activation and cycling, the powders were analysed in Debye-Scherrer geometry, with the powder samples packed in glass capillaries with a diameter of 0.8 mm in a glovebox under Ar atmosphere. Measurements were performed from 30° to 120° in 2θ, steps of 0.016° and a time per scan of 400 s. Pattern's background results to be noisy due to the fluorescence promoted by the presence of Fe in the sample and the use of Cu-Kα radiation.

4.1.2.2.2 Scanning Electron Microscopy (SEM)

The study of the microstructure on the as synthetized sample was performed with the powder embedded in a conductive resin and polished, while morphological investigation was performed on loose powder. Analysis was carried out using a FEG-SEM instrument. The loose powder was also studied by performing EDX measurements at different energy, *i.e.* 2, 5 and 15 keV, to perform Monte Carlo simulations with the software CASINO [10]. Finally, samples after cycling with H_2 as loose and embedded powders were studied with a SEM instrument. On embedded samples, EDX elemental measurements were acquired at 20 keV.

4.1.2.2.3 Volumetric measurements by Sievert's Method

pcT-curves were registered with the instrument PCT-Pro by Setaram at 25 °, 40 °, 55 ° and 70 °C. Vacuum (10^{-3} bar) conditions were applied at about 100 °C between a curve and another, to ensure a complete hydrogen desorption.

4.1.3 Results and discussion

4.1.3.1 Chemical and structural characterization

Figure 1 shows the backscattered electron (BSE) images and the EDX-elemental maps for Ti, Fe, Mn and O acquired with the FEG-SEM instrument on the embedded powder.

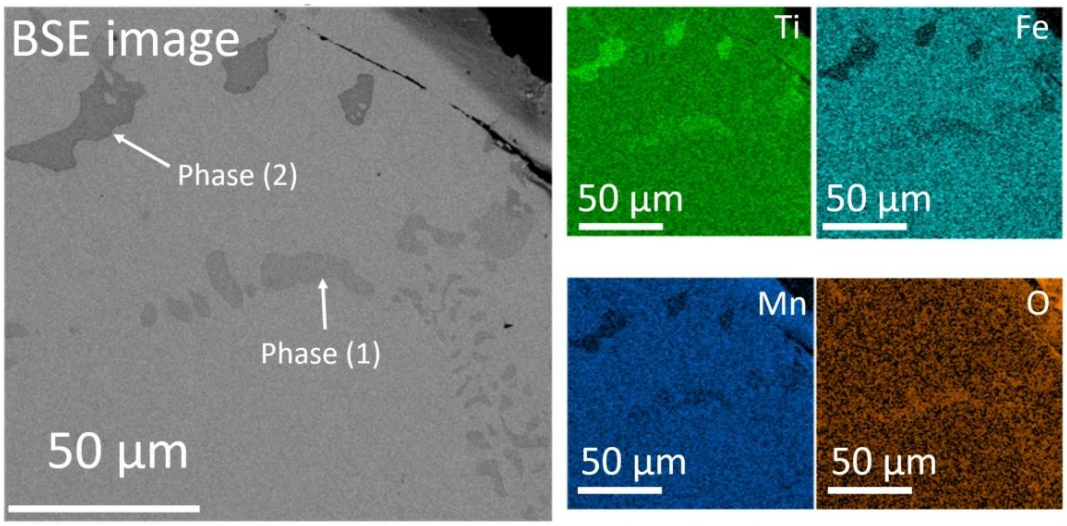

Figure 1: BSE image and EDX elemental maps for Ti, Fe, Mn and O, obtained by FEG-SEM on embedded as-synthetized powder of the $TiFe_{0.85}Mn_{0.05}$ alloy prepared at industrial scale. The two zone darker than the matrix in the BSE image have been named Phase (1) and Phase (2) and correspond to $Ti_4Fe_2O_x$ and β-$Ti_{80}(Fe,Mn)_{20}$, respectively.

From the BSE image in Figure 1, it is possible to observe two zones darker than the matrix, named Phase (1) and (2). From EDX maps, it appears that, compared to the matrix, both of them are richer in Ti and poorer in Fe and Mn, especially for the darkest one, *i.e.* Phase (2). In addition, it is also possible to observe from the EDX maps that Phase (1) presents a higher content of oxygen with respect to Phase (2). According to the EDX punctual analysis (Table 1), the composition of the matrix is confirmed to be $TiFe_{0.85}Mn_{0.05}$. Phase (1) presents an atomic ratio 2:1 in Ti and (Fe,Mn) respectively, and it is linked to a $Ti_4(Fe,Mn)_2O_x$ phase. Phase (2) is the richest in Ti, and according to the elemental fractions reported in Table 1, it is linked to β-$Ti_{80}(Fe,Mn)_{20}$. For the Ti-rich sample, the occurrence of the β-$Ti_{80}(Fe,Mn)_{20}$ phase is expected, in agreement with the Ti-Fe phase diagram [7]. In contrast, $Ti_4Fe_2O_x$ is not expected from the phase diagram and its formation is stabilized by oxygen impurities in raw materials, *e.g.* Ti, and/or from material processing [5,6].

Table 1: Chemical compositions in at.% obtained by EDX analysis for Ti, Fe and Mn

Elemental abundance	**Ti at. %**	**Fe at. %**	**Mn at. %**
Matrix	50.43 ± 3.96	45.78 ± 1.61	2.11 ± 0.44
Phase (1)	63.12 ± 1.15	34.00 ± 1.03	2.88 ± 0.12
Phase (2)	79.65 ± 0.04	16.97 ± 0.27	3.39 ± 0.32

As can be seen by the BSE image of Figure 1, $Ti_4(Fe,Mn)_2O_x$ (Phase (1)) is mainly present at grain boundaries, while the β-$Ti_{80}(Fe,Mn)_{20}$ (Phase (2)) is present as inclusions.

The PXD pattern of the as-synthetized powder (Figure 2-a) was acquired to confirm the presence of the phases observed by SEM analysis.

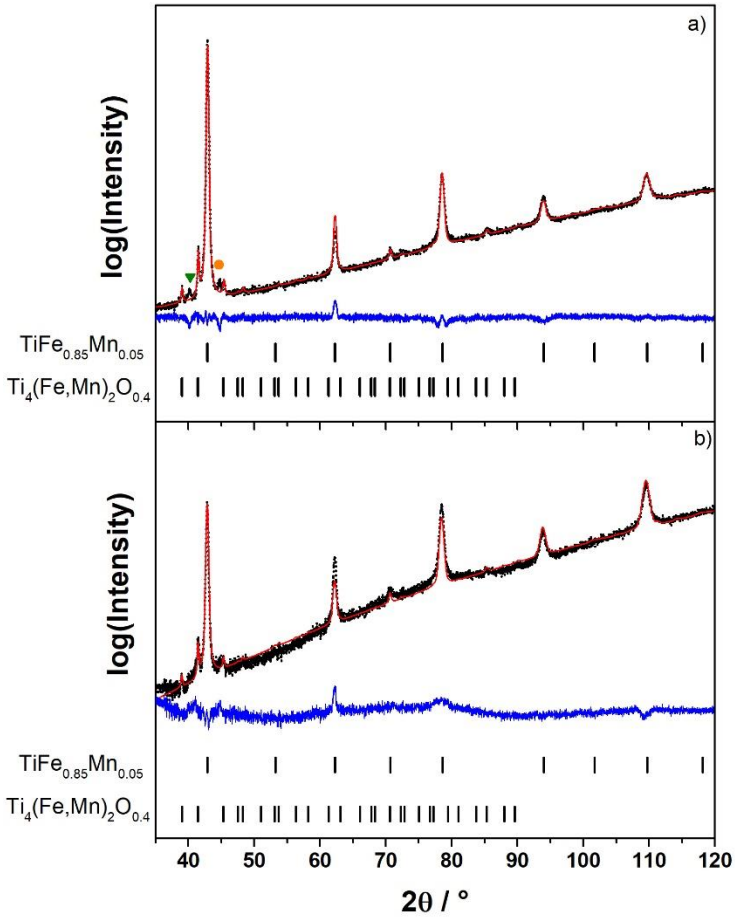

Figure 2: PXD patterns for the $TiFe_{0.85}Mn_{0.05}$ alloy prepared at industrial scale of (a) the as synthetized powder and (b) after activation. Dots represent experimental points, red lines the calculated patterns and blue lines the difference between them. Bars indicate diffraction peak positions for the single phases of $TiFe_{0.85}Mn_{0.05}$ and $Ti_4(Fe,Mn)_2O_{0.4}$, while the green triangle refers to β-$Ti_{80}(Fe.Mn)_{20}$ and the orange circle to an unknown phase.

The phases detected by PXD (Figure 2-a) are in good agreement with the chemical analysis performed with the EDX. Indeed, diffraction peaks related to the presence of $TiFe_{0.85}Mn_{0.05}$, $Ti_4(Fe,Mn)_2O_x$ and β-$Ti_{80}(Fe,Mn)_{20}$ (green triangle) are observed. One diffraction peak, labelled with an orange circle and not assigned to the previous phases, was attributed to the presence of an unknown phase. Its stoichiometry is hard to assign, since only the main diffraction peak is visible with low intensity and no other phases were detected in the EDX analysis (Figure 1). The Rietveld refinement on the experimental patterns was performed to evaluate the lattice constants and phase abundance of $Ti_4(Fe,Mn)_2O_x$ and $TiFe_{0.85}Mn_{0.05}$. β-$Ti_{80}(Fe,Mn)_{20}$ is present in too small amount to be properly quantified. From the Rietveld refinement, 10 wt% of $Ti_4(Fe,Mn)_2O_x$ is detected. The $TiFe_{0.85}Mn_{0.05}$ phase has a cubic

CsCl-type structure space group $Pm\bar{3}m$ with a cell parameter a = 2.984(1) Å. Both Ti and Mn partially substitute Fe, causing a lattice expansion compared to stoichiometric TiFe, a = 2.972 Å [11]. This result is in good agreement with literature for the same $TiFe_{0.85}Mn_{0.05}$ composition, *i.e.* 2.985(6) Å [5,6]. The oxide phase has a cubic structure, space group $Fd\bar{3}m$, with a cell parameter of 11.314(4) Å, in agreement with the literature [8]. The oxide $Ti_4(Fe,Mn)_2O_x$ has been reported in the literature with a variable composition ($0.4 \leq x \leq 1.0$) without significant changes in the lattice constant [8]. It is therefore not possible to determine accurately the stoichiometry of the oxide phase, from the cell parameter. The evaluation of the oxygen in the stoichiometry was instead performed by calculating the elemental amount of Ti, Fe, Mn, O, from the phase abundance obtained by the refinement for different oxygen stoichiometries of the oxide. For x = 0.4, the obtained amount of singe elements is in good agreement with the results provided by the chemical analysis reported by the producer, as reported in Table 2. Thus, according to the results of the refinement, the stoichiometry of the oxide phase was determined to be $Ti_4(Fe,Mn)_2O_{0.4}$.

Table 2: elemental abundance in wt.% of Ti, Fe, Mn and O obtained by the Rietveld Refinement in comparison with the one declared by GKN.

Elemental abundance	**Ti wt. %**	**Fe wt. %**	**Mn wt. %**	**O wt. %**
GKN	46.6	47.09	2.72	0.233
Rietveld Ref.	50.11	47.16	2.52	0.21

Summarising, the industrial synthesis promotes the production of an inhomogeneous sample, with secondary phases present in higher amount compared to laboratory preparation [6]. Indeed, for the same composition, the industrially prepared material contains 10 wt.% of oxide phase $Ti_4(Fe,Mn)_2O_{0.4}$, compared to 2.4 wt.% of $Ti_4Fe_2O_x$ observed in a sample prepared at laboratory scale [6]. In addition, the latter has also a 2.8 wt.% of β-$Ti_{80}(Fe,Mn)_{20}$, resulting in a total amount of secondary phases equal to 5.2 wt.% [6], significatively lower than that observed in the powder prepared at industrial scale.

4.1.3.2 Hydrogen sorption properties

4.1.3.2.1 Activation

The $TiFe_{0.85}Mn_{0.05}$ alloy prepared at laboratory scale can be easily activated after 7 hours of incubation time at 25 bar H_2 and 25 °C, displaying fast hydrogen absorption kinetics [6]. On the contrary, the industrially prepared material, maintained at the same conditions of temperature and pressure, did not absorb H_2 even after 3 days. This result confirms the effect

of the synthesis method on the hydrogen sorption properties of MHs [2,12]. In this case, the material with the same nominal composition, prepared at either laboratory [6] or at industrial conditions, results in differences in phase fractions and microstructure, that strongly affect the hydrogen sorption properties, requiring the need to develop a specific activation procedure for each alloy. However, being the industrially produced powder the material to be used in a real storage system, the activation procedure needs to fit the plant constraints (*i.e*. maximum affordable pressure and temperature), to which the system is designed to operate in safe conditions. Moreover, it is also important to optimize the activation process from an economical point of view, limiting as much as possible the H_2 consumption to reduce the costs of the start-up of the plant. Therefore, for the industrially prepared material, a specific activation procedure was developed, trying to minimize the amount of hydrogen necessary and without exceeding 100 °C and 50 bar, parameters fixed by the storage plant design to ensure efficiency and safety.

The first attempt was done by performing loading and unloading of H_2 under isothermal conditions. Figure 3-a shows a schematic representation of one activation cycle by reporting pressure and temperature as a function of time. Unfortunately, after 30 cycles of 1 h each, the activation was not achieved. On the contrary, the activation was reached by heating the powder from 25 °C up to 90 °C, temperature kept for 6 h under vacuum. Afterwards, 50 bar of H_2 were loaded under isothermal conditions at 90 °C for 4 hours, cooling down the sample to 25 °C in 2 hours and then keeping that temperature for 4 h. The total processing activation time is 16 h and the method requires a single hydrogen load (Figure 3-b).

Analysing a small portion of the sample after the activation and vacuum pumping by PXD (Figure 2-b), it was observed that the oxide phase was still present in a percentage around 10 wt.%, as for the as synthetized powder (Figure 2-a). This result suggests that the activation process is linked to a change in the morphology of the alloys, rather than to a change in the phases fraction.

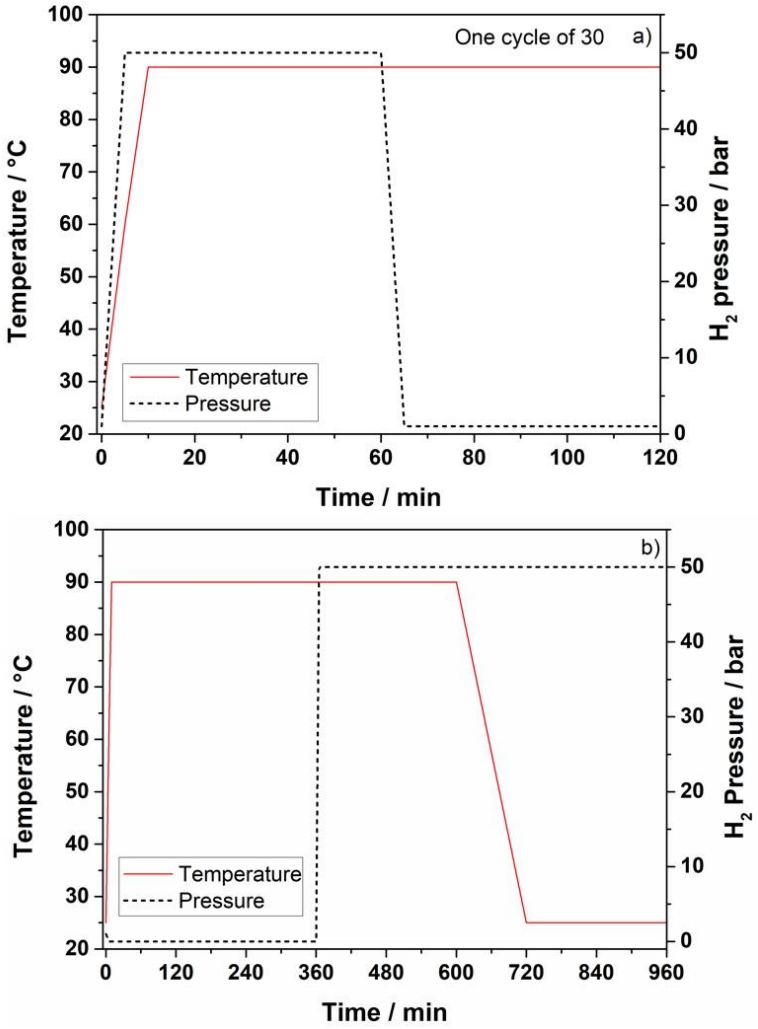

Figure 3: Temperature and pressure trend as a function of time during the activation: (a) one cycle of the 30, performed in isothermal condition; (b) thermal cycle developed with one single loading of H_2.

4.1.3.2.2 Thermodynamic study

pcT-curves for the $TiFe_{0.85}Mn_{0.05}$ alloy prepared at industrial scale, obtained for hydrogen absorption and desorption, are reported in Figure 4.

Differently from what observed at a laboratory scale [5,6] (insert Figure 4) all pcT-curves, in both absorption and desorption, display marked sloped plateaux. The two distinct plateau pressures are not observed. Due to the slope, the values of enthalpy (ΔH) and entropy (ΔS) for the hydrogen sorption reactions have been determined from the average of values obtained by applying the Van't Hoff equation at different H_2 wt.% (*i.e.* 0.4, 0.6 and 0.8). Results are reported in Table 3, as the average with the standard deviation, calculated by the Van't Hoff plots at the different H_2 wt.%, in comparison with data reported in ref. [6] for the same composition prepared at laboratory scale. Thermodynamic data are in the same range of values previously reported in the literature [6].

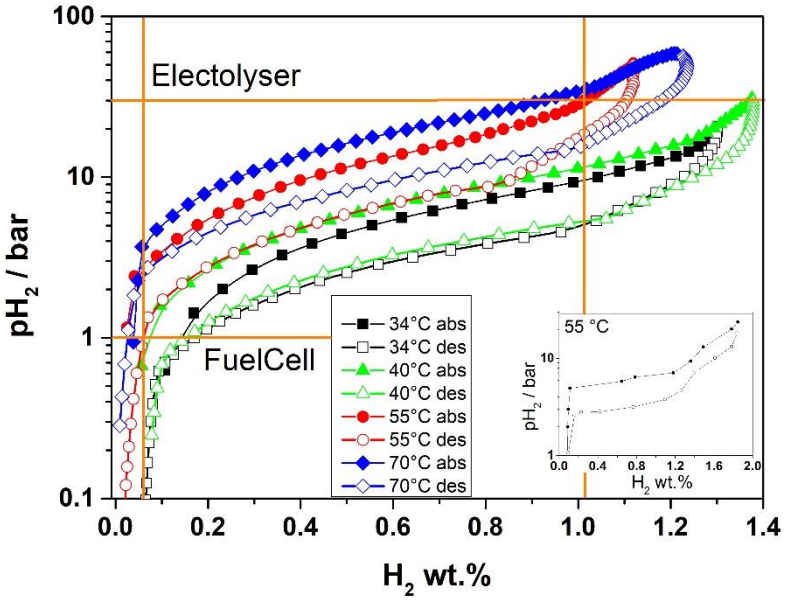

Figure 4: pcT-curves at 34-40-55-70 °C in absorption (full points) and desorption (empty points) for the $TiFe_{0.85}Mn_{0.05}$ alloy prepared at industrial scale, with solid lines as a guide for the eyes. The orange horizontal lines indicate the pressure of a PEM-EL with supply pressure at 30 bar and a possible desorption pressure at 1 bar for a PEM-FC. In the insert, the pcT curve at 55 °C, drawn from ref. [6]*, is reported.*

Table 3: Enthalpy (ΔH) and entropy (ΔS) for the hydrogen sorption reaction, obtained in both absorption and desorption, for the $TiFe_{0.85}Mn_{0.05}$ alloy prepared at industrial scale. Values obtained for the same composition prepared al laboratory scale [6] *are reported for comparison.*

	Absorption	**Desorption**	**Ref.** [6] **Absorption**	**Ref.** [6] **Desorption**
ΔH kJmol^{-1}	-31.2 ± 0.8	31.2 ± 1.0	1st plateau: - 27.8 2nd plateau: -32.5	1st plateau: 30.6 2nd plateau: 35.2
ΔS Jmol^{-1}K^{-1}	-115.7 ± 1.4	110.0 ± 1.3	1st plateau: - 99 2nd plateau: -121	1st plateau: 103 2nd plateau: 126

Considering the use of the material as hydrogen carrier to be supplied by a PEM-EL at 30 bar and to feed a PEM-FC at 1 bar (orange horizontal lines in Figure 4) at a working temperature of 55 °C, a reversible capacity of about 1.0 H_2 wt.% is expected (orange vertical lines in Figure 4), which is significantly lower than the value of 1.63 H_2 wt.% observed for the same composition prepared at the laboratory scale [6] (insert of Figure 4). The marked slope and the reduced capacity for the industrially prepared material are linked to the absence of the annealing treatment after alloy synthesis and to the high fraction of secondary phases, which, as already discussed in section 4.1.3.1, is almost twice compared to that observed in the material prepared at the laboratory scale [6]. In fact, the annealing treatment induces a homogenization of the composition, promoting flat plateaux [4]. On the other hand, annealing is costly and difficult to be performed at industrial level, especially for the laboratory process followed in ref. [5,6], *i.e.* one week annealing at 1000 °C. A progressive

decrease of the H_2 storage capacity was also observed by increasing the quantity of secondary phases in ref. [6]. In this work, the discrepancy between the laboratory and industrial composition is due to the higher fraction of secondary phases observed. Indeed, both the oxide and β-$Ti_{80}(Fe,Mn)_{20}$ do not reversibly absorb hydrogen at the applied conditions [8], decreasing the overall reversible gravimetric capacity.

Finally, the alloy was tested in the defined plant working conditions, *i.e.* 55 °C absorbing hydrogen at 25 bar and releasing it at 1 bar, performing 5 cycles, (Figure 5). Results shows a fast kinetic both in absorption and desorption, with about 10 min required to process the 90 % of the final capacity. The latter is in good agreement with the thermodynamic study, and it is about 1.0 H_2 wt.%.

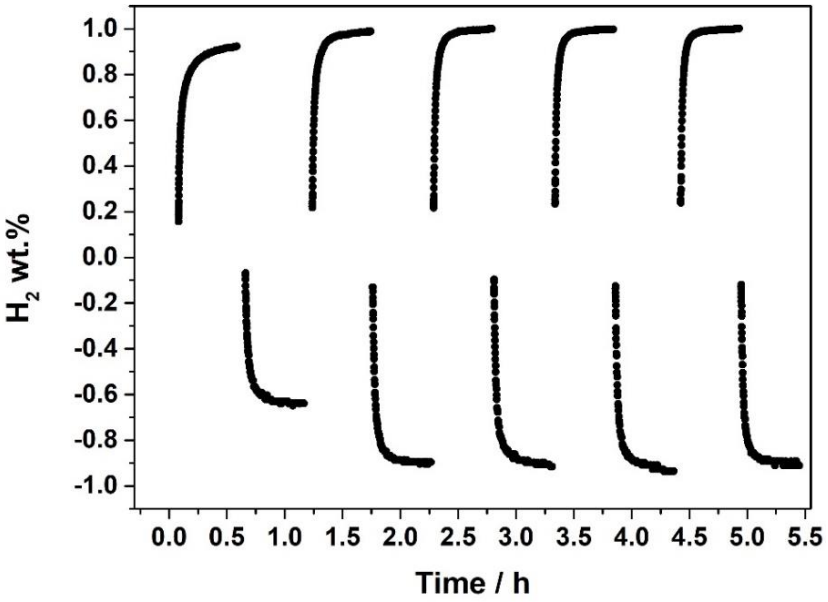

Figure 5: five absorption and desorption cycles at 55 °C at 25 and 1 bar performed.

In another laboratory, the powder was cycled for over than 250 cycles and it was then characterized in the framework of the PhD, by performing SEM-EDX acquiring PXD pattern (Figure 6). A comparison of the particle size of the powder after synthesis and hydrogen sorption cycles suggests that cycling promotes the reduction of the particle size. Indeed, by sieving after synthesis, the powder presents a dimension lower than 420 μm, while from a Secondary Electron SE-SEM image on loose powder after 250 cycles (Figure 6-a), the average particle size results to be lower than 200 μm.

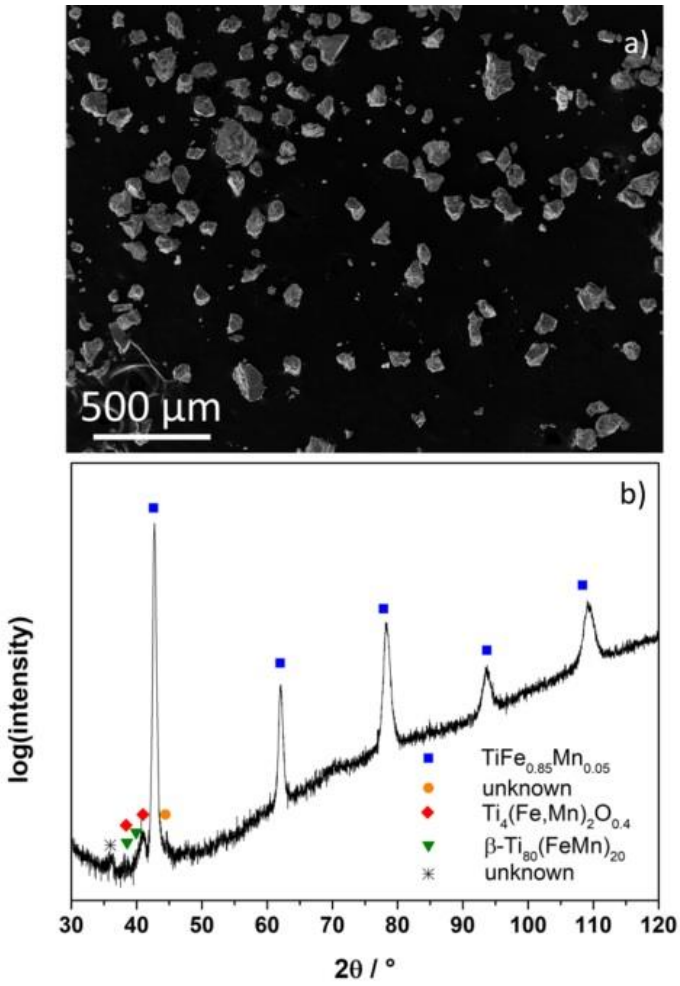

Figure 6: (a) SEM image in SE of the loose powder after 250 cycles; (b) PXD pattern of the powder after 250 cycles under pure H_2, with phases assignation.

The registered PXD pattern (Figure 6-b) shows that the main phase, $TiFe_{0.85}Mn_{0.05}$, is predominant, and the secondary phases detected on the as synthetised powder (Figure 2-a) are basically maintained, observing a reduction of the oxide and the evidence of a new small peak at about 35 ° in 2θ, linked to an unidentified phase. It is worth noting that, performing an EDX-study on the matrix phase in an embedded powder after 250 cycles, the same $TiFe_{0.85}Mn_{0.5}$ composition has been detected (Table 4).

Table 4: Chemical compositions in at.% obtained by EDX analysis for Ti, Fe and Mn on the powder after cycling.

Elemental abundance	**Ti at.%**	**Fe at.%**	**Mn at.%**
Matrix	52.06 ± 0.40	45.80 ± 0.96	2.14 ± 0.59

4.1.2.1 The role of oxygen in material processing and its influence on the sorption properties

It is reported in the literature that the role of the oxygen introduced during the synthesis of TiFe- compounds, resulting in the formation of Ti-Fe-O ternary oxides, *e.g.* $Ti_4Fe_2O_x$ with $0.4 \leq x \leq 1$, Ti_3Fe_3O or $Ti_{10}Fe_7O_3$, as secondary phases and/or as surfaces passive layer, is crucial in the sorption properties, starting already from their activation [8,13,14]. Indeed, ternary Ti-Fe-O oxides are always present in TiFe-based compounds, because of the oxygen immiscibility in the TiFe-based matrix and of the titanium high affinity with O [8]. Nevertheless, different results are reported in the literature regarding the ability of these oxides to be hydrogenated and, as a consequence, on their role in the H_2 sorption properties of the TiFe-compounds. Thus, in the following, the results obtained in these works are briefly summarized to help in the understanding the hydrogen sorption behaviour of the $TiFe_{0.85}Mn_{0.05}$ alloy prepared at industrial level.

Surface oxides as passive layer can be formed because of local concentration of oxygen at the surface, resulting in non-equilibrium Ti-Fe-O species [8,15]. Regarding the surface oxidation, it is reported in ref. [16,17] that the different electronic state of Fe in the matrix and in the surface oxide, when the material is heated, plays a catalytic role in the hydrogenation, promoting the dissociation of the hydrogen molecule. At this point the presence of grain boundaries between these oxides and passivated Ti(Fe,Mn) can act as fast channels for hydrogen diffusion, promoting alloy hydrogenation in bulk and by bulk expansion create cracks and fresh surfaces, helping in the hydrogenation [18–20]. The Ti_3Fe_3O and $Ti_{10}Fe_7O_3$ oxides were reported to be typical oxides present at the surface in TiFe-compounds; in particular, the Ti_3Fe_3O is reported as passive layer for the TiFe-alloys [21]. They do not absorb H_2, decreasing the storage capacity of TiFe-alloys [21–23]. On the other hand, they induce a reduction of the particle size, promoting hydrogenation. In fact, during H_2 absorption and desorption cycles, the combination of a volume change of the matrix with the unchanged volume of the oxides enables particle size refinement [22]. Rupp [8], by investigating the formation of ternary $Ti_{4-x}Fe_{2+x}O_y$ oxides in TiFe samples and their H_2 sorption properties, concluded that these compounds are present in considerably high amount in commercial alloys, *i.e.* when industrial production is used, since high amount of oxygen can be introduced during processing. In particular, for Ti-rich compositions, the $Ti_4Fe_2O_{0.4}$ is formed. $Ti_{4-x}Fe_{2+x}O_y$ oxides were reported to absorb H_2 [8,14,24,25]. Their structure was investigated by neutron diffraction by Stioui et al. [14] and, more recently, by

Density Functional Theory (DFT) calculations by Ha et al. [24]. A common result of investigations on $Ti_{4-x}Fe_{2+x}O_y$ oxides is that the oxygen content does not affect the cell parameter dimension, both in the hydrogenated and non-hydrogenated state, while it influences the amount of H_2 absorbed. The higher the oxygen content, the lower the hydrogen storage capacity [8,14,24,25]. Several results were reported concerning the hydrogen sorption conditions (*i.e.* pressure and temperature) in $Ti_{4-x}Fe_{2+x}O_y$ oxides, but thermodynamic data are not available. Stioui et al. [14] reported easy hydrogenation of Ti_4Fe_2O at room temperature under few (not specified) bars of H_2 without need of activation. Also Rupp [8] observed an easy hydrogenation between 20 °C and 100 °C under less than 1 bar of H_2 for the $Ti_4Fe_2O_{0.4}$, with a capacity of about 1.32 wt.% up to 5 bar, reaching even 1.76 wt.% in capacity hydrogenating the system at 5 bar, after cooling from 200 °C to room temperature. Hiebl et al. [25] reported a hydrogenation at 40 bar and 200 °C for $Ti_4Fe_2O_{0.46}$. It is important to point out that the easy activation and the hydrogenation at low pressures and temperatures observed in ref. [8,14] were obtained with the oxides in bulk form, while, in powder form, the hydrogenation is reported to be harder. Indeed, Rupp [8] observed a deactivation of the oxide by powdering the bulk, in agreement with Matsumoto et al. [26] and observing hydrogenation only at 40 bar and 250 °C, in agreement with ref. [25]. This change in the sorption properties observed for the $Ti_4Fe_2O_{0.4}$ is not clear, but similar behaviour was observed for β-$Ti_{80}Fe_{20}$ [8]. However, for the latter, hydrogenation in bulk form requires hard activation conditions, *i.e.* several cycles at 500 °C and 40 bar, while in powder form the hydrogenation occurs at 300 °C and 40 bar [8]. Finally, by preparing samples with different amount of $Ti_4Fe_2O_{0.4}$ and β-$Ti_{80}Fe_{20}$, together with the pure TiFe matrix, it was found that for high amount of $Ti_4Fe_2O_{0.4}$ at least 200 °C and 40 bar are required for the activation, while when β-$Ti_{80}Fe_{20}$ is present in higher amounts, hydrogenation occurs between 20 and 100 °C at 40 bar [8], in good agreement with ref. [26]. The hydrogenation of the secondary phases requires high pressures and temperatures, resulting in an overall reduction of the storage properties of the alloys, and when β-$Ti_{80}Fe_{20}$ is present in higher amount than the oxide, milder activation conditions are required [8]. Indeed, Nagai et al. in studying TiFeMn-samples, founds that the composition and the amount of the secondary phase, Ti-Fe-Mn-based, is crucial in the activation of the matrix. A proper fraction of secondary phases, even if does not absorb H_2, helps the activation thanks to its interface with the matrix acting as diffusion path for the hydrogen. The activation is empathised only when the secondary phases are even absorbing H_2 in the activation conditions [27]. Finally, the

different thermal expansion between the matrix and the secondary phases helps the hydrogenation process, promoting the cracking of the alloys [3].

Taking into account the information from the literature, it is possible to describe the sorption behaviour of the $TiFe_{0.85}Mn_{0.05}$ sample prepared in this work at industrial level. In fact, the oxygen is affecting its production, with the formation of higher amounts of $Ti_4(Fe,Mn)_2O_{0.4}$ with respect to the same nominal composition prepared at a laboratory scale [5,6], in agreement with ref. [8]. The industrial preparation introduces a high amount of oxygen, because of less pure raw materials and material processing, that can promote the formation of oxides inclusions, together with the formation of a passive layer at the surface. The formation of a passive layer at the surface can be linked to the harsher activation observed if compared to ref. [6], considering that a passive layer is hindering the first hydrogenation, requiring a treatment in temperature and pressure to promote the diffusion through it [28]. Thus, the surface of the as synthetized material was studied by EDX analysis on loose powder with a FEG-SEM instrument, by changing the energy applied of the incident beam, *i.e.* 2, 5, and 15 keV. The rise of the energy of the incident beam implies a deeper penetration of the beam inside the material, allowing a progressive investigation of the composition of the material from the surface to the bulk [29]. The signal of the oxygen is taken as an indicator of the presence of the passive layer. Hence, if the passive layer is present, its value is expected to progressively decrease by increasing the energy, *i.e.* the penetration depth inside the matrix.

The observed counts, normalized by the incident energy, are reported in Figure 7-a, as a function of the emitted energy in keV, up to 1 keV. The EDX signal of oxygen occurs at about 0.5 keV and its decrease can be observed by increasing the beam energy applied, confirming a change in composition between the surface and the matrix. The thickness of the passive layer was investigated by a Monte Carlo simulation with the software CASINO [10] estimating the penetration depth of the electronic beam as a function of the applied energy. When an incident beam penetrates inside the material, the emitted signal comes from various depths. The more the beam penetrates inside the material, the lower the emitted signal is, passing from 90 % to 5 %. It was selected to consider the corresponding depth of the 90 % of the emitted energy, since it represents the zone, from which the majority of the information regarding the material comes from. Figure 7-b shows the elemental amount as a function of beam penetration at 90 % of the emitted energy, obtained with the Monte Carlo simulation.

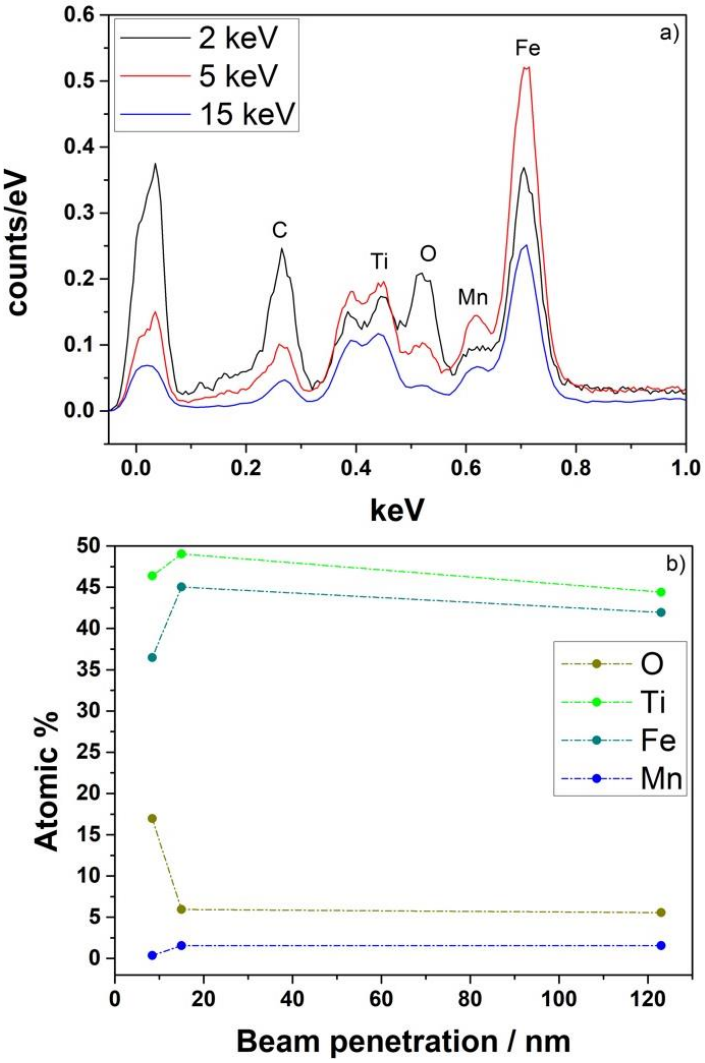

Figure 7: (a) EDX results, from FEG-SEM instrument, for the $TiFe_{0.85}Mn_{0.05}$ alloy prepared at industrial scale in terms of counts/eV as a function of the keV obtained with an experimental energy of 2, 5 and 15 keV; (b) the atomic percentage for Ti, Fe, Mn and O obtained by EDX analysis as a function of beam penetration at the 90 % of the emitted signal per each energy applied, i.e. 2, 5, and 15 keV.

For the values reported in Figure 7-b, the highest amount of oxygen is linked to a beam penetration of 8.4 nm, linked to an applied beam energy of 2 keV, while at 5 keV and 15 keV, the depth is of 15 and 123 nm, respectively. The oxygen content decreases reaching a nearly stable value already at 15 nm, accompanied by a rise for Fe, Ti and Mn content. These results suggest the occurrence of a passive layer less than 15 nm thick, and the atomic percentage obtained from the EDX analysis (Figure 7-b) suggests a Ti:Fe:O atomic ratio equal to 3:2.5:1, *i.e.* similar to the Ti_3Fe_3O, already reported as passive layer of TiFe [21,23]. The presence of the passive layer cannot be confirmed through PXD analysis, since the penetration depth of the X-Rays calculated in the experimental conditions was estimated to be between 1 and 3 μm, significantly deeper than the value of 15 nm estimated from the

Monte Carlo simulation for the EDX analysis. The presence of the $Ti_4(Fe,Mn)_2O_{0.4}$ at the surface of the powder cannot be excluded either, because of its high amount in the material. Indeed, since it was detected along grain boundaries (Figure 1), it can remain at the surface in some cases during the decrepitation of the powder.

On the basis of the literature data previously presented, regarding the sorption behaviour of Ti-Fe-O and β-$Ti_{80}Fe_{20}$ (β-$Ti_{80}(Fe,Mn)_{20}$ in this work), and the results observed for the $TiFe_{0.85}Mn_{0.05}$ prepared in this work at industrial level, Figure 8 shows a schematic illustrating the activation procedure (section 4.1.3.2.1).

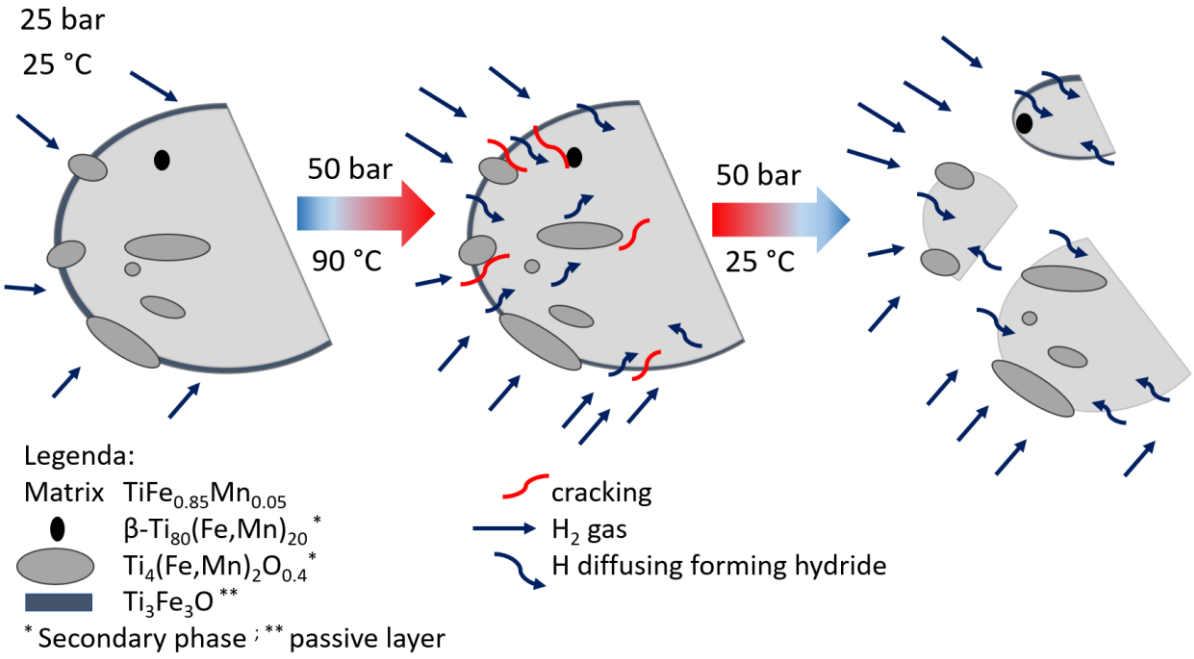

Figure 8: schematic description of the activation mechanism for the industrially prepared $TiFe_{0.85}Mn_{0.05}$ alloy.

At 25 °C and 25 bar (activation conditions of ref. [6]), the passive layer (Ti_3Fe_3O) hinders the first hydrogenation. Rising the temperature and pressure at 90 °C and 50 bar, respectively, promotes the diffusion of hydrogen through the passive layer, hydrogenating the matrix $TiFe_{0.85}Mn_{0.05}$. This process does not allow the hydrogenation the secondary phases β-$Ti_{80}(Fe,Mn)_{20}$ and $Ti_4(Fe,Mn)_2O_{0.4}$, since higher temperature are required for a sample rich in oxide (*i.e.* 40 bar and 250 °C) [8]. However, both the passive layer, Ti_3Fe_3O, and the oxide, $Ti_4(Fe,Mn)_2O_{0.4}$, at the surface can play a crucial role during activation, by for instance, promoting a catalytic effect of the Fe [16,17], inducing the dissociation of H_2 and then, the hydrogenation of the matrix is facilitated due to the interface oxides-matrix [18–20]. The formation of new fresh surfaces occurs thanks to the variation in volume between the matrix and the oxide as unabsorbent species [22], promoting the cracking of the

powder, enhanced also by the presence of β-$Ti_{80}(Fe,Mn)_{20}$ [27]. It is worth noting that a more effective activation was obtained through a thermal cycle, suggesting a synergic effect between a variation in volume promoted by the hydrogenation and the different thermal expansion, especially of the $Ti_4(Fe,Mn)_2O_{0.4}$ presents in high amount and distributed along the grain boundary (Figure 1). The cracking of the powder allowed the formation of fresh surfaces to be hydrogenated, resulting in an activation procedure that still occurs in mild conditions and with only one thermal cycle, without exceeding the maximum affordable temperature and pressure of the plant.

The high amount of secondary phases and their inability to process hydrogen in the same condition of the $TiFe_{0.85}Mn_{0.05}$ industrially prepared [8], promoted a sensible reduction in the storage capacity, compared to the composition prepared at laboratory scale [6].

4.1.4 Conclusion

The $TiFe_{0.85}Mn_{0.05}$ alloy has been selected for the HyCARE hydrogen storage plant and 5 kg in form of powder were prepared at industrial level by induction melting from the parent elements from the industry GKN. It was found that the same composition prepared at laboratory [5,6], and industrial level, has a different microstructure, phase abundance and surfaces properties. These differences are caused by the synthesis itself and have a strong effect on the activation procedure, sorption capacities and thermodynamic. In detail, the activation is harder, as the powder needs to be heated and cooled in hydrogen atmosphere, and the storage capacity is significantly decreased. The thermodynamic is also affected, with a marked sloping plateau characterizing the pcT-curves, due to secondary phase abundance and sample inhomogeneity. The storage capacity is of 1.0 H_2 wt.% at 55 °C. By linking all the structural and morphological characteristics, and phase abundance with the hydrogen sorption properties observed, the hydrogen sorption behaviour during the activation process was fully understood.

Properties determined in this work can be linked to the oxygen introduced during the synthesis either from less pure Ti or from the material processing procedure. This promoted the formation of a significant fraction of oxides as secondary phases, $Ti_4(Fe,Mn)_2O_{0.4}$, and as passive layers, Ti_3Fe_3O.

It can be concluded that metal hydrides are strongly influenced by the synthesis method and the industrial production results in a different H_2 sorption behaviour that needs to be studied to understand if the material is still suitable for the final application. The mild activation

method, the fast kinetic in the defined conditions, found for the $TiFe_{0.85}Mn_{0.05}$ alloy investigated in this work, confirm its suitability as H_2-carrier for the HyCARE plant.

Acknowledgment

The project leading to this work has received funding from the Fuel Cells and Hydrogen 2 Joint Undertaking (JU) under grant agreement No 826352, HyCARE project. The JU receives support from the European Union's Horizon 2020 research, Hydrogen Europe, Hydrogen Europe Research, innovation programme and Italy, France, Germany, Norway, which are all thankfully acknowledged. A special thanks to G. Fiore for the performing of the FEG-SEM analysis.

4.2 Hydrogen - heat storage system based on metal hydride and phase change material

4.2.1 Introduction

A storage system based on MH needs a suitable heat management to operate, since hydride formation implies the production of heat (exothermic reaction), while hydrogen release requires it (endothermic reaction). Hence a thermal fluid is usually used to remove/supply heat. However, in common heat exchangers the heat is generally released to the environment, and therefore the thermal efficiency results quite poor, of the order of a few tens of percentage points, since the heat needs to be totally provided by an external power source. The heat management has an impact on the storage behaviour of the alloys, since, as much it is appropriate the heat remove/release in absorption/desorption as much can be the amount of hydrogen that can be processed, according to the thermodynamics of the equilibrium. An interesting strategy to increase the efficiency of the thermal management, as far as in hydrogen sorption properties, is to store the heat generated during the absorption, to be reused for desorption, allowing to limit the amount of waste heat and of external power. In the last decade, the use of phase change material (PCM) as latent heat thermal storage has been suggested to be an efficient solution for the heat management of MH-tanks [30]. The coupled system implies that, during absorption, the PCM stores the heat released by the MH thanks to its melting, and then, for desorption, the stored heat is released by the PCM in its solidification. The advantage of the latent heat is the storage and emission of high energy density in a close temperature range, *i.e.* the one of solidification and melting of the PCM that differ usually of few degrees [31,32]. Up to now, works in the literature refer mainly to simulations, in which it is in general highlighted the feasibility to increase the thermal efficiency above the 70 %. The scope of simulation works is to model the behaviour of a MH-PCM coupled system to understand the heat and mass transfer, investigating various tank shapes (spherical, tubular) and trying to understand the optimum design and working conditions. Some examples of 2D and 3D models are reported in ref. [33–40]. In the selection of the proper PCM, the physical properties, *e.g* melting temperature and thermal conductivity, are crucial and the latent heat should not be lowered than the reaction one [37,40]. A common proposed layout involves the two modules in close contact, with the MH surrounded by the PCM that acts like a jacket

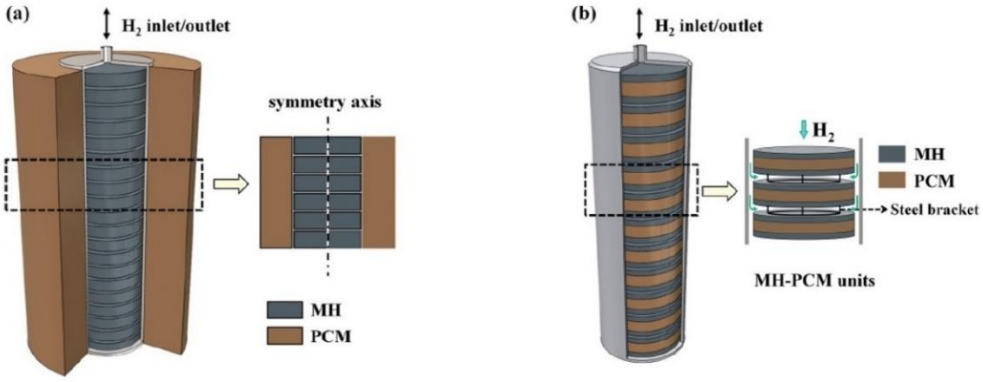

Figure 9: Representation of a MH-PCM tank taken from ref. [41]: (a) with the MH located in the inner tube, while the PCM located in the outer jacket; (b) disk shape module made of three layers: MH-PCM-MH.

(Figure 9-a). In ref. [42], pipes for the flow of a thermal vector fluid (TVF) were also added at the mentioned layout, to transfer the heat between modules. Simulations show a better heat transfer between the PCM and MH, decreasing the filling time of the 72 % compared to the use of the only PCM [42]. To increase the heat transfer and the thermal conductivity of the PCM, other works simulate the usage of pipes inside the MH-bed, and of additives at the PCM itself, like metal foams or graphite [39,43–45]. The suggested layouts often present a limited surface area for the heat exchange. So, to maximize it, an innovative layout was proposed made of a series of modules, as named sandwich configuration, in which each disk shape module consists of a three layers: MH-PCM-MH (Figure 9-b) [41].This configuration was shown to allows a fast heat transfer and in turns a high hydrogen reaction rate, resulting more promising than the conventional one, *i.e.* MH surrounded by the PCM (Figure 9-a) [46]. Another type of sandwich configuration involves the use of more than one PCM, as called at cascade PCM, that was simulated to improve the absorption and desorption rate of the 16 and 30 %, respectively, compared to one single PCM in the common layout [47]. Simulations performed evidenced the sensitivity of the MH-PCM system to the heat dissipation and to the amount of PCM, influencing the H_2 storage capacity, suggesting that a proper insulation and quantity of PCM is fundamental for the system response [33,38,46,48]. Despite a large number of simulations works, few systems have been realized up to now. The first and unique prototype of a system MH-PCM was realized by McPhy, based on MgH_2, working between 360 °C – 300 °C and 10 and 2 bar, using as PCM the $Mg_{69}Zn_{28}Al_3$ alloy [49–51]. The system stores about 7050 Nl of H_2 and involve the use of the two modules designed in close contact, with the MgH_2 present as pellets located in an inner tank, surrounded by the PCM one (like shown in Figure 9-a). McPhy used the developed storage solution for the realization of two plants, integrated with an EL and FC:

in Paglia Orba (FR) they built a plant for the storage of the order of the MWh and in Troia (IT) a plant for the storage of about 750 kg of H_2 [52].

In the frame of the HyCARE project, a prototype of hydrogen and heat storage coupled system, based on MH and PCM, respectively, will be developed and tested. The two modules are separated and connected through pipes for the flow of a TVF. This geometry has never been taken into account in simulations works. The MH selected is the $TiFe_{0.95}Mn_{0.05}$, that is suitable to be integrated with an EL upstream at a supply pressure of about 30 bar, and with an FC downstream to be supplied at about 2 bar (see section 4.1). The system works at about 50-55 °C, close to the melting/solidification temperature of the selected PMC, *i.e.* the CrodaTherm53. The goal of the work is to demonstrate the feasibility of the MH-PCM coupled system, and to individuate the optimal operative conditions to apply in the final HyCARE demonstrator plant, trying to minimize the contribution of an external power. For the first time, a TiFe-based compounds is considered as MH, since, so far, simulations have been performed taking into account Mg-based hydrides or $LaNi_5$-compounds, and it is the first prototype PCM-MH realized for mild temperature applications.

4.2.2 Experimental set-up

The integrated prototype PCM-MH system is set-up as shown in Figure 10. The PCM module was realized by the Italian industry Tecnodelta in Chivasso, while the MH tank was set up by the German industry Sthüff in Geesthacht.

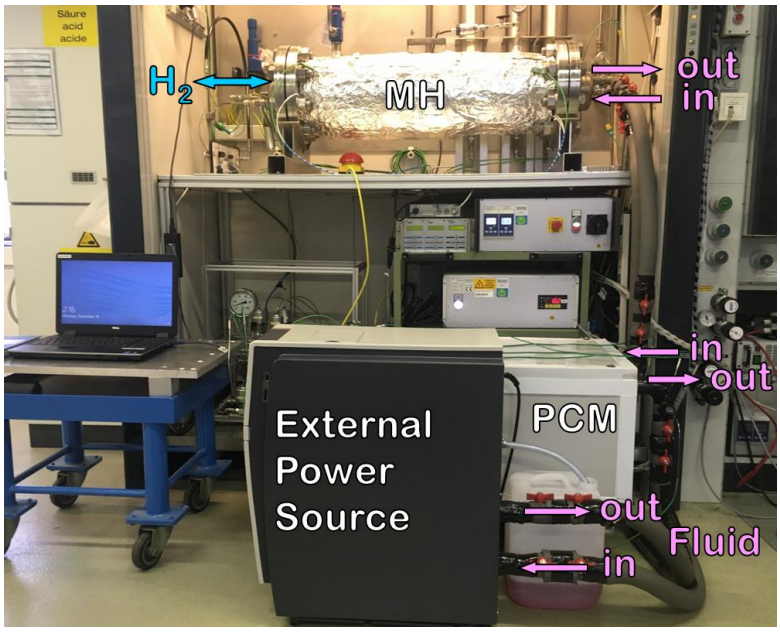

Figure 10: Set-up of the PCM-MH coupled system with the EPS.

An external power source (EPS) is used to circulate the TVF in the system and to control its temperature. The EPS can contribute by heating and cooling the TVF with a maximum power of 2.7 and 1.2 kW, respectively. The fluid flows from the EPS to the MH, then from the MH to the PCM and finally returns to the EPS. The flow is controlled by setting the pressure level in the EPS, resulting in different flowrates depending on the pressure drop of the circuit, and it is measured by a liquid flowmeter placed between the EPS and the MH unit. As thermal fluid, a mixture of water and ethylene-glycol 70 : 30 was used.

The prototype has about 1/5 of the size of the final HyCARE demonstrator, that consists of 12 modules each for PCM and MH, each about 4 - 5 m long. Concerning the prototype, the PCM module involves 24 square aluminium profiles (Figure 11-a) realized in Al 6060 T6 and it is 0.7 m long. Each profile is formed by a central circular tube (Ø 18 mm) and 8 square channels (side equal to 18 mm). The central hole allows the passage of the TVF, while square passages contain the PCM. The TVF flow is divided into two different paths to reduce the pressure drop. The aluminium system is located inside a stainless-steel case and filled entirely with the PCM. Finally, the system is insulated to limit heat dissipation with the environment. As PCM, the CrodaTherm53 was selected, that is an organic, not toxic material and about 60 kg are located inside the PCM module. Six temperatures inside the PCM are monitored thanks to thermocouples placed as shown in Figure 11-a ($T1^{PCM}$-$T6^{PCM}$). Thermal fluid inlet and outlet occur from the same side and thermocouples registered its temperature (Tin^{PCM} and $Tout^{PCM}$). As can be seen from Figure 11-a, for the PCM, the temperature closer the inlet of the TVF is $T1^{PCM}$, while that closer to the outlet is $T6^{PCM}$. The MH-module consists of a tube of 6 inch in diameter, about 1 m long, realized in stainless steel AISI 316T. The H_2-carrier, *i.e.* the$TiFe_{0.85}Mn_{0.05}$, is present in form of 24 pellets, with a disk shape (Figure 11-b). About 50 kg of alloy containing a 20 % of a binder, necessary for pellets manufacturing, were provided by the German industry GKN. The alloy was activated with the activation recipe developed during alloy characterization at laboratory scale, described in the previous section 4.1. As expected, some discrepancy occurs due to the dimension of the system moving from the laboratory to the prototype level, but the methodology of the thermal cycle is maintained. Firstly, six flush with Ar at 10 bar and 25 °C were performed to remove the initial atmosphere (vacuum cannot be applied), followed by the heating of the system up to 90 °C, the load of 50 bar of H_2, and the final cooling in hydrogen atmosphere to 25 °C. Then, while the system was warmed up to the operative temperature of about 50 °C, the hydrogen was removed, promoting the desorption from the MH. Based on results of

the alloy characterization, about 0.5 kg of H_2 is expected to be stored. Thanks to thermocouples, as shown in Figure 11-b, five temperatures are registered inside the MH-bed ($T1^{MH}$-$T5^{MH}$) and at the inlet and outlet of the TVF (Tin^{MH} and $Tout^{MH}$).

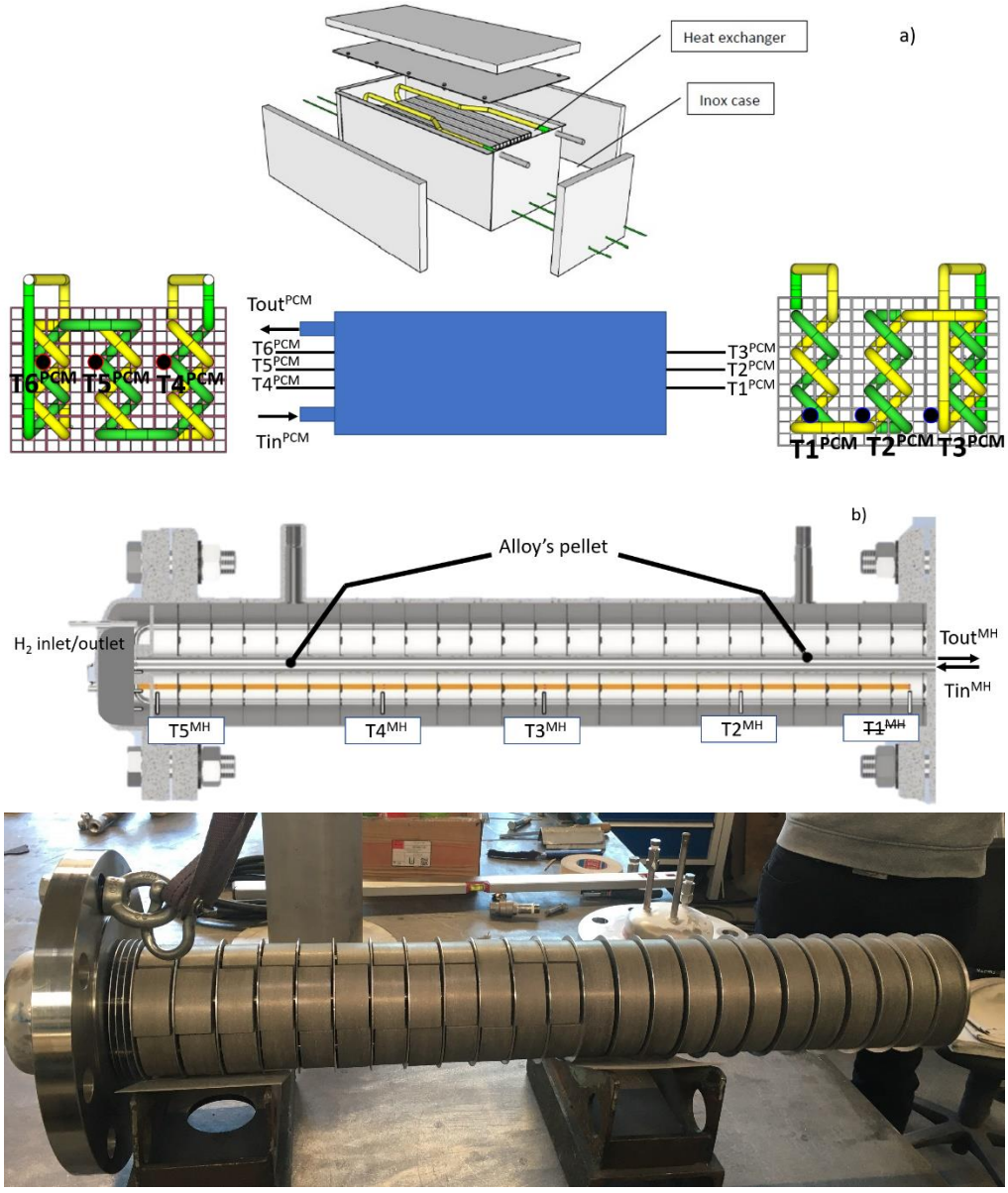

Figure 11:(a) PCM module and thermocouples named and position; (b) MH-tank representation with thermocouple position together with a picture of the 24 pellets of the alloy.

According to tank design, as can be seen from Figure 10 and Figure 11-b, the TVF inlet and outlet occurs from the same side. Hydrogen inlet and outlet occurs also from the same side, but opposite to TVF one and it is regulated thanks to flowmeters and pressure is monitored thanks to sensors. $T1^{MH}$ is not available, due to a broken connection; $T2^{MH}$ is close to the inlet of the thermal fluid, while $T5^{MH}$ is inside the opposite flange, close to the inlet of H_2.

The H_2 uploading (absorption) occurs at about 30 bar, while the downloading (desorption) at about 2 bar, according to the plant operative conditions defined for the selected alloy (section 4.1). The H_2 flows is governed by flowmeters and performed tests occurred at different H_2 flowrates:

- 160 Nl/min, *i.e.* the maximum available flow from the EL in the final HyCARE demonstrator.
- 80 Nl/min, corresponding to half of the maximum flow.
- 32 Nl/min, that is 1/5 of the maximum flow, since the prototype size is about 1/5 of the final module.

According to the selected H_2 flowrates, the flow of the TVF was calculated to properly manage the maximum power developed/required to have a difference in temperature between MH and PCM modules of approximately 7 °C. This boundary condition implies:

- 160 Nl/min of H_2 6 l/min of TVF
- 80 Nl/min of H_2 3 l/min of TVF
- 32 Nl/min of H_2 1 l/min of TVF

The parameters evaluated to individuate the optimal operative conditions are the external power contribution, started working temperature, as well as H_2 and TVF flowrates. Table 5 lists the experiments performed and the applied conditions.

Table 5: Experimental conditions and analysis performed.

Measure Label	**H_2 pressure bar**	**Max H_2 flow Nl/min**	**Fluid flow l/min**	**Ext. power**	**Tstart PCM °C**
C1	30 – 2	160	~ 6.4	Heating/cooling	50/51
C2	30 – 2	160	~ 6.4	-	50
C3	30 – 2	160	~ 3.3	-	~ 50
C4	30 – 2	160	~ 3.3	Heating	~ 50
C5	30 – 2	160	~ 6.4	Heating	~ 50
C6	30 – 2	160	~ 6.4	Heating	52
C7	30 – 2	160	~ 3.3	Heating	52
C8	30 – 2	80	~ 3.3	Heating	52
C9	30 – 2	32	~ 1.2	Heating	52
C10	30 – 2	160	~ 1.4	Heating	52
C11	30 – 2	(fixed) 160	~ 6.4	Heating	52
C12	30 – 2	(fixed) 32	~ 3.3	Heating	52

4.2.3 Results and discussion

4.2.3.1 Role of the EPS

C2 and C3 were performed without any external heat supply, with the heating element of the EPS switched off, to investigate whether the coupled system was able to operate only by recovering and using the heat of reaction. Figure 12 shows the temperature profiles of the TVF at the inlet and outlet of the PCM. As can be seen, the two tests were not successful, since the system is already cooling down during absorption (120 min). Points indicates the end of the absorption which differs from C2 (360 min) and C3 (960 min), since in the latter experiments the absorption was performed overnight. Temperatures are dropping reaching room temperature, during desorption in C2 or even during the absorption in C3. The rise in temperature observed at about 960 min is linked to the switching on of the EPS.

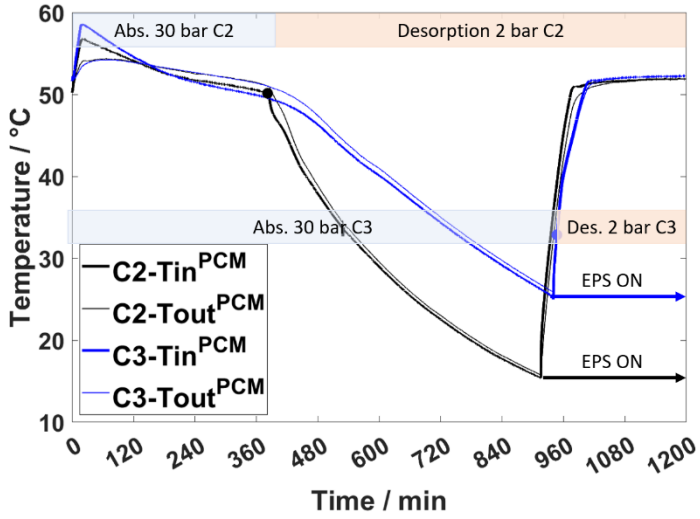

Figure 12: Temperature profile of the thermal fluid at the inlet and outlet of the PCM in measure C2 and C3. The point indicates the end of absorption that is highlight with colour bars.

These results suggest that an external power is fundamental. Indeed, only exploiting the reaction, the system is not able to work, and the EPS needs to prevent the full cooling of the PCM and the starting of its solidification already during hydride formation.

4.2.3.2 Optimization of the temperature control by the EPS

In the following, it is presented how the contribution of the EPS was optimized in managing the temperature of the process. For this purpose, measures C1, C5 and C6 are considered as an example, since they occur at the same H_2 flowrate (160 Nl/min) and TVF flow (6.4 l/min). At the base of the optimisation process there is the goal to minimize the EPS contribution in

managing the temperature of the system. Indeed, thanks to a thermostat and a setpoint, the EPS can contribute to the system, *i.e.* with a setpoint temperature below/above the inlet of the EPS (outlet of the PCM) there is not heating/cooling contribution and the circulator just dissipate heat. While, when temperature goes down/up to the setpoint, the EPS contribute with heating/cooling power. Then, the PCM is storing energy melting, and it occurs when the inlet temperature of the TVF at the PCM-module (Tin^{PCM}) remains higher than its melting one, *i.e.* 53 °C, and higher than the outlet one ($Tout^{PCM}$). This process needs to occur only in absorption, while, when the opposite happens, the PCM is releasing heat, starting solidifying, process that must occur only in desorption. To start the solidification, Tin^{PCM} must go below 53 °C and this happens thanks to the endothermic nature of the release of H_2 by the MH. The phase change implies a constant outlet $Tout^{PCM}$, and, when the process is finished, the outlet temperature starts to follow the profile of the inlet one, Tin^{PCM}.

4.2.3.2.1 C1: EPS power in heating and cooling

Figure 13-a shows the amount of H_2 absorbed and desorbed as a function of time, together with $T2^{MH}$ and $T5^{MH}$ in absorption (b) and desorption (c). The amount of H_2 absorbed is about 1.13 H_2 wt.% at 30 bar. Desorption occurs at 2 bar releasing H_2 until the amount left in the material is displayed as 0.15 H_2 wt.%. In this measure the temperature set at the EPS in absorption is 53 °C, while in desorption it is 50 °C. Considering the temperatures inside the MH-bed (Figure 13-b, c), it is possible to notice a marked difference between $T2^{MH}$ and $T5^{MH}$, especially in absorption. Other temperatures ($T3^{MH}$ and $T4^{MH}$) display values like $T2^{MH}$ and are not reported. $T5^{MH}$ is colder than $T2^{MH}$ of 25 °C, since it is located inside the flange and far from the TVF inlet (Figure 11-b). The flange is colder compared to the rest of the system, and so the pellet located inside of it remains colder than the others. Moreover, from that side, H_2 is inserted (Figure 11-b) at about 10 °C, sensitively lower than about 55 °C of the reaction (storage of hydrogen bottle out from the room). These considerations are valid for all measures.

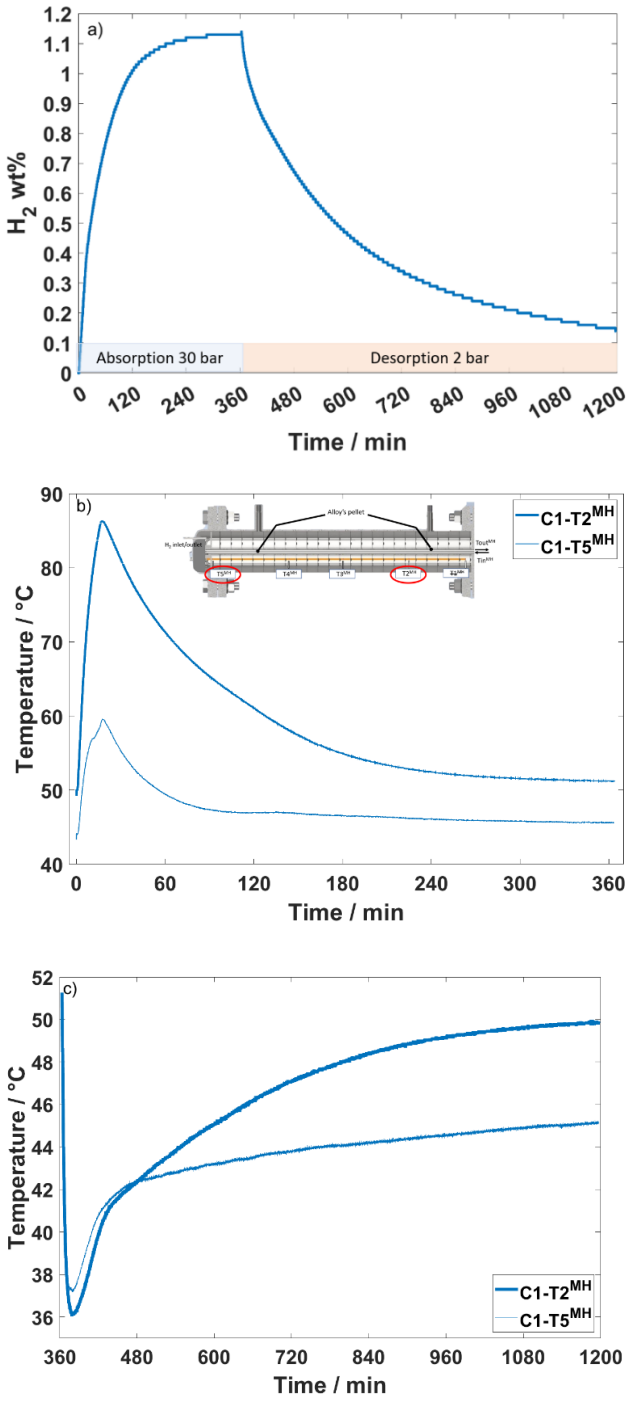

Figure 13: For measure C1 (a) Amount of H_2 abs. and des. in wt.% as a function of time; (b) $T2^{MH}$ and $T5^{MH}$ in absorption; (c) $T2^{MH}$ and $T5^{MH}$ in desorption. The insert in (b) is to remind the placement of the thermocouples to measure $T2^{MH}$ and $T5^{MH}$ that are highlighted with red circles.

Absorption is exothermic and causes a local increase in temperature of the MH-bed, as can be seen from Figure 13-b, reaching a peak in temperature of 86 °C. This implies a rise in temperature of the TVF at the outlet of the MH-tank ($Tout^{MH}$), *i.e.* at the inlet of the PCM one (Tin^{PCM}), as can be observed from Figure 14-a, c, respectively. This effect allows the PCM melting and the storage of the heat of reaction and this phenomenon is observed in

each measure performed. The TVF temperature profiles at the inlet and outlet of the MH and PCM modules (Figure 14-a, c) are comparable with that observed inside the MH-bed (Figure 13-b). There is a difference in temperature of almost 30 °C between the $T2^{MH}$ and $Tout^{MH}$, with about 10 °C between Tin^{MH} and $Tout^{MH}$ (comments valid also for the other measures).

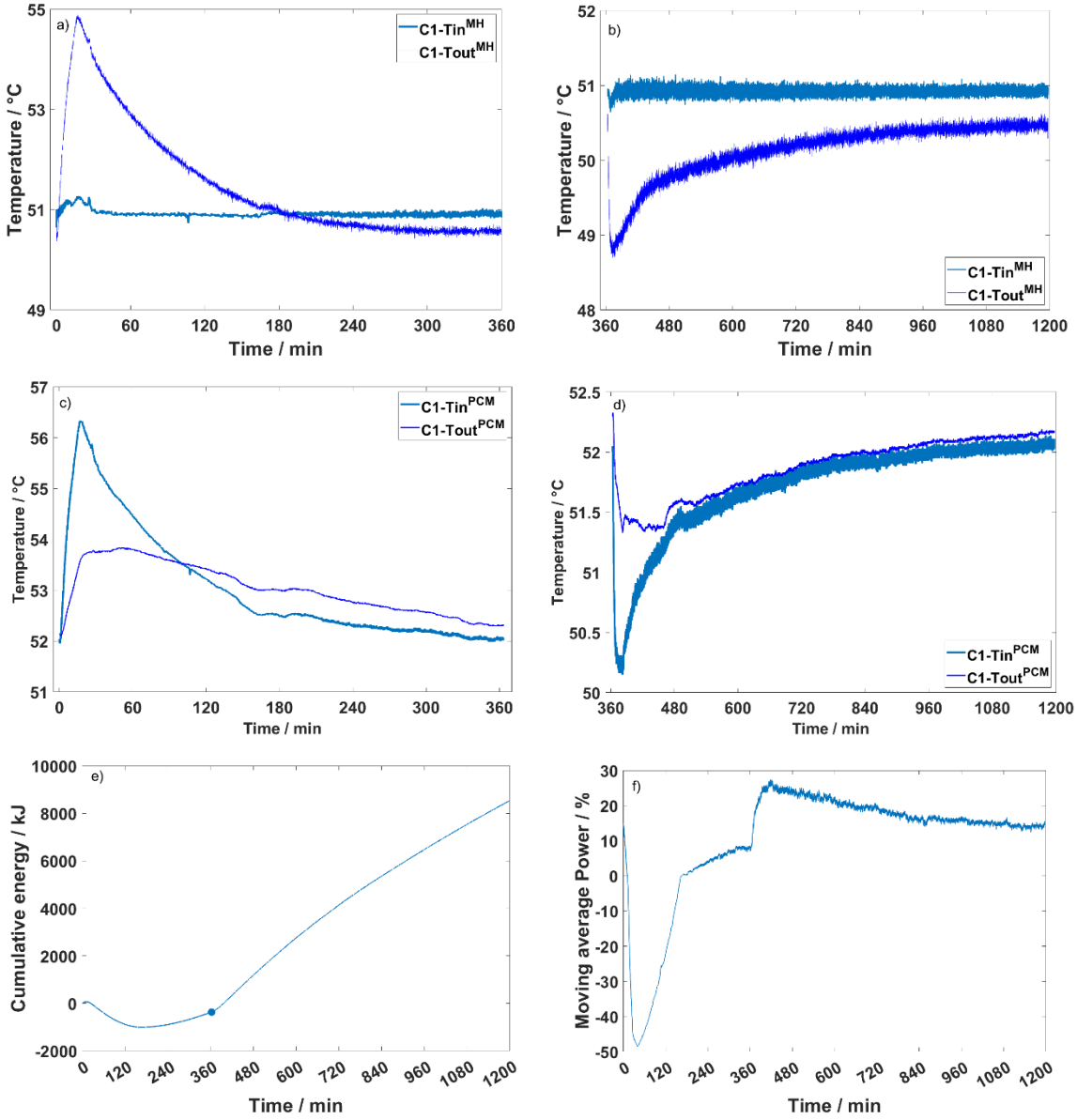

Figure 14: For measure C1: (a) Tin^{MH} and $Tout^{MH}$ as a function of time in absorption; (b) Tin^{MH} and $Tout^{MH}$ as a function of time in desorption; (c) Tin^{PCM} and $Tout^{PCM}$ as a function of time in absorption;(d) Tin^{PCM} and $Tout^{PCM}$ as a function of time in desorption; (e) Cumulative energy as a function of time, with a point that highlights the end of absorption; (f) EPS moving average power % as a function of time made on 60 values.

The rise in temperature of the TVF, causes a cooling contribution of the EPS to stabilize the temperature at about 53 °C (EPS temperature of setpoint). This implies a constant Tin^{MH}, that however is lower than the set temperature and equal to 51 °C (Figure 14-a). This discrepancy is due to the poor internal insulation of the EPS, implying heat dissipation. The

power contribution of the EPS is visible by reporting the cumulative energy of the EPS and the moving average made on 60 values of the percentage of the EPS power, as a function of time in Figure 14-e, f, respectively (points remark the end of absorption). The cooling power contribution is underlined by negative values and the EPS contributes for the entire duration of the absorption process. This is a drawback for the melting of the PCM as well as in the storage of the heat of reaction. Indeed, the PCM already starts solidifying during the absorption, since at about 100 min Tin^{PCM} and $Tout^{PCM}$ lines cross each other. The active contribution of the EPS in keeping a constant temperature decreases the temperature of the system and this does not allow reaching suitable temperatures to transfer enough heat to the PCM, keeping/promoting its melting.

The endothermicity of desorption causes a local decrease in temperature of the MH-bed (Figure 13-c), followed by the thermal fluid at the outlet of the MH-tank (Figure 14-b) and consequently at the inlet of the PCM (Figure 14-d). However, due to the solidification of the PCM in absorption, there is a constant contribution of the EPS with power in heating to face the endothermicity of the process and avoiding the system cooling. (Figure 14-e, f).

This test highlights the importance to have an EPS that contributes only with heating power to have the right procedure of the process with the storage of the heat in absorption. This setup is used in McPhy devices [49,51] and represents the one planned in the HyCARE final demonstrator.

4.2.3.2.2 C5: EPS power heating

In this measure the power of the EPS is limited only in heating, by setting a temperature of setpoint of 53 °C in absorption. For desorption the setpoint at the EPS is 50 °C. Figure 15-a shows the amount of H_2 absorbed and desorbed as a function of time. In absorption a gravimetric capacity of 1.11 H_2 wt.% is reached, while desorption goes until a 0.20 H_2wt.% is left inside the material. To notice is that, in measure C1 compared with measure C5 (Figure 13-a and Figure 15-a), when leaving 6 h in C1 to reach a stable capacity, the amount processed is increased just of 0.02 H_2 wt.% than in C5. It suggests that it is better to limit the time in absorption at about 3 h - 4 h instead of waiting until a stable capacity is reached.

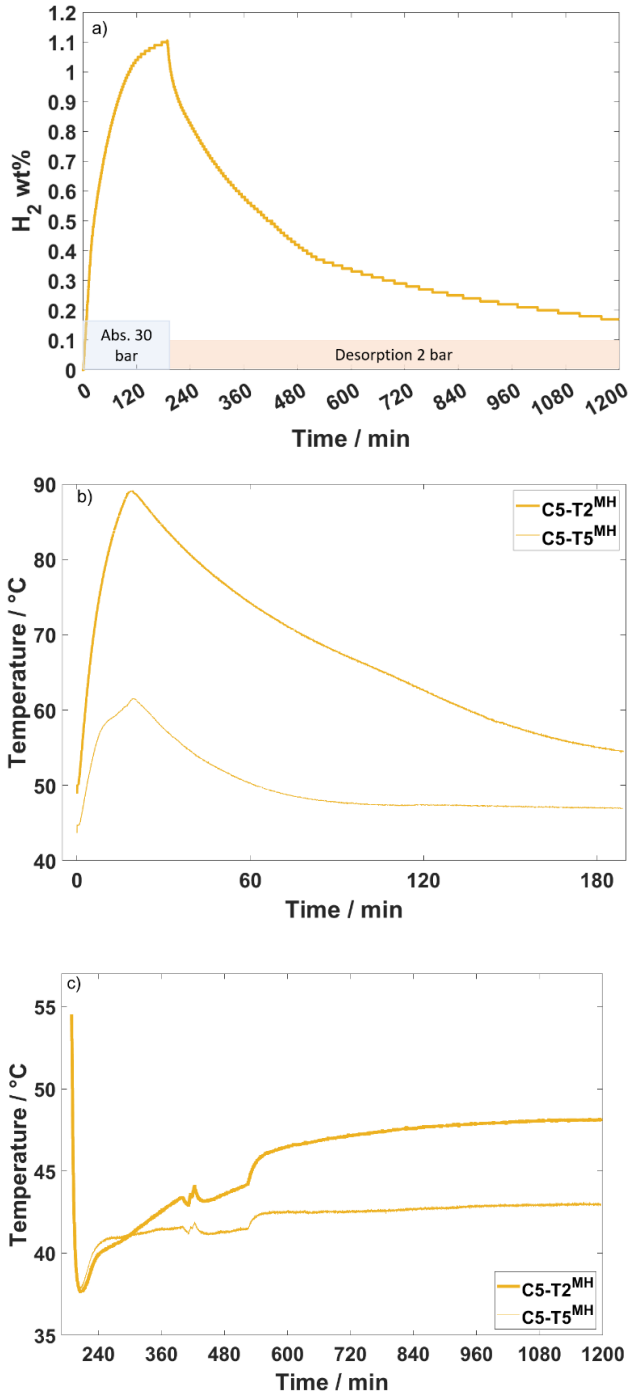

Figure 15: For measure C5 (a) Amount of H_2 abs. and des. in wt.% as a function of time; (b) $T2^{MH}$ and $T5^{MH}$ in absorption; (c) $T2^{MH}$ and $T5^{MH}$ in desorption.

The absence in the cooling power of the EPS to face the increase in temperature caused by absorption, is evident registering a peak in temperature of $T2^{MH}$ of 89 °C (Figure 15-b), slightly higher than in C1 (86 °C). Then, a slower cooling down in temperature of the MH-bed and in turns on the TVF is observed, as can be seen following the temperature profiles

of $Tout^{MH}$, Tin^{PCM} in Figure 16-a, c. This allows to transfer the heat from the MH to the PCM, promoting its melting, thanks to Tin^{PCM} higher than $Tout^{PCM}$ (Figure 16-c). However, after 130 min, the two curves cross each other, suggesting that in the last part of the absorption reaction the solidification of the PCM is already starting. The natural cooling of the system is due to the lower amount of H_2 that is reacting, releasing an amount of heat not sufficient to keep the PCM warm.

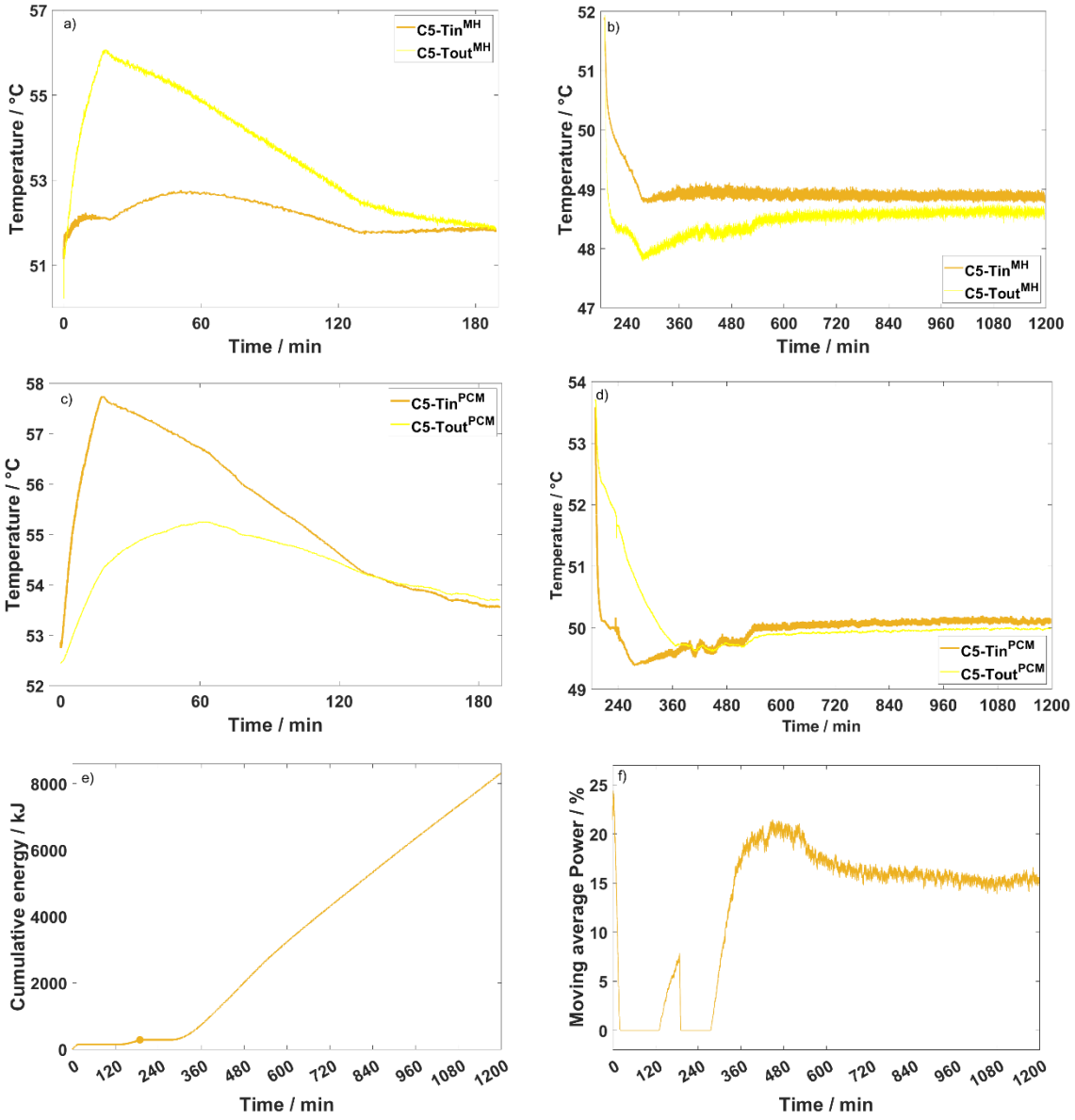

Figure 16: For measure C5: (a) Tin^{MH} and $Tout^{MH}$ as a function of time in absorption; (b) Tin^{MH} and $Tout^{MH}$ as a function of time in desorption; (c) Tin^{PCM} and $Tout^{PCM}$ as a function of time in absorption;(d) Tin^{PCM} and $Tout^{PCM}$ as a function of time in desorption; (e) Cumulative energy as a function of time, with a point that highlight the end of absorption; (f) EPS moving average power % as a function of time made on 60 values.

By following the power contribution of the EPS through the cumulative energy of the EPS and the moving average made on 60 values of the percentage of the EPS power (Figure 16-

e, f), it is possible to see how, in the first part of absorption reaction, the EPS contribution is absent. While from 130 min, it is actively contributing with heating power to face the cooling down of the system.

Desorption occurs thanks to the heat released by the PCM, supplying the MH. Indeed, $Tout^{PCM}$ is higher than Tin^{PCM}, as far as the Tin^{MH}. Some discrepancies occur between Tin^{PCM} and Tin^{MH}, because the EPS is placed in the middle of them, behaving both as a heat sink (due to poor internal insulation) and/or as an active heating element. By following the power contribution of the EPS in desorption (Figure 16-e, f), it can be seen that in the primary stage of reaction, the EPS contribution is zero and the heat management of the MH-tank is totally performed by the PCM, thanks to its solidification. When the phase transformation is finished, $Tout^{PCM}$ and Tin^{PCM} tend to be aligned. Since desorption lasts about 18 h, the EPS supports the process, not allowing the PCM to cool down excessively during the last period of the reaction, as observed in section 4.2.3.1 with the EPS power switched off.

This measure shows the feasibility of the PCM in managing the heat of the MH, observing an EPS contribution, that is limited in heating, only in the final part of the sorption reactions. Indeed, the EPS is fundamental to maintain the system warm, since the heat flow of reaction developed in the last fraction of reactions is low because of the small amounts of H_2 absorbed/released.

4.2.3.2.3 C6: EPS power heating and rise in temperature

The experiments C5 and C6 were both performed with the EPS acting only on heating, but in the measure C6 a strategy was developed to avoid the starting of the crystallization of the PCM in the last fraction of absorption, as observed in measure C5.

Figure 17-a shows the amount of hydrogen absorbed and desorbed at 30 bar and 2 bar, respectively, as a function of time. Results are comparable with measures C1 and C5. In absorption the peak in temperature registered for $T2^{MH}$ is equal to the one observed in C5, *i.e.* 89 °C (Figure 17-b). Before starting the absorption process, the system is kept at 52 °C instead of 50 °C as occurred in measure C5 (Table 5). 52 °C is a temperature close to the melting temperature of the PCM, implying a PCM closely or presumably even partially melted. While at 50 °C (C5) the PCM is totally solidified. The starting temperature of 52 °C allows to store the heat more efficiently, as it can be seen comparing the $Tout^{PCM}$ curved of measure C5 (Figure 15-c) and C6 (Figure 18-c). Indeed, in measure C6 it is possible to have

a flat $Tout^{PCM}$ for a longer interval of time than in measure C5. This implies a higher fraction of PCM melted, as well as heat stored.

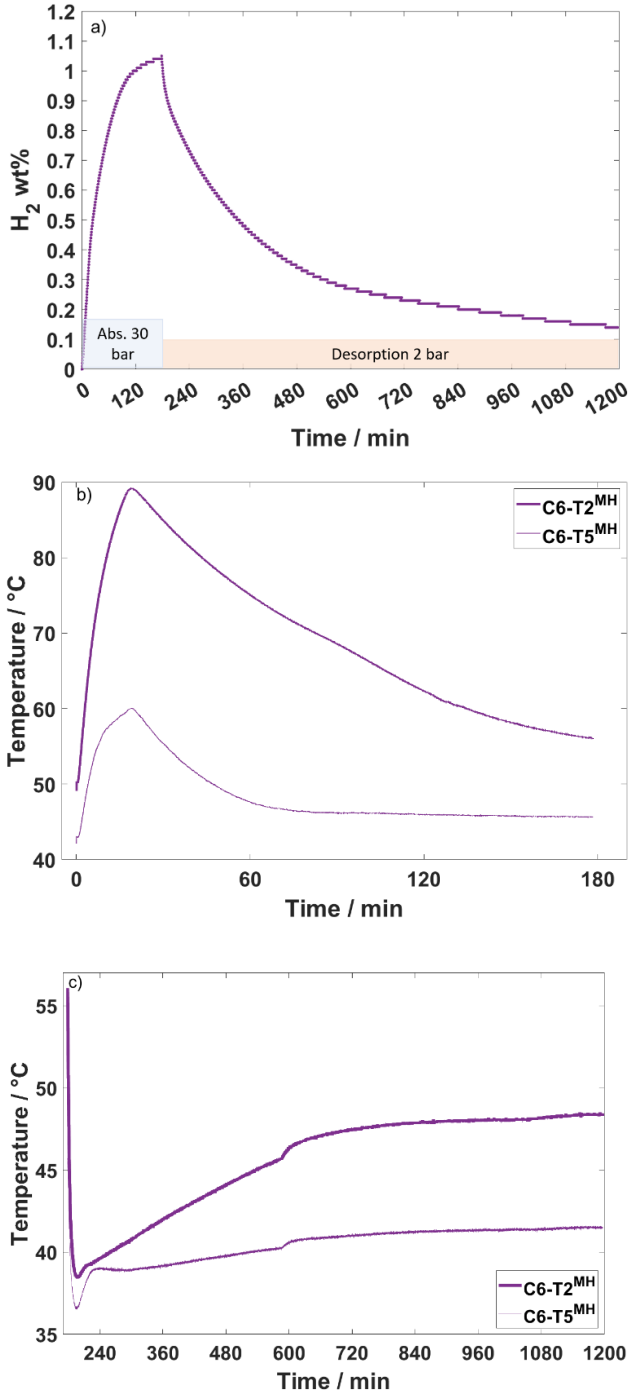

Figure 17: For measure C6 (a) Amount of H_2 abs. and des. in wt.% as a function of time; (b) $T2^{MH}$ and $T5^{MH}$ in absorption; (c) $T2^{MH}$ and $T5^{MH}$ in desorption.

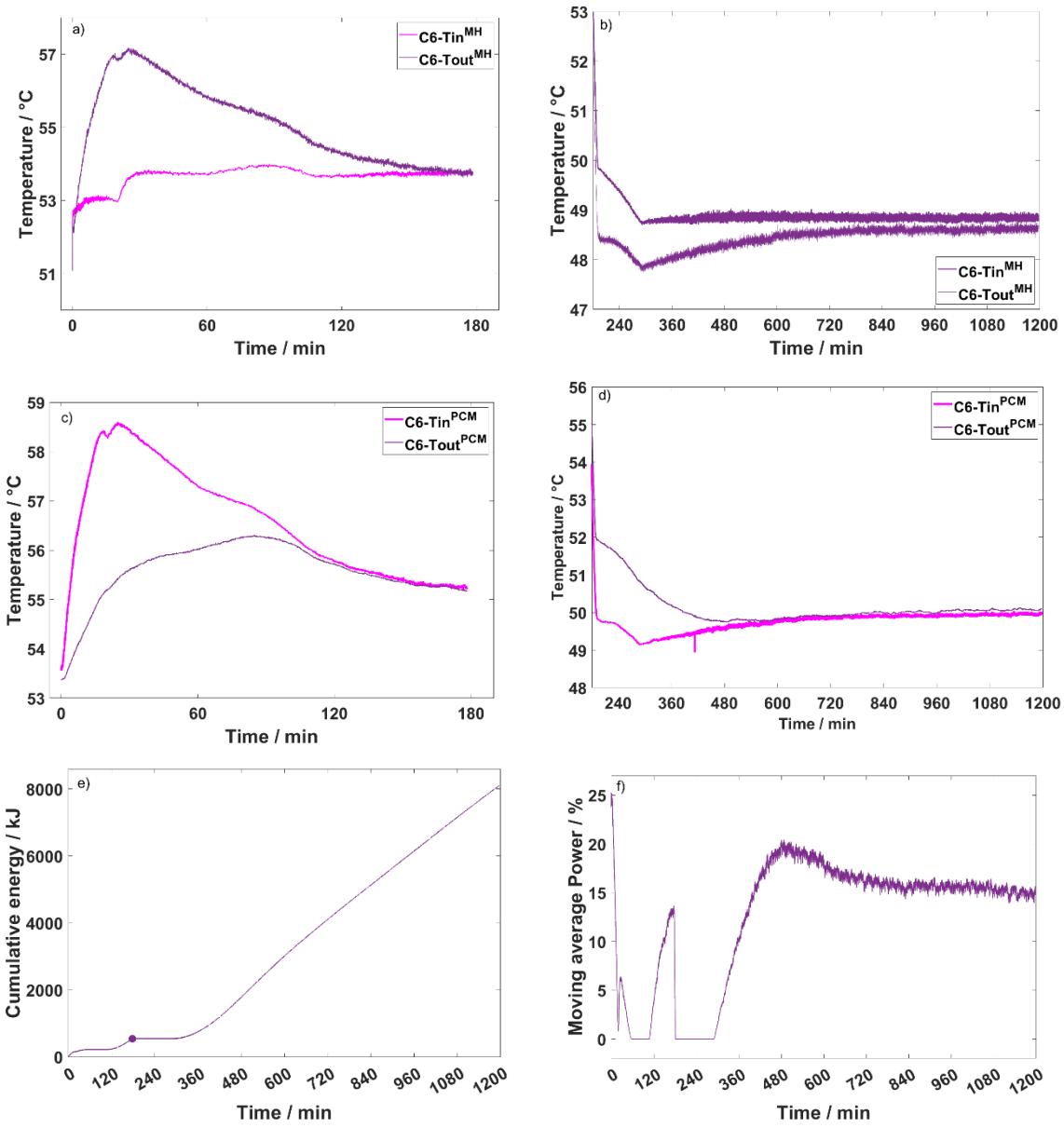

Figure 18: For measure C6: (a) Tin^{MH} and Tout^{MH} as a function of time in absorption; (b) Tin^{MH} and Tout^{MH} as a function of time in desorption; (c) Tin^{PCM} and Tout^{PCM} as a function of time in absorption;(d) Tin^{PCM} and Tout^{PCM} as a function of time in desorption; (e) Cumulative energy as a function of time, with a point that highlight the end of absorption; (f) EPS moving average power % as a function of time made on 60 values.

To allow the melting of the PCM just thanks to the heat of reaction, the set point at the EPS in the primary stage of the reaction was fixed at 54 °C, *i.e.* 1 degree more than the melting temperature. Indeed, in measure C5, with a setpoint of 53 °C, the system cools down during absorption, and, as previously stated, the EPS could determine heat losses, implying even lower temperature at the Tin^{MH}, as observed in measure C1. To slow down the progressive cooling of the TVF, to prolong the time in which Tin^{PCM} is higher than Tout^{PCM}, the set point temperature of the EPS is increased by 1 °C, approximately when the system reached the maximum of the peak in temperature. Prolonging the time in which Tout^{PCM} and Tin^{PCM} are

different from each other, the melting of the PCM is guaranteed, avoiding the beginning of the solidification until it is not required, as was observed in measure C5. The effectiveness of these strategies applied in measure C6 is visible by following the temperature profiles of the TVF registered at the inlet and outlet of the MH-tank and PCM module (Figure 18-a, c). Indeed, Tin^{PCM} and $Tout^{PCM}$ never cross during the entire duration of the absorption reaction, assuring the melting of the PMC, even in the last fraction of reaction. Then, even if the slowing down in temperature inside the MH-bed of $T2^{MH}$ is comparable in both measure C5 and C6, the slowing down of the TVF ($Tout^{MH}/Tin^{PCM}$) is slower in C6 compared to C5. However, the EPS contribution in absorption, in the last part of the reaction is higher in measure C6 than in C5, due to the increase in temperature (Figure 18-e, f and Figure 16-e, f). In desorption, the process results to be sustained for a longer time by the PCM in measure C6 than in C5, as can be seen comparing the power contribution in desorption of the EPS, respectively Figure 18-e, f and Figure 16-e, f. Indeed, maintaining the PCM totally melted for the entire duration of the absorption process, it assures the released of the heat only in desorption. While in measure C5 already in the last period of absorption some heat was lost because of the crystallization of the PCM. The effectiveness of the strategy in desorption can be seen from the temperature profiles of the TVF registered at the MH and PCM modules, Figure 18-b, d.

In conclusion the strategy applied in measure C6 compared to measure C5 assures the full melting of the PCM in absorption, avoiding any solidification. This is advantaging in desorption, allowing to prolong the time in which the PCM is realising the heat to supply the MH-tank. The EPS contribution is fundamental in heating to maintain the system warmed in the last fraction of both reactions, but in particular in desorption, since it lasts for a longer time than absorption. It is to evidence that the change in strategy applied from C5 to C6 doesn't affect the exothermicity and endothermicity of the reaction, that is only linked to the hydrogen flow, registering similar temperature profiles for the MH-bed, $T2^{MH}$ and $T5^{MH}$. The strategy developed to perform measures C6 was then applied in all other experiments, *i.e.* C7-C12.

Finally, in measure C6, pictures were taken at the PCM at the end of absorption and during desorption. In absorption (Figure 19-a), the PCM is totally melted only in the zones in close contact with the heat exchange parts, *i.e.* the pipes and the aluminium profiles, highlighted with red circles, while it remains solid in the rest of the stainless-steel case. The same occurs in desorption (Figure 19-b), in which the crystallization starts immediately in the parts in

contact with the pipes, moving towards the rest of the melted region.

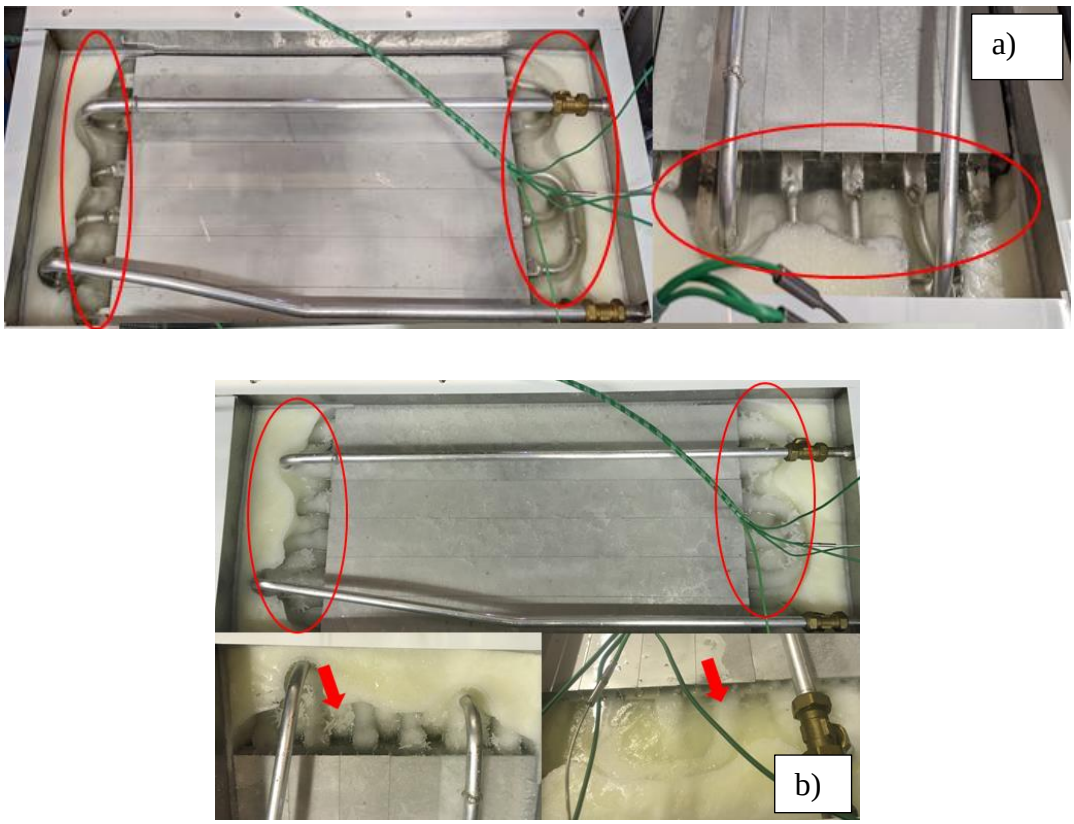

Figure 19: Pictures of the PCM (a) melted after H_2 absorption; (b) during solidification in H_2 desorption.

4.2.3.2.3.1 C6 measures repetition

Measure C6 was repeated for three times. Results present previously linked to the measure C6, in this section refers to the measure labelled third repetition. Figure 20-a reports the amount of hydrogen absorbed and desorbed as a function of time for the three repetitions.

In absorption, the slight discrepancy observed is linked to an ending of the constant flow regime in different timing in repetition (rep.) 3, and to a different timing between rep. 1 and 2. Then difference among the 3rd and the other two repetitions can be linked to an incomplete desorption during the previous measure too. When starting a new measure, the gravimetric capacity is always reset to zero, not considering the small hydrogen amount remained from the previous measure. The desorption is displayed as incomplete in all measures.

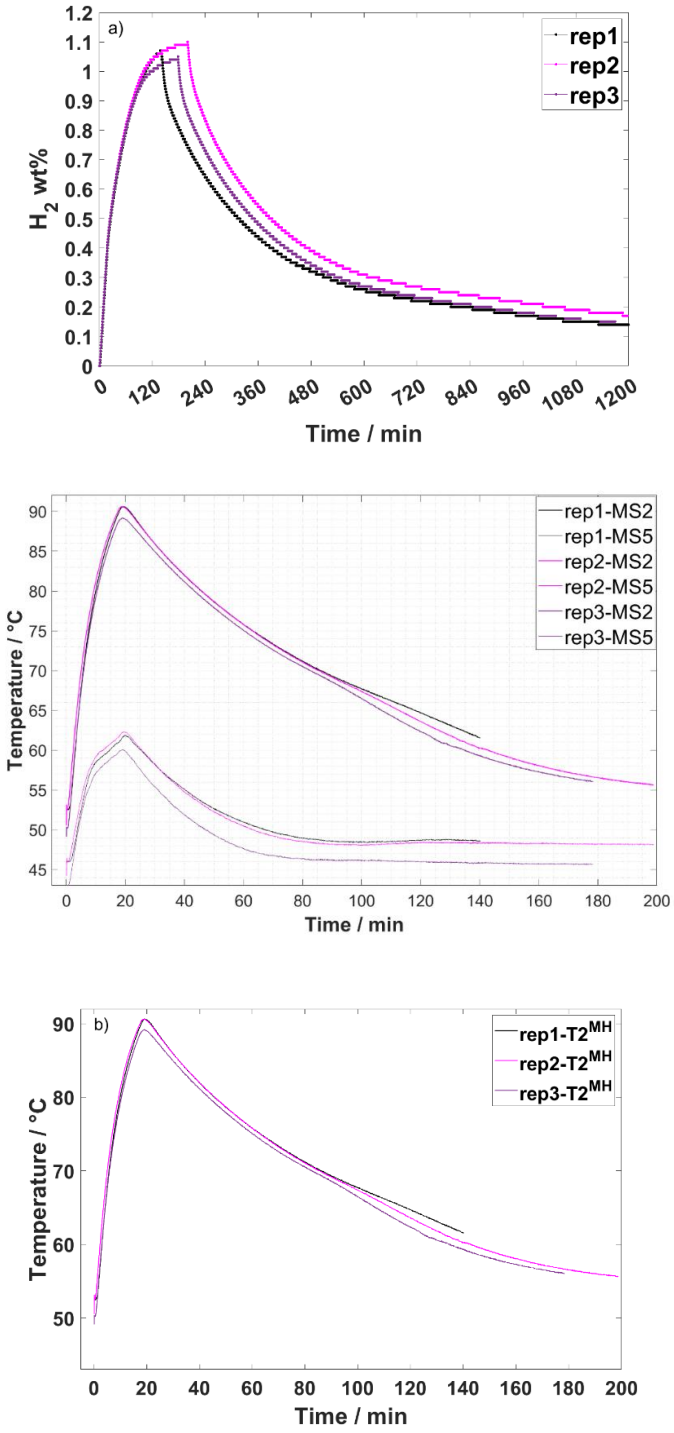

Figure 20: For the three repetitions of measure C6 (a) gravimetric capacity of the system as a function of time absorption and desorption; (b) $T2^{MH}$ as a function of time and (c) Tin^{PCM} and $Tout^{PCM}$ as a function of time in absorption.

The lower amount of H_2 absorbed implies in the 3rd measure the development of less heat of reaction, reaching a peak in temperature of $T2^{MH}$ of 89 °C compared to 90.5 °C of the 1st and 2nd one (Figure 20-b). In the third measure, Tin^{PCM} (*i.e.* Tin^{MH}) is colder too, as it is shown in Figure 20-c. The $Tout^{PCM}$ is kept more constant in repetition 1 and 2, compared to rep. 3.

Moreover, in rep. 2 and 3 the increase in temperature of 1 °C was made already during system cooling and so two peaks can be observed, Figure 20-c. While in the first repetition the increase was made exactly during the peak and so two distinct peaks in temperature are not visible. In rep.1 is possible to maintain a higher temperature for more time and a slower cooling profile than in the other cases. Independently for the period in which the increase of temperature occurs, in rep. 1 and 2, the melting of the PCM has the same duration, while in rep. 3, it seems that the change of phase ends about 25 min earlier (Figure 20-c).

The difference in the heat flow released by the reaction might have an impact on the contribution of the EPS. Indeed, as it can be seen from the cumulative energy and the moving average of the EPS power a function of time, (Figure 21-a, b, respectively) in absorption, the EPS contribution is almost absent in rep. 1. On the contrary, in rep. 2 and 3 it is possible to notice a small contribution of the EPS, with a higher contribution at the end of the process, when the system is approaching 54 °C. Then, the absorption in rep. 2 lasts more than in rep. 1, and a higher EPS contribution is observed in rep. 2 than in rep.1. This depends on the lower amount of heat flow developed in the final part of the process, with a low H_2 flowrate. These considerations are fundamental, since, if the increase of temperature of 1 °C is performed exactly at the maximum exothermicity and if the reaction is limited in time without succeeding a fully absorption, the contribution of the EPS can be totally eliminated for the entire duration of the reaction, even in the last fraction.

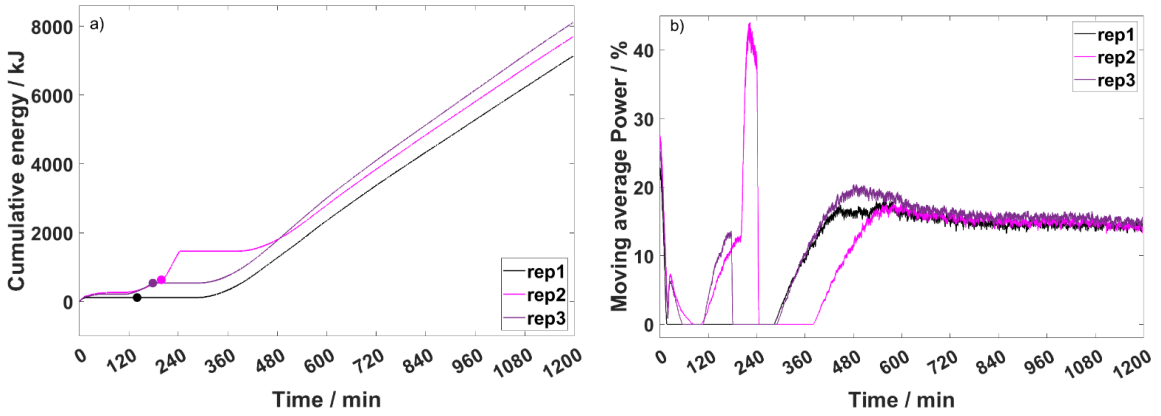

Figure 21: (a) cumulative energy as a function of time, with points highlighting the end of absorption; (b) moving average of the EPS% power as a function of time made on 60 values.

Temperature curves for desorption are not reported since they are similar to the one reported in section 4.2.3.2.3. Concerning the EPS contribution in desorption, it is absent in the first part of reaction, followed by a constant contribution for the last part of the process, as discussed in the previous section. In repetition 2, it is possible to notice an EPS contribution

in the first part of desorption, linked to a practical error.

In conclusion, from the same setup of thermal fluid flow and H_2 flow, a small delay in the increase of temperature results in a higher energy request to the EPS. Moreover, increasing the final amount of H_2 stored from 1.07 wt.% (rep. 1) to 1.09 wt.% (rep. 2) a higher contribution of the EPS is required in the final parts of absorption, since the heat of reaction is no more sufficient. Results suggest that achieving a complete absorption in the MH does not just mean reaching slightly lower temperatures in the system and letting the desorption starts at not optimal conditions, but it may even remove heat from the PCM unit or consume energy from the EPS.

4.2.3.3 Influence of the hydrogen and TVF flow

4.2.3.3.1 Consideration on H_2 flow controller

Three H_2 flowrates of *i.e.* 160 Nl/min, 80 Nl/min and 32 Nl/min. (Table 5) are considered. For the latter two flows, measures C8 and C9 are evaluated, and results are compared with measure C6 (section 4.2.3.2.3). These measures are comparable, since they involve the proper TVF flow according to the assumption described in section 4.2.2. Figure 22-a shows the amount of H_2 absorbed and desorbed as a function of time for measures C8 and C9.

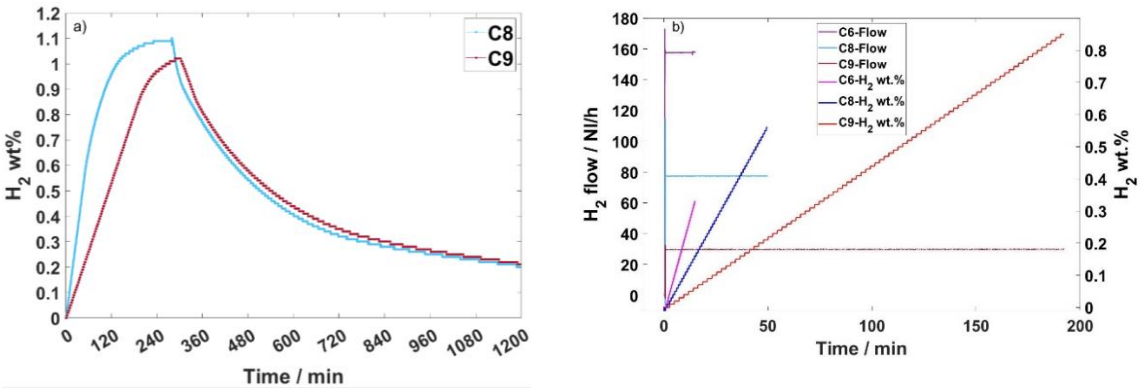

Figure 22: (a) Amount of H_2 in absorption and desorption for measure C8 and C9 as a function of time; (b) H_2 flow and amount of H_2 stored in wt.%, as a function of time for C6, C8 and C9.

The gravimetric capacities observed are comparable with the measures considered so far C1, C5 and C6 and also with other experiments. The amount of H_2 absorbed is around 1.0 - 1.1 H_2 wt.% at 30 bar. Desorption occurs down to 2 bar, releasing H_2 until the amount left in the material is displayed as 0.1 - 0.2 H_2 wt.% of the MH. Results agree with the storage capacity expected from the study performed on the alloys and it is about 0.5 kg of H_2 (section 4.1). The incomplete release of H_2 from the MH could imply a progressive decrease of the amount

of H_2 registered with the further cycles, but this would result in a severe loss of measured capacity of the system with time. As an example, considering 0.1 wt.% left for each cycle, it would take less than 10 cycles to observe a significant worsening in the loading capacity. Since this is not supported experimentally, the amount of H_2 apparently left inside the system has to be ascribed to the regime of low flow rate and intermittent switches between flowmeters occurring at the end of the process, when the pressure difference is low, and a higher output cannot be maintained. Therefore, small amount of gas flows through undetected each time a flow controller is opening and/or adjusting, in addition to the quantities that are simply below the sensitivity of the instruments.

In all measures performed, independently by the condition of H_2 and TVF flowrate, the observed reaction rates are comparable, both in absorption and in desorption. Absorption processes are faster compared to desorption ones, requiring in general about 2 h to process most of the H_2 and about 4 h to reach the total amount. On the contrary, in desorption about 14 hours are generally necessary up to display a stable capacity. At laboratory scale (section 4.1, Figure 5), not a big difference was detected between absorption and desorption reaction rates. Therefore, it might be that the slow reaction rate is mostly linked to the setup of the measure (*e.g.* H_2 flow controller) and/or to the heat management. Concerning the H_2 flow controller, for an initial interval of time, the set flowrate is maintained constant and represents the limit to the reaction rate. Then, the flow decreases gradually from the initial setpoint, following the metal hydride capability to absorb/desorb H_2. The main difference between absorption and desorption concerning the H_2 flow controller is linked to the impossibility to maintain the control on the flow rate in desorption at 160 and 80 Nl/min. Indeed, the flow decreases to about 30 Nl/min, resulting almost equal in each measure. On the contrary in absorption, it is possible to maintain the flow set, resulting in different reaction rate depending on the flow, as can be seen in Figure 22-b, reporting the constant flow regime registered for measure C6, C8 and C9 coupled with the amount of H_2 processed in the same period. As can be seen, the slope of the line registered for the H_2 wt.% as a function of the time is proportional to the flowrate. With low H_2 flowrates, the interval in which the flow remains constant is longer compared to high ones, *e.g.* the C9 segment compare to C6, resulting in a higher gravimetric capacity at the end of the constant flow regime, *i.e.* 0.85 H_2 wt.% with 32 Nl/min compare to 0.33 H_2 wt.% with 160 Nl/min.

4.2.3.3.2 Consideration on PCM physical properties

As previously mentioned, the discrepancy in the reaction rate between absorption and desorption is linked to the heat management and so to the melting and solidification rate of the PCM. Performing a test heating only the PCM module up to 65 °C followed by a cooled down to 40 °C using only EPS (so not exploiting the MH reaction), Figure 23 shows the temperature profiles registered inside the PCM ($T1^{PCM}$-$T6^{PCM}$) and the Tin^{PCM} and $Tout^{PCM}$. Between 40 and 125 min, the PCM is melting, while, between 225 and 400 min, it is solidifying (constant temperature profile).

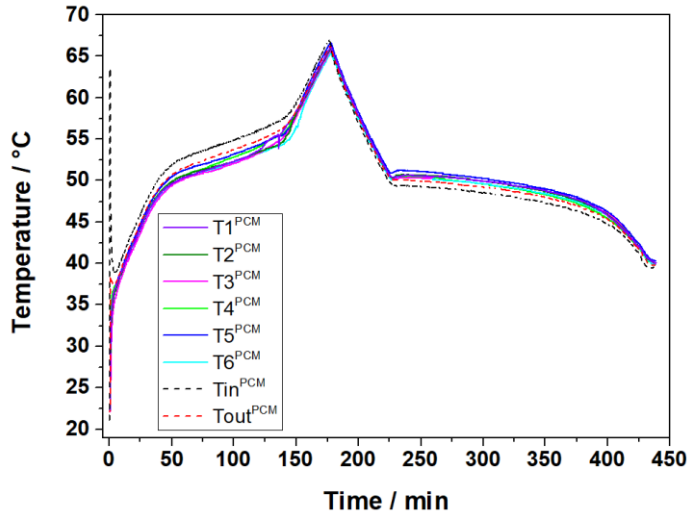

Figure 23: Temperature profile inside the PCM and of the TVF the inlet and outlet as a function of time, heating up to 65 °C and cooling down to 40 °C using the single PCM module connected with the EPS.

It is visible that solidification lasts more than the double of the melting, and in literature comparable results were reported in PCM reactor based on CrodaTherm53 [53]. Assuming that the influence of the control of the bath is negligible and considering that the latent heat of melting and crystallization are almost the same, the reason can be found in other properties. It could be explained by the combination of the effect of the heat capacity and thermal conductivity, which are changing between the solid and liquid phase of PCM. This phenomenon was explained in ref. [53] by investigating the solidification behaviour of PCM based on paraffin wax, as is the CrodaTherm53. It was found that solidification slows down as much as the solid fraction increases due to the limited thermal conductivity of the material. Thus, the thermal natural convection decreases despite an increase of conductive resistance of the solidified fraction. The effectiveness of the strategy to start the absorption reaction with the system at 52 °C (C6 section 4.2.3.2.3) can be explained with the higher thermal conductivity of the liquid phase compared to the solid phase, implying an easier heat transfer

when starting with the PCM close to the melting point. Referring to the literature about MH-PCM system, a sensitive decrease between absorption and desorption was not detected as in this work. This is linked to the use of inorganic or hydrated salts, that presents higher thermal conductivity than organic PCM [34]. Nevertheless, also different designs are considered in literature compared to the realized item, that can also play a role in the heat transfer, making harder the comparison. Summarizing, desorption is slower than absorption due to instrumental limitation in H_2 flowrate and intrinsic properties of the PCM.

4.2.3.3.3 Influence of the H_2 flow

The temperature profiles considered inside the MH-bed and at the TVF are only $T2^{MH}$ and Tin^{PCM} and $Tout^{PCM}$. Indeed, as it was observed evaluating in measures C1, C5 and C6 (section 4.2.3.2) referring to the MH-bed, $T2^{MH}$ is the most representative, while the TVF profile of the Tin^{PCM} and $Tout^{PCM}$ is index also of the $Tout^{MH}$ and Tin^{MH}, respectively, but they help in visualize the PCM phase transition.

To evaluate the influence of the H_2 flow rate on the performances of the couple system, measured C6, C8 and C9 are considered. However, as previously explained, the influence of the H_2 flowrate is visible only in absorption. Figure 24-a shows the temperature curve registered for $T2^{MH}$ for measures C8 and C9 to compare with the one acquired in measure C6 (Figure 17-b). The peak in temperature in $T2^{MH}$ is progressively broader by decreasing the H_2 flow from 160 Nl/min (C6) to 32 Nl/min (C9). To reach the peak in temperature with a flowrate of 160 Nl/min, a waiting time of about 20 minutes is required, that becomes almost one hour in the case of 80 Nl/min and 3 hours for 32 Nl/min. In the latter case, the temperature profile cannot be properly described by a peak, but rather by a smooth profile, where values are almost constant for a relevant interval of time. The time to reach the maximum temperature of the MH-bed is strictly related to the duration of the constant flow of H_2 observed in Figure 22-b. The higher is the flowrate, the greater is the amount of H_2 provided to react, the higher is the exothermicity and the sharper is the increase in temperature. This behaviour is then visible in the Tin^{PCM} and $Tout^{PCM}$ (Figure 24-b for measure C8 and C9, Figure 18-c for measure C6). Low H_2 flows allow to develop the heat in longer time, assuring PCM melting. To investigate the melting of the PCM, Figure 24- c, d, e shows Tin^{PCM} and $Tout^{PCM}$ together with the temperature acquired inside the PCM from $T1^{PCM}$ to $T6^{PCM}$, highlighted with a colour band, as a function of time, respectively for measure C6, C8 and C9. To have a more effective comparisons, same axes range are set.

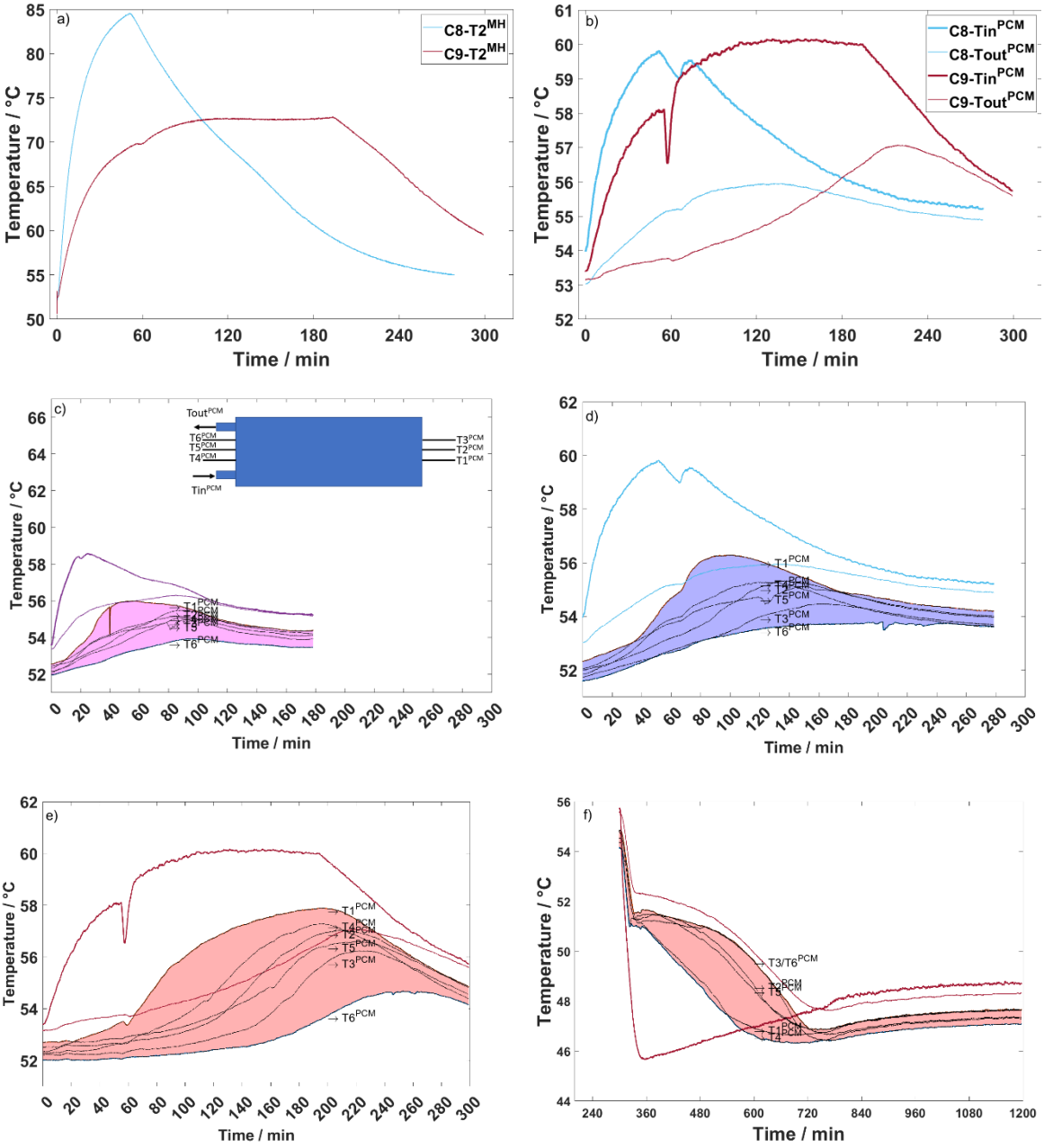

Figure 24: For measures C8 and C9 (a) $T2^{MH}$ registered in absorption and (b) Tin^{PCM} and $Tout^{PCM}$ registered in absorption. (c) Tin^{PCM} $Tout^{PCM}$ and $T1^{PCM}$-$T6^{PCM}$ for measure C6 in absorption; (d) Tin^{PCM} $Tout^{PCM}$ and $T1^{PCM}$-$T6^{PCM}$ for measure C8 in absorption; (e) Tin^{PCM} $Tout^{PCM}$ and $T1^{PCM}$-$T6^{PCM}$ for measure C9 in absorption;(f) Tin^{PCM} $Tout^{PCM}$ and $T1^{PCM}$-$T6^{PCM}$ for measure C9 in desorption. A schematic representation of the PCM module showing the thermocouple location is reported in (c).

In $T1^{PCM}$, the PCM is always already partially/completely melted thanks to the strategy developed to start the reaction at 52 °C, since its temperature profile follows Tin^{PCM}. While in the other temperature curves of the PCM, it is possible to follow the phase transformation, *i.e.* stable values. The PCM close to the position $T6^{PCM}$ is the last part that melts, and always the lower in the coloured bands, since it is the one close to $Tout^{PCM}$ and remains colder (insert in Figure 24-c). Thanks to a more stable Tin^{PCM}, promoted by low H_2 flowrate, it is possible

to achieve a uniform melting of the PCM, as can be seen in measure C9, Figure 24-e. In this measure, also $T6^{PCM}$ melts homogenously and in about 150 min, the PCM is totally melted. Whereas with 160 and 80 Nl/min of H_2 (Figure 24-c, d), melting is less homogeneous, and in $T6^{PMC}$ the melting of the PCM starts when the absorption is towards the end.

Concerning desorption, 160 Nl/min and 80 Nl/min of H_2 flow cannot be sustained for long timeframes, resulting in a similar behaviour (in both cases the flow goes down to 30 Nl/min). Temperature profiles registered inside the MH-bed and at the TVF for measure C8 are comparable with the one reported for measure C6 (Figure 17-c and Figure 18-b, d) and are not reported. Only in measure C9 a difference is detected, since it is possible to maintain 32 Nl/min, observing a more evident drop in temperature compared to C6 (Figure 17-c and Figure 18-b, d). Figure 24-f shows Tin^{PCM} and $Tout^{PCM}$ together with $T1^{PCM}$ -$T6^{PCM}$ as a function of time. A homogeneous solidification is observed by following the $T1^{PCM}$ -$T6^{PCM}$ and similar trend is registered also in the other measures. Indeed, crystallization appears to be a more homogeneous process than the melting, and lasts more, due to a homogenous energy distribution in time (low flowrate, 30Nl/min), but also due to the different thermal conductivity of the PCM between solid and liquid.

Finally, concerning the contributions of the EPS in absorption and desorption, Figure 25 shows the cumulative energy (a) and the moving average of the power (b) as a function of time. Results can be compared with those obtained for measure C6, Figure 18-e, f.

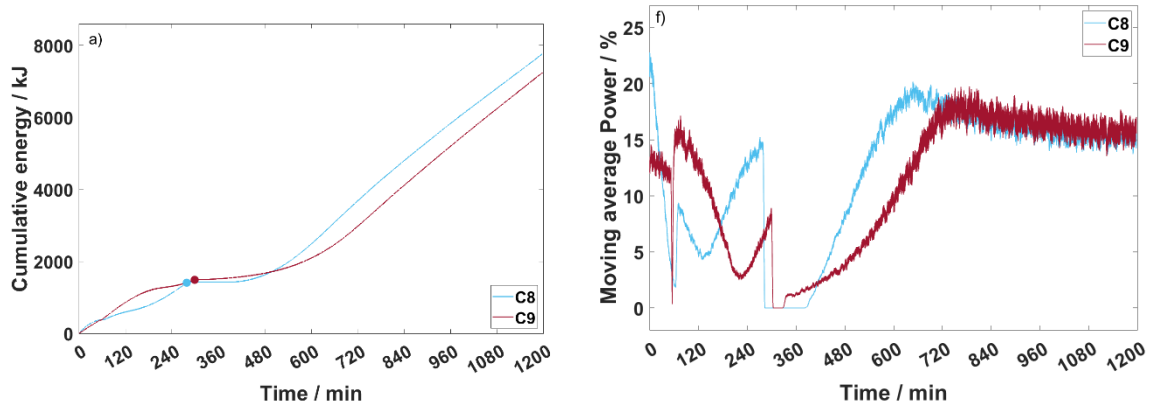

Figure 25: For measures C8 and C9 (a) cumulative energy as a function of time, with points highlighting the end of absorption; (b) moving average of the EPS% power as a function of time made on 60 values.

In both measures C8 and C9, the less amount of heat flow generated implies a continuous EPS contribution in absorption to keep the system warm, compared to measure C6. In desorption, the power contribution is comparable with other measures (C5, C6), observing a lower amount of energy and power from the EPS in measure C9.

4.2.3.3.4 Influence of the TVF flow rate

The influence of the TVF flow rate is evaluated by considering the same H_2 flow of 160 Nl/min, with a variable TVF flow, *i.e.* 6.4 l/min measure C6 (section 4.2.3.2.3), 3.3 l/min measure C7 and 1.4 l/min measure C10. Figure 26-a reports the amount of H_2 absorbed and desorbed as a function of time.

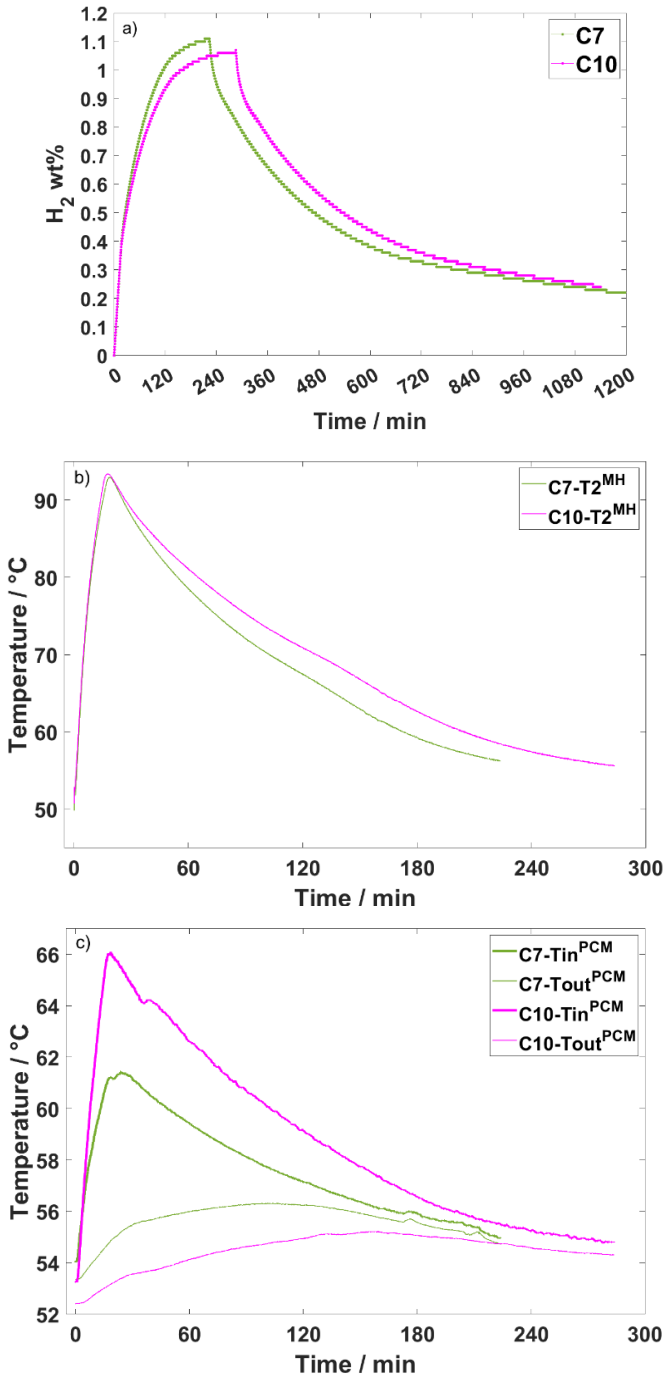

Figure 26: For measures C7, C10 (a) amount of H_2 absorbed and desorbed as a function of time; (b) $T2^{MH}$ as a function of time in absorption; Tin^{PCM} and $Tout^{PCM}$ as a function of time in absorption.

Same considerations made so far about the time of reaction rate and the amount of hydrogen processed in both reactions are valid for measure C7 and C10. The effect of the TVF flow rate is remarkable in temperature. The lower is the flow rate, the higher is the peak in temperature registered inside the MH-bed. Considering $T2^{MH}$, a peak in temperature of 93.4 °C is reached in measure C10 with 1.4 l/min of TVF flow, while 92.9 °C in C7 with 3.3 l/min (Figure 26-b) and 89.2 °C in C6 with 6.4 l/min.

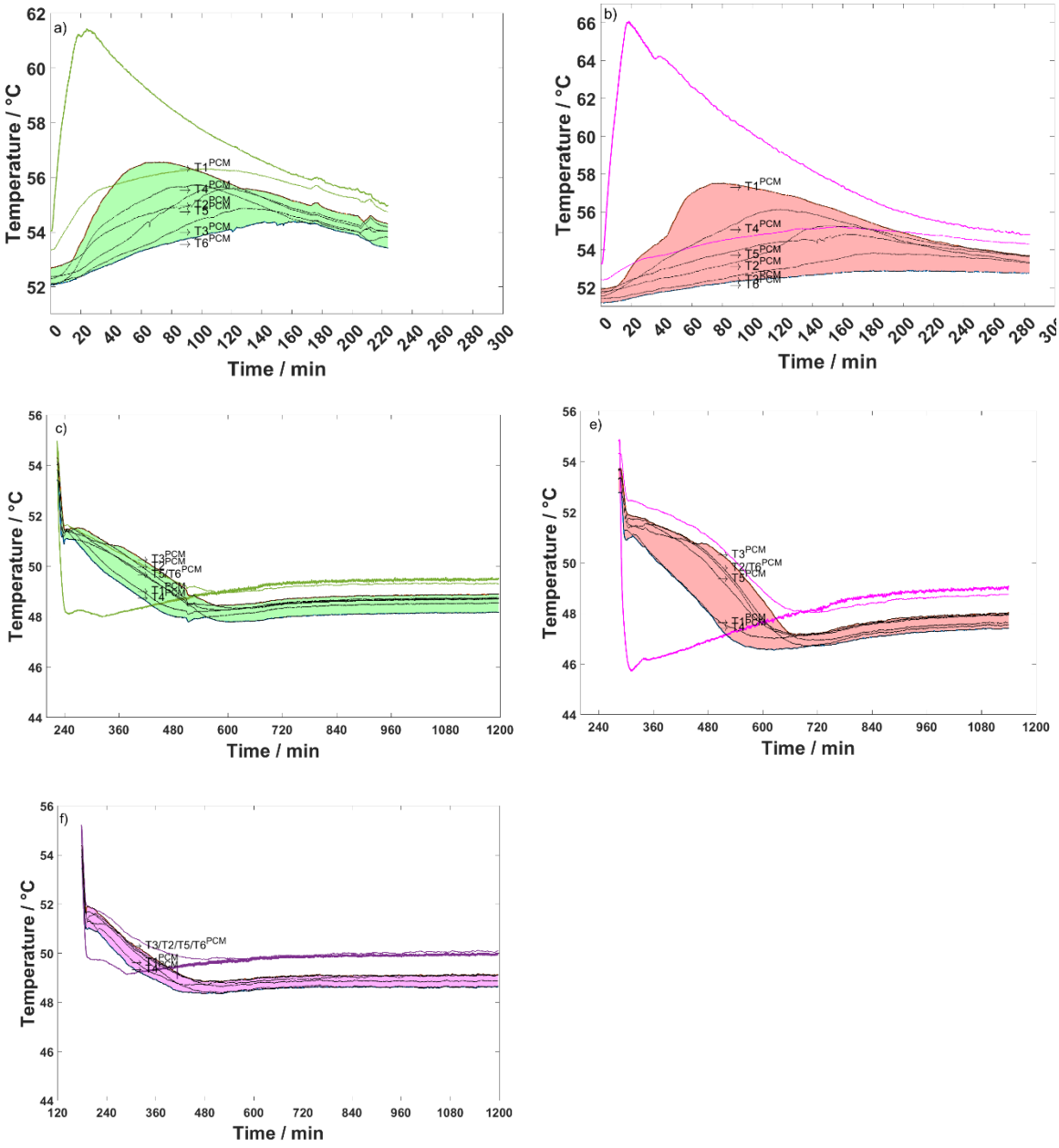

Figure 27: (a) Tin^{PCM} $Tout^{PCM}$ and $T1^{PCM}$-$T6^{PCM}$ for measure C7 in absorption; (b) Tin^{PCM} $Tout^{PCM}$ and $T1^{PCM}$-$T6^{PCM}$ for measure C10 in absorption; (c) Tin^{PCM} $Tout^{PCM}$ and $T1^{PCM}$-$T6^{PCM}$ for measure C7 in desorption; (d) Tin^{PCM} $Tout^{PCM}$ and $T1^{PCM}$-$T6^{PCM}$ for measure C10 in desorption; (e) Tin^{PCM} $Tout^{PCM}$ and $T1^{PCM}$-$T6^{PCM}$ for measure C6 in desorption.

This result occurs since a low flow rate removes less heat, implying a high warming up of the MH-bed. Therefore, the decrease in TVF flow rate from 6.4 to 1.4 l/min, causes an increase of the Tin^{PCM} (Figure 26-c), allowing a slower cooling down of the system. The higher temperature generated by the absorption reaction and the less efficient removal of heat by the TVF with low flow rates has an effect on PCM melting, as can be visualized in Figure 27- a(C7), b(C10) and Figure 24-c (C6), reporting $T1^{PCM}$-$T6^{PCM}$ together with Tin^{PCM} and $Tout^{PCM}$. The lower TVF flow rate implies a longer and homogeneous melting of the PCM, until the conclusion of the process. This phenomenon is more evident following the temperature profile in $T6^{PCM}$, since in measure C6 melting is starting in the last period of absorption. While, especially in measure C10 with 1.4 l/min, the PCM in $T6^{PCM}$ is melting during the entire process.

Evaluating the effect of the TVF flow rate in desorption, the supply of the heat to face the endothermicity of the reaction is not enough by decreasing the flow rate. This implies a peak in temperature as lower as the flowrate decreases. This can be observed, by following the PCM phase of change in measure C7, C10 and C6 reporting the Tin^{PCM} and $Tout^{PCM}$ together with $T1^{PCM}$-$T6^{PCM}$ as a function of time in Figure 27- c-f, respectively. Nevertheless, as it was observed evaluating the effect of the H_2 flowrate, the solidification of the PCM is homogenous independently by the TVF flow rate.

Finally, Figure 28 shows the cumulative energy (a) and the moving average of the power (b) as a function of time, for measure C7 and C10. Results are comparable with measure C6, Figure 18-e, f.

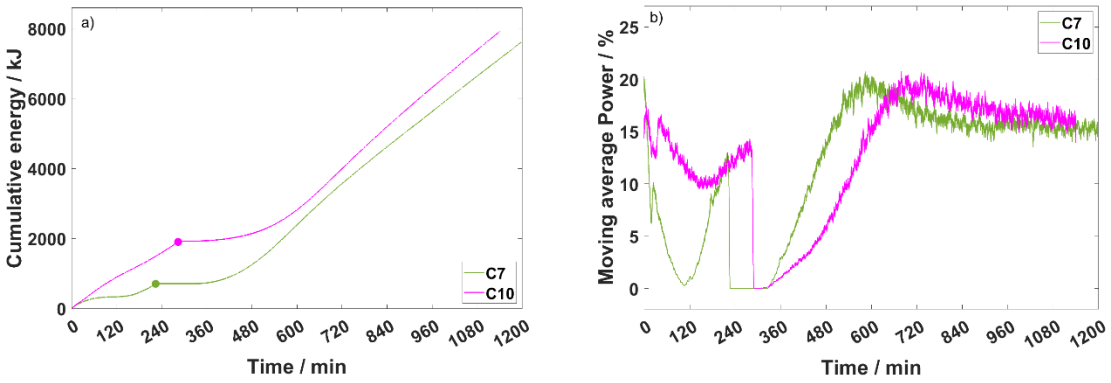

Figure 28: For measures C7 and C10 (a) cumulative energy as a function of time, with points highlighting the end of absorption; (b) moving average of the EPS% power as a function of time made on 60 values.

In measure C10, the less amount of heat removed by the system, implies a higher and continuous EPS contribution in absorption to keep the system warm, compared to measure

C7 and C6. In desorption, the power contribution is comparable with other measures (C5, C6), observing a lower amount of energy and power from the EPS in measure C7, and an absence in the first period in C7.

4.2.3.4 Consideration on the EPS power/energy contribution

The heat exchanged at the MH tank and at the PCM module is calculated for measure C4-C9. Detailed results of measure C4 were not reported so far. This measure was performed applying the same strategy of C5, with an H_2 flow of 160 Nl/min and a TVF flow of 3.3 l/min, thus consideration made for C5 and C7 are valid even for C4. Results of the power/energy exchanged about measure C10 are not reported, since not reliable. Indeed, the power is considerably higher than the 3 kW expected by the reaction of H_2 at 160 Nl/min and not even linked to the EPS contribution, since it was higher than the maximum power in heating of the EPS (2.7 kW). This is linked to an imprecise measure of the TVF flow rate (*i.e.* 1.4 l/min). It is not possible to set about 1.0 l/min on the EPS, but it is necessary to manually set it by closing partially valves. Thus, the test is not easily reproducible, and the liquid flow sensor might be crossed by a flow too low to be properly measured by the system, promoting an error in measuring that affects the calculation of the power as far as of the energy.

Figure 29 shows the exchanged power (a, b) and energy (c, d) at the MH-tank and PCM module. Points highlight the end of absorption. The energy/power flow is intended from the units to the outside, so positive values mean a heat release and vice versa. For the MH the inlet contribution comes from the EPS and the PCM, while for the PCM everything is related to the MH. Considering the layout of the circuit and the convention adopted for the energy flow, the contribution is opposite, so that when at the MH there are positive values (for instance in the case of in absorption), the heat released is then transferred and used by the PCM, implying negative ones in the second graph. The opposite is valid for desorption, during which PCM is releasing heat flow that is used by the MH. Ideally, all the heat released by the MH is used, *i.e.* stored, by the PCM and then, the situation is reversed during desorption. The amount of energy/power released by the MH in absorption appears almost independent by the thermal flow (C4-C7) and it is strictly linked to the H_2 flow (C4-C7 with C8 and C9). Only the reaction, and so the amount of H_2 absorbed, has a significant impact on the heat flow produced and therefore exchanged. For an H_2 flow of 160 Nl/min, power values are of the order of 1.7 kW for C6-C7 and 1.5 kW for C4-C5, while for 80 Nl/min (C8)

about 1.1 kW and for 30 Nl/min (C9) about 0.5 kW. The values of power exchanged for lower hydrogen flowrates are closer to those of the power generated by the reaction, *i.e.* 1.1 kW is the 73 % of the maximum expected of about 1.5 kW for 80 Nl/min (C8). Then, 0.5 kW is the 83 % of the expected of 0.6 kW for 32 Nl/min (C9), while, for 160 Nl/min 1.7-1.5 kW are only the 56-50 % of the theoretical value of about 3 kW. Considering that the prototype under examination is ~1/5 of the HyCARE demonstrator and that the most effective heat exchange occurs with flowrates that are ~1/5 (32 Nl/min) of the design values of 160 Nl/min (EL flow, section 4.2.2), the results can be deemed as positive. On the contrary higher H_2 flow seems to be not proper for the designed system.

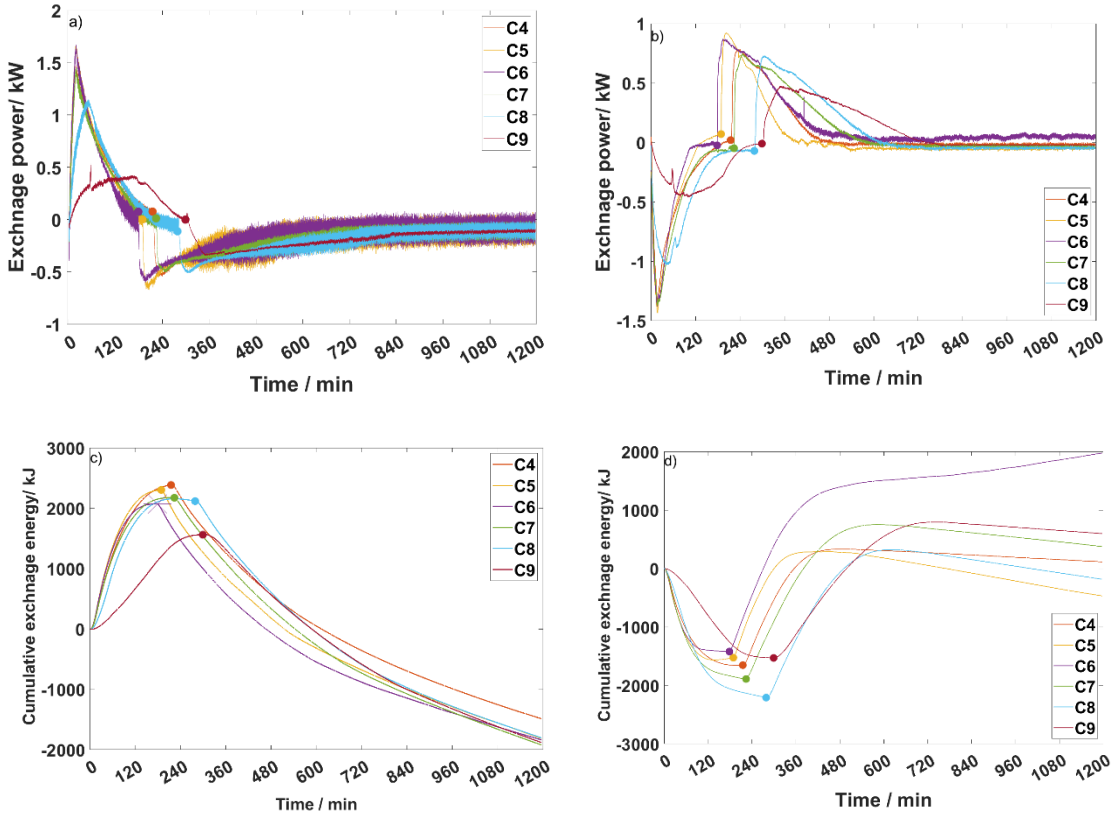

Figure 29: The exchange power (a) at MH tank and (b) at the PCM module as a function of time. The cumulative exchange energy (c) at the MH tank and (d) at the PCM module as a function of time.

In absorption, comparing values of the MH unit with the one of the PCM unit, it seems that almost all the heat released is used for PCM melting. Indeed, the difference in power with the PCM is low, as it can be better seen from Figure 30-a, that reports the moving average of the difference in power between the MH and PCM, as a function of time. The difference is of the order of few hundreds of W, with positive values during absorption, meaning that

more energy is released than used. It is worth noticing that considering the EPS contribution observed in the previous section 4.2.3.2 and 4.2.3.3 for each measure, the higher is the contribution of the EPS in the system, the lower is the difference in energy between the MH and PCM. As an example, a lower EPS contribution was registered for measure C6 compared to C9, but then the energy/power exchange is higher in C9 than in C6 (Figure 30). This could imply that the difference is mostly related to heat losses. When the EPS is giving more power, the heat losses can be compensated almost completely. Then, in general, in the final part of the absorption, the H_2 flow is low, in turn the heat flow generated, and the power contribution of the EPS is more evident, but at the PCM no more power/energy is exchanged, since it is totally melted. So, the difference in power and energy detected can be related to the EPS in facing the heat losses and in keeping the system warm.

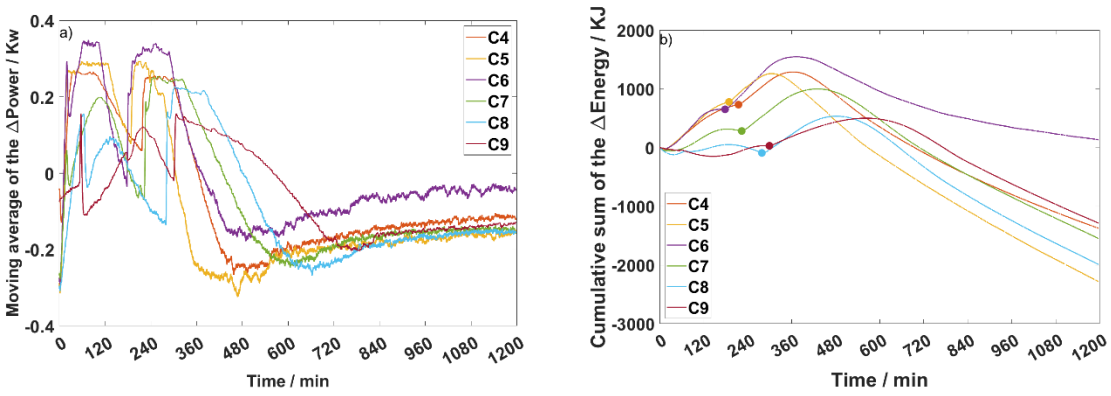

Figure 30: (a) moving average of the difference in power between MH and PCM made on 60 values; (b) difference of the cumulative sum energy between the MH and the PCM, with asterisk highlighting the end of absorption.

In desorption, the influence of the H_2 flow is less evident, since in most of the cases it gets uniformed and reduced to 30 Nl/min. The amount of heat flow released by the PCM is slightly higher than that consumed by the MH in desorption. Indeed, the PCM is releasing about 0.7-0.8 kW for C4-C8 and 0.5 kW at the maximum, and the MH is receiving at the maximum about 0.55 kW and 0.3 kW, respectively. Also in this case, a difference in power/energy is observed as reported in Figure 30. Indeed, differences can be ascribed almost exclusively to heat losses, since comparing the EPS curve in each measure (section 4.2.3.2 and 4.2.3.3) with those obtained with the MH and PCM, in the same period of time, the EPS has a constant power contribution, almost negligible. Peaks observed in Figure 30 for absorption and desorption have same difference in power. Afterwards, the difference between the two increases with contributions in the positive direction, which are due to the increasing contribution required to the EPS to maintain the temperature stable. This is more

evident when comparing the energy difference between the MH and PCM (Figure 30-b) with the single EPS energy curve (section 4.2.3.2 and 4.2.3.3). The difference for the MH and PCM, become more negative after the maximum event. This means that more energy goes to the MH tank, which is not interconnected anymore with the solidification, but is given by the EPS. For C9, in absorption it is evident that the PCM is absorbing more energy than that released by the MH. A similar effect, but more remarkable, happens in measurement C10 (not given). In C9 a TVF flow of 1.4 Nl/min is applied as in C10, thus it seems that a small error occurred due to the TVF also in C9 as for C10, but it is not as remarkable.

In conclusion, the heat of reaction in both absorption and desorption can be manage by the PCM, with a fundamental contribution of the EPS in face internal losses in the EPS itself and of the thermal circuit and in keeping the system warm. Starting the H_2 absorption in the MH tank with PCM partially melted helps in promoting its total melting during the process, storing the heat of reaction by means of phase change (latent heat) rather than mere temperature increase (sensible heat). Then the increase of 1° in temperature during the absorption avoid its PCM solidification for the entire duration of the process. In the last part of the reaction, the EPS contribution is higher, especially in desorption, since lasts for longer time and it needs to avoid system cooling when the solidification of the PCM is completed.

4.2.3.5 Influence of a constant hydrogen flow

Two analyses were performed displaying only the constant H_2 flow regime, C11 with 160 Nl/min and C12 with 32 Nl/min. Figure 31-a, b shows the H_2 flowrate registered as a function of time in absorption and desorption, respectively, for measure C11, while Figure 31-c, d refers to measure C12. As already presented in Figure 22, in absorption, the constant flow at 160 Nl/min lasts considerably less than the one set at 32 Nl/min. Being the tank in dimension 1/5 of the final system, a flow of 32 Nl/min (*i.e.* 1/5 of 160 Nl/min) results to be more appropriate for the prototype. This implies that in one continuous charge at 32 Nl/min of H_2 flow, the amount of hydrogen absorbed is considerably higher than with the first continuous step at 160 Nl/min, as suggested also by Figure 32-a, reporting the amount of hydrogen absorbed and desorbed for the two measures as a function of time.

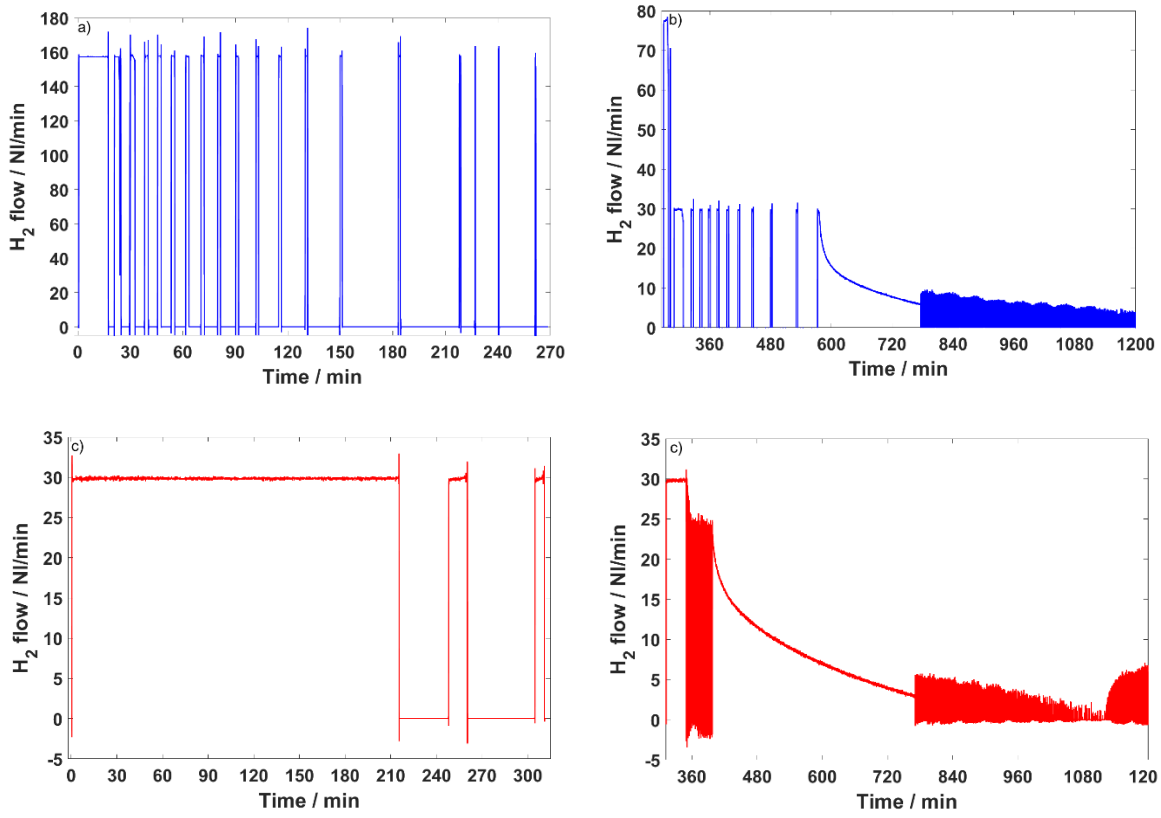

Figure 31: H_2 flow as a function of time (a) for measure C11 in absorption; (b) for measure C11 in desorption; (c) for measure C12 in absorption; (d) for measure C12 in desorption.

The capacity reached with the first linear segment is much higher for 32 Nl/min, even if the slope, as far as the reaction rate, is obviously lower since it is directly proportional to the H_2 flowrate. In one loading step, in measure C12, the 0.97 H_2 wt.% is reached in absorption, compared to 0.39 H_2 wt.% of the first step in measure C11. Then, with other two charges with intervals of shorter duration, a final capacity of 1.05 H_2 wt.% is reached in C12, while several shorter intermittent steps are necessary for the final one of 1.07 H_2 wt.% of C11. When the supply of H_2 is stopped, the pressure drops, since the material is absorbing the hydrogen gas remained in the free volume, as it can be seen from the pressure profile of measure C11, reported as an example (Figure 32-b). The strategy used in absorption consist of a pressure triggered control, so that when the pressure drops down to 20 bar (level chosen arbitrarily), the H_2 supply is reopened. With an outlook on the flow and pressure profiles, it can be seen that the time necessary to drop to 20 bar increases with the cycle number, due to the progressive loading of the alloys, and so less time is necessary in the firsts steps because the alloy is almost empty. Then, gradually, the alloy is absorbing, and more time is necessary to reach the lower limit for pressure. This happen also in measure C12, as can be deduced from the H_2 amount curve of Figure 32-a.

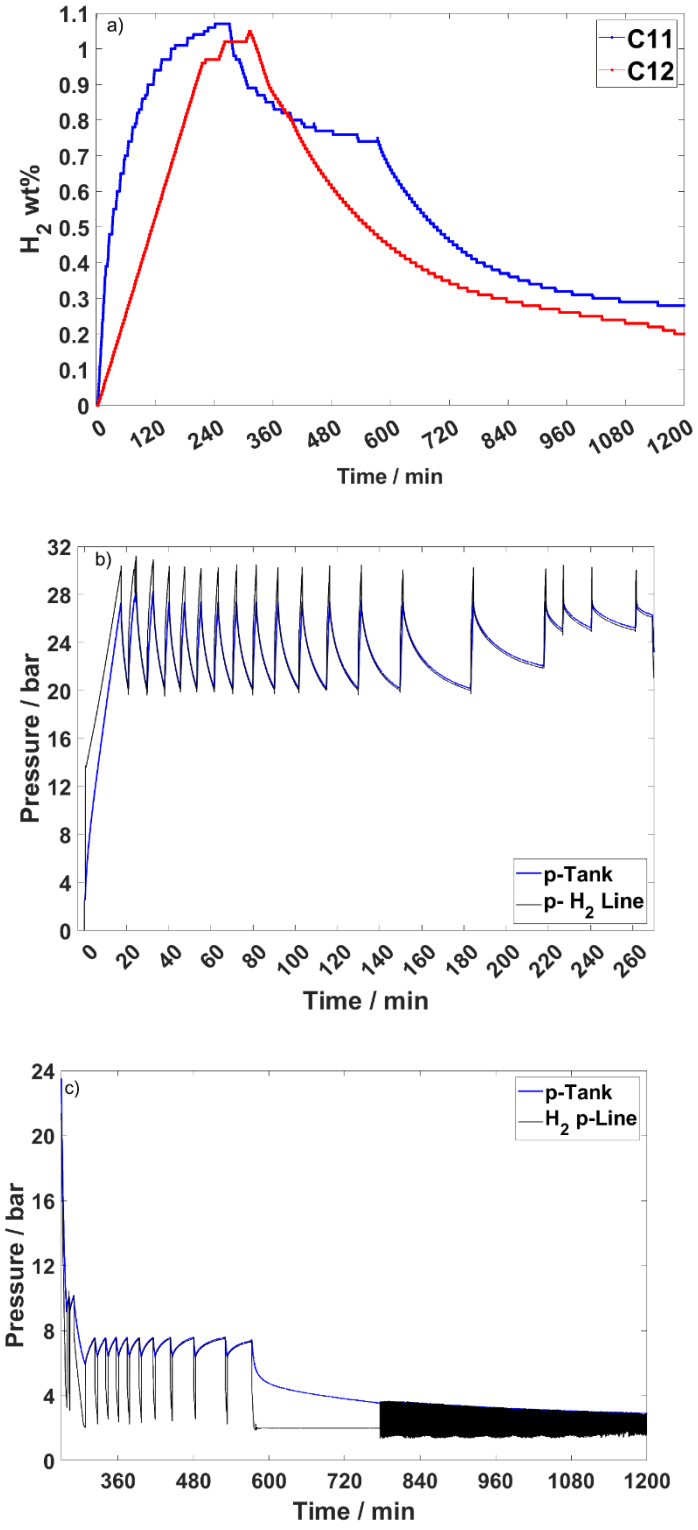

Figure 32: (a) Amount of H_2 absorbed and desorbed as a function of time for measures C11 and C12; (b)H_2 pressure registered inside the MH tank and H_2 line as a function of time for measure C11 in absorption (c) H_2 pressure registered inside the MH tank and H_2 line as a function of time for measure C11 in desorption.

In, desorption, the same consideration can be made, but, as already mentioned, high flow rate are not achievable. So, instead of 160 Nl/min, 80 Nl/min are initially used for desorption

in measure C11. However, as it can be seen, the flow had to be decreased to 30 Nl/min after the second cycle (Figure 31-b). The strategy applied is like absorption, however, in this case, when closing the connection with the free volume used to promote the desorption, the MH is releasing H_2, so the pressure increases, as shown in Figure 32-c. In this case, the target fix in pressure to reopen the connection is 7.5 bar. In both processes, for the final parts of desorption, the concept of the constant/intermittent flow was abandoned since it was not anymore able to maintain the constant flow (Figure 32-c). Figure 33-a shows $T2^{MH}$ as a function of time for the absorption process.

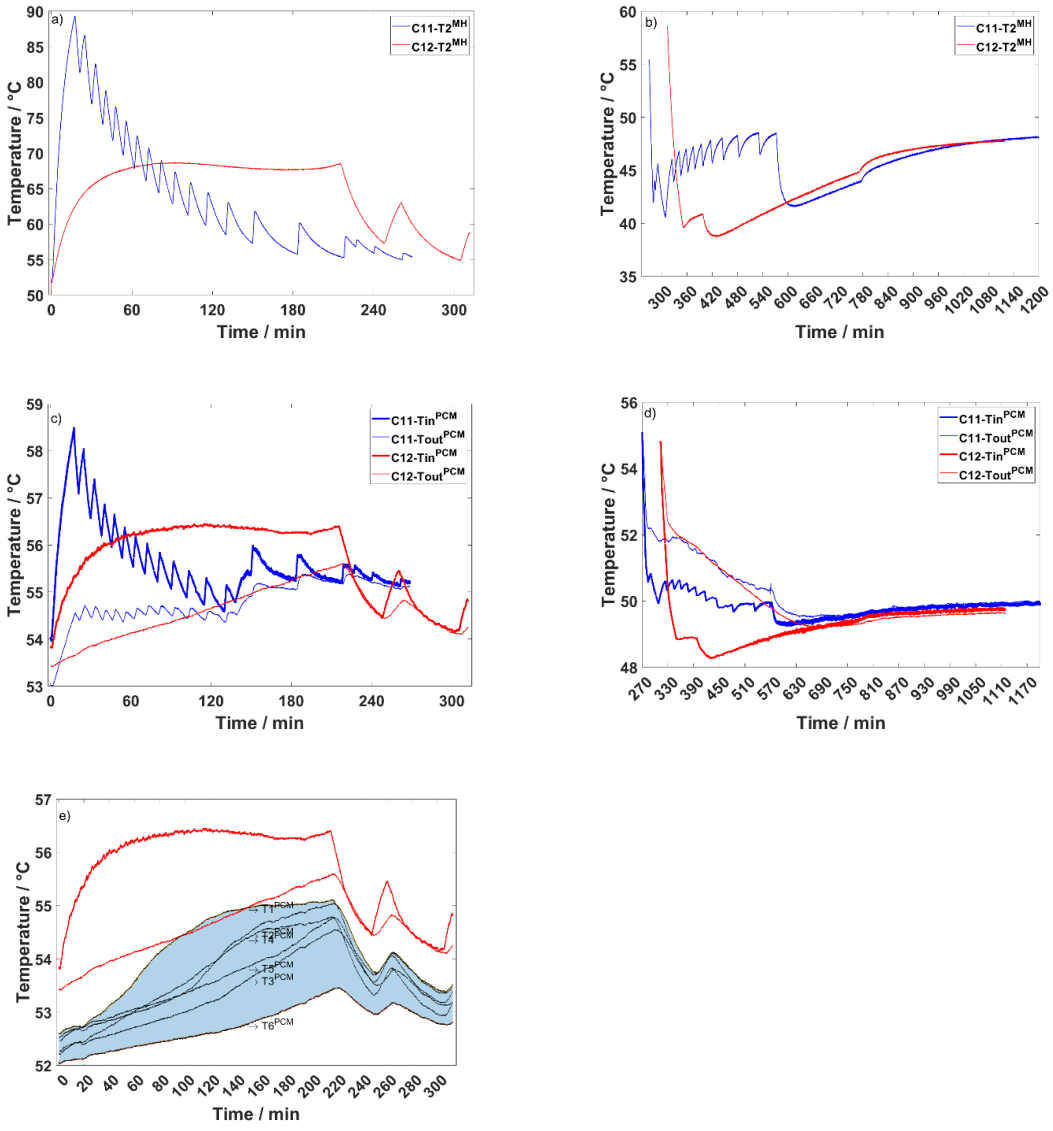

Figure 33: For measures C11 and C12 (a) $T2^{MH}$ as a function of time in absorption; (b) $T2^{MH}$ as a function of time in desorption; (c) Tin^{PCM} and $Tout^{PCM}$ as a function of time in absorption; (d) Tin^{PCM} and $Tout^{PCM}$ as a function of time in desorption; (e) for measure C12 Tin^{PCM} and $Tout^{PCM}$ and $T1^{PCM}$-$T6^{PCM}$ as a function of time in absorption.

The trend of temperature follows the one of the flows and pressure, with an intermittent profile characterized by an increase in temperature when the tank is filled at constant flow and by a decrease when the supply is closed. More heat is developed when the absorption is made under direct flow and the pressure is increasing. As already seen for measure C9 with 32 Nl/min of H_2, a lower rise in temperature is reached, since less H_2 is supplied. Decreasing the number of cycles, the maximum temperature decreases since less H_2 is absorbed step by step. Comparing the maximum of the peak in the first absorption step, *i.e.* C6 for C11 and C9 for C12, temperatures are similar. Tin^{PCM} and $Tout^{PCM}$ follow the same trend of $T2^{MH}$ (Figure 33-c). The increase of 1 ° of the thermal fluid at the inlet of the MH tank was applied in measure C11, at about 137 min. The increase was made to maintain the system far from 53 °C, since that temperature was approaching and a small ΔT (Tinlet-Toutlet) was observed. This causes a visible increase in temperature profiles. However, the ΔT is continuing to be close zero, suggesting that the PCM melting was already achieved. In C12, the increase in temperature was not applied. Concerning the PCM, its melting is assured in both measures, as it can be deduced by the inlet and outlet temperature profiles of the TVF (Figure 33-c). Melting is also confirmed looking at the PCM temperatures profiles $T1^{PCM}$-$T6^{PCM}$, reported as an example for measure C12 in Figure 33-e. Already during the first step of absorption the PCM is almost completely melted, also at the position monitored by $T6^{PCM}$.

For desorption, the same considerations of absorption can be made on the temperature profiles, as it shown in Figure 33-b for $T2^{MH}$ and Figure 33-d for Tin^{PCM} and $Tout^{PCM}$. In the same setup conditions, the temperature drop in C12 is less pronounced than in C9, while is comparable between C11 and C6. Tin^{PCM} temperature oscillations are less evident than in absorption. The solidification in both measures proceed as previously described.

Finally, concerning the contribution of the EPS in these two measures, Figure 34-a, b shows respectively the cumulative energy and the moving average of the EPS power as a function of time. In absorption the amount of energy and power required by the EPS is low, and the system is almost self-sustained. As also observed in the other measures, the amount of energy increases at the end of the process when lower amounts of H_2 are finally absorbed. The marked increment for C11 is linked to the increase of 1 °, set for the final part of the process. At the beginning of desorption, the contribution is almost absent and, also in this case, the PCM is able to supply the MH, and for longer time in C11. Then, the contribution increases to maintain the set temperature of 50 °C, as previously discussed.

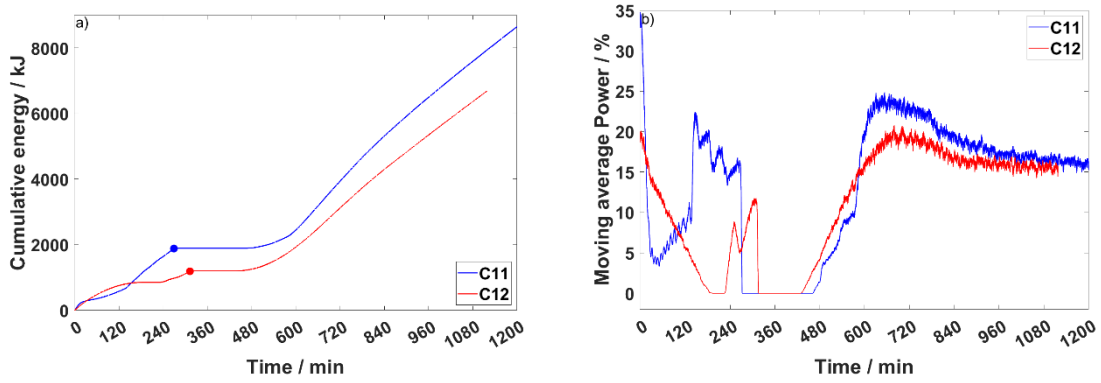

Figure 34: For measure C11 and C12 (a) cumulative energy values; (b) moving average of power made on 60 values for the EPS.

The use of the constant H_2 flow, at intermittent intervals, allows to sensitively limit the contribution of the EPS, especially in absorption, since the heat flow developed is constant, and always at the maximum. In desorption, since the system should not cool down, not significant changes in EPS contribution can be seen, with the process almost self-sustain in the first stages.

4.2.4 Conclusion

The use of PCM in the heat management of a MH-tank was proposed in the last years, thanks to several simulations works, as an efficient solution of heat recovery and reduction of external power contribution in the hydrogen storage. In the storage of renewable energies thanks to the production and storage of green hydrogen, it is extremely advantageous the reduction of external power for the running of MH system. Indeed, the external power should be supply or by grid current, or if possible, also by renewable. The moving towards a completely self-sustainable hydrogen storage system could be particularly promising in this time of energy crisis.

The use of PCM-MH coupled system was successfully demonstrated in this work by testing a prototype based on $TiFe_{0.85}Mn_{0.05}$ alloy as H_2-carrier and an organic PCM, the CrodaTherm53. By varying the parameters, like the hydrogen and thermal fluid flowrates and the starting working temperature, it was possible to achieve the goal to individuate the optimal conditions that allow to reduce the amount of external power required to sustain the process. The external power contribution cannot be totally eliminated, as demonstrated in a series of measures performed without any contribution. Nevertheless, it was found that its role limited in heating power is fundamental to face heat losses and in avoiding the cooling to room temperature of the system. In absorption, the contribution of the external power

source in the reaction can be limited by displaying only constant hydrogen flow, since in this way, the heat of reaction is enough to promote the melting of the PCM with the EPS just facing the heat losses. On the contrary, the contribution in the reaction is necessary in the final part of the process, since the H_2 flow decreases with time, as far as the amount of heat released by the reaction, resulting fundamental the external power contribution to maintain the PCM warm and melted. In desorption, the process is almost self-sustained, with the PCM that can successfully provide heat to the MH with an external power contribution only necessary to face the naturally cooling down on the PCM. The reaction rate in absorption is generally faster than desorption, independently by applied conditions, due to intrinsic PCM properties and instrumental setup. Because of the intrinsic properties of the PCM, it results optimal to start the absorption process at a temperature close to the melting point instead of when the PCM is totally crystallized. The system works properly storing an amount of hydrogen in line with laboratory investigation performed on the $TiFe_{0.85}Mn_{0.05}$ (section 4.1). These tests put the bases in the realization of the final HyCARE demonstrator, suggesting the right procedure to successfully store the hydrogen limiting the amount of external power contribution: performing the storage by exploiting constant hydrogen flow.

Acknowledgment

The project leading to this work has received funding from the Fuel Cells and Hydrogen 2 Joint Undertaking (JU) under grant agreement No 826352, HyCARE project. The JU receives support from the European Union's Horizon 2020 research, Hydrogen Europe, Hydrogen Europe Research, innovation programme and Italy, France, Germany, Norway, which are all thankfully acknowledged. A gratefully acknowledges to the Erasmus+ Traineeship programme of the European Union for the financial support and for allowing the mobility between the University of Turin (Italy) and the Helmholtz-Zentrum Hereon (Germany).

Final remarks

The goal of the European project HyCARE is to realize a demonstrator that can store about 40-50 kg of H_2 with metal hydrides, by exploiting renewable energy, by limiting the consumption of energy required for the management of the MH system. At this regard, phase change material is proposed for the heat management of the hydrogen storage system. This

project wants to show the feasibility of an integrated systems: renewables, hydrogen, heat recovery, to produce green energy in mild conditions.

As H_2-carrier a TiFeMn-based alloys was chosen, the $TiFe_{0.85}Mn_{0.05}$. When realizing a large-scale storage system, the industrial production of the alloys is fundamental and the advantage of this type of compound is also it is economical advantage, thanks to abundance and cheapness elements. The alloy was prepared industrially, as it will be done for the final HyCARE demonstrator, and, in this work, was deeply characterized morphologically, chemically and in the hydrogen sorption properties. The alloy is suitable to be used in the final HyCARE demonstrator, thanks to an easy activation that can be performed in mild conditions in 50 bar of H_2, through a thermal cycle from 90 °C to 25 °C, without exceeding the plant maximum affordable temperature and pressure dictated by the design of the plant. Then, the suitable thermodynamic and good absorption and desorption kinetics allow to integrate the alloys with a PEM-electrolyzer upstream and a PEM-fuel cell downstream, storing H_2 between 30 and 2 bar at 55 °C, with a capacity of about 1.0 H_2 wt.%. One of the main results of the work was to highlights the discrepancy in morphology, phase abundance and surface properties that the synthesis promotes, passing from laboratory (literature data) to industrial production, that strongly affect the final hydrogen sorption properties for a given composition.

Realizing a MH tank with the $TiFe_{0.85}Mn_{0.05}$ alloys and a PCM module based on the CrodaTherm53, it was proven the feasibility of the HyCARE concept. The item realized is 1/5 of the final HyCARE demonstrator and represents the first prototype realized based on an organic PCM and a TiFe-based MH that works in mild conditions of pressure and temperature. The final system can process about 0.5 kg of H_2 in the defined condition of pressure and temperature from the alloy's study, with an efficient management of the reaction heat by the PCM module. Indeed, the heat of reaction can be successfully stored by the PCM thanks to its melting during the abortion of hydrogen, without any contribution of external power, when a constant flow of hydrogen is supplied. The same occur in the desorption process, in which the PCM is able to totally sustain the desorption of H_2 thanks to its solidification. The external power is necessary to face heat losses and maintain the system warm especially in desorption, to avoid the cooling down of the system to room temperature. In general, the contribution of external power is essential in the final parts of

the reactions, so when the amount of heat processed by the reaction is no more enough to sustain the PCM.

Results on the $TiFe_{0.85}Mn_{0.05}$ alloys and on the prototype MH-PCM highlight the potential to develop green energy exploiting hydrogen as energy vector, limiting the use of external power to manage the storage of hydrogen as MH, moving towards an almost self-sustaining storage of renewables.

References

[1] HyCARE web page: https://hycare-project.eu.

[2] G.K. Sujan, Z. Pan, H. Li, D. Liang, N. Alam, An overview on TiFe intermetallic for solid-state hydrogen storage: microstructure, hydrogenation and fabrication processes, Crit. Rev. Solid State Mater. Sci. (2019) 1–18. 10.1080/10408436.2019.1652143.

[3] E.M. Dematteis, N. Berti, F. Cuevas, M. Latroche, M. Baricco, Substitutional effects in TiFe for hydrogen storage: a comprehensive review, Mater. Adv. (2021). 10.1039/D1MA00101A.

[4] J.R. Johnson, J.J. Reilly, The Use of Manganese Substituted Ferrotitanium Alloys for Energy Storage, Altern. Energy Sources. 8 (1978) 3739–3769.

[5] S. Challet, M. Latroche, F. Heurtaux, Hydrogen Storage in TiFe(0.70+x)Mn(0.20-x) (0 <= x <= 0.15) and TiFe(0.70)Mn(0.20-y)Ni(y) (0 <= y <= 0.08) Metallic Alloys, Mater. Sci. Technol. 3 (2005) 13–21.

[6] E.M. Dematteis, D.M. Dreistadt, G. Capurso, J. Jepsen, F. Cuevas, M. Latroche, Fundamental hydrogen storage properties of TiFe-alloy with partial substitution of Fe by Ti and Mn, J. Alloys Compd. 874 (2021) 159925. 10.1016/j.jallcom.2021.159925.

[7] D. Dew-Hughes, L. Kaufman, Ternary phase diagrams of the manganese-titanium-iron and the aluminum-titanium-iron systems: A comparison of computer calculations with experiment, Calphad. 3 (1979) 175–203. 10.1016/0364-5916(79)90003-8.

[8] B. Rupp, On the change in physical properties of Ti4−xFe2 + xOy during hydrogenation I: Activation behaviour of ternary oxides Ti4−xFe2 + xOy and β-Ti, J. Less Common Met. 104 (1984) 51–63.10.1016/0022-5088(84)90435-1.

[9] D.J. Chronister, S.W. Scott, D.R. Stickle, D. Eylon, F.H. Froes, Induction Skull Melting of Titanium and Other Reactive Alloys, Jom. 38 (1986) 51–54. 10.1007/BF03258690.

[10] P. Hovington, D. Drouin, R. Gauvin, CASINO: A New Monte Carlo Code in C Language for Electron Beam Interaction - Part I: Description of the Program, Scanning. 19 (1997) 1–14.

[11] P. Thompson, F. Reidinger, J.J. Reilly, L.M. Corliss, J.M. Hastings, Neutron diffraction study of β-iron titanium deuteride, J. Phys. F Met. Phys. 8 (1978) L75–L80. 10.1088/0305-4608/10/2/001.

[12] M. Dornheim, S. Doppiu, G. Barkhordarian, U. Boesenberg, T. Klassen, O. Gutfleisch, R. Bormann, Hydrogen storage in magnesium-based hydrides and hydride composites, Scr. Mater. 56 (2007) 841–846. 10.1016/j.scriptamat.2007.01.003.

[13] M.H. Mintz, S. Vaknin, S. Biderman, Z. Hadari, Hydrides of ternary TiFexM1-x(M=Cr, Mn, Co, Ni) intermetallics, J. Appl. Phys. 52 (1981) 463–467. https://doi.org/10.1063/1.329808.

[14] C. Stioui, D. Fruchart, absorption d'hydrogene par Ti4Fe2O et diverses phases M6O, Mat. Res. Bull. 16 (1981) 869–876.

[15] J.J. Reilly, F. Reidinger, Surface aggregates produced on activated FeTi as determined by X-ray diffraction, J. Less Common Met. 85 (1982) 145–153. 10.1016/0022-5088(82)90066-2.

[16] L. Schlapbach, A. Seiler, F. Stucki, A NEW MECHANISM FOR LENGTHENING THE LIFETIME OF HYDROGENATION CATALYSTS, Mater. Res. Bull. 14 (1979) 785–790.

[17] L. Schlapbach, A. Seiler, F. StucKi, SURFACE SEGREGATION IN FeTi AND ITS

CATALYTIC EFFECT ON THE HYDROGENATION II: AES AND XPS STUDIES, Mater. Res. Bull. 13 (1978) 1031–1037.
[18] K. Edalati, E. Akiba, Z. Horita, High-pressure torsion for new hydrogen storage materials, Sci. Technol. Adv. Mater. 19 (2018) 185–193. 10.1080/14686996.2018.1435131.
[19] K. Edalati, J. Matsuda, H. Iwaoka, S. Toh, E. Akiba, Z. Horita, High-pressure torsion of TiFe intermetallics for activation of hydrogen storage at room temperature with heterogeneous nanostructure, Int. J. Hydrogen Energy. 38 (2013) 4622–4627. 10.1016/j.ijhydene.2013.01.185.
[20] T. Schober, On the activation of FeTi for hydrogen storage, J. Less Common Met. 89 (1983) 63–70. 10.1016/0022-5088(83)90249-7.
[21] C.S. Pande, M.A. Pick, R.L. Sabatini, THE "ACTIVATION" OF FeTi FOR HYDROGEN ABSORPTION; AN ELECTRON MICROSCOPIC STUDY, Scr. Met. URGICA. 14 (1980) 899–903.
[22] G.D. Sandrock, THE METALLURGY AND PRODUCTION OF RECHARGEABLE HYDRIDES, in: Hydrides for Energy Storage, 1978: pp. 353–393.
[23] M.A. Pick, H. Wenzl, PHYSICAL METALLURGY OF FeTi-HYDRIDE AND ITS BEHAVIOUR IN A HYDROGEN STORAGE CONTAINER, Int. J. Hydrogen Energy. 1 (1977) 413–420.
[24] T. Ha, Y.W. Cho, S.-I. Lee, J.-Y. Suh, J. Lee, J.-H. Shim, Y.-S. Lee, Hydrogen occupation in Ti4M2Oy compounds (M=Fe, Co, Ni, Cu, and y = 0, 1) and their hydrogen storage characteristics, J. Alloys Compd. 891 (2021) 162050. 10.1016/j.jallcom.2021.162050.
[25] K. Hiebl, E. Tuscher, H. Bittner, Untersuchungen an Hydriden im Bereich der ~-Phase Ti4Fe20, Monatshefte Fiir Chemie. 110 (1979) 9–19.
[26] T. Matsumoto, M. Amano, Y. Sasaki, Hydrogenation of FeTi-based alloys containing β-Ti, J. Less Common Met. 88 (1982) 443–449. https://doi.org/10.1016/0022-5088(82)90255-7.
[27] H. Nagai, K. Kitagaki, K. Shoji, Microstructure and hydriding characteristics of FeTi alloys containing manganese, J. Less-Common Met. 134 (1987) 275–286.10.1016/0022-5088(87)90567-4.
[28] D.P. Broon, Hydrogen Storage Materials The Characterisation of their storage properties, Springer-Verlag London, 2011.
[29] J.I. Goldstein, D.E. Newbury, P. Echlin, D.C. Joy, A.D. Roming, C.E. Lyman, C. Fiori, E. Lifshin, Scanning Electron Microscopy and X-Ray Microanalysis, Second Edi, n.d.
[30] M. V. Lototskyy, I. Tolj, L. Pickering, C. Sita, F. Barbir, V. Yartys, The use of metal hydrides in fuel cell applications, Prog. Nat. Sci. Mater. Int. 27 (2017) 3–20. 10.1016/j.pnsc.2017.01.008.
[31] B. Zalba, J.M. Marìn, L.F. Cabeza, H. Mehling, Review on thermal energy storage with phase change : materials , heat transfer analysis and applications, Appl. Therm. Eng. 23 (2003) 251–283.
[32] A.M. Khudhair, M.M. Farid, A review on energy conservation in building applications with thermal storage by latent heat using phase change materials, Energy Convers. Manag. 45 (2004) 263–275. 10.1016/S0196-8904(03)00131-6.
[33] S. Mellouli, N. Ben Khedher, F. Askri, A. Jemni, S. Ben Nasrallah, Numerical analysis of metal hydride tank with phase change material, Appl. Therm. Eng. 90 (2015) 674–682. 10.1016/j.applthermaleng.2015.07.022.
[34] H. Ben Mâad, F. Askri, S. Ben Nasrallah, Heat and mass transfer in a metal hydrogen reactor equipped with a phase-change heat-exchanger, Int. J. Therm. Sci. 99 (2016) 271–278. 10.1016/j.ijthermalsci.2015.09.003.
[35] P. Marty, P. De Rango, B. Delhomme, S. Garrier, Various tools for optimizing large scale magnesium hydride storage, J. Alloys Compd. 580 (2013) S324–S328. 10.1016/j.jallcom.2013.02.169.
[36] A.A. Rabienataj Darzi, H. Hassanzadeh Afrouzi, A. Moshfegh, M. Farhadi, Absorption and desorption of hydrogen in long metal hydride tank equipped with phase change material jacket, Int. J. Hydrogen Energy. 41 (2016) 9595–9610. 10.1016/j.ijhydene.2016.04.051.
[37] H. El Mghari, J. Huot, J. Xiao, Analysis of hydrogen storage performance of metal hydride reactor with phase change materials, Int. J. Hydrogen Energy. 44 (2019) 28893–28908. 10.1016/j.ijhydene.2019.09.090.
[38] H. Ben Mâad, F. Askri, J. Virgone, S. Ben Nasrallah, Numerical study of high temperature

metal-hydrogen reactor (Mg2Ni-H2) with heat reaction recovery using phase-change material during desorption, Appl. Therm. Eng. 140 (2018) 225–234. 10.1016/j.applthermaleng.2018.05.009.
[39] L. Tong, Y. Yuan, T. Yang, P. Bénard, C. Yuan, J. Xiao, Hydrogen release from a metal hydride tank with phase change material jacket and coiled-tube heat exchanger, Int. J. Hydrogen Energy. 46 (2021) 32135–32148. https://doi.org/10.1016/j.ijhydene.2021.06.230.
[40] J. Yao, P. Zhu, L. Guo, L. Duan, Z. Zhang, S. Kurko, Z. Wu, A continuous hydrogen absorption/desorption model for metal hydride reactor coupled with PCM as heat management and its application in the fuel cell power system, Int. J. Hydrogen Energy. 45 (2020) 28087–28099. 10.1016/j.ijhydene.2020.05.089.
[41] Y. Ye, J. Lu, J. Ding, W. Wang, J. Yan, Numerical simulation on the storage performance of a phase change materials based metal hydride hydrogen storage tank, Appl. Energy. 278 (2020) 115682. 10.1016/j.apenergy.2020.115682.
[42] S. Mellouli, F. Askri, E. Abhilash, S. Ben Nasrallah, Impact of using a heat transfer fluid pipe in a metal hydride-phase change material tank, Appl. Therm. Eng. 113 (2017) 554–565. 10.1016/j.applthermaleng.2016.11.065.
[43] M. Pan, Y. Zhong, Experimental and numerical investigation of a thermal management system for a Li-ion battery pack using cutting copper fiber sintered skeleton/paraffin composite phase change materials, Int. J. Heat Mass Transf. 126 (2018) 531–543. 10.1016/j.ijheatmasstransfer.2018.06.014.
[44] L. Tong, J. Xiao, P. Bénard, R. Chahine, Thermal management of metal hydride hydrogen storage reservoir using phase change materials, Int. J. Hydrogen Energy. 44 (2019) 21055–21066. 10.1016/j.ijhydene.2019.03.127.
[45] S.S. Ardahaie, M.J. Hosseini, M. Eisapour, A.H. Eisapour, A.A. Ranjbar, A novel porous metal hydride tank for hydrogen energy storage and consumption assisted by PCM jackets and spiral tubes, J. Clean. Prod. 311 (2021) 127674. /10.1016/j.jclepro.2021.127674.
[46] Y. Ye, J. Ding, W. Wang, J. Yan, The storage performance of metal hydride hydrogen storage tanks with reaction heat recovery by phase change materials, Appl. Energy. 299 (2021) 117255.10.1016/j.apenergy.2021.117255.
[47] T. Alqahtani, A. Bamasag, S. Mellouli, F. Askri, P.E. Phelan, Cyclic behaviors of a novel design of a metal hydride reactor encircled by cascaded phase change materials, Int. J. Hydrogen Energy. 45 (2020) 32285–32297. 10.1016/j.ijhydene.2020.08.280.
[48] H.Q. Nguyen, B. Shabani, Metal hydride thermal management using phase change material in the context of a standalone solar-hydrogen system, Energy Convers. Manag. 224 (2020) 113352. 10.1016/j.enconman.2020.113352.
[49] S. Garrier, B. Delhomme, P. De Rango, P. Marty, D. Fruchart, S. Miraglia, A new MgH2 tank concept using a phase-change material to store the heat of reaction, Int. J. Hydrogen Energy. 38 (2013) 9766–9771. 10.1016/j.ijhydene.2013.05.026.
[50] M. Jehan, D. Fruchart, McPhy-Energy's proposal for solid state hydrogen storage materials and systems, J. Alloys Compd. 580 (2013) S343–S348. 10.1016/j.jallcom.2013.03.266.
[51] S. Garrier, A. Chaise, P. De Rango, P. Marty, B. Delhomme, D. Fruchart, S. Miraglia, MgH2 intermediate scale tank tests under various experimental conditions, Int. J. Hydrogen Energy. 36 (2011) 9719–9726. 10.1016/j.ijhydene.2011.05.017.
[52] McPhy website: www.mcphy.com.
[53] D. Ghosh, C. Guha, J. Ghose, Numerical investigation of paraffin wax solidification in spherical and rectangular cavity, Heat Mass Transf. Und Stoffuebertragung. 55 (2019) 3547–3559. 10.1007/s00231-019-02680-4.

Chapter 5
Hydrogen compression

5.1 A two stage MHC based on commercial alloys for a small-scale hydrogen refuelling station

5.1.1 Introduction

Few examples of MHCs exist at the prototype level and even fewer are commercially available. The commercial items and prototype systems proposed till now can work generally between room temperature up to a maximum of 150 °C, delivering pressure up to 200 - 250 bar [1–5]. A commercially available compressor is the compact HyCo developed by GRZ Technologies for laboratory purposes [1,6]. Always at commercial level, the Norwegian company HYSTORSYS AS [2] provides compressors able to release up to 250 bar at 150 °C, with an hydrogen flow up to 30 Nm^3/h, depending on client needs [3]. A common use of MHC is its integration in H2RS, and representative examples are the systems built for the refuelling of forklifts in South Africa at the HySA laboratory and in Croatia, in the framework of the project HYDRIDE4MOBILITY, in which MHCs were provided by HYSTORSYS AS [2,4]. The latter company integrated an MHC as first compression stage of a refuelling station for cars in Lillestrøm (NO), in substitution of a diaphragm compressors [3,7]. A high-pressure prototype was also reported with an output pressure of 414 bar at about 130 °C [8], and a low temperature prototype of MHC has been developed by the HYSTORE Technology Ltd, that delivers H_2 at 220 bar working at 80 °C, resulting advantageous since water is used as thermal fluid [9]. The commercial/prototype systems reported above, have in common the use of IMC (mostly AB_5 $LaNi_5$-based and AB_2 Ti-based) in which the powders are not available on the market, so a private production can be inferred for these systems [1–4,8,9]. This is not advantaging for an industrial scale production of MHC. Indeed, large realization implies the use of large quantity of compounds that can be satisfied only through an industrial production based on already commercially available alloys. The advantage of realizing prototype based on already commercially used compounds is their availability, allowing an easy scaling up and possible placing on the market. Only one example was found in the literature in which the use of commercial hydrides powder was explicitly cited [10]. The MHC realized compresses thanks to $LaNi_5$ and $La_{0.5}Ce_{0.5}Ni_5$ alloys acquired from the industry Whole Win [10]. By using these commercial alloys, H_2 is released at 150 bar at 150 °C and has a size for medium/large scale application [10].

In this section, it is presented the work performed in collaboration with the industry

Technodelta of Chivasso (Italy), linked to the realization of a two stage MHC based on commercial IMCs and integrated in a small-scale H2RS, developed in the framework of the project Clean-DronHy, supported by Regione Piemonte. The work aims to show the feasibility of a completely green H2RS based on renewable, exploiting the production of H_2 by an EL driven by photovoltaic and an MHC based on commercial alloys. The use of commercial alloy was mandatory for the project, since thanks to the use of commercial devices from the photovoltaic panels to the alloys, there is the advantage to assure an easy scale-up of the system. Thinking to a commercial use, large scale production of MHC implies a large-scale production of alloys that only industries can satisfy. There are already spread around the world industries that produce IMCs, AB, AB_2 and AB_5. The MHC involves two stages based on the $La_{0.9}Ce_{0.1}Ni_5$ supply by LabTech and the Hydralloy-C5, commercialized by Gfe. This work presents the alloys selection and characterization, the building and integration of the MHC in the H2RS, and MHC performances. Tests aimed to optimize the process according to plant design, evaluating also the power involved and compression performances, in terms of delivery pressure and H_2 flow.

5.1.1.1 Project Clean-DronHy

Nowadays, drones are used in a wide range of applications, from civil to military. It is therefore of interest to develop systems with increasing performances, in terms of energy efficiency and running time. In this regard, the use of Fuel Cell (FC) is a possible solution, since hydrogen has a higher energy density compared to batteries [11], allowing to reach higher time of flights. In the comparison with batteries, FCs are promising for high amount of hydrogen stored, assuring higher autonomy [12]. As an example, Intelligent Energy for a 650 W Fuel Cell plans a time of flights of 85 min with 2.0 l of compressed H_2 with 256 Wh/kg and 10 h 50 min with 6.0 l of liquid H_2 [13]. In 2019, with the time of flight of 12 h 7 min and 22 sec the drone developed by the MetaVista team, powered with FC by Intelligent Energy, was awarded in the Guinness World Record. The drone was based on the 800 W Fuel Cells power module equipped with 6.0 l of liquid hydrogen [14].

A hydrogen powered drone has been developed in the project Clean-DronHy financed by Regione Piemonte in Italy. A 3.0 l type IV cylinder with compressed H_2 at 300 bar is located on the drone, which has a diameter of 1.3 m and a weight of about 6.5 kg. The latter increases up to 10 kg when integrated with all the components (*e.g.* all the electronics, the H_2 bottle).

Two PEM-FCs commercialized by Intelligent Energy of 650 W each together with a battery guarantee a total power of 1.3 kW. The peak power is about 1 kW, and the H_2 consumption is of 13 Nl/min per kW. In primary flying tests, thanks to the compressed H_2 loaded, the drone was able to fly continuously for 70 min. To underline the feasibility of H_2 technology, the project also required the development of the H2RS to produce and compress on site the daily amount of gas required by the H_2-powered drone. At this regard, it was decided to exploit renewable energy, producing H_2 from an electrolyser driven by photovoltaic panels (PVP), and using MH for gas compression.

5.1.2 Experimental

The structural and morphological characterization of the IMCs for the MHC was performed by SEM and PXD analysis. Alloys were analysed as loose powder by acquiring secondary electron (SE) images for the morphological study, while EDX elemental mapping was performed at 20 keV. Phases and structural analysis occurred by acquiring PXD patterns. Samples preparation involved that the powder is manually grinded in a mortar to be packed in glass capillaries with a diameter of 0.8 mm (Debye Scherrer geometry). Measurements have been performed with steps of 0.016 °, from 25 ° to 120 ° in 2θ, time per scan of 130 s, for the (LaCe)Ni_5-alloys; from 25 ° to 80 ° in 2θ, time per scan of 255 s, for the $MmNi_{4.15}Fe_{0.85}$; from 35 ° to 120 ° in 2θ, time per scan of 194 s, for the $Ti(Fe,Mn)_{0.9}$; from 25 ° to 100 ° in 2θ, time per scan of 250 s for the Hydralloy-C5. Finally, the H_2 sorption measurements occurred in the AMC of Pittsburgh (Chapter 2).

5.1.3 Results and discussion

5.1.3.1 H2RS design

As reported in section 5.1.1.1 the project presents constraints in the design of the H2RS to satisfy the daily amount of H_2 required by drone. Fixing at least 1 flight per day, the H2RS needs to produce about 80 g of H_2 per flight, since the drone has a 3.0 l cylinder that need to be charged at 300 bar to allow 70 min of continuous flight. Then, the H2RS should provide the H_2 exploiting electrolysis and compression based on MH. Concerning the production of H_2, after a market survey evaluating EL performances in terms of delivery pressure, working temperature, the possibility to be integrated with PVP, output H_2 flow and costs, the EL model *EL250* commercialized by Enapter was selected. It is an alkaline EL, based on KOH, which produces H_2 at 35 bar, working at an ambient temperature between 5 °C and 45 °C,

and presenting a H_2 flow of about 250 Nl/h. It can be supplied by grid current or by photovoltaic panels. For the H2RS the PV plant developed involves 10 panels of 300 W, commercialized by Hanover Solar. At 35 bar, the producer declared an output H_2 purity of 99.94 %, and oxygen and water are expected as contaminants. In particular, the producer declares about 600 ppm of water in the outer H_2 gas at 30 bar, while at the same outlet pressure, there are not data available concerning the oxygen content. To increase the purity of the outer gas, a homemade purification stage was integrated at the outlet of the EL, that consists of a stainless-steel tube filled with *Zeolite 13X*, to reduce the impurities of water, thanks to their adsorption. Based on the EL characteristic, the MHC have been designed and some parameters needed to be fixed to select the proper alloys. Another requirement of the plant is to avoid the usage of pumps for the H_2 flow, that must be spontaneous exploiting the different pressure between stages, *i.e.* from a high pressure towards a lower one. Thus, the MHC needs to compress H_2 directly form the EL at $\leq$ 30 bar to $\geq$ 300 bar to fill the drone cylinder at 300 bar. To select the proper MH, it is important to fix the values of temperature in absorption, T_{low}, and the one in desorption, T_{high}. For absorption, an ambient temperature of 20 - 30 °C was chosen, in order to have a similar working temperature of the EL, avoiding any cooling or heating. While in desorption, it was chosen to not exceed 150 °C, in line with commercially available MHC and prototype realised so far [1,2,4,10]. Moreover, the goal was to find an alloy that can reach the 300 bar at even lower temperatures. Indeed, the lower is the temperature in desorption, the easier would be the plant design concerning the heat exchanger and management. The selection of the proper alloys involved a market survey of the commercially available IMCs, AB, AB_2 and AB_5 in the frame of international producers. For each alloy, the equilibrium pressure was estimated at the T_{low} and T_{high}, by applying the Van't Hoff equation [15], using values of $\Delta H_{abs/des}$ and $\Delta S_{abs/des}$ reported in literature and/or declared by the producers for the considered compositions. From the performed study, five alloys were selected, and their producers, cost and shipping time are summarized Table 1. The market survey pointed out that the maximum pressure that can be achieved at 150 °C is about 250 bar, with the Hydralloy C-5, an AB_2 IMC, that however is sensitive to O_2 and H_2O contaminations [15]. Since H_2 is produced by the EL, a previous stage was planned as purification based on AB/AB_5 alloys, since they have more resistance to impurities. Thus, the MHC is composed of two stages: the first one involves an alloy selected between the AB/AB_5 bought (Table 1) and a second stage with the Hydralloy-C5.

Table 1: Alloys producer, type, cost, and shipping time.

Producer (Country)	**Alloy**	**Type**	**Cost €/kg**	**Shipping Time**
GKN (D)	$Ti(FeMn)_{0.9}$	AB	-	-
LabTech (BG)	$La_{0.9}Ce_{0.1}Ni_5$	AB_5	500	1 month
WholeWin (RC)	$La_{0.6}Ce_{0.4}Ni_5$	AB_5	269	4 months
JMC (J)	$MmNi_{4.15}Fe_{0.85}$	AB_5	780	10 months
Gfe (D)	Hydralloy-C5 $(TiZr)(MnVFe)_2$	AB_2	100	1 month

This result highlights the impossibility to decrease the T_{high} below 150 °C, and to reach 300 bar with commercially available IMCs. All alloys were commercialized in form of powder and stocked in air. During the study, to select the proper IMC for the first stage, it was important to consider that, if the alloy requires an activation, both stages should be able to be processed in the same conditions of pressure and temperature to allow an easier plant management. The activation must be performed directly on the plant, without exceeding the maximum affordable pressure and temperature, *i.e* 350 bar and 150 °C. Then, alloys costs and shipping time has been also considered. Indeed, when realizing a system and thinking to its possible scale-up, the economical aspect plays a key role, and an advantage of the Hydralloy-C5 in the second stage is also its cheapness.

To satisfy the target of production of 300 bar of H_2 by the H2RS, the compression unit involves the MHC joined by a commercial booster commercialized by Maximator, that has a compression ratio 1 : 20, with a pressure ratio air : H_2 of 1 : 60.

5.1.3.2 Alloys study

5.1.3.2.1 Hydralloy-C5

The Hydralloy-C5 was studied to obtain the data to consider for the selection of the proper alloy for the first stage. Figure 1 and Table 2 report the SE images and the EDX elemental amount acquired in the SEM analysis on the Hydralloy-C5 in the form of powder. As can be seen from the SE-image reported in Figure 1, the powder present coarse size, with a particle dimension lower than 2 mm, in agreement with producer declaration. The Hydralloy C-5 is a $TiMn_2$-based alloy substituted with Zr, Fe and V [16]. The composition declared by the producer was confirmed through EDX elemental analysis. Experimental data are in line with producer datasheet (Table 2) resulting in a possible composition $Ti_{0.95}Zr_{0.05}Mn_{1.55}V_{0.45}Fe_{0.09}$,

in good agreement with literature [17–19].

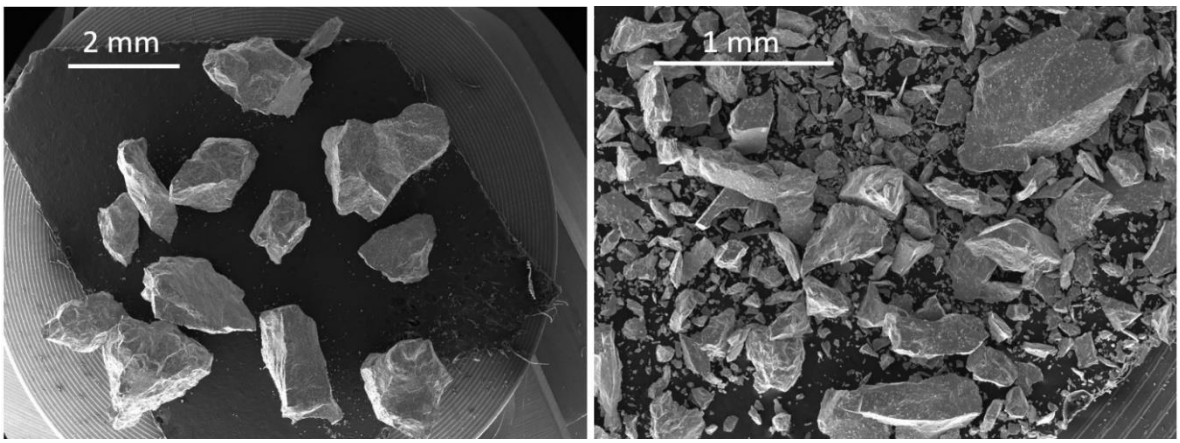

Figure 1: SEM-SE images as loose powder of the Hydralloy C-5.

Table 2: Atomic and weight percentage obtained by the EDX elemental maps performed on the Hydralloy-C5, together with values declared by the producer.

Elements	**at. %**	**wt. %**	**Gfe datasheet**
Ti	31	28	25 – 35 wt.%
Zr	2	3	
Mn	49	52	45 – 55 wt.%
V	15	14	15 – 25 wt.%
Fe	3	3	

Acquiring the PXD pattern, no secondary phases were detected, and the Rietveld refinement was performed to evaluate structural information (Figure 2). The Hydralloy-C5 has the hexagonal phase Laves (C14), with cell parameters *a* equal to 4.873(3) Å and *c* to 7.988(5) Å.

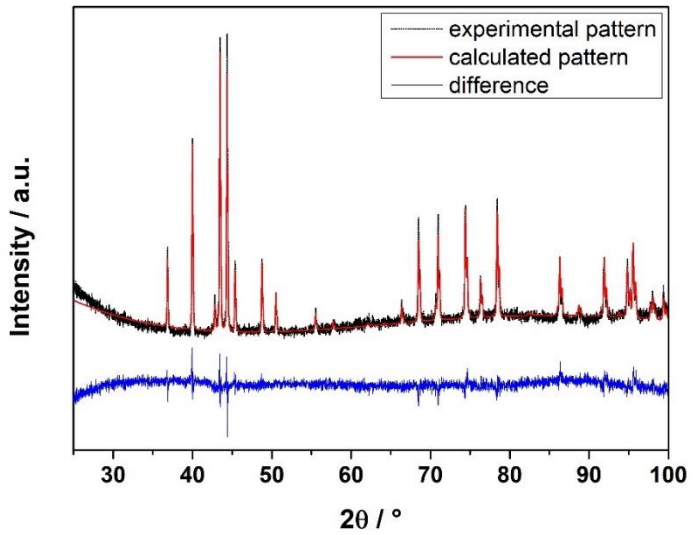

Figure 2: Rietveld refinement of the acquired pattern performed on the Hydralloy-C5.

The alloy requires an activation before the first hydrogenation and since the plant can afford high temperature and pressure, it was possible to activate the powder at 150 °C (*i.e.* T_{high}) and 50 bar, alternating loading and unloading of hydrogen, resulting in ten cycles. The use of a temperature of 150 °C is advantageous for the plant management since it is not necessary to change the temperature conditions between the activation and the compression stage. After the activation, pcT-curves were acquired at 32 °, 56 ° and 79 °C and are shown in Figure 3. Table 3 reports the thermodynamic parameters of $\Delta H_{abs/des}$ and $\Delta S_{abs/des}$, obtained by applying the Van't Hoff plot, comparing data with literature. The experimental thermodynamic data of $\Delta H_{abs/des}$ and $\Delta S_{abs/des}$ are comparable with literature (Table 3).

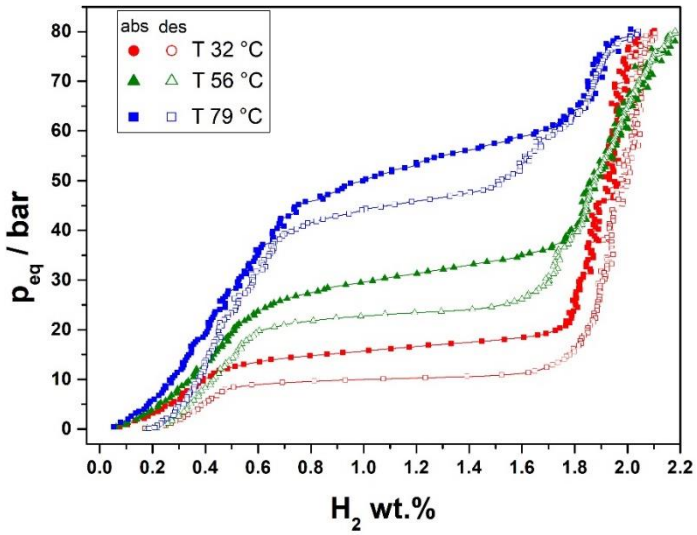

Figure 3: pcT curves in absorption (full points) and deposition (empty points) registered for the Hydralloy-C5.

From the pcT-curves, it can be seen that the slope progressively increases with temperature, especially in absorption (Figure 3). There is the occurrence of hysteresis which energy is

0.9 ± 0.4 kJ/mol. Using the thermodynamic data obtained, by applying the Van't Hoff equation [15], the equilibrium pressure (p_{eq}) in absorption and desorption at the T_{low} and T_{high} was evaluated, and results are reported in Table 3.

Table 3: Experimental and literature values of $\Delta H_{abs/des}$ and $\Delta S_{abs/des}$ and the equilibrium pressure calculated at the T_{low} and T_{high} for the Hydralloy-C5.

ΔH_{abs} kJ/mol$_{H2}$ ΔS_{abs} J/mol$_{H2}$K	**ΔH_{des} kJ/mol$_{H2}$ ΔS_{des} J/mol$_{H2}$K**	**p_{eq} T_{low} bar p_{eq} T_{high} bar**	**ΔH ΔS [Ref.] Abs.**	**ΔH ΔS [Ref.] Des.**
23	29	13	23	28
98	113	236	97	112
			[20]	[20]

As expected by the market survey, the Hydralloy-C5 should release H_2 at pressure higher than 200 bar at 150 °C, *i.e.* 236 bar. It is worth noting that it shows also a low equilibrium pressure at T_{low}, *i.e.* 13 bar, being able to absorb H_2 directly form the EL, resulting suitable for a single stage MHC, if high purity H_2 would be available.

5.1.3.2.2 AB and AB_5 compounds

Concerning the study of AB and AB_5 alloys to select as first stage of the MHC, Table 4 reports the results of the EDX analysis performed to confirm their composition. Composition are confirmed for all compounds by the EDX elemental analysis, and for the $Ti(Fe,Mn)_{0.9}$ and $MmNi_{4.15}Fe_{0.85}$ data are in agreement with producer declaration available in the datasheet (Table 4). The precise composition is $La_{0.84}Ce_{0.12}Ni_{5.04}$, $La_{0.59}Ce_{0.44}Ni_{4.97}$, $Mm_{1.08}Ni_{4.07}Fe_{0.84}$, observing in the first and latter case that when La or Mm is slightly underestimate, Ni and Ce are overestimate and vice versa. The same occurs for the $Ti(Fe,Mn)_{0.9}$ alloy, that results in $Ti_{1.05}(Fe,Mn)_{0.85}$ due to an overestimation of Ti despite the Fe,Mn. However, considering the error on the measure of composition of about 1 at. %, compositions agree with producer declaration for all compounds.

Table 4: Elemental amounts obtained by EDX analysis for the $Ti(Fe,Mn)_{0.9}$, the $La_{0.9}Ce_{0.1}Ni_5$, $La_{0.6}Ce_{0.4}Ni_5$ and $MmNi_{4.15}Fe_{0.85}$, with values reported in the datasheet when available from the producer.

Alloys	Elements	at. %	wt. %	datasheet
$Ti(Fe,Mn)_{0.9}$	Ti	55	52	40 – 60 wt.%
	Fe	39	42	40 – 60 wt.%
	Mn	6	6	4 – 6 wt.%
$La_{0.9}Ce_{0.1}Ni_5$	La	14	27	-
	Ce	2	3	
	Ni	84	70	
$La_{0.6}Ce_{0.4}Ni_5$	La	10	19	-
	Ce	7	14	
	Ni	83	67	
$MmNi_{4.15}Fe_{0.85}$	(La,Ce,Pr,Nb)	18	34	33 wt.%
	Ni	68	55	56 wt.%
	Fe	14	11	11 wt.%

PXD patterns were acquired to determine phases present in the alloy, and their structure (Figure 4). From the PXD analysis, only in the $Ti(Fe,Mn)_{0.9}$ an oxide was detected as secondary phases (9.8 wt% of $Ti_4Fe_2O_x$ with $0.4 \leq x \leq 1$) (Figure 4-a), while other compounds are single phase (Figure 4-b,c,d). Structural information obtained by the refinement are summarized in Table 5. The $Ti(Fe,Mn)_{0.9}$ has the cubic CsCl-type structure, space group $Pm\bar{3}m$, of TiFe and the substitution of Mn despite Fe causes an increase of the cell parameter, in agreement with the literature [21]. While all the AB_5 alloys has the same hexagonal $CaCu_5$ structure, space group *P6/mmm*, of $LaNi_5$. The substitution of La with Ce causes a decrease in *a* cell parameter, compared to pure $LaNi_5$[22]. While, and as can be seen from Table 5, comparing results of $La_{0.9}Ce_{0.1}Ni_5$ with those of $La_{0.4}Ce_{0.6}Ni_5$, by increasing the Ce content, the cell parameter decreases in both *a* and *c* parameters, in agreement with the literature [23]. Finally, considering the $MmNi_{4.15}Fe_{0.85}$, the use of the Mm instead of La and the substitution of Ni with Fe promote a decrease in *a* parameter and an increase in *c* parameter, compared to pure $LaNi_5$ [22]. For the $MmNi_{4.15}Fe_{0.85}$ the value of *a* and *c* parameters is respectively the lowest and the highest compared to the two $(La,Ce)Ni_5$ alloys.

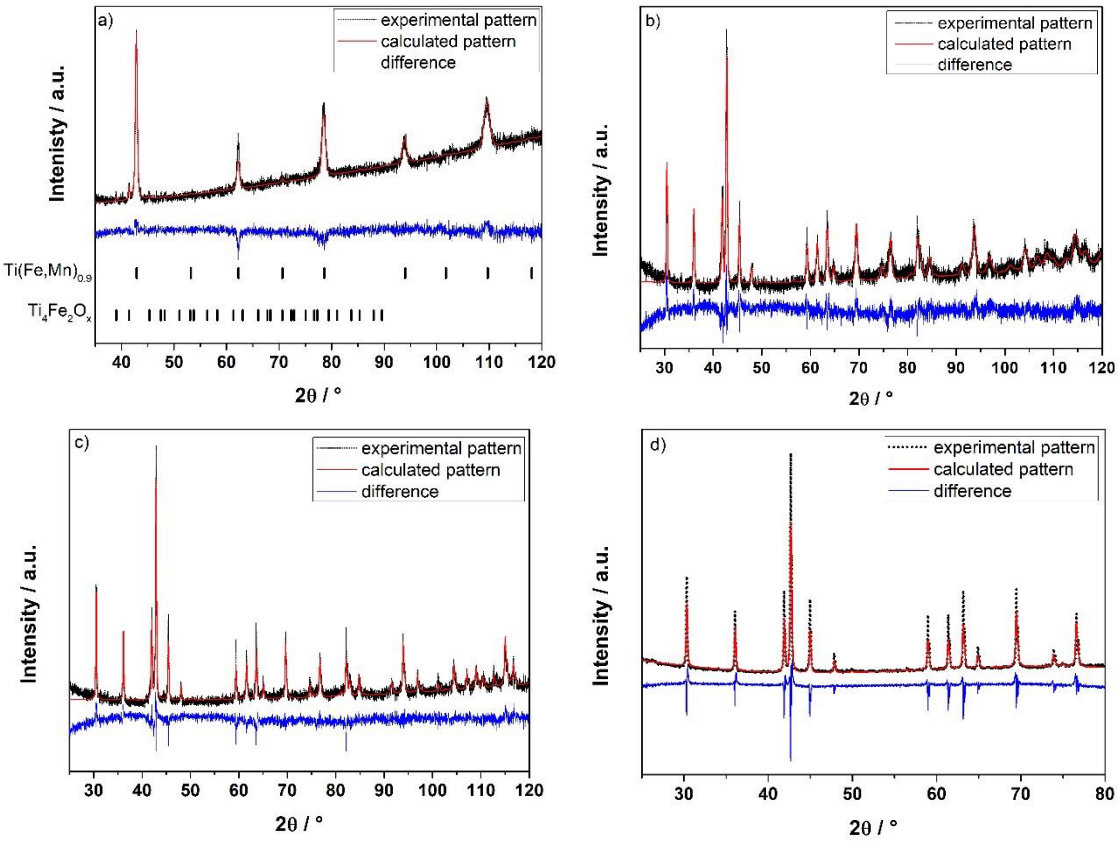

Figure 4: Rietveld refinement of the PXD patterns: (a) $Ti(Fe,Mn)_{0.9}$, (b) $La_{0.9}Ce_{0.1}Ni_5$; (c) $La_{0.6}Ce_{0.4}Ni_5$; (d) $MmNi_{4.15}Fe_{0.85}$.

Table 5: Structural results obtained from the refinement of the PXD pattern for $Ti(Fe,Mn)_{0.9}$, the $La_{0.9}Ce_{0.1}Ni_5$, $La_{0.6}Ce_{0.4}Ni_5$ and $MmNi_{4.15}Fe_{0.85}$. Literature values of pure TiFe and $LaNi_5$ are also reported for comparison.

Alloys	Space group	Cell parameters	Reference
$Ti(Fe,Mn)_{0.9}$	$Pm\bar{3}m$	a = 2.985(0) Å	TiFe [21] a = 2.972 Å
$La_{0.9}Ce_{0.1}Ni_5$	*P6/mmm*	a = 4.980(7) Å c = 3.992(2) Å	$LaNi_5$ [22] a = 5.01(8) Å c = 3.98(7) Å
$La_{0.6}Ce_{0.4}Ni_5$	*P6/mmm*	a = 4.964(1) Å c = 3.989(6) Å	
$MmNi_{4.15}Fe_{0.85}$	*P6/mmm*	a = 4.972(2) Å c = 4.028(5) Å	

All alloys required an activation, that was investigated trying to process the alloys at 150 °C and 50 bar as for the Hydralloy-C5 (section 5.1.3.2.1). In these conditions, the $La_{0.9}Ce_{0.1}Ni_5$ and the $La_{0.6}Ce_{0.4}Ni_5$ alloys can be activated in 6 cycles, while more than 30 cycles were necessary for the $MmNi_{4.15}Fe_{0.85}$. Finally, a different activation procedure was necessary for the $Ti(Fe,Mn)_{0.9}$, which involves three cycles at 90 °C at 20 - 30 - 40 bar of H_2 followed by

33 cycles at 60 °C with 40 bar of H_2. After the activation, pcT-curves were acquired (Figure 5) and results from the thermodynamic study ($\Delta H_{abs/des}$ and $\Delta S_{abs/des}$) and the equilibrium pressure obtained at the T_{low} and T_{high} are reported in Table 6.

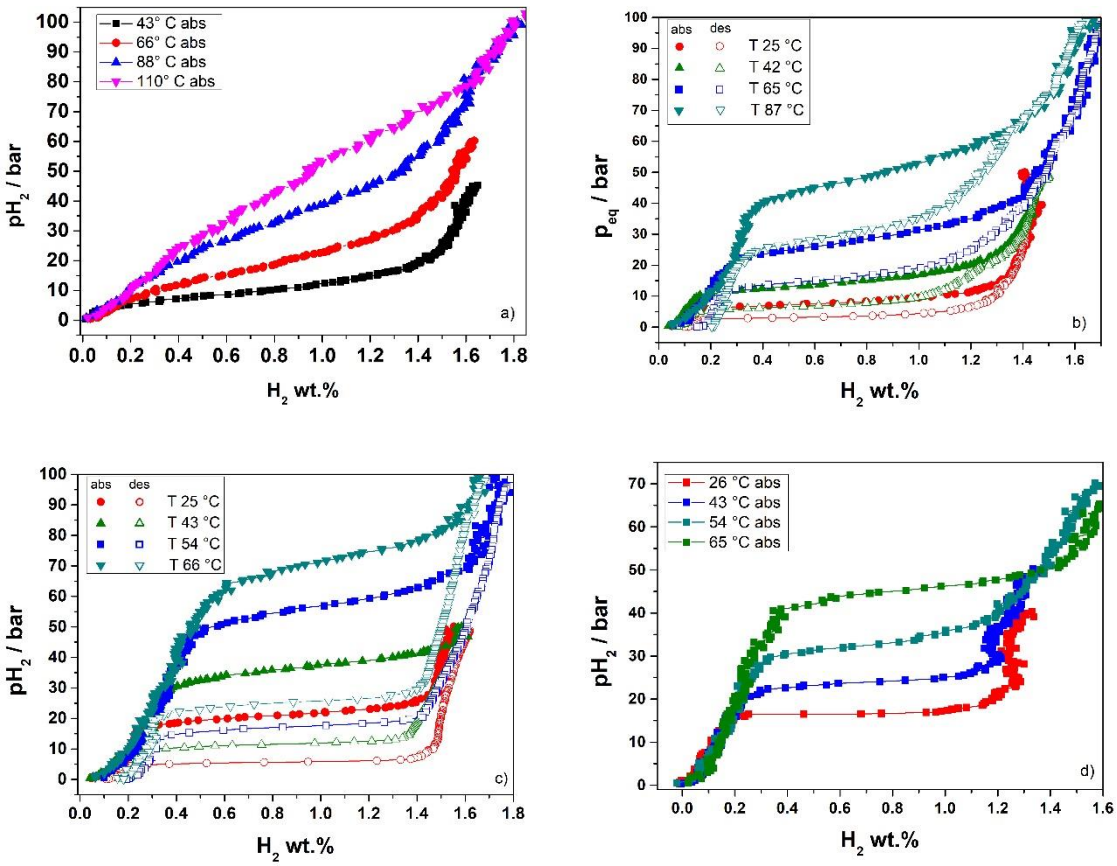

Figure 5: pcT curves in absorption (full points) and desorption (empty points): (a) Ti(Fe,Mn)$_{0.9}$, (b) La$_{0.9}$Ce$_{0.1}$Ni$_5$; (c) La$_{0.6}$Ce$_{0.4}$Ni$_5$; (d) MmNi$_{4.15}$Fe$_{0.85}$.

Ti(Fe,Mn)$_{0.9}$ and MmNi$_{4.15}$Fe$_{0.85}$ do not present the curves in desorption, because of the occurrence of instrumental problems. Ti(FeMn)$_{0.9}$ has marked sloping plateau in absorption, as already observed for the TiFe$_{0.85}$Mn$_{0.05}$ (Chapter 4), due to inhomogeneity in the composition [24,25]. On the contrary, in the AB_5 alloys, the phenomenon is less marked, observing an increase of the slope increasing the temperature, especially in absorption. Hysteresis occurs both in La$_{0.9}$Ce$_{0.1}$Ni$_5$ and La$_{0.6}$Ce$_{0.4}$N$_i$ alloys, with an energy of 1.8 $\pm$ 0.3 kJ/mol and 3.2 $\pm$ 0.1 kJ/mol, respectively. Studying the two (La,Ce)Ni$_5$ alloys, it can be concluded that increasing the amount of Ce, an increase in hysteresis and in the equilibrium pressure is observed, in agreement with the literature [23]. The latter phenomenon is linked to the decrease of the cell parameters that Ce promoted, causing an increase in the equilibrium pressure, both in absorption and in desorption, making the class of the AB_5 alloys La-Ce-Ni particularly interesting for compression. Moreover, the substitution with Ce

was observed to be advantageous in limiting the disproportion along cycling, as stated in in ref. [10] during the long cycling study on the MHC realized. It is worth noting that the $La_{0.6}Ce_{0.4}Ni_5$ could release H_2 at about 216 bar, resulting also competitive with the Hydralloy-C5, that anyway allows to reach a pressure slightly higher at the T_{high}.

Table 6: Experimental and literature values of $\Delta H_{abs/des}$ and $\Delta S_{abs/des}$ and the equilibrium pressure calculated at the T_{low} and T_{high} for the $Ti(Fe,Mn)_{0.9}$, $La_{0.9}Ce_{0.1}Ni_5$, $La_{0.6}Ce_{0.4}Ni_5$ and $MmNi_{4.15}Fe_{0.85}$..

Alloy	**ΔH_{abs}** **kJ/mol$_{H2}$** **ΔS_{abs}** **J/mol$_{H2}$K**	**ΔH_{des}** **kJ/mol$_{H2}$** **ΔS_{des}** **J/mol$_{H2}$K**	**p_{eq} T_{low}** **bar** **p_{eq} T_{high}** **bar**	**ΔH** **ΔS** **[Ref.]** **Abs.**	**ΔH** **ΔS** **[Ref.]** **Des.**
$Ti(Fe,Mn)_{0.9}$	21 ± 3 93 ± 11	-	15 -	31.1 114 [25]	35.4 124 [25]
$La_{0.9}Ce_{0.1}Ni_5$	26 106	31 115	9 150	26.3 100 [26]	31.5 113 [26]
$La_{0.6}Ce_{0.4}Ni_5$	26 113	31 118	22 216	45.7 116.3 [15]	20.1 109.7 [15]
$MmNi_{4.15}Fe_{0.4}$	21 93	-	13 -	-	-

Concluding, results agree with the literature and are in line with the estimations from the market survey. In the light of the results linked to AB and AB_5 compounds, it is possible to select the 1st stage of compression, considering cost, shipping time (Table 1), activation procedure in relation to the Hydralloy-C5, and the equilibrium pressure in absorption (Table 6). Because of the cost and shipping time, the $MmNi_{4.15}Fe_{0.85}$ is not practical, moreover it has a longer activation than Hydralloy-C5. Relating to the activation, also $Ti(FeMn)_{0.9}$ is not a good candidate, because of different conditions. The choice is between the two $(LaCe)Ni_5$ alloys, which have affordable cost, shipping time and an activation similar to Hydralloy-C5. The key parameter is the absorption rate, due to the integration with EL in the final plant. The reaction rate is described as a first order equation in which the rate (v) is directly proportional to the difference between the operative pressure (p) and the equilibrium one (peq), representing one of the main driving forces of the reaction [27] (Equation (1):

$$v = k(p - peq) \qquad \text{Eq. (1)}$$

Where *k* is the constant reaction rate. Thus, the higher is the difference between the supply pressure, *i.e*. 30 bar of the EL, and the equilibrium pressure at the T_{low} (Table 6), the higher would be the expected absorption rate. According to this observation, the $La_{0.9}Ce_{0.1}Ni_5$ has a lower equilibrium pressure than $La_{0.6}Ce_{0.4}Ni_5$. Acquiring the absorption curve at 25 bar and 25 °C for the $La_{0.9}Ce_{0.1}Ni_5$, the 90 % of the capacity is processed in 10 min, achieving 1.2 H_2 wt.%, while the maximum amount of about 1.4 H_2 wt.% was reached in 20 min. Thus, the $La_{0.9}Ce_{0.1}Ni_5$ is the alloy selected as first stage of the MHC and Figure 6 shows the SE image acquired with SEM instrument. Compared to the Hydralloy-C5 (Figure 1), the $La_{0.9}Ce_{0.1}Ni_5$ is present as fine powder, with an average particle size lower than 0.8 mm.

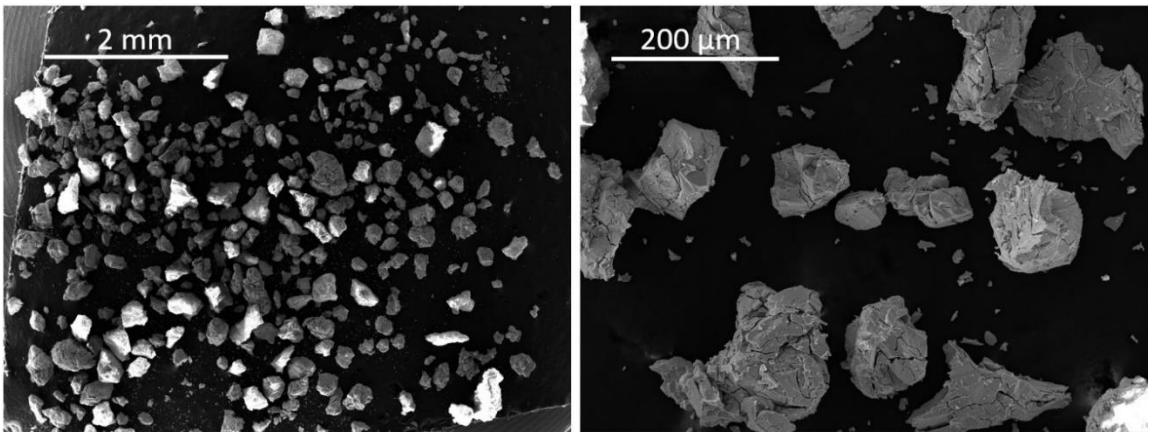

Figure 6: SEM-SE images of loose powder of the $La_{0.9}Ce_{0.1}Ni_5$.

In conclusions, the MHC involves two stages: the $La_{0.9}Ce_{0.1}Ni_5$ followed by the Hydralloy-C5. In the 1st stage, a fast absorption rate is expected, when supplied by the EL, then at 150 °C, H_2 should be desorbed at 150 bar. This release pressure would also ensure a fast absorption rate, when the Hydralloy-C5 is absorbing from the $La_{0.9}Ce_{0.1}Ni_5$, thanks to the high Δp between 150 bar and the 13 bar of Hydralloy-C5 equilibrium pressure (Table 3).

5.1.3.3. Building of the H2RS

5.1.3.3.1 MH reactors

The amount of IMC to allocate inside the reactors was calculated considering compressing H_2 only with the MHC. This implies to load the drone cylinder at 236 bar (p_{eq} of the Hydralloy-C5 at 150 °C, Table 3) in about 5 - 7 h, to guarantee at the drone one flight per day. The selected amount of IMC must consider absorbing the same amount of H_2 in both stages taking into account the different H_2 storage capacity of alloys, *i.e.* 1.2 H_2 wt. % for

the $La_{0.9}Ce_{0.1}Ni_5$ and 1.6 H_2 wt.% for the Hydralloy-C5 (Figure 3). It results in a lower amount of Hydralloy-C5 in the second stage compared to the first one, and 880 g of $La_{0.9}Ce_{0.1}Ni_5$ and 700 g of Hydralloy -C5 were calculated as suitable for the process. Reactors are made in AISI 316 stainless steel, they have a double tube geometry and same volumes. The reactor's dimension is evaluated from the first stage, R1, that was designed considering leaving 30 % of free volume to allow the expansion of the alloy in absorption. Because the second reactor, R2, has the same dimension, but a lower amount of powder, it results in almost a 50 % of free volume inside the reactor. Table 7 reports the dimension of R1 and R2.

Table 7: R1 and R2 reactor dimensions.

Internal diameter (Øint) porous metallic filter	12 mm
Porosity of the metallic porous filter	0.2 μm
Reactor length	389 mm
Internal reactor volume	0.363 dm^3
Øint inner tube	42.2 mm
Øint outer tube	52 mm
Thickness	4.85 mm
Øint capillary for the heat exchange	3 mm

Figure 7-a, b shows, respectively, the design of one reactor through a CAD representation and a corresponding picture. The IMC is located as loose powder in the inner tube of the reactor (Figure 7-a-i). Inside the reactor, a homemade porous metallic filter (Figure 7-a-i) is located to allow a homogeneous distribution of the H_2 in the powder-bed. The filter consists of a tube in steel with holes coated with a porous metallic sheet to prevent the spread of the powder out from the reactor. The gas supply and removal occur from the same side of this filter, and at the connection of the reactor with the hydrogen line an additional filter of 0.5 μm is present to assure that the powder is not spread along the gas line. In the double tube geometry, the external jacket is dedicated to the flow of the thermal fluid that is forced thanks to a small metallic capillary (Figure 7-a-ii-iv, b). Finally, the reactor is insulated with rock-wool and closed in an aluminium coating.

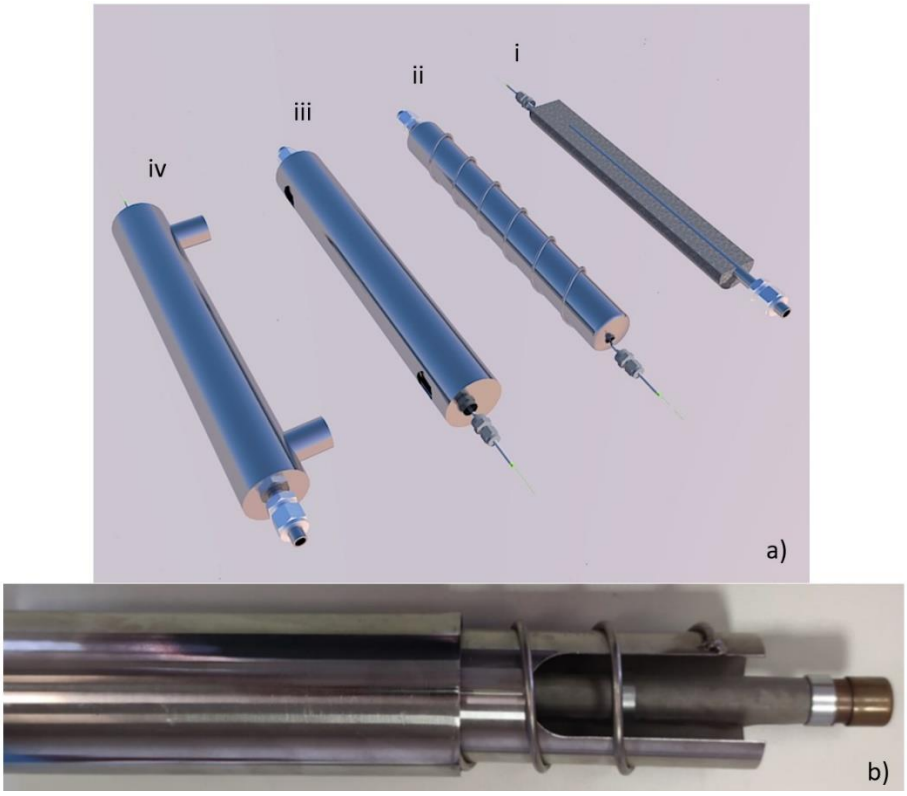

Figure 7: Details of the design of the MH- reactor: (a) CAD highlighting i) the powder with inside the porous filter for the flow of H_2, ii) the external part of the inner tube with the capillary, iii) and iv) the external jacket and coating; (b) picture of the reactor with a detail of the parts shown in the CAD.

5.1.3.3.2 System integration

Figure 8-a shows a picture of the H2RS realized at the Tecnodelta Srl. of Chivasso, while Figure 8-b shows the Process Flow Diagram (PFD) of the plant. As can be observed in Figure 8, the H2RS consists of three main parts:

1) The hydrogen production and purification unit, integrated with the PV panels (Figure 8-b).
2) The compression stage composed of the MHC and the booster.
3) The high-pressure storage that consists of the drone cylinder.

The control panel allows the opening/close of the pneumatic valves of the H_2 line and thermal fluid, the switching on/off of the components of the thermal circuit and it allows the power on/off of the booster. The hydrogen line is realized entirely using tubes in AISI 316L stainless steel, with Øext of 6 mm and thickness of 1.5 mm. Tests were performed supplying the EL with grid current at 220 V.

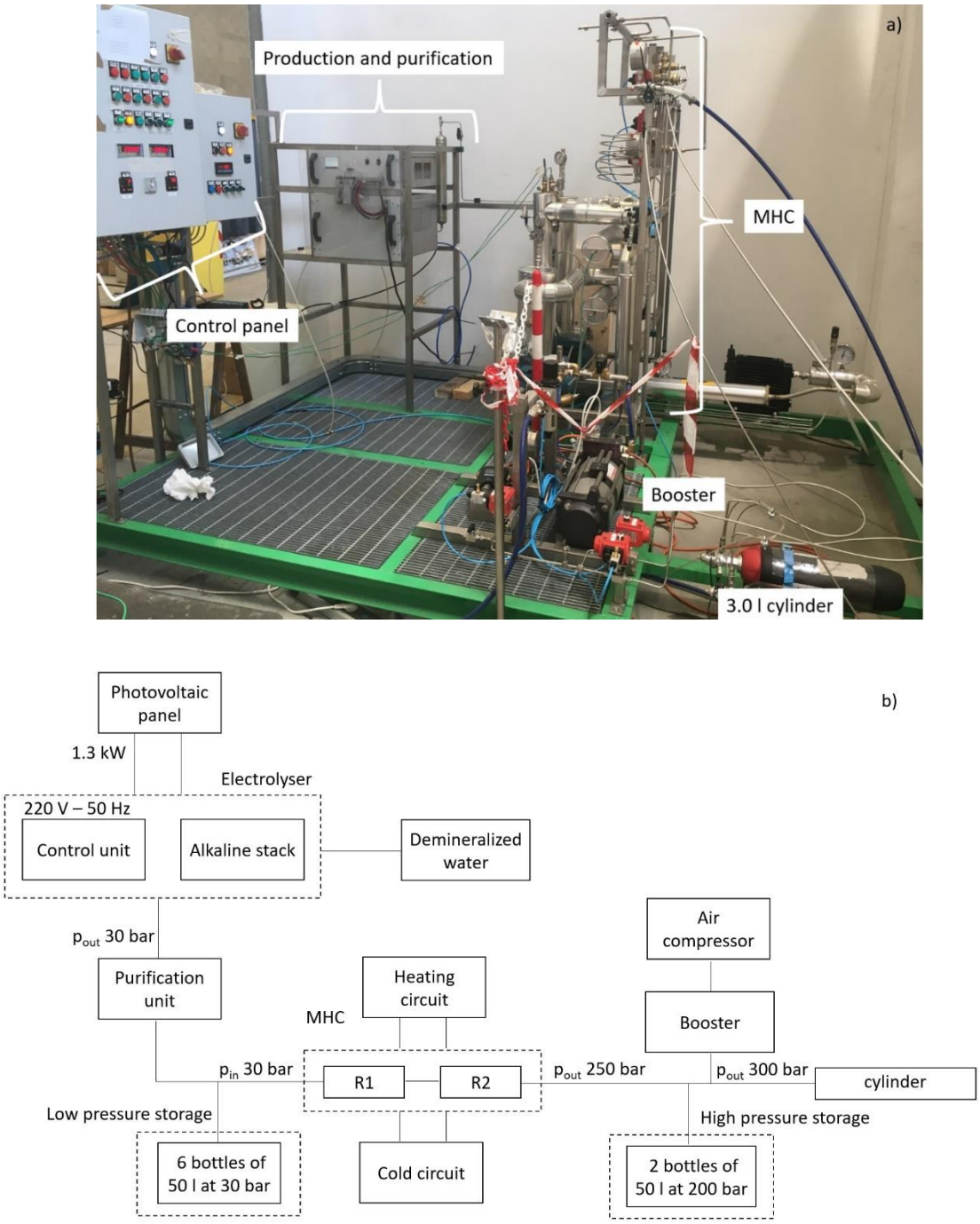

Figure 8: (a) Picture of the H2RS realized in Tecnodelta srl.; (b) the PFD of the H2RS.

At the stack of the EL, H_2 is produced at 42 °C with a pressure of 32 bar. As can be seen from the PFD (Figure 8-b), downstream of the purification unit a bundle of 6 cylinders of 50 l is present and it is filled with the H_2 produced with the EL. It is a low-pressure storage to guarantee a constant pressure head of about 28 - 30 bar at the supply of the MHC and to assure the operability of the H2RS in case of stop of the H_2 production through electrolysis.

At the outlet of the purification stage, H_2 flows towards the bundle and then to the MHC. A detailed picture of the MHC is shown in Figure 9.

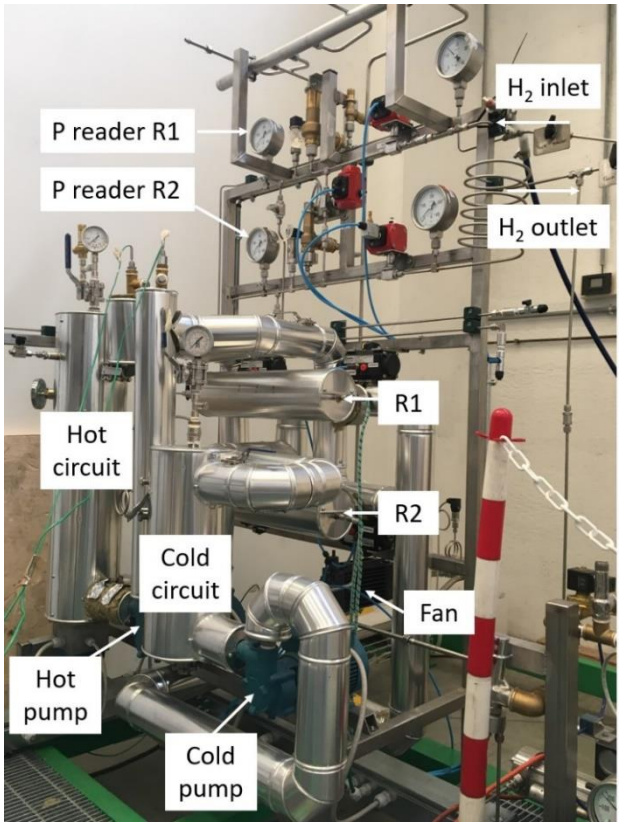

Figure 9: Detailed picture of the MHC

MH-reactors are located horizontally, to avoid tension on the reactor wall [28]. Temperature and pressure are registered as a function of time during absorption/desorption steps. A thermocouple is located inside the MH-bed, while digital and analogical pressure readers are present along the H_2 line. Thermocouples are also located at the input and output of the two-thermal circuits. The design of the thermal management allows that, while one reactor is warmed (*i.e.* desorption stage), the other is cooled (*i.e.* absorption stage), but it is also possible to heat/cool both reactors in parallel, as necessary in the activation process, to allow the simultaneous processing of the alloys. The two thermal circuits are separated (Figure 9) and the switch at the reactor from hot to cold stage and vice versa occurs thanks to pneumatic valves, controlled by the control panel. As thermal fluid, the oil Therminol was used, that flowed thanks to pumps, one per each circuit. In the hot circuit, the oil is warmed up by a resistance, regulated by a thermostat, while in the cold one, it is cooled using a fan. The H_2 at the outlet of the MHC can be directly stored or further compressed by the booster. Thanks to valves, reactors can be insulated from the rest of the H_2 line, to allow a H_2 flow directly

from the EL to the booster, if necessary, and for safety reasons or in case of maintenance of the gas line. The MHC and the booster can work in series or independently, since the booster can compress up to 300 bar the H_2 coming from the MHC or from the EL. Finally, the compressed gas is stored in the drone cylinder. At the outer of the compression unit, it is also possible to fill a high-pressure storage of 2 cylinders of 50 l up to 200 bar, to assure a fast refuelling of the drone, when necessary (Figure 8-b).

Tests were performed using the MHC to fill the 3.0 l cylinder, but even a 0.5 and 1.1 l cylinders were considered, to evaluate the influence of the final volume on the H_2 flow. A test was also performed compressing H_2 up to 300 bar coupling the MHC with booster.

5.1.3.4 Test on the H2RS

5.1.3.4.1 Compression unit: MHC

One cycle of compression with the MHC is schematically explained with a Van't Hoff plot through the various steps in Figure 10, showing connections among EL, R1, R2 and the drone cylinder.

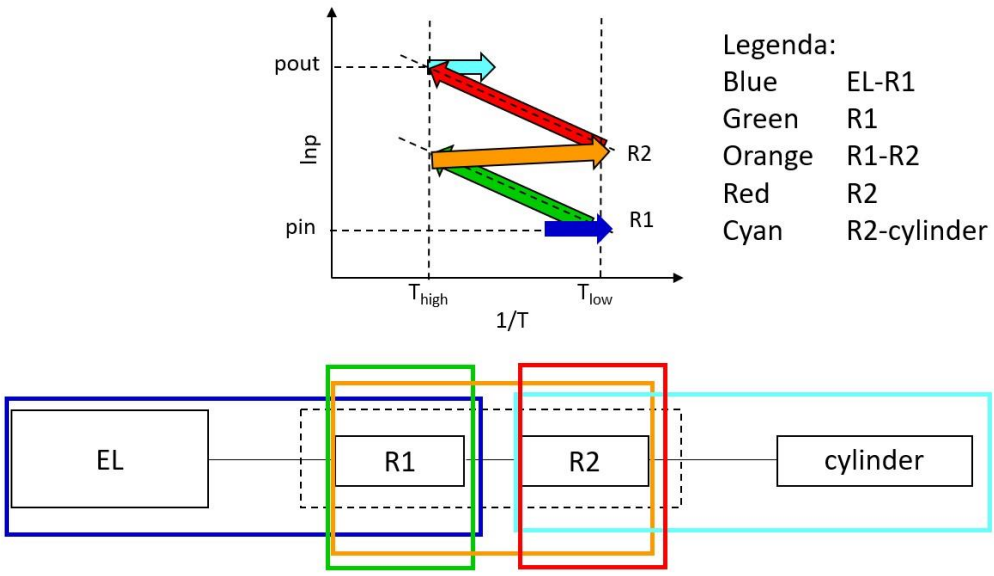

Figure 10: Schematic representation of one cycle of compression through a Van't Hoff plot and the connection between EL, R1, R2 and the drone cylinder, using colours to link the same step in the two representations.

As can be seen in Figure 10, one compression cycle starts with the absorption of H_2 in step R1 directly from the EL at the T_{low} (blue step). When absorption is terminated, the connection with the EL is closed, and R1 starts to be heated at the T_{high} (green step). In this stage, H_2 is compressed increasing the pressure. Then, H_2 is transfered from R1 to R2 at a

higher pressure than that used for absorption. R2 is at the T_{low} and received continuously the H_2 released by R1 that is at the T_{high}. When the transfer of H_2 is finished and in R2 the MH is formed, the valve between R1 and R2 is closed, R1 is cooled down to T_{low}, while R2 is heated to T_{high} (red step). As occurred for R1, the heating of R2 implies the release of H_2 at high pressure, and when R2 is in connection with the drone cylinder (cyan step), the H_2 desorbed by the Hydralloy-C5 is directly transfer from R2 into the cylinder, filling it.

Figure 11 shows the variation in temperature and pressure registered during one cycle of compression in R1 and R2, named, for the pressure, as pR1 and pR2 and, for the temperature, as TR1 and TR2, respectively. Temperature is monitored inside the reactors powder-bed, while the pressure it taken along the H_2 line at the outlet of the reactor. Colours are used to visualize various steps shown in Figure 10. The cycle refers to the first cycle of the day, in which there is already some H_2 in the gas line left from the previous day.

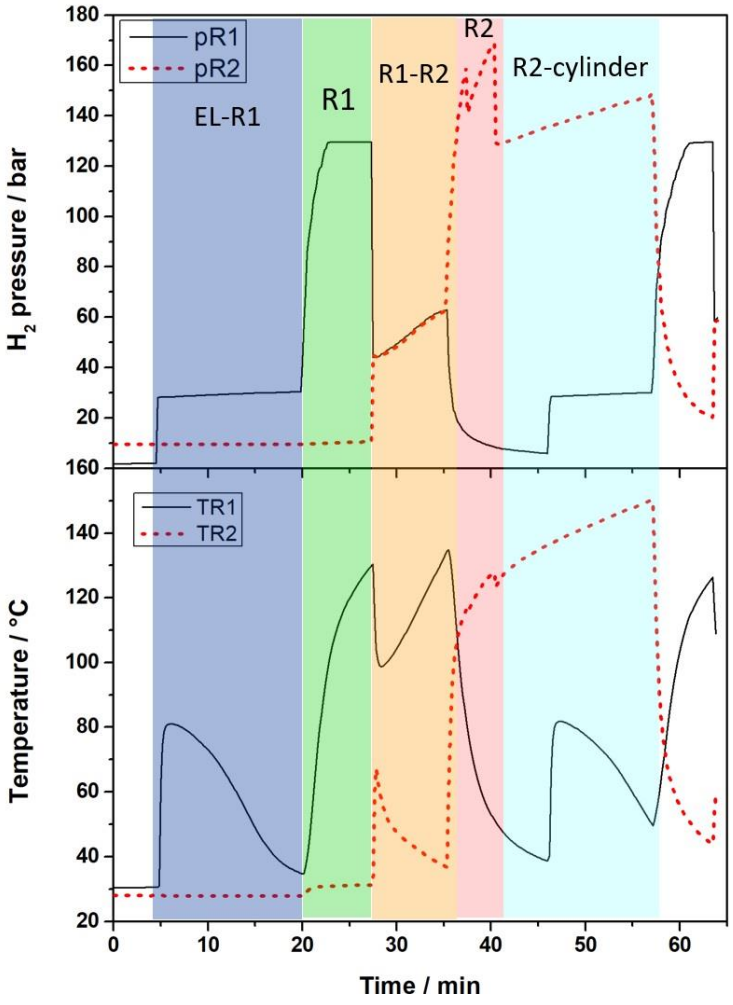

Figure 11: The H_2 pressure and temperature for R1 (black continuous lines) and R2 (red dashed lines) as a function of time, reported for one cycle of compression. Colours are used to distinguish various steps as reported in Figure 10 (steps that occur before/after the one compression cycle are not coloured).

The various steps are briefly described here below.

- As reported in Figure 10, and as can be visualized in the zone highlighted in blue in Figure 11, at the beginning the H_2 is absorbed by the alloy in R1 at the constant pressure of 30 bar (pR1) supplied by the EL, at the T_{low}. The latter depends on the temperature of the room, that was about 30 °C during the test, as can be seen from the value TR1 and TR2 at the 0 point in time. The hydrogen absorption causes a sharp increase in temperature of the powder-bed in R1 (TR1), linked to MH formation, that is an exothermic reaction. In the last part of reaction, a low amount of H_2 is absorbed, the heat generated from the reaction decreases and TR1 progressively decreases, driven by the thermal fluid, moving back to the initial value of about 30 °C. Being the connection between EL and R1 always open, pR1 remains constant at about 30 bar.
- Afterwards, the connection with the EL is closed and R1 is warmed up to 130 °C (TR1), as can be seen in the green zone of Figure 11. pR1 increases due to the desorption of H_2 from the alloy, reaching a constant value of 130 bar. Following TR1, about 7 minutes are required to reach 130 °C, implying a stable value in pressure, resulting useless to wait the achievement of the T_{high} selected of 150 °C (section 5.1.3.1). When a stable value for pR1 is reached, the connection between R1 and R2 is opened (orange zone). TR1 decreases down to 100 °C, while TR2 increases up to about 70 °C, and the pressure of the two reactors reaches a common value. As soon as the connection is opened, the $La_{0.9}Ce_{0.1}Ni_5$ in R1 starts to desorb H_2, which is simultaneously absorbed by Hydralloy-5 in R2, promoting the local cooling of the MH bed in R1 since the process is endothermic (TR1 decreasing) and a local warming in R2 because of the exothermicity of absorption (TR2 increasing). As the reaction proceed, both pR1 and pR2 maintain the same value and a progressive increase of internal pressure of the system is observed. In the meantime, TR1 moves back toward higher values driven by thermal fluid, and, similarly, TR2 is driven back to 30 °C.
- At the end of the hydrogenation of the Hydralloy-C5, the connection between R1 and R2 is closed, and the circuits of the thermal fluid are swapped, so that R1 is cooled down to T_{low} and R2 is heated up to T_{high} (red zone in Figure 11). In R1, the cooling causes a reduction of the pressure and the progressive absorption of the free hydrogen left at the end of the previous step. In the meantime, the increase of TR2 leads to an increase of pR2, as expected.

- Finally, the connection between R2 and the drone cylinder is opened (cyan zone). As can be seen in Figure 11, there is a drop in TR2, due to the endothermicity of the desorption reaction in R2, as already mentioned for R1. Also, pR2 has a drop due to the filling of the drone cylinder, and then it increases, because of the continuous desorption of H_2 from the Hydralloy-C5. pR2 refers also to the pressure of the drone cylinder, since, as occurred when the two reactors were connected (orange zone), also in this case when connecting R2 with the drone cylinder, the pressure is equilibrated.
- When the connection between R2 and the drone cylinder is interrupted (end of the cyan zone, min 58), the compression cycle is finished and the temperature in R2 is brought again to T_{low}.
- Thanks to the design of the thermal circuit, *i.e.* to the fact that while one stage is warmed the other is cooled, it is possible to start a new compression cycle in the last 10 min of desorption from R2. Indeed, as far as R1 reaches the T_{low} (min 46) a new absorption cycle started again (see TR1).
- As can be seen in Figure 11, following the increase of TR2 in desorption (red and cyan zone), the heating rate to reach 150 °C is quite slow, requiring about 20 min. The heat released/absorbed during the hydrogen sorption reactions is observed as a temperature decrease/increase of the MH powder bed and it is an indication of the amount of hydrogen exchanged in the specific stage. Indeed, as higher is the variation in temperature, the higher is the amount of gas exchanged.

Two filling tests were performed to identify the proper compression methodology. Timing per step used for the two tests are reported in Table 8.

Table 8: Time per each step of a compression cycle in test 1 and 2.

	EL - R1	**R1**	**R1-R2**	**R2**	**R2-cylinder**
Test 1	10 - 15 min	5 min	2 - 5 min	15 min	5 min
Test 2	10 - 15 min	5 min	2 - 10 min	5 min	15 min

The time in each step takes into account also the one required to heating and cooling reactors. Then, for the step EL-R1, there is no difference in time in the two tests (*i.e.* 10-15 min, Table 8), since it is the reaction time observed in laboratory for the $La_{0.9}Ce_{0.1}Ni_5$ when testing its absorption rate (section 5.1.3.2.2). Considering the temperature profile registered inside the reactor (Figure 11), the room temperature never exceeded 32 °C, implying for absorption a temperature of the powder bed 40 °C < T_{low} < 45 ° C, that is the minimum temperature at

which the fan was able to cool down the reactor from the previous desorption stage. Despite the high temperature of the MH-powder, the equilibrium pressure of the $La_{0.9}Ce_{.01}Ni_5$ is still lower than the supply pressure, *i.e.* 25-30 bar (Figure 5-b). In the worst conditions, *i.e.* high temperature and low supply pressure of 45 °C and 25 bar, respectively, it was not necessary to exceed the 15 min. Considering the primary desorption step, *i.e.* the step R1 and R2 (green and red, respectively in Figure 10 and Figure 11), for R1 5 min are fixed in both tests, since as explained previously, a stable values of release pressure is achieved (Figure 11). While a different time was investigated in the two tests for step R2, and R1 – R2 and R2 – cylinder. Figure 12 shows, as a function of time, pR2 acquired in the two tests, that, as previously mentioned, refers also to that of the drone cylinder, when it is filled. Dashed lines in Figure 12 connect the pR2 values registered at the end of each compression cycle in R2, representing the variation of pressure inside the drone cylinder during the tests of charging. Tests were performed filling the drone cylinder totally empty, and the difference between the two processes is linked to the time left in the various steps (Table 8). The goal was to individuate the procedure allowing to reach the final charge pressure as highest as possible in the shortest time.

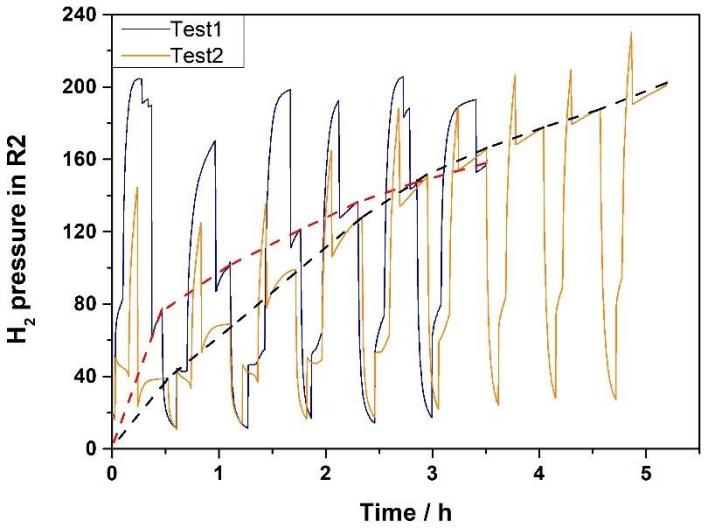

Figure 12: Hydrogen pressure of R2 (pR2) as a function of time observed in the two tests. Dashed lines refer to the progressive charging of the drone cylinder.

Concerning test 1, the R1 – R2 connection time was fixed at about 2-5 min, followed by 15 min of step R2 and a final connection time R2 – cylinder of 5 min. Since 20 min are required to warm up R2 up to 150 °C, the overall time of the steps named R2 and R2 - cylinder should not be lower than 20 min, if a high pressure is desired to be reached, in agreement with the thermodynamic study of the Hydralloy C-5 (Table 3). In this test, the observed charging

pressure of the cylinder, *i.e.* the red dashed line in Figure 12, moves towards a plateau of about 150 bar. In the second test, it was decided to increase the connection time, between R1 – R2 at 2 – 10 min and the one between R2 – cylinder at 15 min, despite of only 5 min for step R2 (Table 8). This strategy should imply the promotion of the desorption in the downstream volumes, *i.e.* promoting the absorption of the Hydralloy C-5 in R2 during the connection step R1 – R2 and the release of H_2 in the cylinder in the connection R2 – cylinder. Indeed, the H_2 flow moves from a high pressure to a lower one, reaching an equilibrium, as happen when two volumes of gas are put in communication. However, in this case, the equilibrium is driven by the amount of H_2 that the Hydralloy-C5 can release inside drone cylinder. This strategy promotes a constant increase of the charging pressure inside the drone cylinder, as can be seen following the black dashed line in Figure 12. At the initial stages, the charging pressure is lower compared to test 1, but it allowed to reach 200 bar of charge without reaching a plateau. It is possible to observe that the Hydralloy-C5, in step R2, was able to always reach 200 bar, rising even up 250 bar (peaks in pressure Figure 12), more than 236 bar expected by the thermodynamic study (Table 3). The latter pressure can be linked to an increase of the slope with temperature, as was already observed during the thermodynamic study (Figure 3), allowing to reach a pressure higher than expected. Not only, but even the gas remained in the free volume of the reactor contributed to the compression, increasing the overall pressure observed in this stage.

The average time for one cycle of compression was about 47 min in both tests. Nevertheless, test 2 turned out more suitable for the filling of the drone cylinder up to 200 bar, thanks to a higher connection time in steps R1 - R2 and R2 - cylinder, that allowed to the Hydralloy-C5, respectively, to absorb and desorb more H_2. The connection R1 - R2 lasted for a different time in the two tests (Table 8) depending on the amount of H_2 desorbed by the Hydralloy-C5. Indeed, during first cycles, the greater free volume of the drone cylinder promotes the desorption of H_2 from the Hydralloy-C5, that, therefore, in the following compression cycles, required a higher amount of time to be completely charged during the connection R1 – R2. Afterwards, while the volume of H_2, as well as the pressure, inside the drone cylinder increased, the Hydralloy-C5 desorbed less and less hydrogen, and a shorter absorption time was required for its charging in connection R1 – R2. It resulted in a variable H_2 flow, as can be seen in Figure 13-a, which reports the H_2 flow and the charge pressure as a function of time, as obtained during the filling of the drone cylinder. The flow was calculated from the amount of H_2 added in each compression cycle over the duration of it.

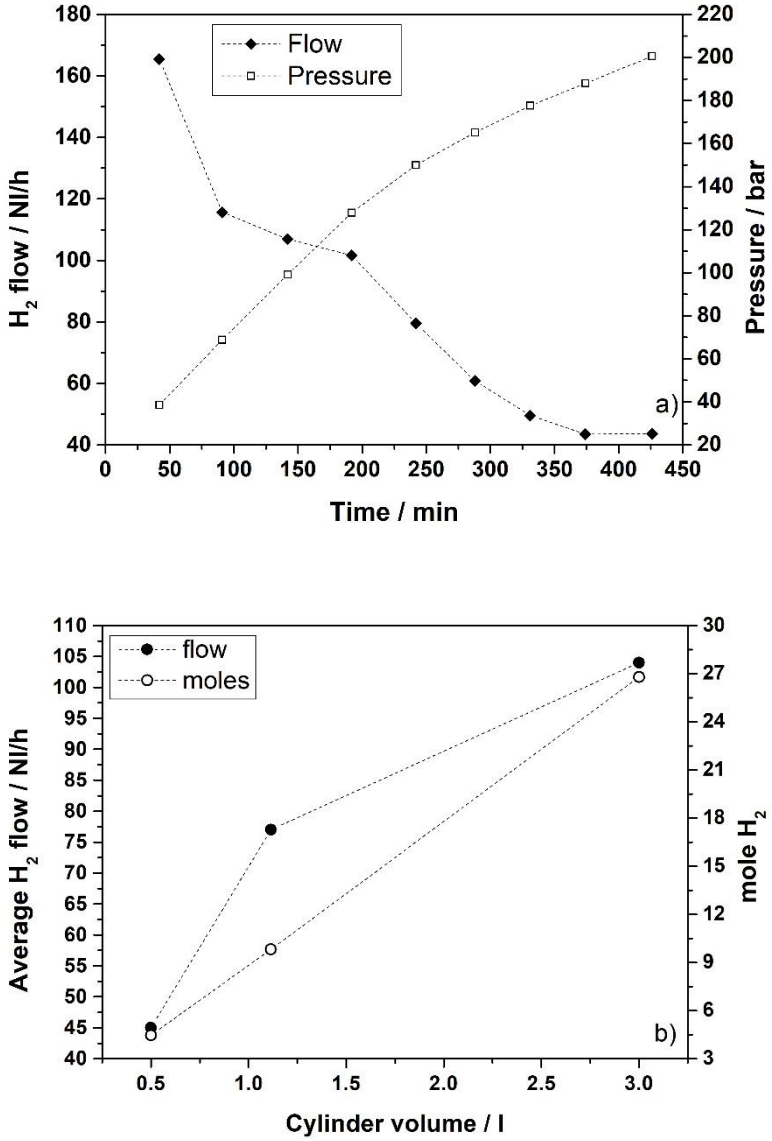

Figure 13: (a) Hydrogen flow and the pressure of the drone cylinder as a function of the time of charge; (b) average hydrogen flow and the compressed number of moles as a function of the volume the cylinder.

Cycle by cycle the flow decreased, moving towards a plateau, passing from 165 Nl/h to 42 Nl/h and resulting in an average flow of 85 Nl/h. Nevertheless, the design of the system allows to start a compression cycle in the final 10 minutes of the previous one, decreasing the overall time for filling the cylinder. It means that, instead of 426 min required considering the sum of times necessary for each single cycle, 374 min were effectively necessary to fill the drone cylinder, resulting in an effective average flow of 104 Nl/h instead of 85 Nl/h. Regarding the charging pressure, it has a linear increase up to 130 bar, and with its further increase, the amount of H_2 progressively discharged by the Hydralloy-C5 decreases, resulting in a progressively reduction in the flow by cycle. This result highlights that the

driving force of the process is the difference in volume and in turn in pressure between hydrogen inside the cylinder and the effective amount of H_2 discharged from R2, *i.e.* the equilibrium pressure of the Hydralloy-C5 at the T_{high}. As far as this difference is high the desorption from the Hydralloy-C5 is promoted. Then, continuing compressing, rising the charged pressure inside the cylinder and so the volume of H_2, the amount of hydrogen released by the Hydralloy-C5 decreased. To evaluate the variation of the H_2 flow according to the volume of the cylinder, tests on filling were also carried out with 1.1 l and 0.5 l cylinders. The average flow and pressure trends as a function of the filling time is like that described in Figure 13-a for the 3.0 l drone cylinder. The same occurs for the temperature and pressure profiles of Figure 11, so they are not reported. Figure 13-b shows the average H_2 flow as a function of the volume of the filling cylinder (3.0 l (drone), 1.1 l and 0.5 l), and Table 9 reports corresponding values, together with the maximum H_2 flow, *i.e.* the flow in the first cycle of compression, and the maximum loaded pressure.

Table 9: Maximum hydrogen flow, average flow and maximum loading pressure related to different volumes of the cylinder.

Cylinder volume	**Maximum flow**	**Average flow**	**Max load pressure**
l	**Nl/ h**	**Nl/ h**	**bar**
3.0	165	104	200
1.1	165	77	206
0.5	105	45	212

For the 1.1 l cylinder, the final charge pressure is 206 bar, having an average flow of 77 Nl/h, while for the 0.5 l, 212 bar was achieved with 45 Nl/h (Table 9, Figure 13-b). Applying the same filling strategy developed for the drone cylinder (test 2), the average duration of the whole compression cycle was 44 min and 42 min for the 1.1 l and 0.5 l, respectively. As it can be seen from Table 9, the maximum hydrogen flow registered in the first cycle of compression for 1.1 l and 3.0 l is the same (165 Nl/h), to be compared with 105 Nl/h observed for the 0.5 l. 165 Nl/h is attributable to a gravimetric capacity of $La_{0.9}Ce_{0.1}Ni_5$ alloy in R1 of about 1.2 H_2 wt.%, in line with laboratory test (section 5.1.3.2.2). Indeed, considering an average time of cycle, independently from the filling volume, and excluding the amount of free volume per stage, a flow of H_2 of about 161 Nl/h is obtained, not far from the observed value of 165 Nl/h, in which also the free volume in the gas line contributed to the final flow. This means that, in the first cycle, in 3.0 l and .1.1 l, it is possible to promote the discharge of the total amount of H_2 available from the MHC. While in 0.5 l cylinder, the volume is not

sufficient to optimize the compression process. Figure 13-b shows the number of moles compressed as a function of the volume of the cylinder, together with the average flow. As it can be seen, the flow increases, increasing the volume, not linearly. While a linear trend is observed regarding the final amount of moles, meaning that, the greater the volume of the cylinder, the greater is the hydrogen desorption from the Hydralloy-C5 per cycle, as explained previously in merit of the driving force of the process. Comparing the average flow with the flow registered in the first cycle, for the 3.0 l and 1.1 l cylinder, it represents, respectively, the 63 % and 47 % of the maximum one of 165 Nl/h, while for the 0.5 l cylinder, it is the 43 % of the maximum observed of 105 Nl/h, and it is the 27 % of the maximum potential of the MHC (165 Nl/h).

During these series of tests, the MHC performed about 111 cycles, resulting in an average working time of 84 h, without loss in performances. The maximum pressure reached by the $La_{0.9}Ce_{0.1}Ni_5$ in R1 was 130 bar at 130 °C, and it is higher than the value of 100 bar expected by thermodynamic prediction at the same temperature. This increase can be associated to the slope of the equilibrium pcT-curve at 130 °C, and the compression of the free moles left inside the reactor post-absorption. As already mentioned, the same occurred at the Hydralloy-C5 in R2, which desorbs at a maximum pressure of 250 bar at 150 °C. These pressure values were found during desorption in reactor not connected with the downstream volumes. The supply pressure for the R1 considering the connection with the EL had an average of 28 bar, with a minimum value down to 25 bar, and resulting in a compression ratio, CR, (desorption pressure in R2 over the supply pressure in R1) equal to 9 - 10. Taking into account that from a thermodynamic point of view the $La_{0.9}Ce_{0.1}Ni_5$ could absorb H_2 at even lower pressure (Table 6), the supply pressure might be even decreased, in favour of an increase in CR.

5.1.3.4.1.1 Thermal fluid considerations and power balance

Temperature and pressure in the thermal fluids, per each circuit, were monitored at the inlet and outlet of reactors, to evaluate the flow of the fluids, allowing a calculation of a power balance. The flow of both thermal fluids remained constant during MHC operations, and it was equal to 1 m^3/h for the hot circuit and 0.8 m^3/h for the cold one.

Figure 14 shows, for one cycle of compression, the temperature profiles of the thermal fluids, as called $T_{in/out}$ Hot for the hot circuit and $T_{in/out}$ Cold for the cold one. Colours are used to highlight the single steps of the compression cycle, referring to Figure 10 and Figure 11.

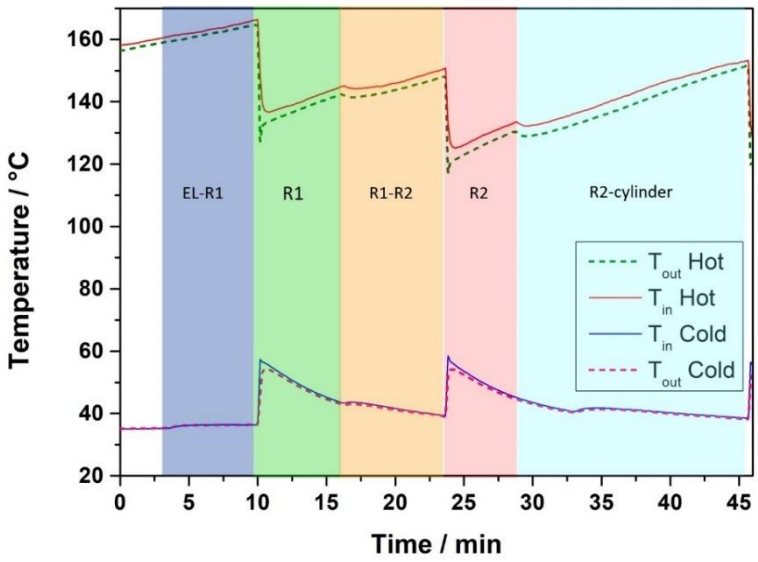

Figure 14: Thermal fluid temperature inlet and outlet registered at the hot and cold circuit during one cycle of compression. Colours are used to distinguish various compression steps as reported in Figure 10.

Looking at the temperature of the thermal fluid in the cold circuit, when the hydrogen absorption occurs in R1, *i.e.* blue zone EL-R1, and in R2, *i.e.* orange zone R1 – R2, there is an increase of temperature during the process of about 1 °, with a difference between inlet and outlet of about 0.5 °. This means that, while locally inside the MH-powder there is a substantial increase in temperature of about 20 – 30 °C, as observed in Figure 11, the system at macroscopic scale is not warmed up. Indeed, the role of the cold thermal circuit in absorption is to avoid the warming up of the entire system due to the exothermicity of the reaction. In this case, the thermal fluid is efficiently removing the heat generated, since only 0.5 °Care attributed to the warming up of the system because of the absorption reaction. The same consideration is valid in desorption, considering the hot thermal fluid. In this case, to contrast the decrease in temperature promoted by the endothermicity, visible at local level inside the MH powder (Figure 11) when $La_{0.9}Ce_{0.1}Ni_5$ is desorbing in R1-R2 connection (orange zone), and the Hydralloy C-5 in R2-cylinder connection (cyan zone), the thermal fluid needed to efficiently release heat to avoid the cooling down of the system. In this case, the difference between inlet and outlet is always approximately of 2 °, with a decrease due to the reaction of 2 °. The hot thermal fluid reached a maximum temperature of 165 °C to guarantee a powder temperature in R2 of 150 °C. When the circuit needed to be swapped, *i.e.* from cold to hot and vice versa, it is always observed an increase in temperature of the cold fluid of about 30 ° and a decrease in the hot one of approximately the same amount. These stages occurred in the red and green zone, respectively step R1 and R2, that refer to

the change from absorption to desorption.

Experimentally, through an amperometric clamp, it was possible to monitor the power consumed by the MHC during its operation, that is constant and equal to 1.20 kW. It is linked to the two pumps of the thermal circuits, the heating resistance, the fan and the consumption related to the electronics of the control panel (LEDs, etc.). Table 10 reports the electric consumption measured for each component. Two power values are reported for the resistance, as its operation is regulated by a thermostat that switches off the resistance when the system is at the right temperature. Consequently, it does not always consume 100% of its power, but an average working power of 80% is estimated, when the system is working at full capacity.

Table 10: Electric power consumption measured for the components of the thermal circuit.

Cold circuit pump	374 W
Hot circuit pump	330 W
Resistance	435 W
Resistance 80%	348 W
Fan	22 W

A power balance involved in MHC operations has been set (Equation (2)-(5)) to evaluate the sizing of the system and therefore its possible oversizing, considering the filling of the drone cylinder.

$$Pin = Pout + Accumulation \quad \text{Eq. (2)}$$

$$Pin - Pout = 0 \quad \text{Eq. (3)}$$

with

$$Pin = Pconsumed \quad \text{Eq (4)}$$

$$Pout = Pdissipated + Pabs + Pdes + Ppump \quad \text{Eq. (5)}$$

The accumulation component can be neglected, considering a continuous system (Eq. (2)-(3)). The input power Pin (Eq. (4)) is equal to the power consumption of the MHC, *i.e.* 1.07 kW, that is obtained by adding the contributions of the individual components of Table 10, taking into account the resistance at 80 %. The value is slightly lower than the 1.20 kW measured, as the additional components are not considered. The outgoing power Pout (Eq. (5)) is linked to four contributions: Pdissipated, Pabs, Pdes, Ppump. The total power dissipated (Pdissipated) is given by the sum of the powers dissipated by the non-insulated

surfaces (hot pump, handwheels of the thermal circuit, brass components of the hot circuit in which the thermocouples are located), by the pipes and by the tank of the hot circuit. The absorption (Pabs) and desorption (Pdes) power take into account the energy to cool/heat the powder, the reactor and the reaction energy, considering the filling of the drone cylinder. The theoretical contribution of the pump (Ppump) is the power necessary to move the thermal fluid to heat the powder during the change of circuit from cold to hot. If the system is properly sized, the difference between the input and output power (Pin-Pout) should be zero, while a positive value implies oversizing and vice versa. In this case, Pin-Pout (Eq. (3)) is equal to 460 W, meaning that system is oversized. Thus, the MHC in a compression cycle consumes the 62 % of the entire power consumed by the system (referring to the 1.20 kW). The calculated value is comparable to a theoretical one, as calculated by the maximum power that should be available in the plant. In this case, in the Pin component the resistance is considered at 100% power. While, in Pout, the Pdes and Pabs are calculated taking into account the flow of the EL of 256 Nl/, resulting in a final power difference, Pin-Pout, equal to 439 W. This implies that, consuming all available power, it could be possible to increase the dimension of the MHC, by increasing the amount of MH used and so the amount of H_2 to compress.

The energy required to start-up of the entire plant was calculated, considering the energy necessary to heat the plant from room temperature up to 150 °C. Calculations take into account the energy to heat up the pump, the tank, the oil, the pipes and the reactor, resulting in 3107 kJ, corresponding to about 1 kWh.

Finally, it was evaluated the isentropic efficiency, η, that represents the ratio between the isentropic work of compression (W) and the energy used for compression (Q) (Equations (6) - (8)) [29].

$$\eta = \frac{W}{Q} \qquad \text{Eq. (6)}$$

with

$$W = \frac{\gamma}{\gamma-1} m_{H2} T_{abs} \left[\frac{R}{M_{H_2}}\right] \left[\left(\frac{P_{des}}{P_{supp}}\right)^{\frac{\gamma-1}{\gamma}} - 1\right] \qquad \text{Eq. (7)}$$

$$Q = n\Delta H_{des} + \left(C_{steel} m_{steel} + C_{alloy} m_{alloy}\right)(T_{des} - T_{abs}) \qquad \text{Eq (8)}$$

Where γ is the compression index, C is the specific heat, R is the gas constant, m is the mass, M the molecular mass, P is the pressure and T temperature. Considering the filling of the

drone cylinder, and the contribution of both reactors in calculating system heat, a value in η of 11 % is obtained with a CR of 9, while 12 % with a CR of 10, implying that the efficiency is higher when decreasing the supply pressure, as was already concluded by Muthukumar et al. [30].

Considering the other volumes of cylinders, with a CR of 9, it is possible to detect a progressively increase in η, increasing the volume, but not linearly, as can be observed in Figure 15. This trend is linked to the amount of H_2 processed, highlighting that the 0.5 l volume is not suitable for the realized system and that 3.0 l (drone) represents a proper filling volume, observing the highest amount H_2 compressed and isentropic efficiency. This result states that the system was properly sized during the design of the MHC (section 5.1.3.3.1).

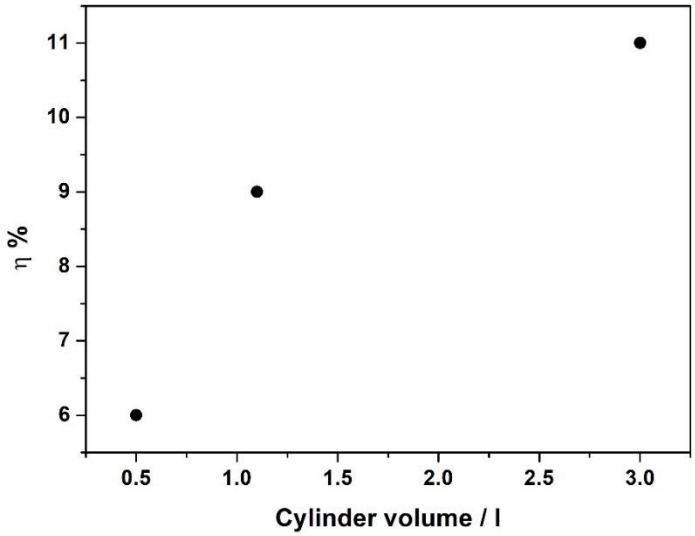

Figure 15: Isentropic efficiency in percentage as a function of the cylinder volume.

4.1.3.4.2 Compression unit: MHC + booster

Including the booster in the compression unit, it was possible to reach the 300 bar of charge, that allows 70 min of continuous flight for the drone. The hydrogen compressed by the MHC is consequently further compressed and stored. A test with the MHC and booster coupled system was performed filling the 1.1 l cylinder. An H_2 flow of 152 Nl/h was observed, that is almost double than 77 Nl/h reached with the single MHC, filling the cylinder at 200 bar (Figure 13-b). Thus, the compression unit including the booster results in a final CR of 10.7-12, with 28 and 25 bar for the hydrogen supply.

5.1.4 Cyclability study

In the framework of the master thesis of Davide Violi, the H2RS was used to perform a cycling study of the MHC, to evaluate the stability in performances of the alloys in the operative conditions. Main conclusions are here briefly summarized, since the work was obtained in close collaboration during the PhD activities here reported.

The H2RS performed 352 compression cycles, taking into account the 111 performed in the primary tests presented previously. It results in an average working time of about 245 h, without detecting significant losses in performances. The process was further optimized by reducing some compression steps *i.e.* the as called step R1 and R2 in Figure 10 and Figure 11. In this way, the optimized compression cycle includes just three steps: EL-R1, R1-R2 and R2-cylinder (Figure 10 and Figure 11), without affecting the results of the process, in terms of hydrogen average flow and pressure reached. The time of each step was fixed, taking also into account considerations made in the previous tests (Table 8). The optimized cycle involves 10 min for EL-R1, 10 min for the connection R1-R2 and 20 min for R2-cylinder, resulting in a total compression cycle time of 40 min. This optimization results advantageous for the realization of an MHC totally automatized, since each step is standardized in time, without considering the amount of hydrogen released by the Hydralloy-C5 in each cycle, as occurred during the previous tests. In this condition the totally absorption and desorption of H_2 should be always assured (section 5.1.3.4.1).

Few grams of alloys were taken out from the reactors after the cycling study, to be characterized morphologically and chemically through SEM and PXD analysis and also in the Sievert's apparatus (pcT-Pro Setaram, Chapter 2). The cycling in hydrogen promotes a sensitive reduction of the particle size, thanks to the variation in volume between the hydride form and the compounds in absorption and desorption [31], as was investigating through SEM-SE. Considering the $La_{0.9}Ce_{0.1}Ni_5$, the average particle size pass from less than 0.8 mm (Figure 6) to less than 125 µm after the cycling in plant. While in the Hydralloy-C5, a most homogenous dimension of less than 150 µm was observed compared to a coarse particle size of less than 2 mm (Figure 1). The chemical composition of the alloys after the cycling in plant was investigated by EDX of the embedded powders. Concerning the $La_{0.9}Ce_{0.1}Ni_5$, when the matrix is detected, its composition is maintained, while some free Ni and La (rich in oxygen) were detected. These results highlight the occurrence of disproportion, that is confirmed also by acquiring the PXD pattern (Figure 16-a). Together with those of the main

phase, diffraction peaks related to Ni (fcc) and to an unknown phase are highlighted in the pattern with black continuous line and dots, respectively. The proper stoichiometry of the unknown phase is hard to assign due to background noise and the amorphous band at low angles related to the capillary. From the qualitative analysis, the unknown phase is not related to the LaH_2 (phase expected from the disproportion of $LaNi_5$-based alloys [28,32]), but likely to an La-oxide, La_2O_3, or La-hydroxide phase, $La(OH)_3$. In the literature, it is reported the occurrence of a disproportion in $LaNi_5$-alloys in presence of oxygen, forming $La(OH)_3$, La_2O_3 and Ni particles [33]. The hydrogen absorption in $La_{0.9}Ce_{0.1}Ni_5$ acts as a purification stage for the Hydralloy-C5 and so the occurrence of oxidation could be linked to the impurities of oxygen/water present in the supply flow. In addition, it is to be considered that the removal of the alloys from the reactor occurred not in a proper inert atmosphere and after several months after the final usage in the plant. This might have promoted a possible oxidation too.

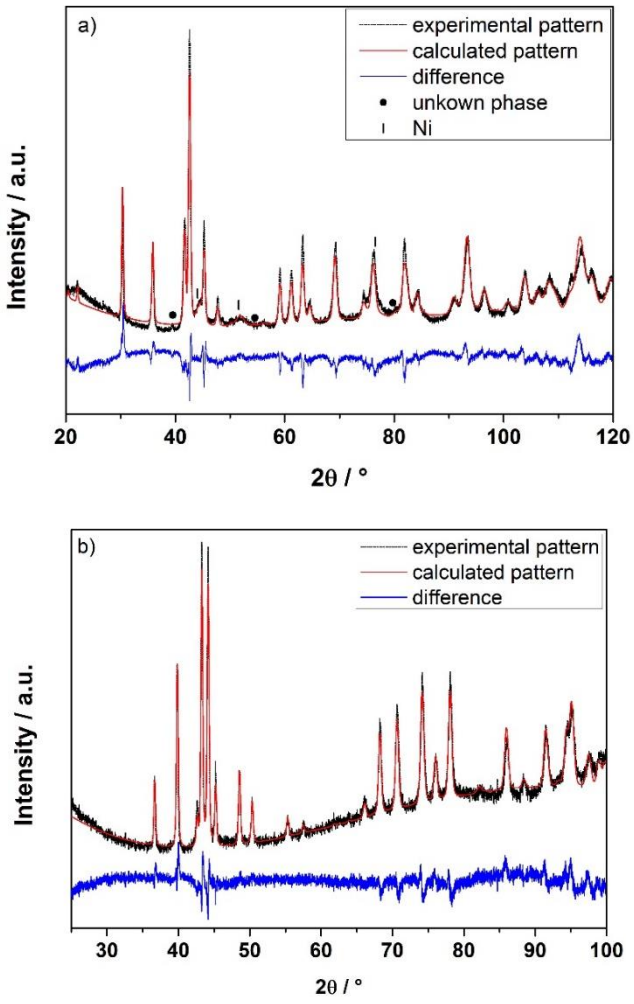

Figure 16: Rietveld refinement of the PXD pattern of the alloys after cycling: (a) $La_{0.9}Ce_{0.1}Ni_5$; (b) Hydralloy-C5.

A Rietveld refinement was performed on the collected diffraction patterns, neglecting the unknown phase. From the refinement, a 17 % of Ni was detected. However, it is worth to say that the absence of the unknown phases in performing the refinement sensitively affects the goodness of the result, as can be seen comparing the experimental and calculated patterns. The reduction of particle size observed by SEM-SE image was also confirmed by the reduction of the scattering domains between the alloys before and after the use in the plant. Indeed, scattering domains obtained as results of the refinement pass from 107 nm to 80 nm after cycling in MHC, and the reduction is visible in the peak broadening comparing the two patterns of Figure 4-b and Figure 16-a. Concerning the Hydralloy-C5, from the EDX analysis, the composition of the matrix is maintained, and no degradation or oxidation occurred during cycling. Indeed, from the PXD pattern, no secondary phases were detected (Figure 16-b). As for the $La_{0.9}Ce_{0.1}Ni_5$, also in this case, a reduction of the domain size is visible in the pattern, thanks to the broadening of the peak, to be compared to the pattern acquired on the as-received Hydralloy-C5 reported in Figure 2. From the refinement, the scattering domains pass from 612 nm to 85 nm.

The significant decrease of the domain size detected by PXD and of particle size observed by the SEM-SE images, promotes a sensitively increase in the sorption rate, as it was observed by acquiring an absorption curve for the $La_{0.9}Ce_{0.1}Ni_5$ in the same temperature and pressure conditions registered before and after its use in the MHC (Figure 17-a). The curve in Figure 17-a called "*Before MHC*" refers to the first hydrogenation cycle after the activation in the laboratory. As can be seen, a stable value is reach in about 10 min, on the contrary of less than 1 min in the alloys after cycling in the MHC. For the Hydralloy-C5 the kinetic curve, registered in the same condition applied for the $La_{0.9}Ce_{0.1}Ni_5$, evidence also a high sorption rate, with about 2 min required to reach a stable value (Figure 17-b). The increased kinetics is likely linked to the reduction of the particle size promoted by the continuous cycling, that increases the reactive surface area [34]. Finally, by comparing an absorption and desorption pcT-curve at 43 °C for the $La_{0.9}Ce_{0.1}Ni_5$ (Figure 17-c) and at 56 °C for the Hydralloy-C5 (Figure 17-d) after the usage in the plant with the one reported in Figure 3 and Figure 5-b, it was observed that the thermodynamics was basically maintained, registering similar equilibrium pressures. Nevertheless, in both cases, the hydrogen capacity is decreased of about 0.3 – 0.4 H_2 wt.%, as observed for the absorption curves reported in Figure 17-a, b. A decrease in capacity of the $La_{0.9}Ce_{0.1}Ni_5$ can be attributable to the occurrence of disproportion. Indeed, inside the plant during the cycling tests, by calculating

the capacity absorbed by the alloy, a value of 1.1 H_2 wt.% was obtained compared to 1.2 H_2 wt.% of the previous tests. However, the loss registered at laboratory level is even lower. Then, the same loss is observed for the Hydralloy-C5 without any explanation since material does not undergo to material degradation/oxidation. Thus, the sensitive reduction registered might be assigned to the laboratory instrumental setup. Indeed, as reported in ref. [28], while locating reactor vertically, due to the refinement of particle size, a material self-densification is promoted, which can cause a decrease of hydrogen diffusion and of the storage capacity. The instrument used for the analysis has a long and narrow tube displaced vertically. It could be that, because of the fine powder obtained after the cycling in the plant, when analysing the powder inside the pcT-instrument the self-densification occurred, registering the loss in capacity. This phenomenon was then confirmed by removing the powder after the study in the Sievert's apparatus. Indeed, in both case, powder results to be compact and hard to be removed from the instrument tube.

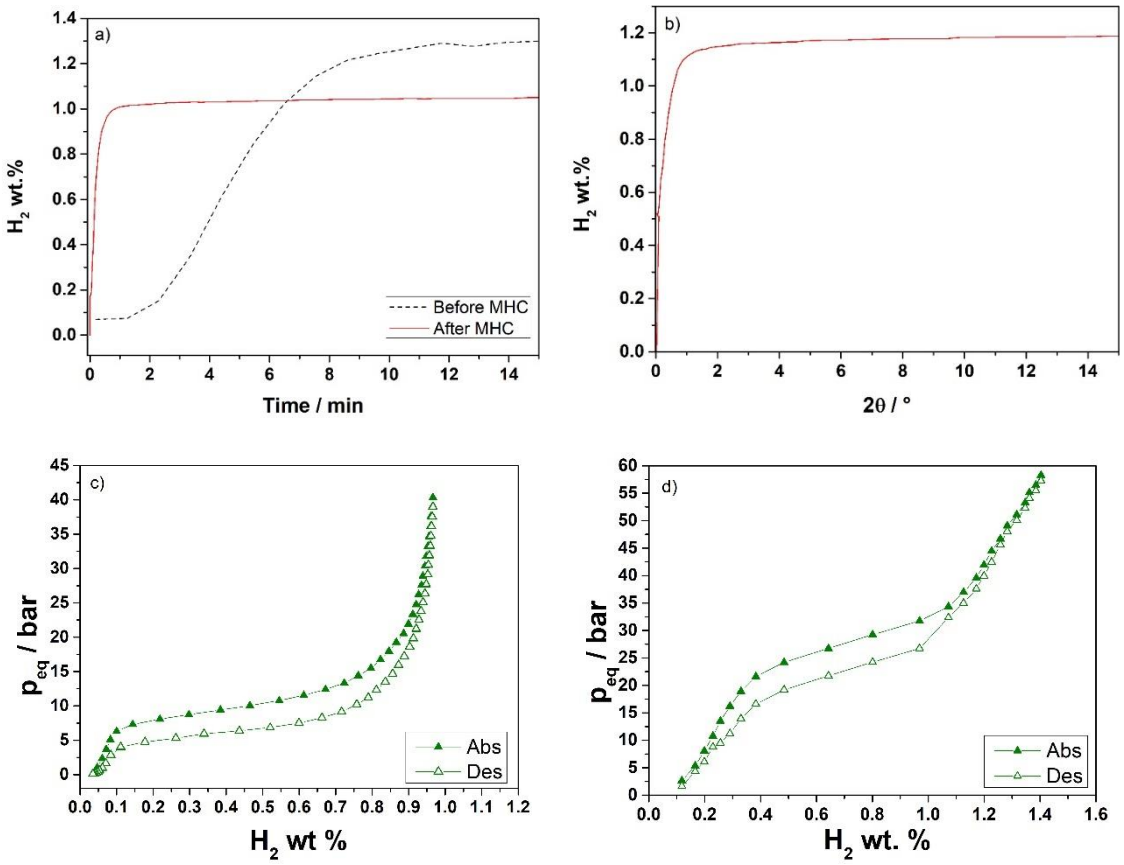

Figure 17: (a) absorption curve $La_{0.9}Ce_{0.1}Ni_5$ before and after the use in the MHC; (b) absorption curve of the Hydralloy-C5 after the cycling in the MHC. Measures occurred at 25 °C and about 25 bar. (c) pcT-curve registered at 43 °C for the $La_{0.9}Ce_{0.1}Ni_5$ powder after cycling; (d) pcT-curve registered at 56 °C for the Hydralloy-C5 powder after cycling.

Thus, the cycling in the plant promoted the occurrence of $La_{0.9}Ce_{0.1}Ni_5$ disproportion due to impurities of the gas supply. Since this alloy is acting as purification step of the Hydralloy-C5, this result is important for a possible scale-up of the system. Not significant loss in performances were detected in plant management and with the obtained results it is hard to predict how could go on the degradation of the $La_{0.9}Ce_{0.1}Ni_5$ up to registering significant losses in performance of the MHC. Thinking to a possible scale-up, this phenomenon should be taking into account. It should be evaluated if it would be more economically advantageous delete the $La_{0.9}Ce_{0.1}Ni_5$ stage in favour of a more efficient purification stage after the EL, that must remove the impurities of oxygen and water. Indeed, the Hydralloy-C5 properties are maintained, thanks to the purification of the $La_{0.9}Ce_{0.1}Ni_5$.

5.1.5 Conclusion

A small-scale MHC at prototype level has been realized based on intermetallic compounds available on the market and integrated in a hydrogen refuelling station. It includes two stages, with a $La_{0.9}Ce_{0.1}Ni_5$ alloys in the first one and the Hydralloy-C5 in the second one, with the former used as purification step for the latter. The system can compress hydrogen from 25 - 28 bar up to 250 bar filling cylinders at 200 bar and working between a temperature of the room of about 30 °C and 150 °C, resulting in a compression ratio of 9-10. Performances are in line with the H2RS realized in South Africa and Croatia with MHC based on IMCs not available in the market [24]. While considering the prototype based on commercial IMCs, working in the same temperature range, a higher delivery pressure is achieved [27]. A compression cycle lasts about 47 min, resulting in an average H_2 flow of 104 Nl/h when filling a 3.0 l cylinder. An improvement has been detected in the average H_2 flow and isentropic efficiency by increasing the storage volume from 0.5 to 3.0 l. As observed for the hydrogen flow, the isentropic efficiency increases with the filling volume, resulting in 11 % with the 3.0 l cylinder. The MHC can be easily integrated with an electrolyser and a booster, to reach up to 300 bar of compressed gas. Finally, it was detected that for less than 1 kg of powder in each reactor, the effective amount of power consumed is about 740 W. Cycling the system for about 245 h, no losses in performances were detected. Nevertheless, because of the presence of impurities in the gas supply, the $La_{0.9}Ce_{0.1}Ni_5$ started to degrade, but, on the contrary, Hydralloy-C5 maintained good performances.

This work highlighted the potential of MHC integrated in refuelling station, thanks to the performances detected so far and to alloys availability. Nevertheless, this work points out the limited pressure that can be achieved with commercial alloys, resulting necessary the integration with a booster. So, there is a need to develop alloys able to compress hydrogen at high pressure, for possible applications in refuelling stations based on MHC.

Acknowledgment

The project Clean-DronHy received the financial support from the Regione Piemonte (Italy), POR-FESR 2014/2020.

5.2 $Ti_{1.1}(Cr,Mn,V)_2$ and $Ti_{1.1}(Cr,Mn,V,Fe)_2$ alloys for high pressure hydrogen compression

5.2.1 Introduction

In developing MHC, it is important to find alloys that can release H_2 working at a T_{high} around or below 100 °C, reaching pressure above 200 bar (Chapter 1). At this regards, the AB_2 alloys hexagonal Laves phase (C14) based on Ti, Cr and Mn, such as $TiCr_2$, $TiMn_2$ and $Ti(Cr,Mn)_2$, are promising [6,15]. The binary and ternary hydrides can be easily substituted in both A and B elements and an over stoichiometry can be used to give rise to a large number of compounds, with a wide range of properties. Depending on the mutual amount of Cr and Mn and on the substitution with other elements like V and/or Fe, compounds can display high plateau pressures even below 100 °C, making these alloys excellent candidates for high pressure applications [15,35]. However, small variation on the composition could have a high impact on the sorption properties.

The Ti-based binary alloys display two hydrides, with not stoichiometric hydrogen content, like $TiB_2H_{\sim 3}$ and $TiB_2H_{\sim 4}$, visible with two district plateaux in the pcT-diagrams, in general for temperatures below 0 °C [36]. While hydrogenating the alloy, hydrogen occupies two tetrahedral interstitial sites, named Ti_2B_2 and TiB_3, forming the two consequential hydrides. However, by increasing the Mn content in $TiCr_{2-x}Mn_x$ with $0 \leq x \leq 1$, for $x > 0.75$ it was observed the absence of the $TiB_2H_{\sim 4}$ [36].

Results from the literature suggest that the Cr/Mn ratio is important for the hysteresis, since increasing the Mn content, the hysteresis is more remarkable. The addition of V and Fe despite Mn to the ternary system is beneficial in reducing the hysteresis [35,37]. Hysteresis decreases also by increasing the Ti content, resulting in composition richer in Ti, over the stoichiometry Ti 1 : B 2 [38]. Compounds with over stoichiometry and/or substituted with V and/or Fe present milder activation conditions, if compared to the stoichiometric binary and ternary alloys [35,37,39]. The beneficial effect due to the over stoichiometry could be linked to both structural and surface effects. In the first case, the over stoichiometry in Ti promotes an increase in cell dimension, thanks to Ti atom occupation also of the Cr/Mn sites. The enlargement of the cell is due to the bigger dimension of Ti compared to Cr/Mn. The rise in cell dimensions causes a lowering in the equilibrium pressure. Thus, if the hydrogenation occurs in mild conditions, the cracking of the particle size is promoted, enhancing the activation of the material. Then, the substitution of Cr/Mn site by Ti promotes

the creation of vacancies in the Cr/Mn sublattice, that seems to act as diffusion path for hydrogen atoms [40]. An effect of the surface properties cannot be excluded, even if there are no evidence reported in the literature. Indeed, the oxidation of the surface of the material due to the high affinity of Ti with oxygen might have a beneficial effect in hydrogenation, with the oxide acting as hydrogen channel, as discussed for the $TiFe_{0.85}Mn_{0.05}$ in Chapter 4. On the other hand, the substitution of Cr and Mn with elements like V and Fe, affect the mechanical properties of the compounds, in terms of hardness compared to the binary alloys [40], enhancing the cracking of the material during the activation, promoting the hydrogenation. The effect of the added elements and their mutual amount on cell dimension is important for the working conditions of pressure and temperature too. The enlargement of the cell occurs also with V that occupy both Cr/Mn and Ti site, while Fe being slightly smaller than Cr, decreases cell dimensions [40]. The same effect is observed by increasing the Mn content, not affecting the activation conditions [38]. Then, the enlargement of the cell promoted by the increase of the Ti content was observed to be beneficial also in the storage capacity, with a value of 1.6 H_2 wt.% observed for TiCrMn, to be compared with a value of 1.8 H_2 wt.% for $Ti_{1.1}CrMn$ [38]. The beneficial effect in storage capacity and the decrease of hydrogen equilibrium pressure is strictly linked to the dimension of the interstitial sites. The larger are their dimensions, the lower is the energy required for hydrogen allocation, decreasing the pressure and increasing the storage capacity [41,42]. Depending on observations reported so far, it seems that effective effects on the interstitial size, and in turns in the hydrogenation properties, are linked to the A element and on its occupation site [39]. Literature works show how minimal changes in the composition of Ti-Cr-Mn-V-(Fe) system can imply several changes in the temperature and pressure working ranges and in activation conditions. Wang et al. [35] by preparing and studying a series of $Ti_{1+x}Cr_{2-y}(Mn,V)_y$ alloys with x = 0-0.2 and y = 0.4-0.8, selected the $Ti_{1.2}Cr_{1.5}Mn_{0.4}V_{0.1}$, as second stage of a MHC, producing H_2 at 450 bar at 170 °C, thanks also to an easy activation (conditions not given). In ref. [37], by studying $TiCrMn_{1-3x}Fe_{2x}V_x$ with x = 0, 0.05, 0.1, 0.15 and 0.2, all the alloys, except the TiCrMn, were activated at about 150 bar and 20 °C. The $TiCrMn_{0.4}Fe_{0.4}V_{0.2}$ has no hysteresis, however the increase in Fe and V promotes a sensitive decrease of the storage capacity by increasing temperature, resulting not practical for temperatures above 60 °C [37]. The optimal composition was the $TiCrMn_{0.55}Fe_{0.30}V_{0.15}$ [37], that, integrated as 3rd stage in an MHC, was able to compress H_2 at 60 °C at 200 bar [43]. In the light of presented works from literature, it can be concluded that a promising composition

based on these elements should have an excess in Ti and a limited content of V and Fe, in order to have an easy activation, to maintain the high storage capacity of $TiMn_2$ and $TiCr_2$, *i.e.* about 2.0 H_2 wt.%, and to avoid a sensitive decrease of the operative temperatures. Finally, the Cr/Mn ratio plays a role on the hysteresis and equilibrium pressure.

Based on these considerations, five compositions AB_2 Laves (C14) based on Ti, Cr, Mn, V and Fe were investigated: $Ti_{1.1}Cr_{1.5}Mn_{0.4}V_{0.1}$ and $Ti_{1.1}Cr_{1.2}Mn_{0.7}V_{0.1}$; $Ti_{1.1}Cr_{1.3}Mn_{0.4}V_{0.1}Fe_{0.2}$, $Ti_{1.1}Cr_{0.9}Mn_{0.8}V_{0.1}Fe_{0.2}$ and $Ti_{1.1}Cr_{0.7}Mn_{1.0}V_{0.1}Fe_{0.2}$. The goal is to analyse the effect of the ratio between Mn and Cr, comparing results obtained for $Ti_{1.1}(Cr,Mn,V)_2$ and $Ti_{1.1}(Cr,Mn,V,Fe)_2$ at a fixed composition of Fe and V (Fe0.2 and V0.1, following the work of Hagstrom et al. [37]). The relationship between the chemical and structural of the alloys and the hydrogen sorption will be investigated. The over stoichiometry was evaluated based on the work of Wang et al. on the composition $Ti_{1.2}Cr_{1.5}Mn_{0.4}V_{0.1}$ [35]. It was defined to prepare the same composition in the B elements of ref. [35], decreasing the Ti content, in order to investigate a possible decrease of the temperature necessary to reach an equilibrium of 450 bar (*i.e.* <170 °C). Boghilla and Niyas, in modelling MHC to integrate in a H2RF, investigated the use of $Ti_{1.1}Cr_{1.5}Mn_{0.4}V_{0.1}$, predicting an equilibrium of 350 bar at 150 °C [29].

The aim of this study is to individuate, among these five compositions, a possible alloy for the 3rd stage, to integrate in the MHC realized in the framework of the project Clean-DronHy, presented in section 5.1, in substitution of the booster. The possible composition should release H_2 at pressure ≥ 250, with a T_{high} lower than 150 °C, allowing the decrease of the working temperature of the plant, resulting advantagous for plant management and safety. Then, as discussed in Chapter 4 concerning the $TiFe_{0.85}Mn_{0.05}$, material synthesis and handling affect the microstructure, surface properties and phase abundance of prepared samples, resulting in sensitively different sorption properties from a work to another and from industrial to laboratory processes. In the literature reports, in most of the cases, for the Ti-Cr-Mn-based alloys an annealing at about 1000-1200 °C is usually performed for a couples of days [37,39,44–46]. So, it was chosen to not perform any treatment after synthesis, like annealing, since it cannot be performed at industrial level. Anyway, it should be considered that still some discrepancy between the prepared compositions at laboratory level and a possible composition prepared at industrial level can occur due to purity of the starting elements (Chapter 4). In this work, compounds were prepared by arc melting and

characterized in powder form chemically, morphologically and a thermodynamic study was carried out to simulate the delivering pressure and their possible integration in the Clean-DronHy refuelling station.

5.2.2 Experimental

Alloys were synthesized by parent elements, commercialized by Alfa Aesar, with arc melting, with a purity of metals of Ti = 99.99 %, Cr = 99.99 %, Mn = 99.9 %, V = 99.5 % and Fe = 99.99 %. Compared to the nominal composition, synthesis involved a 5% and 2 % weight excess of Mn and V, respectively, since they can evaporate during the melting process. About 13 g of alloy were prepared, by turning and melting the ingot about 5-7 times to homogenize the composition. A slice of the ingot was embedded in a conductive resin and polished to investigate the microstructure and the chemical composition by SEM-EDX. Ingots were manually grinded in air in Ar atmosphere inside a glovebox and the obtained powder size was evaluated before and after hydrogenation at the SEM. The $Ti_{1.1}Cr_{1.5}Mn_{0.4}V_{0.1}$ ingot after being cooled with liquid nitrogen, was primary manually broken and then milled in a SPEX miller model 8000M for 5 min, since it was too hard to be manually grinded. Phase composition and structural studies were performed by PXD in Bragg-Brentano geometry on powdered sample before and after hydrogenation, acquiring patterns between 15 ° and 100 ° in 2θ, step of 0.017° and time per scan of 400 s. Hydrogen sorption properties were investigated in a homemade volumetric apparatus built at the Universidad Autonoma de Madrid (Chapter 2). Table 11 reports the sample label and the corresponding composition.

Table 11: Couple of sample label and the corresponding composition.

Sample label	Chemical composition
Mn0.4	$Ti_{1.1}Cr_{1.5}Mn_{0.4}V_{0.1}$
Mn0.7	$Ti_{1.1}Cr_{1.2}Mn_{0.7}V_{0.1}$
FeMn0.4	$Ti_{1.1}Cr_{1.3}Mn_{0.4}V_{0.1}Fe_{0.2}$
FeMn0.8	$Ti_{1.1}Cr_{0.9}Mn_{0.8}V_{0.1}Fe_{0.2}$
FeMn1.0	$Ti_{1.1}Cr_{0.7}Mn_{1.0}V_{0.1}Fe_{0.2}$

5.2.3 Results and discussion

5.2.3.1 Chemical and structural characterization

Figure 18 shows the SEM-BSE image acquired for the sample FeMn0.8 and reported as an example for the other samples. Together with the matrix at high magnification (Figure 18-a), other zones with different greyscale are visible (white arrows), highlighting a not homogeneous sample, as can be deduced by the EDX elemental amount reported for each sample in Table 12. The latter reports the values of the matrix and of the various zone observed with the different greyscale. Number associate to the zone indicate the progressive increase of the scale of grey from the lightest to the darkest one compared to the matrix, as it is shown in Figure 18. In Table 12, it is present also the stoichiometry calculated from the elemental amount detected in the matrix. The calculated stoichiometry is comparable with the nominal composition reported in Table 11. Most of the values in Table 12 are reported as the average with the standard deviation obtained by several points of measure. On the contrary, when the result is present as a single value, it refers to just one site of measure.

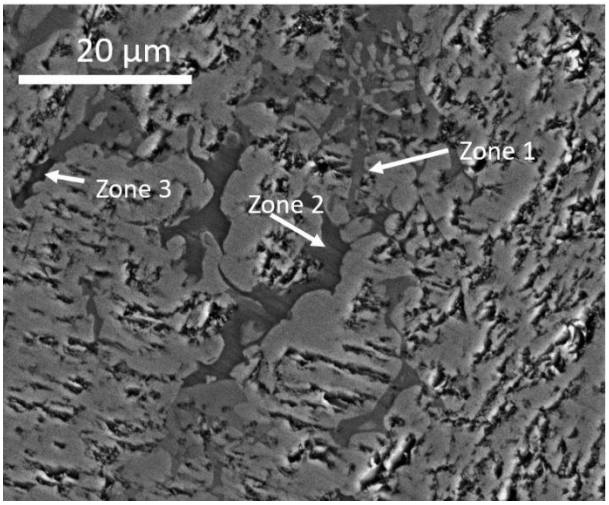

Figure 18: SEM-BSE image acquired for sample FeMn0.8. White arrows highlight various greyscale zone compared to the matrix.

From the chemical composition of the as named zones, in some cases oxygen is detected, suggesting the presence of some oxide phases (Table 12), visible in the SEM-BSE images as inclusions in the matrix or inside grain boundaries. The oxygen might be introduced during the synthesis from the raw materials and alloy's processing. Also, the zones detected without oxygen are mostly distributed among grain boundaries. These zones maintained an atomic ratio Ti 1.1 : B elements (Cr,V,Mn,(Fe)) 2, as the matrix, but it is detected a slightly different elemental amount compared to the matrix, *e.g.* in zone 2 and 3 of sample FeMn0.8.

In sample Mn0.4, this phenomenon is not observed, and the zones 1 and 2 have an atomic ration Ti : B similarly to 1 : 1 (Table 12). The same is also detected in sample FeMn0.4 (zone 1 and 2) and in FeMn1.0 (zone 4).

Table 12: EDX elemental amount in at.% for Ti, Cr, Mn, V, Fe and O for each samples, reporting the average values and the standard deviation. The stoichiometry evaluated by the elemental amount of the matrix.

Sample	**Elements**	**EDX elemental amount at.%**					
		Stoich.	**Matrix**	**Zone 1**	**Zone 2**	**Zone 3**	**Zone 4**
Mn0.4	Ti	1.10	37.1±2.6	50.5±0.3	61.1±0.7	35.3±0.2	/
	Cr	1.42	47.8±1.9	35.1±0.7	26.5±0.7	49.7±0.5	
	Mn	0.34	11.6±1.6	9.7±0.2	5.8±0.1	12.2±0.3	
	V	0.10	3.5±0.8	4.8±0.8	6.7±0.1	2.9±0.1	
	O		-	-	-	10.7±0.1	
Mn0.7	Ti	1.10	33.2±0.2	35.6±1.9			
	Cr	1.32	39.8±0.7	38.0±1.3			
	Mn	0.76	22.9±0.6	22.3±0.5			
	V	0.14	4.1±0.3	4.0±0.1			
	O		-	-			
FeMn0.4	Ti	1.10	34.5±0.2	42.6±2.4	59.4±2.7	36.9±0.8	46.3
	Cr	1.37	44.0±1.2	35.4±1.5	4.6±0.4	40.2±0.6	19.6
	Mn	0.39	12.1±0.3	11.9±0.5	23.0±1.5	12.9±0.1	7.3
	V	0.11	3.0±0.8	3.5±0.1	8.3±0.8	3.8±0.1	2.5
	Fe	0.20	6.3±0.0	6.5±0.3	4.7±0.0	6.2±0.1	4.3
	O		-	-	-	-	20.0
FeMn0.8	Ti	1.10	33.8±0.4	30.3±1.1	36.4±0.6	33.8±0.1	
	Cr	1.05	32.3±0.7	28.5±0.5	28.0±0.4	32.8±0.2	
	Mn	0.80	24.7±0.2	22.1±0.8	25.6±0.7	24.5±0.5	
	V	0.09	2.8±0.1	2.5±0.2	3.6±0.3	2.8±0.1	
	Fe	0.21	6.3±0.2	5.5±0.4	6.3±0.1	6.1±0.3	
	O		-	11.1±3.0	-	-	
FeMn1.0	Ti	1.10	35.1±1.2	35.2±0.5	36.8±1.3	42.7	60.6±2.2
	Cr	070	22.5±0.7	22.9±0.3	21.0±1.7	13.9	10.1±1.9
	Mn	1.03	32.8±1.8	32.3±0.7	32.3±0.3	24.0	21.8±1.1
	V	0.10	3.3±0.2	3.2±0.5	3.7±0.3	3.1	2.3±0.5
	Fe	0.20	6.3±0.2	6.4±0.1	6.2±0.1	5.1	5.1±0.2
	O		-	-	-	11.1	-

Summarizing, the synthesis promotes the formation of a not homogeneous samples, but a different variation in chemical compositions is observed among grain boundaries. An oxide is also detected in some samples, likely linked to the impurities in the raw materials or introduced in sample preparation. Then, zones with an atomic ratio $AB_{\sim 1}$ are also observed. The crystal phases occurring on the synthetized samples were investigated, by acquiring the PXD patterns, that are reported in Figure 19.

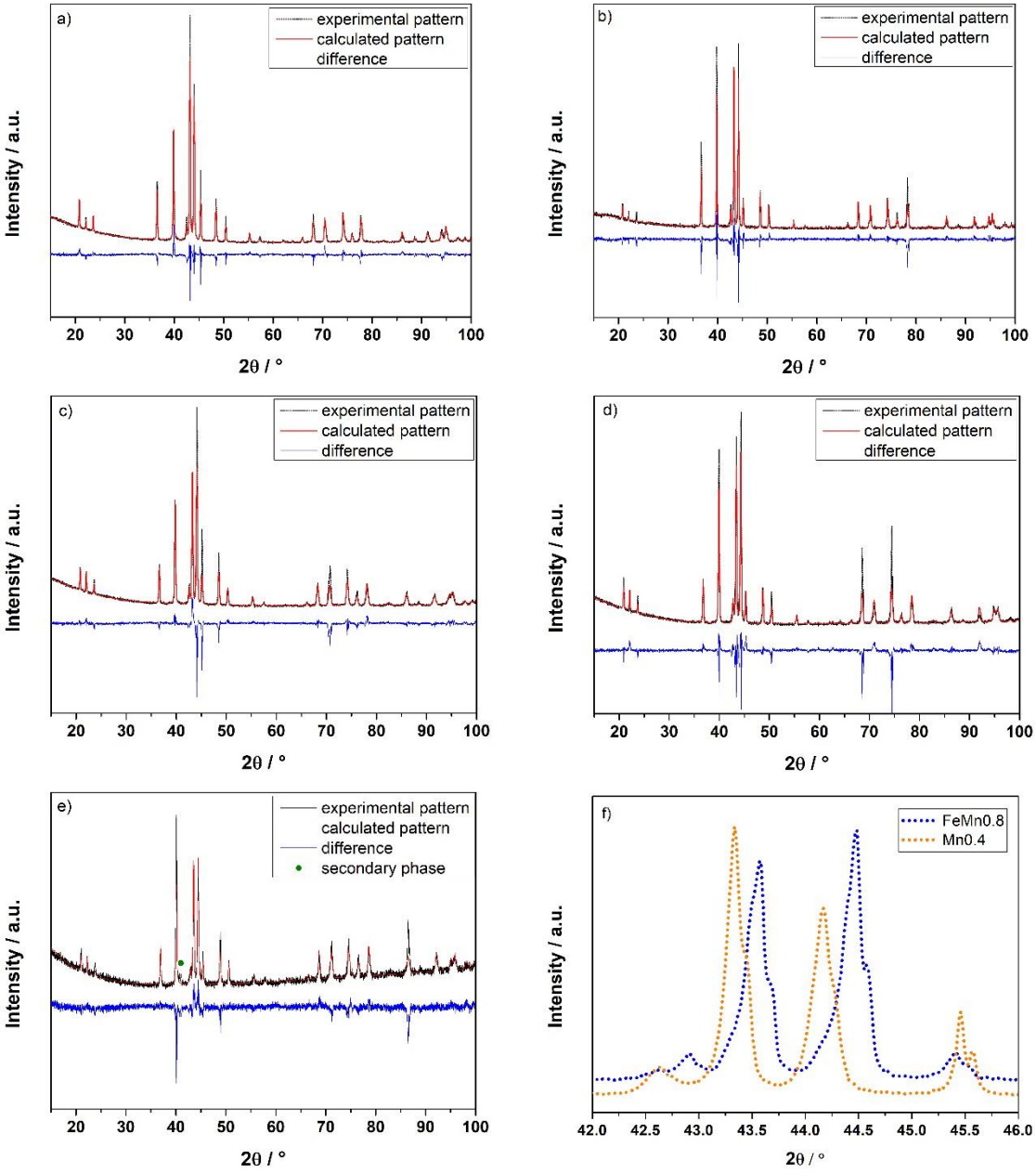

Figure 19: Experimental and calculated PXD patterns, together with their differences and phase assignation: (a) Mn0.4; (b) Mn0.7; (c) FeMn0.4; (d) FeMn0.8; (e) FeMn1.0; (f) zoom of the patterns for Mn0.4 and FeMn0.8.

When at the EDX it was registered the slight variation in the chemical composition, PXD

diffraction peaks related to the Laves (C14) are asymmetric and broad. This can be visualized in Figure 19-f, comparing the diffraction peaks between 42 ° and 46 ° in 2θ for sample FeMn0.8 and Mn0.4 (AB_2 chemical variation not detected). Results from the PXD and EDX analysis imply that the inhomogeneity of the compositions is linked to the occurrence of phase segregation. A secondary phase is clearly visible in samples FeMn1.0 (green circle), that could be related both to an AB TiMn-based and to an oxide phase ($Ti_4(Cr,Mn,V,Fe)_4O$). Its exact structure is hard to be defined due to the overlapping with the peaks of the Laves phase. In addition, from the chemical analysis performed both phases are possible (Table 12). On the other hand, in other patterns, no peaks due to secondary phases are visible. This suggest that the possible phases with stoichiometry $AB_{\sim 1}$ (FeMn0.4, Mn0.4) and the oxide (FeMn0.4, FeMn0.8) detected at the EDX are present in small amount, resulting not visible in the PXD patterns and, in turns, their role in the sorption properties could be neglected [47]. The Rietveld refinement was performed for all patterns considering only the Laves (C14), even in FeMn1.0, due to the uncertainty on the structure of the secondary phase. Table 13 reports the obtained cell parameters for the Laves phase.

Table 13: Cell parameters obtained from the Rietveld refinement of PXD patterns for all samples.

Sample	**Cell parameter**	
	***a* / Å**	***c* / Å**
Mn0.4	4.908(6)	7.992(6)
Mn0.7	4.875(7)	7.993(1)
FeMn0.4	4.885(8)	8.003(9)
FeMn0.8	4.869(2)	7.984(9)
FeMn1.0	4.866(3)	7.977(9)

The refinement was performed considering only one phase for the AB_2, and because of the occurrence of phase segregation, the calculated pattern doesn't fit properly the experimental one. However, the calculated peak positions are in good agreement with the experimental ones, resulting in reliable cell parameters. As expected, Mn and Fe substitutions despite Cr promote a decrease in cell dimension [40]. Comparing Mn0.4 with Mn0.7, the decrease is observed in *a* parameter. Then, thanks to the substitution of Cr with Fe the decrease is more remarkable and evident also in *c*, as can be seen comparing results obtained for Mn0.4 with FeMn0.4. Afterwards, in the three samples containing Fe, the increase in Mn promotes a decrease in cell dimension in both parameters.

For sample Mn0.4, the EDX and the PXD analysis was performed after the milling to evaluate a possible Fe contamination, that was not detected and so results are not reported. Figure 20-a shows the SEM-SE image acquired for FeMn0.8 after the manual grinding, used as an example for other samples, while Figure 20-b reports the image for Mn0.4 after milling.

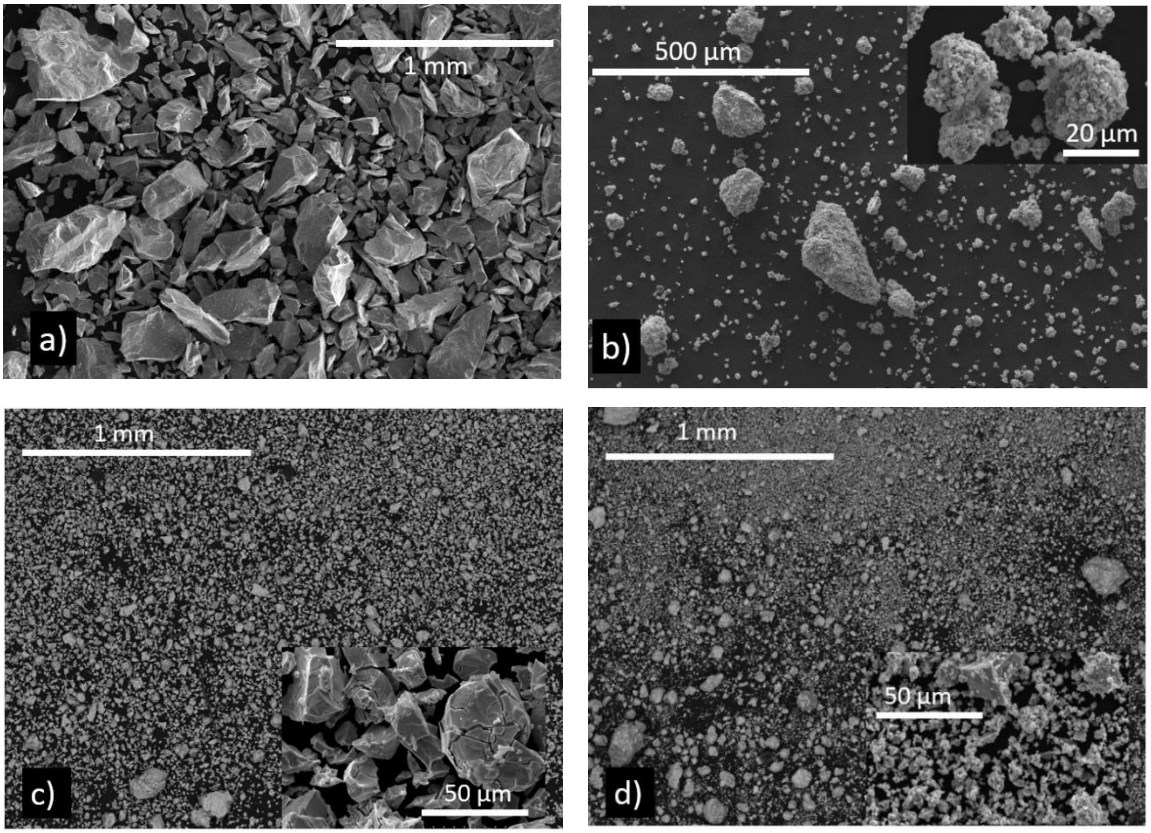

Figure 20: SEM-SE images: (a) after manual grinding of FeMn0.8; (b) after milling of Mn0.4; (c) after hydrogenation for FeMn0.8; (d) after hydrogenation for Mn0.4.

The manually grinded samples present a coarse particle size, as reported in the SEM-SE image for FeMn0.8 in Figure 20-a. Powder's dimension was evaluated by the SEM-SE images. For the samples containing Fe, the powder size is lower than 0.7 mm for FeMn1.0 and FeMn0.4 and lower than 0.5 mm for FeMn0.8. A slightly lower particle size was detected for sample Mn0.7 with a dimension lower than 0.2 mm. For the milled Mn0.4, as can be seen by the SEM-SE image reported in Figure 20-b, a smaller dimension was obtained, observing a powder agglomeration (zoom in Figure 20-b), resulting in agglomerates with dimension lower than 0.3 mm.

5.2.3.2 Hydrogen sorption properties

5.2.3.2.1 Activation

The activation of the over stoichiometry Ti-Cr-Mn- based compounds resulted to be easier than in parent AB_2 one, due to the beneficial effect of the enlargement of the cell dimension and, in turns, of the interstitial sites [38]. These effects allow to enhance the diffusion of the H_2, helping in lowering the temperature and pressure conditions in the activation. Then the substitution of both V and Fe presents beneficial effect too [35,37,39]. The activation is reported to occur even at room temperature, or in a pressure range lower than 150 bar and even at 50 bar [37,47]. Thus, for studied compounds it was decided to investigate the activation in mild conditions, at the temperature of the room (22 °C) and at about 50 bar of H_2. This pressure is the same of the one used for the activation of the commercial alloys employed in the MHC developed in the project Clean-DronHy (section 5.1). The full activation of all samples was reached at about 55 bar at room temperature in 2 cycles, expect for Mn0.7. One cycle consists of an absorption of 2 h followed by a desorption of 1 h (desorption occurs in a dead volume until 0.2 bar are left inside the sample, followed by dynamic vacuum). In Mn0.7, after one cycle at 55 bar, in which no absorption was observed, two cycles were performed at 120 bar. A hardening of the activation is detected by increasing the Mn content also in the literature [38], linked to the decrease of the cell dimension and of the interstitial sites. However, this affect is less remarkable than when the decrease of the cell dimension is promoted by Ti [38,39]. The temperature profile of the sample is an index of the hydrogen sorption and by following it in the first cycle of activation, as reported in Figure 21, it can be seen that in general compounds are already reactive, easily absorbing H_2. Comparing Mn0.4 with FeMn0.4, the activation starts immediately after the H_2 supply, not observing any influence in the activation concerning the Fe substitution. On the contrary, Mn plays a role, since as can be seen by comparing the temperature profile in FeMn0.4 with FeMn1.0, in the latter sample, the hydrogenation is still fast, but starts after a short incubation time. This phenomenon was not observed in FeMn0.8, that presents a temperature profile like FeMn0.4 and so it is not reported. Nevertheless, FeMn1.0 has still an easy activation even presenting a higher content of Mn compared to the Mn0.7, in which 55 bar were not enough to succeed in the activation.

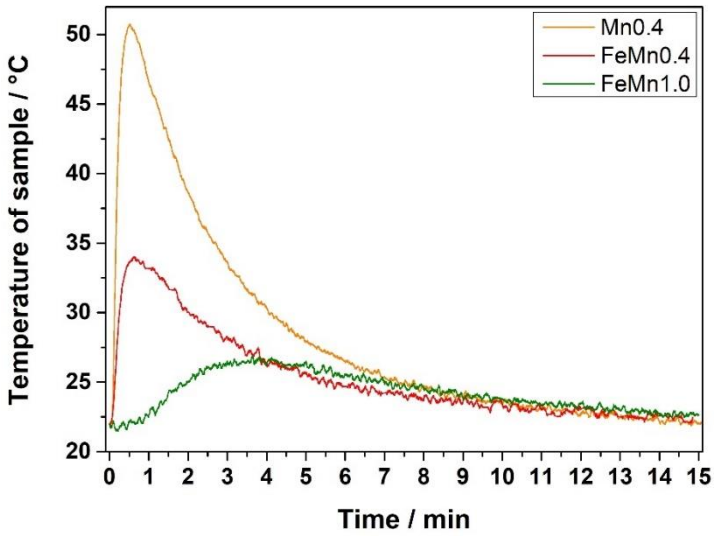

Figure 21: Temperature profile of Mn0.4, FeMn0.4 and FeMn1.0 as a function of time, acquired in the first cycle of activation.

From these observations, it seems that the hardening of the activation is not strictly related to the Mn content. To point out is that sample Mn0.7 is the only one in which were not detected any secondary phase $AB_{\sim 1}$ or oxide by the chemical investigation performed at the EDX (Table 12). On the contrary a certain amount of these phases is present in FeMn1.0, being even visible in the PXD pattern (Figure 19). So, the presence of secondary phases among grain boundaries has a beneficial effect on the activation, acting as H_2 diffusion path, promoting the cracking of the particle and in turns in enhancing the activation. Thus, in FeMn1.0, the high amount of secondary phase compensates the harder activation that Mn content should have promoted. On the contrary, on Mn0.7, the absence of a secondary phase results in a harder activation, requiring higher pressures. Thus, the secondary phase seems to play a crucial role in the activation even if present in limited amount.

5.2.3.2.2 Thermodynamic study

In each sample, the pcT-curves have been acquired in absorption and desorption at 10 °C, 21 °C, 36 °C and 51 °C (Figure 22) to evaluate the values of ΔH and ΔS that are reported in Table 14.

Table 14: Values of enthalpy and entropy calculated by the Vant'Hoff plot in absorption and desorption for each sample.

Sample	Absorption		Desorption	
	ΔH	**ΔS**	**ΔH**	**ΔS**
	kJ/molH_2	**J/molH_2K**	**kJ/molH_2**	**J/molH_2K**
Mn0.4	14±1	76±2	13±1	72±3
Mn0.7	19±1	96±1	20±1	100±3
FeMn0.4	21±1	100±2	21±1	100±6
FeMn0.8	17±1	92±1	24±1	111±3
FeMn1.0	15±1	87±1	23±1	109±4

Figure 22-a, b shows for samples Mn0.4 and Mn0.7, the pcT-curves acquired at 21 °C (a) and 51 °C (b). Figure 22-c, d shows the pcT-curves of all the three-sample containing Fe, FeMn04, FeMn0.8 and FeMn1.0 at 21 °C (c) and 51 °C (d). Figure 22-e shows again the pcT-curves of sample Mn0.4 with FeMn0.4 at 21 °C to allow a better visualisation of the results between two composition having the same amount of Mn, but a different amount of Cr despite its substitution with Fe. Curves have sloping plateaux that are linked to the inhomogeneity of the samples observed at the chemical study, as it was also observed in ref. [47]. The slope increases increasing the temperature, especially in sample containing Fe, as can be observed comparing pcT-curves at 21 °C and 50 °C (Figure 22-c, d). By increasing the Mn content in $Ti_{1.1}(Cr,Mn,V)_2$ (Figure 22-a, b) the equilibrium pressure in both absorption and desorption increases. While in sample $Ti_{1.1}(Cr,Mn,V,Fe)_2$ (Figure 22-c, d) the absorption pressure increases with Mn, on the contrary of the desorption one, registering comparable equilibrium pressure in desorption between FeMn0.8 and FeMn1.0. This is due to a remarkable hysteresis in FeMn1.0, as can be seen in Figure 22-f, by reporting the calculated hysteresis energy as a function of the Mn content. Finally, evaluating the substitution with Fe, comparing the pcT-curves of Mn0.4 and FeMn0.4 (Figure 22-e) the equilibrium pressure in both absorption and desorption increases as expected by the decrease of the cell parameters (Table 13). Finally, the H_2 storage capacity is maintained high, about 1.8 H_2 wt.% in all samples.

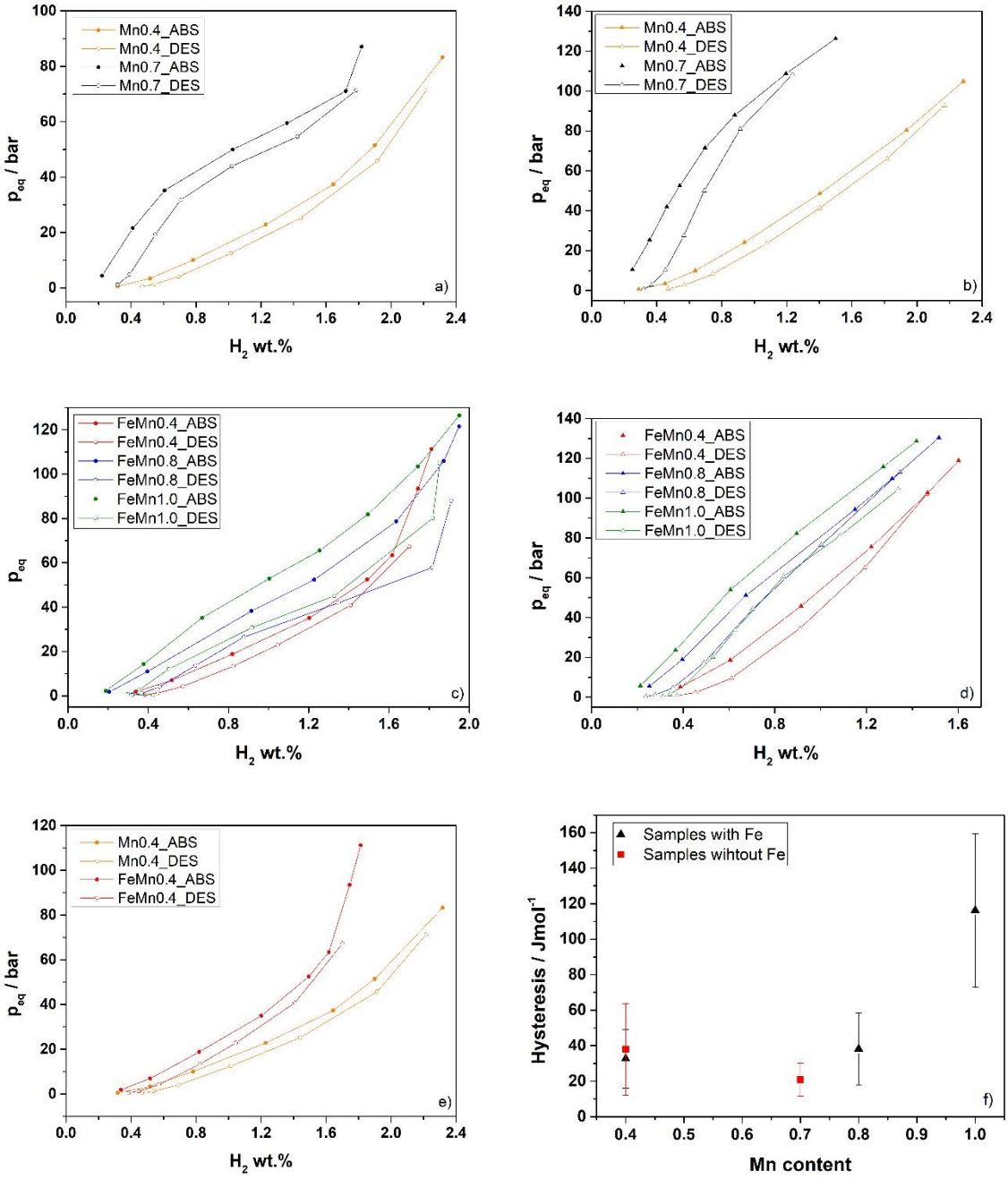

Figure 22: pcT-curves in absorption (full marker) and desorption (empty marker): (a) Mn0.4 and Mn0.7 at 21 °C; (b) Mn0.4 and Mn0.7 at 51 °C; (c) FeMn0.4, FeMn0.8 and Mn1.0 at 21 °C (d) FeMn0.4, FeMn0.8 and Mn1.0 at 51 °C; (e) Mn0.4 and FeMn0.4 at 21 °C; (f) Hysteresis energy as a function of the Mn content for all samples.

In sample $Ti_{1.1}(Cr,Mn,V,Fe)_2$ since at least three values of ΔS and ΔH are present, it was evaluated a linear dependence of enthalpy and entropy in absorption and deposition, as it is shown in Figure 23. This linear correlation of the thermodynamic values states the presence of a compensation effect [48–50]. When this compensation effect occurs, ΔS and ΔH are described like in Equation (9):

$$\Delta H = \beta \Delta S + cost \qquad Eq.(9)$$

where β is the isokinetic temperature. This term represents the temperature at which all the systems considered react at the same rate, *i.e.* isokinetic [49], and it is observed in various reactions of different systems, from biological to metals [50]. In case of reaction that involve the diffusion of atoms into metals (like in this case the diffusion of H_2), it is supposed the linkage among the occurrence of the compensation effect and the presence of vacancies, the energy of the interstitial sites and in turns the diffusion path [50]. However, this phenomenon is complicated, and this thermodynamic relation still not find a physical and fully understood explanation [49]. In this case, by plotting the thermodynamic values it can be seen that in absorption the linearity is also associated with the rise in the Mn content in the compounds, while in desorption does not. The evaluated isokinetic temperature, resulting by the linear fitting of the values is 398 K in absorption and 239 K in desorption.

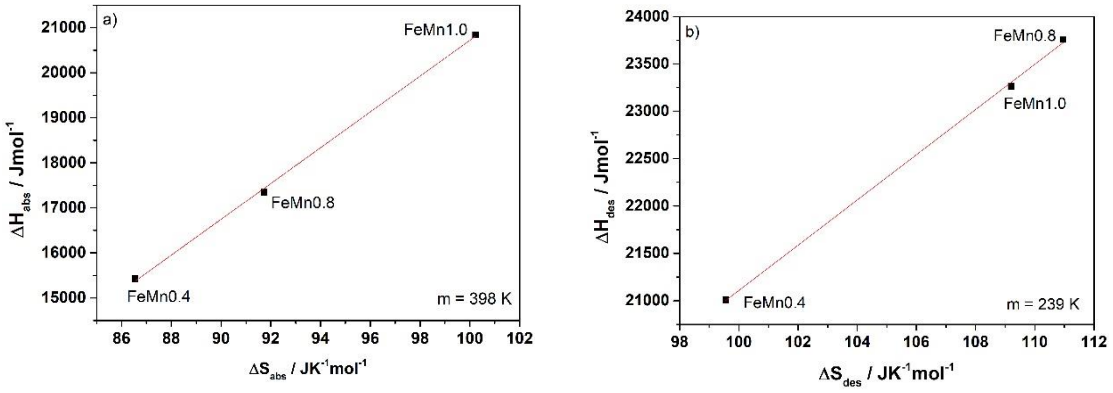

Figure 23: ΔH values as a function of the ΔS in samples $Ti_{1.1}(Cr,Mn,V,Fe)_2$ (a) for absorption; (b) for desorption. Values are reported together with the fitting curve (red line) and the values of slope, m.

Summarising, the decrease in cell dimension promoted by Mn and Fe allows to increase the equilibrium pressure almost linearly, especially in absorption. On the contrary, when Mn exceeds the Cr content, the hysteresis increases resulting not advantaging in compression purposes in which the desorption pressure is important to determine the delivery pressure of the MHC. At this regard, the desorption equilibrium pressure of the compounds is evaluated from the obtained thermodynamic data (Table 14) by applying the Van't Hoff relationship [15], considering as T_{high}, 100 °C, 120 °C and 150 °C. The goal is to reach a delivery pressure of about ≥ 300 bar, to substitute the booster integrated in the Clean-DronHy MHC. 100 °C is considered to evaluate the possibility to use water as thermal fluid. Then, 150 °C is the actual working T_{high} of the realized MHC presented in section 5.1 and it is a common MHC

working temperature [6]. Finally, 120 °C is also evaluated, since it is lower than the actual working temperature of 150 °C, being in any case beneficial in the thermal management and in the power consumption of the MHC.

Table 15: Values of the desorption equilibrium pressure calculated at T_{high} at 100 °C, 120 °C and 150 °C.

Sample	**100 °C** p_{eq} **in bar**	**120 °C** p_{eq} **in bar**	**150 °C** p_{eq} **in bar**
Mn0.4	76	95	127
Mn0.7	255	355	548
FeMn0.4	182	257	405
FeMn0.8	295	436	729
FeMn1.0	280	411	680

As can be observed from Table 15, Mn0.4 has a sensitive low p_{eq}, resulting not promising as third stage in all the investigated temperature range, presenting equilibrium pressures even lower than those of alloys employed in the MHC (section 5.1). The substitution with Fe despite Cr, *i.e.* sample FeMn0.4, promotes a remarkable increase in pressure, allowing to reach up to 405 bar at 150 °C. To point out is that, in this calculation, the influence of the slope is not evaluated, but it might bring to higher pressures, as observed for the $La_{0.9}Ce_{0.1}Ni_5$ and the Hydralloy-C5 during their use in the MHC (section 5.1). Thus, already at 120 °C, the alloy has a possible delivery pressure close to the goal. Mn0.7 alloy can reach higher pressure compared to FeMn0.4, linked to a lower cell dimension (Table 13). Sample Mn0.7 should reach the goal at 120 °C, with 355 bar arriving at 548 bar at 150 °C. The possibility to increase the delivery pressure above the goal of 300-350 bar is important thinking to a possible commercial use and scaling up of the MHC. Indeed, if these types of alloys will be commercially available, their use in MHC is promising in H2RS for buses or cars, where a range of pressure between 400 – 700 is required [51]. The highest pressure can be reached in FeMn0.8. Already at 100 °C, the pressure is close to the goal with 295 bar, and, at 120 °C, 436 bar might be reached. Interesting is the possibility to achieve 729 bar at 150 °C with this alloy, resulting very promising in real applications. FeMn1.0 presents similar delivery pressures of FeMn0.8. The increase of the Mn content in $Ti_{1.1}(Cr,Mn,V,Fe)_2$ system, when exceeding the Cr one (sample FeMn1.0) results in a slower activation, starting after an incubation time, and a lower equilibrium pressure in desorption by increasing the temperature compare to sample FeMn0.8. The rise in Mn content in $Ti_{1.1}(Cr,Mn,V)_2$ alloys

causes a harder activation requiring 120 bar of H_2 instead of 55 bar, but the equilibrium pressure increases in desorption, comparing sample Mn0.4 with Mn0.7. Finally, for $Ti_{1.1}Cr_{1.5}Mn_{0.4}V_{0.1}$, the equilibrium pressure observed in this work is sensitivity lower than the one reported in ref. [29,35]. Discrepancy can be linked to the different synthesis method used, confirming the sensitivity of the H_2 sorption properties on the material handling. Moreover, the comparison between the compound synthetised in this work and the one of ref. [29,35] is difficult, since only the performances observed by its integration in a MHC were reported, neglecting any chemical and structural characterisation.

After the H_2 sorption study, the alloys were characterized by performing SEM-EDX and acquiring PXD patterns. The powder dimension is sensitively reduced after the hydrogen test, as can be seen comparing the SEM-SE images acquired before and after hydrogenation for sample FeMn0.8 and Mn0.4, reported in Figure 20-c, d, respectively. In the manually grinded samples, as can be noted from FeMn0.8 images, the powder dimension is reduced but no agglomerations are present. Powders have a dimension lower than 0.2 mm for FeMn0.4 and FeMn0.8 and lower than 0.1 mm for FeMn1.0 and Mn0.7. While the milled Mn0.4 has smaller powder dimensions, resulting in agglomerates lower than 0.2 mm. By acquiring EDX on the loose powder (considering flat surfaces) and comparing results obtained on the same samples after synthesis (Table 12) the general composition is maintained (Table 16). Some discrepancies can be linked to the different instruments used in the two analyses.

Table 16 EDX elemental amount in at.% for the samples after hydrogenation

	EDX elemental amount at.%				
Sample	**Ti**	**Cr**	**Mn**	**V**	**Fe**
Mn0.4	38.6	46.0	12.2	3.2	
Mn0.7	36.6	40.1	20.9	2.5	
FeMn0.4	39.2	41.7	11.3	2.9	5.0
FeMn0.8	39.4	27.4	24.2	3.3	5.6
FeMn1.0	40.3	19.4	31.0	3.6	5.8

The PXD patterns acquired after hydrogenation for all samples are reported in Figure 24. The main Laves (C14) phase is always present. Peaks are shifted, broader and more asymmetric (present of shoulders) that those observed after the synthesis. The broadening of the peak can be related to the refined of the particles size. While the shift and the asymmetry of the peaks might be linked to the coexistence of totally dehydrogenated phases with those

in which some H_2 is remained in the α-phase due to a not complete dehydrogenation. This can be linked to the phase segregation, confirming that the variation in the chemical composition of the main phase results in various contribution in absorbing/desorbing H_2 (sloping plateaux of Figure 22). Black full points are reported to state the presence of some secondary phases. However, the identification of the phases is difficult, due to the noise registered in the pattern and the broad peak of the Laves phase. The secondary phases might be linked to some oxides, which formation results from the collection of the powders and the acquisition of the pattern in air. Indeed, the oxidation of the powder could be promoted by the small powder dimension obtained after the hydrogenation (Figure 20-c, d).

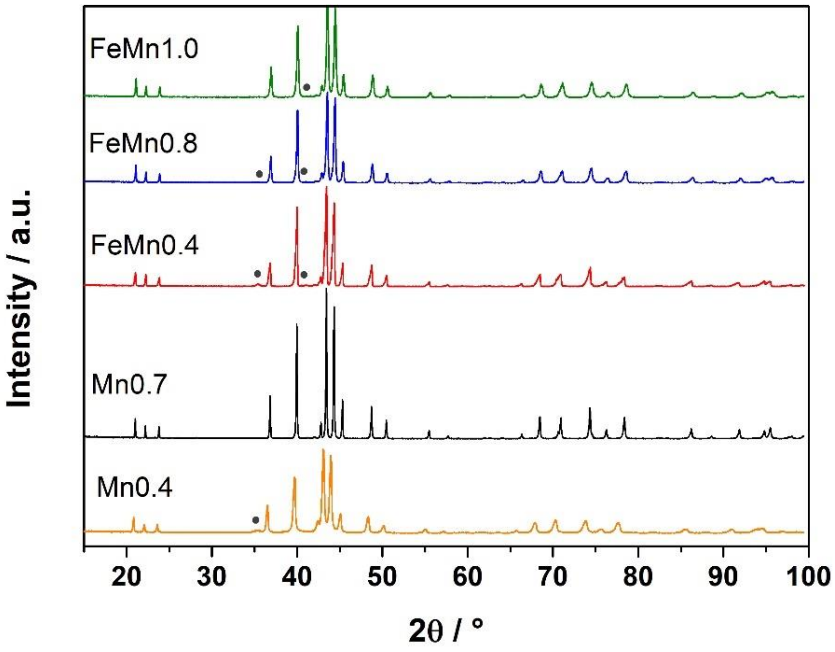

Figure 24: PXD patterns of all samples acquired after hydrogenation. Dark full points indicate the presence of a secondary phase.

According to the results observed so far, the alloy to be selected as potential third stage of the MHC realized in the frame of the project Clean-DronHy is the $Ti_{1.1}Cr_{0.9}Mn_{0.8}Fe_{0.2}V_{0.1}$. The alloy has an easy activation and suitable thermodynamic properties. Concerning desorption, the MHC working between 100 °C and 150 °C should release H_2 between 300 and 700 bar. Table 17 reports the pressure involved in a possible three stage MHC based on the $La_{0.9}Ce_{0.1}N_5$, the Hydralloy-C5 and the $Ti_{1.1}Cr_{0.9}Mn_{0.8}V_{0.1}Fe_{0.2}$ estimating the absorption and desorption pressure at a T_{low} of 40 °C and a T_{high} of 100 °C, 120 °C and 150 °C, respectively. Pressures and temperatures considered take also into account the observed working conditions registered in the test of the MHC (section 5.1).

Table 17: Absorption and deposition equilibrium pressure evaluated for a three stage MHC working at 40 °C of T_{low} and at various T_{high}.

	$La_{0.9}Ce_{0.1}Ni_5$	**Hydralloy-C5**	**$Ti_{1.1}Cr_{0.9}Mn_{0.8}V_{0.1}Fe_{0.2}$**
T_{low}	**P_{eq} absorption / bar**		
40 °C	16	21	79
T_{high}	**P_{eq} desorption / bar**		
150 °C	130	200	729
120 °C	77	127	436
100 °C	46	80	295

For the T_{high} considered, the third stage should absorb H_2 from the Hydralloy-C5 only at 120 °C and 150 °C, since at 100 °C the delivery pressure of the second stage is equal to the absorption one of $Ti_{1.1}Cr_{0.9}Mn_{0.8}V_{0.1}Fe_{0.2}$. The T_{low} of 40 °C is the temperature registered inside the MH-bed for a temperature of the room of 30 °C, by using a fan in the cooling. Thus, the only way to allow a decrease in temperature of the MH-bed should involve the use of a refrigerator, resulting in a higher plant energy demand. Thus, it seems that the three stages MHC, should compress hydrogen from 28 to 436 or 729 bar, working between the temperature of the room and 120 °C or 150 °C, resulting promising in real applications if the $Ti_{1.1}Cr_{0.9}Mn_{0.8}V_{0.1}Fe_{0.2}$ would be commercially available.

5.2.3.2.3Kinetic study of $Ti_{1.1}Cr_{0.9}Mn_{0.8}V_{0.1}Fe_{0.2}$

On the selected $Ti_{1.1}Cr_{0.9}Mn_{0.8}V_{0.1}Fe_{0.2}$ alloy, a kinetic study was performed by considered three different temperatures, *i.e.* 11 °C, 22 °C and 36 °C. The study implies that at the three considered temperatures, the absorption/desorption of H_2 occurs maintaining a constant Δp between the supply pressure and the final one, to assure the same driving force of the reaction. The Δp analysed are 4.0, 9.0 and 18.0 bar in absorption and 4.0, 1.6 and 0.7 bar in desorption. According to the Johnson–Mel–Avrami (JMA), the transformed fraction α can be described as in Equation (10) [52,53]:

$$\alpha = 1 - e^{-(kt^m)} \qquad \text{Eq. (10)}$$

where *t* is the reaction time, *k* is the rate constant and *m* a constant. From tabulated values of *m* is possible to determine the rate-limiting mechanism [54]. In each case study, by plotting α as a function of time, *t*, the values of *k* and *m* are determined by the fitting of the curve. Then, per a given Δp from the *k* obtained at the three different temperatures it should be possible to evaluate the activation energy of reaction *Ea*. Indeed, *Ea* follows the Arrhenius

relation, and it can be obtained by plotting the *lnk* as a function of the inverse of the temperature. Concerning absorption, the values of *m* obtained at each temperature in the three considered Δp, are in a range between 0.5 and 0.7, suggesting a diffusion driven mechanism, according to ref. [54]. Figure 25-a, b, c shows the *lnk* as a function of the inverse in temperature obtained at the three Δp of 4.0, 9.0 and 18.0, respectively.

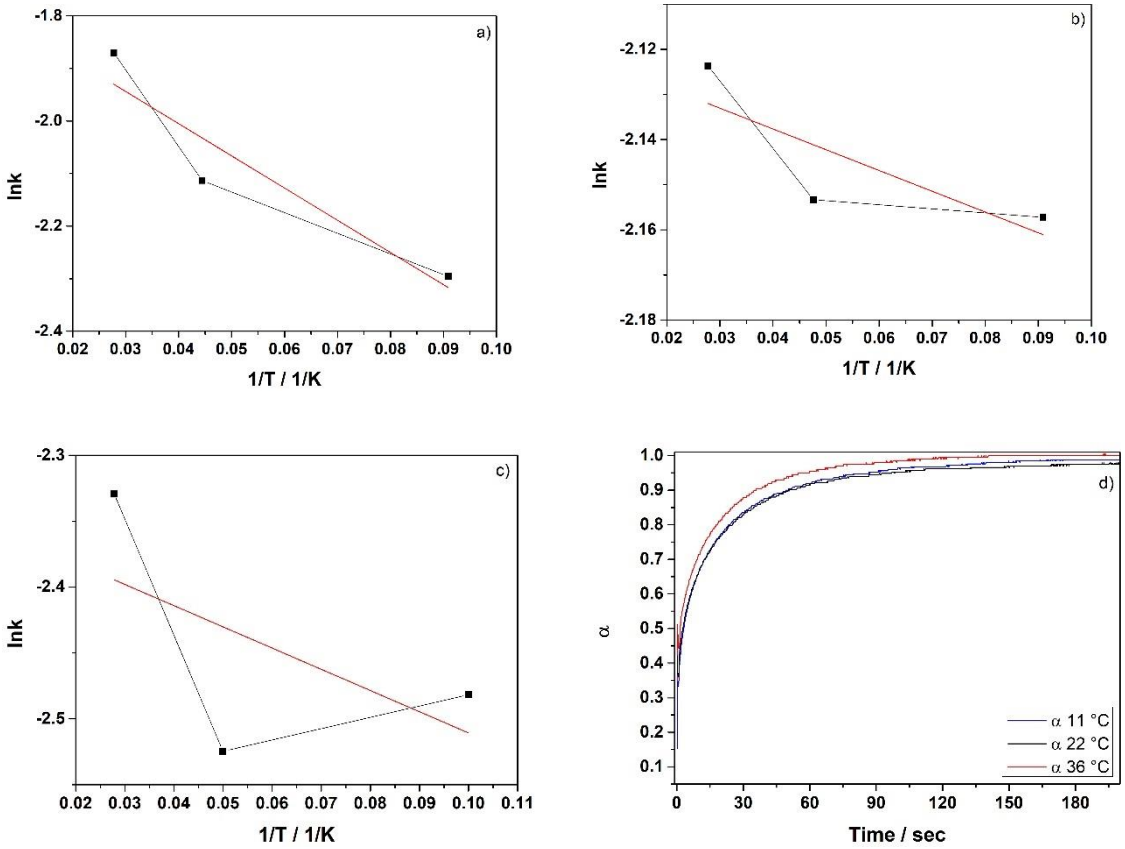

Figure 25: lnk as a function of the inverse temperature obtained in absorption with (a) Δp4; (b) Δp9; (c) Δp18; (d) reports the α as function of the reaction time at the three-reaction temperatures of 11 °C, 22 °C and 36 °C with a Δp9.

The *Ea* should be obtained by the slope of the linear fitting of the values (red line), but as can be observed in the three graphs of Figure 25, not a good linear fit is obtained, since values are not changing linearly with temperature. This is likely due to the experimental set-up. Indeed, the limited pressure achievable doesn't allow to perform a hydrogenation above the 40 °C. For a given Δp, to perform the kinetic study, an increment in temperature at least of 15 ° - 20 ° should be necessary between one measure to another. Indeed, an increment in temperature of only 10 ° is not enough to perform an appropriate kinetic study, resulting in an error in the *k* at 11 °C and 22 °C, leading to similar reaction rate constants, as can be observed in Figure 25-d, by reporting the *α* values as a function of the time for the three

temperatures, with a Δp of 9.0. At 11° and 22 °C the alloy reacts in the same way, and only at 36 °C is possible to notice a slightly difference. This results in an error in the *k* value, not allowing a proper evaluation of the *Ea*. An important observation is the high reaction rate, with the 90 % of the capacity reached in about 49 s.

Figure 26 shows the results for desorption. In this case the error on the *k* values depends also on the low Δp involved. Indeed, at Δp of 1.6 and 0.7, the reaction rate is high, with few seconds necessary to reach a stable pressure, resulting in a difficult evaluation of the *α* and in turns of the *k* values. The calculation of *Ea* is again not possible, as can be seen reporting the *lnk* as a function of the inverse temperature for the measures performed with a Δp of 4.0 used as an example (Figure 26).

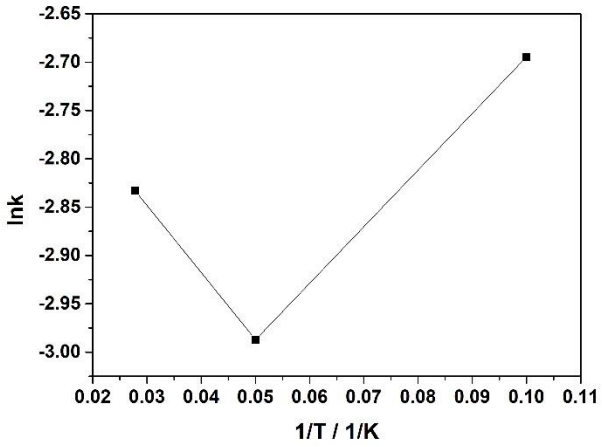

Figure 26: lnk as a function of the inverse in temperature obtained in desorption with (a) Δp4; (b) Δp9; (c) Δp18; (d) reports the α as function of the reaction time at the three-reaction temperatures of 11 °, 22 ° and 36 °C with a Δp9.

Because of the experimental set-up, it was not possible to perform a suitable kinetic study to obtain proper values of *k* and in turns of *Ea*. Anyway, the study highlights a high reaction rate of the selected alloy, implying few minutes to fully process all the hydrogen.

5.2.4 Conclusion

By investigating five AB_2 Laves (C14) compounds based on Ti,Cr, Mn it was observed their potential in hydrogen compression for high pressures. It was evidenced a crucial role of the structural and chemical composition on the sorption properties. By comparing results between $Ti_{1.1}Cr_{1.5}Mn_{0.4}V_{0.1}$ and $Ti_{1.1}Cr_{1.2}Mn_{0.7}V_{0.1}$ alloys, the decrease in cell dimension, promoted by the substitution of Mn with Cr, implies a sensitive increase in the equilibrium in both absorption and desorption. In the compound as called Mn0.7, H_2 can be compressed

at about 300-500 bar working between 120 °C and 150 °C, while only 127 bar could be reached with the sample Mn0.4 at 150 °C. In the latter composition, by substituting Cr with Fe in $Ti_{1.1}Cr_{1.3}Mn_{0.4}V_{0.1}Fe_{0.2}$, the decrease in cell parameters was observed, resulting lower than that of Mn0.7, allowing to achieve a desorption pressure of 257 bar at 120 °C and 405 bar at 150 °C. This highlights how small changes in the composition can already have high impact in the absorption and deposition equilibrium pressure. Then, maintaining the Fe substitution, but changing the Cr/Mn ratio, in the $Ti_{1.1}Cr_{0.9}Mn_{0.8}V_{0.1}Fe_{0.2}$ and in $Ti_{1.1}Cr_{0.7}Mn_{1.0}V_{0.1}Fe_{0.2}$ it was observed an almost linear decrease in cell parameters, coupled with a linear increase in the absorption pressure. However, a sensitive increase in hysteresis occurs, resulting in comparable desorption pressure during the thermodynamic study, but predicting a higher delivery pressure in sample Mn0.8 compared to Mn1.0. All the investigated samples can be activated easily in mild conditions in two cycles at 22 °C and 55 bar of hydrogen. However, the easy activation was shown to be linked to the present of small amount of secondary phases, like $AB_{\sim 1}$ compound or oxide among grain boundaries. Indeed, a higher pressure of 120 bar was required for the activation of sample Mn0.7, in which no secondary phases were detected. The Fe-substituted compounds have a linear dependence of ΔH and ΔS in absorption and desorption, implying a compensation effect and resulting in an isokinetic temperature of 398 K in absorption and 239 K in desorption. Samples presents the occurrence of phase segregation in the AB_2 composition, resulting in sloping plateaux. The composition $Ti_{1.1}Cr_{0.9}Mn_{0.8}V_{0.1}Fe_{0.2}$ is very promising for real applications, thanks to high equilibrium pressure observed, implying the feasibility to reach already 300 bar at about 100 °C moving up to 700 bar at about 150 °C. In the studied conditions, the powder is already active and can process all the hydrogen in few minutes, resulting in a high reaction rate.

This work highlighted the extraordinary wide range of application of the Ti-Cr-Mn-V-(Fe)-based compounds, in which slight variations in the chemical composition can imply wide changes in the processing of hydrogen.

Acknowledgment

A gratefully acknowledges to the Erasmus+ Traineeship programme 2020-2021 of the European Union for the financial support and for allowing the mobility between the University of Turin (Italy) and the Universidad Autonoma de Madrid (Spain).

Final remarks

The compression of hydrogen plays a crucial role in the realization of a hydrogen economy, since the storage as compress gas is one of the most used technologies and it found already a wide range of applications, especially in the mobile sector. Nevertheless, the use of hydrogen as compress gas requires the achievement of extremely high pressures, even up 700 bar, to allow to store huge amounts in small volumes. Nowadays, only mechanical compressor can satisfy this demand, implying low efficiency and huge economic investments in terms of maintenance and running costs, due to the high energy demand of the process. Many alternatives to mechanical compressors are under study and thermal compressors based on MH result to be promising, because of reduced costs of maintenance, and, if waste heat could be used, even of running. Indeed, only by exploiting the heating and cooling of metal hydride, hydrogen can be compressed directly from an electrolyser, as an example. In fact, the use of intermetallic compounds in MHC allows not only mild conditions in absorption, but to reach up to 700 bar in desorption, working in a range of temperatures ≤ 150 °C. The goal of the research is then the development of a MHC in which, thanks to a series of alloys, hydrogen can be compressed from an electrolyser up to more than 700 bar, in the as lowest as possible temperature, even below 100 °C.

The number of compressors available on the market and realized at prototype level is small, and they involve the achievement of about 200-250 bar working in a range of temperature from 80 °C to 150 °C [6]. Even fewer are realized using commercially available alloys, implying a difficult scale-up and a limited production of MHC to be placed in the market. In the frame of a regional project, a two stages MHC was realized and integrated in a small scale H2RS at prototype level for the storage of hydrogen for a FC powered drone. The MHC involves, as a first stage, a $La_{0.9}Ce_{0.1}Ni_5$ alloy commercialized by LabTech and, at the second stage, the Hydralloy-C5 alloy, commercialized by Gfe. Since H_2 is produced by an EL with a gas purity of 99.94 %, the first alloy is used as purification stage for the second one. The MHC compresses hydrogen from 28 bar to 250 bar, filling a cylinder at 200 bar and exploiting a CR of about 9. The power consumption is lower than 1 kW, with a thermal efficiency of 11%, for less than 1 kg of powder in each stage. The system is easily integrated with a booster to achieve a final delivery pressure of 300 bar. The work highlighted the limit pressure that can be reached with commercial compounds, implying a limited range of application in the market.

Then the potential of the AB_2 Laves (C14) based on Ti-Cr-Mn alloys as high-pressure compounds have been evaluated by preparing and performing a deep characterization of five compounds in $Ti_{1.1}(Cr,Mn,V)_2$ and $Ti_{1.1}(Cr,Mn,Fe,V)_2$ systems. The alloys need an easy and mild activation procedure. The structural analyses showed a crucial role of small amounts of secondary phases among grain boundaries, that help the activation. Samples are not homogeneous, showing a phase segregation of the AB_2 compositions, which is evidenced by sloping plateaux in the pcT-curves. The hydrogen absorption and desperation pressures are linked to cell dimension observing an increase in pressure by reducing the dimension. The latter is observed with the rise in the Mn content despite Cr and with the adding of Fe. However, the hysteresis increases with the Mn amount, especially in the compounds containing Fe, resulting in a slight desorption difference between $Ti_{1.1}Cr_{0.9}Mn_{0.8}V_{0.1}Fe_{0.2}$ and $Ti_{1.1}Cr_{0.7}Mn_{1.0}V_{0.1}Fe_{0.2}$. The developed alloys cover a wide range of delivery pressure between 100 °C and 150 °C, passing from 76 bar at 100 °C of the $Ti_{1.1}Cr_{1.5}Mn_{0.4}V_{0.1}$ to the 729 bar at 150 °C of the $Ti_{1.1}Cr_{0.9}Mn_{0.8}V_{0.1}Fe_{0.2}$. The latter alloy allows to reach the highest delivery pressure and it is promising as a third stage of the MHC presented previously, working at 120 °C or 150 °C.

References

[1] GRZ Technologies website:. https://grz-technologies.com.

[2] HYSTORSYS SA website: http://www.hystorsys.no.

[3] V.A. Yartys, M. Lototskyy, V. Linkov, D. Grant, A. Stuart, J. Eriksen, R. Denys, R.C. Bowman, D. Grant, A. Stuart, Metal hydride hydrogen compression : recent advances and future prospects, Appl. Phys. A. 122 (2016) 1–18. 10.1007/s00339-016-9863-7.

[4] V.A. Yartys, M. V Lototskyy, V. Linkov, S. Pasupathi, M. Wafeeq, I. Tolj, G. Radica, R. V Denys, J. Eriksen, K. Taube, J. Bellosta, V. Colbe, G. Capurso, M. Dornheim, F. Smith, D. Mathebula, D. Swanepoel, ScienceDirect HYDRIDE4MOBILITY : An EU HORIZON 2020 project on hydrogen powered fuel cell utility vehicles using metal hydrides in hydrogen storage and refuelling systems, Int. J. Hydrogen Energy. (2021) 1–14. 10.1016/j.ijhydene.2021.01.190.

[5] B.P. Tarasov, M.S. Bocharnikov, Y.B. Yanenko, P. V Fursikov, Metal hydride hydrogen compressors for energy storage systems : layout features and results of long-term tests Metal hydride hydrogen compressors for energy storage systems : layout features and results of long-term tests, JPhys Energy. 2 (2020) 024005.

[6] J. Bellosta von Colbe, J.-R. Ares, J. Barale, M. Baricco, C. Buckley, G. Capurso, N. Gallandat, D.M. Grant, M.N. Guzik, I. Jacob, E.H. Jensen, T. Jensen, J. Jepsen, T. Klassen, M.V. Lototskyy, K. Manickam, A. Montone, J. Puszkiel, S. Sartori, D.A. Sheppard, A. Stuart, G. Walker, C.J. Webb, H. Yang, V. Yartys, A. Züttel, M. Dornheim, Application of hydrides in hydrogen storage and compression: Achievements, outlook and perspectives, Int. J. Hydrogen Energy. 44 (2019). 10.1016/j.ijhydene.2019.01.104.

[7] Ø. Ulleberg, J. Meyer, J. Eriksen, A. Norheim, J.C. Gjerløw, Hynor Lillestrøm - A renewable hydrogen station & technology test center, in: 20th World Hydrog. Energy Conf., 2014: pp. 132–139.

[8] N.A. Kelly, R. Girdwood, Evaluation of a thermally-driven metal-hydride-based hydrogen compressor, Int. J. Hydrogen Energy. 37 (2012) 10898–10916. 10.1016/j.ijhydene.2012.04.088.
[9] G. Karagiorgis, C.N. Christodoulou, H. von Storch, G. Tzamalis, K. Deligiannis, D. Hadjipetrou, M. Odysseos, M. Roeb, C. Sattler, Design, development, construction and operation of a novel metal hydride compressor, Int. J. Hydrogen Energy. 42 (2017) 12364–12374. 10.1016/j.ijhydene.2017.03.195.
[10] B.P. Tarasov, M.S. Bocharnikov, Y.B. Yanenko, P. V. Fursikov, M. V. Lototskyy, Cycling stability of RNi5(R = La, La+Ce) hydrides during the operation of metal hydride hydrogen compressor, Int. J. Hydrogen Energy. 43 (2018) 4415–4427. 10.1016/j.ijhydene.2018.01.086.
[11] N. Belmonte, S. Staulo, S. Fiorot, C. Luetto, P. Rizzi, M. Baricco, Fuel cell powered octocopter for inspection of mobile cranes: Design, cost analysis and environmental impacts, Appl. Energy. 215 (2018) 556–56510.1016/j.apenergy.2018.02.072.
[12] T. Donateo, A. Ficarella, L. Spedicato, A. Arista, M. Ferraro, A new approach to calculating endurance in electric flight and comparing fuel cells and batteries, Appl. Energy. 187 (2017) 807–819. 10.1016/j.apenergy.2016.11.100.
[13] M.N. Boukoberine, M.F. Zia, M. Benbouzid, Z. Zhou, T. Donateo, Hybrid fuel cell powered drones energy management strategy improvement and hydrogen saving using real flight test data, Energy Convers. Manag. 236 (2021) 113987. 10.1016/j.enconman.2021.113987.
[14] M. Ball, Fuel Cell Module Powers Record-Breaking UAV, (2019). https://www.unmannedsystemstechnology.com/2019/04/intelligent-energy-fuel-cell-module-powers-record-breaking-uav/.
[15] M. V. Lototskyy, V.A. Yartys, B.G. Pollet, R.C. Bowman, Metal hydride hydrogen compressors: A review, Int. J. Hydrogen Energy. 39 (2014) 5818–5851. 10.1016/j.ijhydene.2014.01.158.
[16] S. Nayebossadri, D. Book, Development of a high-pressure Ti-Mn based hydrogen storage alloy for hydrogen compression, Renew. Energy. 143 (2019) 1010–1021. 10.1016/j.renene.2019.05.052.
[17] K. Herbrig, L. Röntzsch, C. Pohlmann, T. Weißgärber, B. Kieback, Hydrogen storage systems based on hydride-graphite composites: Computer simulation and experimental validation, Int. J. Hydrogen Energy. 38 (2013) 7026–7036. https://doi.org/10.1016/j.ijhydene.2013.03.104.
[18] M. Dieterich, C. Pohlmann, I. Bürger, M. Linder, L. Röntzsch, Long-term cycle stability of metal hydride-graphite composites, Int. J. Hydrogen Energy. 40 (2015) 16375–16382. 10.1016/j.ijhydene.2015.09.013.
[19] C. Pohlmann, L. Röntzsch, F. Heubner, T. Weißgärber, B. Kieback, Solid-state hydrogen storage in Hydralloy-graphite composites, J. Power Sources. 231 (2013) 97–105. 10.1016/j.jpowsour.2012.12.044.
[20] G. Capurso, B. Schiavo, J. Jepsen, G. Lozano, O. Metz, A. Saccone, S. De Negri, J.M.B. von Colbe, T. Klassen, M. Dornheim, Development of a modular room-temperature hydride storage system for vehicular applications, Appl. Phys. A Mater. Sci. Process. 122 (2016). 10.1007/s00339-016-9771-x.
[21] P. Thompson, F. Reidinger, J.J. Reilly, L.M. Corliss, J.M. Hastings, Neutron diffraction study of β-iron titanium deuteride, J. Phys. F Met. Phys. 8 (1978) L75–L80. 10.1088/0305-4608/10/2/001.
[22] D. Chartouni, F. Meli, A. Züttel, K. Gross, L. Schlapbach, The influence of cobalt on the electrochemical cycling stability of LaNi5-based hydride forming alloys, J. Alloys Compd. 241 (1996) 160–166. 10.1016/0925-8388(96)02331-6.
[23] M. Odysseos, P. De Rango, C.N. Christodoulou, E.K. Hlil, T. Steriotis, G. Karagiorgis, G. Charalambopoulou, T. Papapanagiotou, A. Ampoumogli, V. Psycharis, E. Koultoukis, D. Fruchart, A. Stubos, The effect of compositional changes on the structural and hydrogen storage properties of (La-Ce)Ni5type intermetallics towards compounds suitable for metal hydride hydrogen compression, J. Alloys Compd. 580 (2013) S268–S270. 10.1016/j.jallcom.2013.01.057.
[24] B. Rupp, On the change in physical properties of Ti4−xFe2 + xOy during hydrogenation I: Activation behaviour of ternary oxides Ti4−xFe2 + xOy and β-Ti, J. Less Common Met. 104 (1984) 51–63. 10.1016/0022-5088(84)90435-1.
[25] E.M. Dematteis, D.M. Dreistadt, G. Capurso, J. Jepsen, F. Cuevas, M. Latroche, Fundamental

hydrogen storage properties of TiFe-alloy with partial substitution of Fe by Ti and Mn, J. Alloys Compd. 874 (2021) 159925. 10.1016/j.jallcom.2021.159925.
[26] I.A. Romanov, V.I. Borzenko, A.N. Kazakov, Using the copper-foam for thermal conductivity improvement of La0.9Ce0.1Ni5-alloy bed during interaction with hydrogen, J. Phys. Conf. Ser. 1359 (2019) 1–6. 10.1088/1742-6596/1359/1/012103.
[27] M. Martin, C. Gommel, C. Borkhart, E. Fromm, Absorption and desorption kinetics of hydrogen storage alloys, J. Alloys Compd. 238 (1996) 193–201. 10.1016/0925-8388(96)02217-7.
[28] E.H. Jensen, M. Dornheim, S. Sartori, Scaling up metal hydrides for real-scale applications: Achievements, challenges and outlook, Inorganics. 9 (2021) 1–20. 10.3390/inorganics9050037.
[29] S.S. Bhogilla, H. Niyas, Design of a hydrogen compressor for hydrogen fueling stations, Int. J. Hydrogen Energy. 44 (2019) 29329–29337. 10.1016/j.ijhydene.2019.02.171.
[30] P. Muthukumar, M. Prakash Maiya, S. Srinivasa Murthy, Performance tests on a thermally operated hydrogen compressor, Int. J. Hydrogen Energy. 33 (2008) 463–469. 10.1016/j.ijhydene.2007.07.019.
[31] D.P. Broon, Hydrogen Storage Materials The Characterisation of their storage properties, Springer-Verlag London, 2011.
[32] M. Palumbo, J. Urgnani, D. Baldissin, L. Battezzati, M. Baricco, CALPHAD : Computer Coupling of Phase Diagrams and Thermochemistry Thermodynamic assessment of the H – La – Ni system, CALPHAD Comput. Coupling Phase Diagrams Thermochem. 33 (2009) 162–169. 10.1016/j.calphad.2008.09.003.
[33] A. Boonstra, G.J.M. Lippits, T.N.M. Bernards, Degradation processed in a LaNi5 electrode, J. Less Common Met. 255 (1989) 119–131.
[34] F. Laurencelle, Z. Dehouche, J. Goyette, Hydrogen sorption cycling performance of LaNi 4 . 8 Sn 0 . 2, J. Alloys Compd. 424 (2006) 266–271. 10.1016/j.jallcom.2005.11.085.
[35] X.H. Wang, Y.Y. Bei, X.C. Song, G.H. Fang, S.Q. Li, C.P. Chen, Q.D. Wang, Investigation on high-pressure metal hydride hydrogen compressors, Int. J. Hydrogen Energy. 32 (2007) 4011–4015. 10.1016/j.ijhydene.2007.03.002.
[36] O. Beeri, D. Cohen, Z. Gavra, M.H. Mintz, Sites occupation and thermodynamic properties of the TiCr2-xMnx-H2 ($0 \leq x \leq 1$) system: Statistical thermodynamics analysis, J. Alloys Compd. 352 (2003) 111–122. 10.1016/S0925-8388(02)01155-6.
[37] M.T. Hagström, J.P. Vanhanen, P.D. Lund, AB2 metal hydrides for high-pressure and narrow temperature interval applications, J. Alloys Compd. 269 (1998) 288–293. 10.1016/S0925-8388(98)00213-8.
[38] Y. Kojima, Y. Kawai, S. Towata, T. Matsunaga, T. Shinozawa, M. Kimbara, Development of metal hydride with high dissociation pressure, J. Alloys Compd. 419 (2006) 256–261. 10.1016/j.jallcom.2005.08.078.
[39] X. Wang, R. Chen, Y. Zhang, C. Chen, Q. Wang, Hydrogen storage alloys for high-pressure suprapure hydrogen compressor, J. Alloys Compd. 420 (2006) 322–325. 10.1016/j.jallcom.2005.11.001.
[40] K.C. Chen, S.M. Allen, J.D. Livingston, Stoichiometry and alloying effects on the phase stability and mechanical properties of TiCr2-base laves phase alloys, Mater. Res. Soc. Symp. - Proc. 364 (1995) 1401–1406. 10.1557/proc-364-1401.
[41] M. Kandavel, V. V Bhat, A. Rougier, L. Aymard, G. Nazri, J. Tarascon, D.P.J. Verne, Improvement of hydrogen storage properties of the AB 2 Laves phase alloys for automotive application, Int. J. Hydrogen Energy. 33 (2008) 3754–3761. 10.1016/j.ijhydene.2008.04.042.
[42] G.U.O. Xiumei, W. Shumao, L.I.U. Xiaopeng, L.I. Zhinian, L.Ü. Fang, M.I. Jing, H.A.O. Lei, Laves phase hydrogen storage alloys for super-high-pressure metal hydride hydrogen compressors, Rare Met. 30 (2011) 227–231. 10.1007/s12598-011-0373-7.
[43] J.P. Vanhanen, M.T. Hagström, P.D. Lund, Combined hydrogen compressing and heat transforming through metal hydrides, Int. J. Hydrogen Energy. 24 (1999) 441–448.
[44] O. Beeri, D. Cohen, Z. Gavra, J.R. Johnson, M.H. Mintz, Thermodynamic characterization and statistical thermodynamics of the TiCrMn–H 2 (D 2) system, J. Alloys Compd. 299 (2000) 217–226.
[45] M. Feenstra, G. Özerol, Energy justice as a search light for gender-energy nexus: Towards a conceptual framework, Renew. Sustain. Energy Rev. 138 (2021) 110668.

10.1016/j.rser.2020.110668.
[46] C. Corgnale, M. Sulic, High pressure thermal hydrogen compression employing Ti 1 . 1 CrMn metal hydride material, JPhys Energy. 2 (2020) 014003.
[47] A.R. Galvis E, F. Leardini, J. Bodega, J.R. Ares, J.F. Fernandez, Realistic simulation in a single stage hydrogen compressor based on AB2 alloys, Int. J. Hydrogen Energy. 41 (2016) 9780–9788. 10.1016/j.ijhydene.2016.01.125.
[48] S. V Alapati, J.K. Johnson, D.S. Sholl, Predicting Reaction Equilibria for Destabilized Metal Hydride Decomposition Reactions for Reversible Hydrogen Storage, (2007) 1584–1591.
[49] W.S. Tang, P. Raybaud, R. Janot, S. Lrcs, U.M.R. Cnrs, U. De Picardie, J. Verne, Enthalpy − Entropy Compensation E ff ect in Hydrogen Storage Materials : Striking Example of Alkali Silanides MSiH 3 (M = K , Rb , Cs), J. Phys. Chem. C. 118 (2014) 3406–3419. 10.1021/jp411314w |.
[50] M.J. Boots, Theory of Enthalpy-Entropy Compensation ., (1989) 8240–8243.
[51] J. Topler, J. Lehmann, Hydrogen and Fuel Cell, Springer Berlin Heidelberg, 2016. 10.1007/978-3-662-44972-1.
[52] G. Ruitenberg, E. Woldt, A.K. Petford-long, Comparing the Johnson ± Mehl ± Avrami ± Kolmogorov equations for isothermal and linear heating conditions, Thermochim. Acta. 378 (2001) 97–105.
[53] L. Pasquini, E. Callini, E. Piscopiello, A. Montone, M.V. Antisari, L. Pasquini, E. Callini, E. Piscopiello, A. Montone, M.V. Antisari, Metal-hydride transformation kinetics in Mg nanoparticles Metal-hydride transformation kinetics in Mg nanoparticles, Appl. Phys. Lett. 041918 (2009) 10–13. 10.1063/1.3077186.
[54] J.D. HANCOCK, J.H. SHARP, Method of Comparing Solid-State Kinetic Data and Its Application to the Decomposition of Kaolinite, Brucite, and BaCO3, J. Am. Ceram. Soc. 55 (1972) 74–77. 10.1111/j.1151-2916.1972.tb11213.x.

Thesis final remarks

The main conclusions that can be stated from this PhD work related to the use of MH based on AB, AB_2 and AB_5 intermetallic compounds to compress and store hydrogen are:

- The volumetric and gravimetric capacity of the system are strongly affected by the material of the reactor and the hydride. When selecting intermetallic compounds, a system gravimetric capacity less or near 1.0 H_2 wt.% and a volumetric capacity between 15 and 30 kgH_2/m^3 are expected, independently by the amount of hydrogen stored. The design of the system can slightly affect these values.
- The storage of hydrogen as MH sensitively decreases the footprint of storage systems, resulting more suitable than compressed gas, at least at 200 bar.
- Moving from laboratory to industrial production of a hydride, the different surface properties, microstructure and phase abundance strongly affects the hydrogen sorption properties, in terms of activation, thermodynamics and kinetics, that in turns depends on the purity of the gas supply.
- The use of Phase Change Materials for the heat management of a metal hydride tank results to be promising. By performing experiments on a H2SS of about 1 kg of stored hydrogen, it was evidenced the need of an external power source just to face heat losses. Indeed, both absorption and desorption of hydrogen can be successfully managed by the PCM, especially exploiting constant hydrogen flow.
- By using commercial alloys to develop a metal hydride compressor, the maximum release pressure achievable is 250 bar working at 150 °C and filling cylinder at 200 bar.
- Studying $Ti_{1.1}(Cr,Mn,V)_2$ and $Ti_{1.1}(Cr,Mn,V,Fe)_2$ alloys, it was observed that the substitution of Fe despite Cr allows to increase the equilibrium pressure, both in absorption and in desorption. The same effect occurred increasing the amount of Mn despite Cr. Nevertheless, a remarkable increase in hysteresis is observed, concluding that Mn should not be in excess than Cr. These type of AB_2 compounds result promising for real application of high-pressure hydrogen compression thanks to an ease activation, suitable thermodynamic properties and fast kinetics of reactions. The composition $Ti_{1.1}Cr_{0.9}$ $Mn_{0.8}V_{0.1}Fe_{0.2}$ is the most promising, allowing to release H_2 up to 729 at 150 °C.

Acknowledgment

I would like to acknowledge each person that I met during these years. I had the opportunity to be involved in projects that allow me to meet people from various background, helping me in growing up professionally. A grateful acknowledge goes to the staff of Tecnodelta, to professors Xose and Paco and their group at the UAM and to Giovanni and Helge at HEREON. I would like to thank professors Baricco and Rizzi for the opportunity to improve my knowledge day after day and gave me the possibility to perform all these extraordinary professional experiences. In these years in the laboratory of Metallurgy I've found also new friends that are continuing to support and advise me: thanks Vale, Bine, Fra and Deepti. Gian says thank you is very reductive, you helped me a lot and I've learnt so much from you. Thanks for all the patience and for the support also in the difficulties.

Thanks to my friend, that stand all my *"sclero"* upon the years, Pop, Bera and Sarah.

Thanks to Giorgio for your continuous support and advice.

This work is dedicated to my mum and brother. You stand by me in all this long and eventful trip. This work is yours.

Finally, to myself (#15)